



ISSN 1028-8546

Volume XVI, Number 3-4

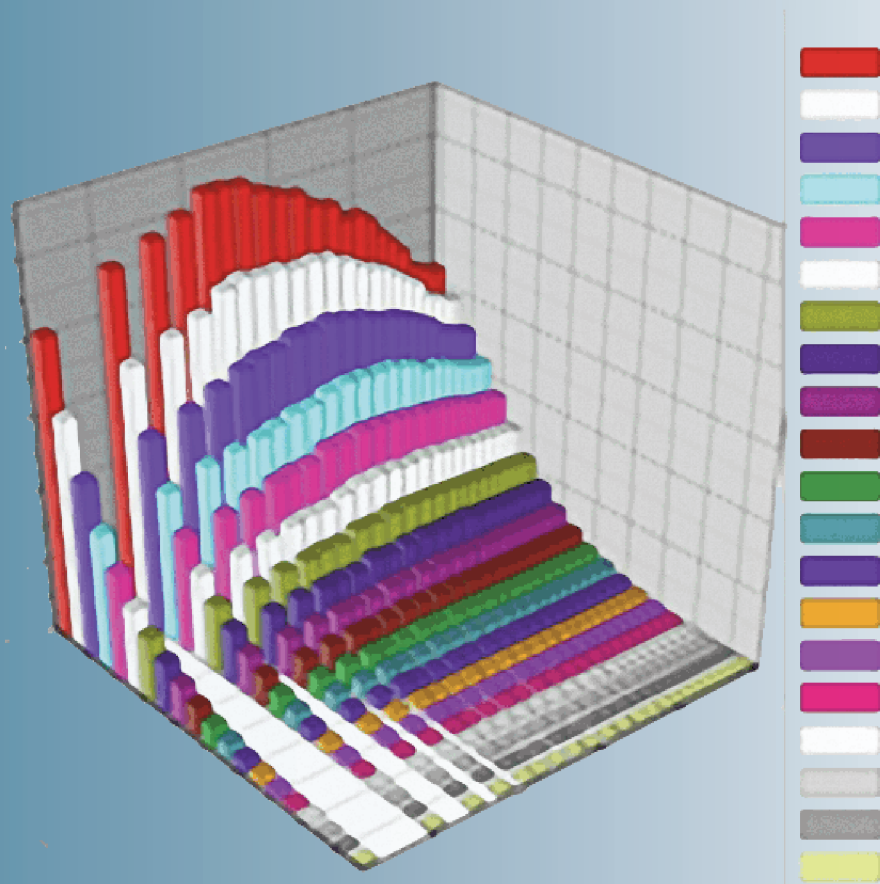
Series: En

December, 2010

Azerbaijan Journal of Physics

Fizika

www.physics.gov.az



G.M. Abdullayev Institute of Physics
Azerbaijan National Academy of Sciences
Department of Physical, Mathematical and Technical Sciences

Azerbaijan Journal of Physics

Fizika

*G.M.Abdullayev Institute of Physics
Azerbaijan National Academy of Sciences
Department of Physical, Mathematical and Technical Sciences*

HONORARY EDITORS

Arif PASHAYEV

Mahmud Kerimov

EDITORS-IN-CHIEF

Arif Hashimov
Chingiz Qajar

SENIOR EDITOR

Talat Mehdiyev

INTERNATIONAL REVIEW BOARD

Ivan Scherbakov, Russia
Kerim Allahverdiyev, Turkey
Mehmet Öndr Yetiş, Turkey
Gennadii Jablonskii,
Buelorussia
Rafael Imamov, Russia
Vladimir Man'ko, Russia
Eldar Salayev, Azerbaijan
Dieter Hochheimer, USA
Victor L'vov, Israel
Vyacheslav Tuzlukov, South
Korea

Firudin Hashimzadeh, Azerbaijan
Majid Ebrahim-Zadeh, Spain
Anatoly Boreysho, Russia
Mikhail Khalin, Russia
Hasan Bidadi, Tebriz, East
Azerbaijan, Iran
Mamed Emin Shahtakhtinskii,
Azerbaijan
Maksud Aliyev, Azerbaijan
Bahram Askerov, Azerbaijan
Vali Huseynov, Azerbaijan
Javad Abdinov, Azerbaijan

Bagadur Tagiyev, Azerbaijan
Tayar Djafarov, Azerbaijan
Natiq Atakishiyev, Mexico
Talat Mehdiyev, Azerbaijan
Nazim Mamedov, Azerbaijan
Emil Guseynov, Azerbaijan
Ayaz Baramov, Azerbaijan
Tofiq Mammadov, Azerbaijan
Rauf Guseynov, Azerbaijan
Shakir Naqiyev, Azerbaijan

TECHNICAL EDITORIAL BOARD

Talat Mehdiyev, Elmira Akhundova, Narmin Babayeva, Nazli Guseynova, Sakina Aliyeva, Nigar Akhundova

PUBLISHING OFFICE

33 H.Javid ave, AZ-1143, Baku
ANAS, G.M.Abdullayev Institute of Physics

Tel.: (99412) 439-51-63, 439-32-23
Fax: (99412) 447-04-56
E-mail: joph@physics.ab.az; joph2009@rambler.ru
Internet: www.physics.gov.az

It is authorized for printing: 12.20.2010

Published at: "ŞƏRQ-QƏRB"

17 Ashug Alesger str., Baku

Typographer :Aziz Gulaliyev

Sent for printing on: __.12. 2010
Printing approved on: __.12.2010
Physical binding: _____
Number of copies: _____200
Order: _____

METHODS OF INTEGRATION OF YANG-MILLS SELF-DUALITY EQUATIONS

M.A. MUKHTAROV

*Institute of Mathematics and Mechanics
370602, Baku, F. Agayev str. 9, Azerbaijan*

The present work is the review of the effective group-theoretical methods developed by the author of construction of the exact solutions of the Yang-Mill's autoduality equations.

1. INTRODUCTION

Over the last few years self-dual Yang-Mills equation has attracted a fair amount of attention. It has been shown [1-8] that a large number of one, two and (1+2)-dimensional integrable models such as Korteweg-de Vries, N-waves, Ernst, Kadomtsev-Petviashvili, Toda lattice, nonlinear Schrodinger equations and many others can be obtained from the four-dimensional self-dual Yang-Mills equation by symmetry reduction and by imposing the constraints on Yang-Mills potentials.

The universality of the self-dual Yang-Mills (SDYM) model as an integrable system has been confirmed in the paper [9] where the general scheme of the reduction of the Belavin-Zakharov Lax pair for self-duality [10] has been represented over an arbitrary subgroup from the conformal group of transformations of $R_{\mathcal{F}}$ space. As the result of this reduction one has the Lax pair representation for the corresponding differential equations of a lower dimension.

The problem of constructing of the instanton solutions in the explicit form for semisimple Lie algebra, rank of which is greater than two, remains also important for the present time.

The present work is the review of the effective group-theoretical methods developed by the author together with Prof. A.N.Leznov of construction of the exact solutions of the Yang-Mill's autoduality equations.

The algebraic perturbation method, known in the scientific literature as Leznov-Mukhtarov method, the Riemann problem method and a method of discrete transformations have allowed to obtain for the first time new classes of exact decisions of autoduality equations of for an arbitrary semisimple algebras [11-17].

2. ALGEBRAIC PERTURBATION METHOD

Self-dual equations are the systems of equations for the parameters of a group element G considering as the functions of four independent arguments z, \bar{z}, y, \bar{y} .

$$(G_{\bar{z}}G^{-1})_z + (G_{\bar{y}}G^{-1})_y = 0, \quad (2.1)$$

where $G_t = \partial_t G$.

The system of equations (2.1) can be partially solved

$$G_{\bar{z}}G^{-1} = +f_y, \quad G_{\bar{y}}G^{-1} = -f_z,$$

where the element f takes values in the algebra of corresponding group.

System of equations on f has the following form

$$f_{z\bar{z}} + f_{y\bar{y}} + [f_z, f_y] = 0 \quad (2.2)$$

The coupling constant in gauge theories is always introduced as a coefficient at the terms quadratic on fields and from this point of view the introduction of the interaction constant corresponds to adding of the factor g^2 at the term $[f_z, f_y]$ in eq.(2.2). From the experience of working with two-dimensional system we introduce the interaction constant in a different way as the parameter of group Inonu-Wigner deformation in the corresponding semisimple algebra, i.e., we will consider that the element f belongs not to semisimple algebra but to an algebra following from it by Inonu-Wigner deformation. Technically it means that the commutation relations between simple roots and Cartan elements of the semisimple algebra

$$[X_{\alpha}^{+}, X_{\beta}^{-}] = \delta_{\alpha\beta} h_{\alpha}, \quad [h_{\alpha}, X_{\beta}^{\pm}] = \pm K_{\beta\alpha} X_{\beta}^{\pm} \quad (2.3a)$$

transform into

$$[X_{\alpha}^{\prime+}, X_{\beta}^{\prime-}] = g^2 \delta_{\alpha\beta} h'_{\alpha}, \quad [h'_{\alpha}, X_{\beta}^{\prime\pm}] = \pm K_{\beta\alpha} X_{\beta}^{\prime\pm}. \quad (2.3b)$$

It is easy to note that when the parameter is equal to zero the semisimple algebra transforms into a solvable one but the structure of its positive and negative spaces is the same as in a semisimple algebra. Incidentally the linear equations correspond to a vanishing value of the interaction constant and the integration of the equations is trivial. The internal symmetry algebra is not semisimple but solvable, defined by relations (2.3a) and (2.3b) when $g=0$. Then the algebra of nonlinear system and of the linear system following from it by the contraction operation are the same and this makes it possible to connect them through the Backlund transformation and integrate them in an explicit form.

The contraction operation is equal to multiplication of the compound root X_{α} on $g^{n_{\alpha}}$, where n_{α} is its height (the number of simple roots from which it is formed). The generators of the space with zero graduate index are Cartan elements. The terms gX_{α}^{\pm} are the elements of the space with graduate index unity. All pair commutations $[gX_{\alpha}^{\pm}, gX_{\beta}^{\pm}]$ and the Cartan elements $g^2 X_{\alpha}^{\pm}$ are the elements of the space of graduate index 2, that is, the selection of corresponding order terms from system (2.2) is equivalent to considering that the element f belongs to the infinite dimensional solvable algebra, whose structure of graduate subspaces is described above.

We will consider the algebra of eq. (2.2) as being finite solvable or infinite dimensional. The basic vectors of the zero invariant subspace will be denoted by h_α and their corresponding functions by τ_α , that is, the element of the zero invariant subspace H is identical equal to $H = \sum_{i=1}^r h_i \tau_i$.

From (2.2) it follows that

$$\square H = 0 \quad (2.4)$$

or

$$\square \tau_i = 0, \quad (2.5)$$

i.e., τ_α is the solution of the D'Alambert equation, whose general solution depends on two arbitrary functions of three independent variables.

For the functions of the first invariant subspace X^1 , equal to $X^1 = \sum_{i=1}^r X_i^+ a^i$ we have from (2)

$$\square X^1 + [H_z, X_y^1] + [X_z^1, H_y] = 0, \quad (2.6)$$

$$\square a^i = \rho_y^i a_z^i - \rho_z^i a_y^i,$$

where ρ^i is defined by the relation

$$[H, X_i^+] = \rho^i X_i^+.$$

For the often occurring combination of the functions $(\varphi_y f_z - \varphi_z f_y)$ we introduce the notation $\{\varphi, f\}_{y,z}$. Equation (2.6) possesses the Backlund transformation of the following form:

$$\begin{aligned} a_z^i - \rho_y^i a^i &= b_y^i, \\ a_y^i + \rho_z^i a^i &= -b_z^i. \end{aligned} \quad (2.7)$$

From these relations it follows that the functions b^i satisfy the same equation (2.6) when ρ^i satisfy

$$\square \rho^i = 0$$

We will make the assumption that $b^i = \lambda a^i$. Then one rewrites system (2.7) in the form

$$\begin{aligned} a_z^i &= \rho_y^i a^i + \lambda a_y^i, \\ a_y^i &= -\rho_z^i a^i - \lambda a_z^i. \end{aligned} \quad (2.8)$$

Solving (2.8) we obtain the particular solution for (2.6) of the following form:

$$a^i = A^i(y + \lambda \bar{z}, z - \lambda \bar{y}, \lambda) \exp B^i, \quad (2.9)$$

where

$$B^i = \frac{1}{2} \left(\frac{\partial / \partial y}{\partial / \partial \bar{z} - \lambda(\partial / \partial y)} - \frac{\partial / \partial \bar{z}}{\partial / \partial \bar{y} + \lambda(\partial / \partial z)} \right) \exp \rho^i$$

Due to the fact that λ is an arbitrary parameter and the initial equation is linear for a^i , the sum of solutions is again a solution and therefore $\int a^i(\lambda) d\lambda$ will be solution of eq.(2.6) too. As is seen from the explicit relation (2.9) the solution depends on one arbitrary function of three independent arguments, but the general solution must depend on two arbitrary functions, thus the constructed solution is a particular one.

The equation of the second invariant subspace X^2

$$X^2 = \sum_{\alpha < \beta} X_{\alpha\beta}^+ a^{\alpha\beta}, \quad X_{\alpha\beta}^+ = [X_\alpha^+, X_\beta^+],$$

has the form

$$\square X^2 + [H_z, X_y^2] + [X_z^2, H_y] + [X_z^1, X_y^1] = 0$$

or

$$\square a^{\alpha\beta} + \{\rho^\alpha + \rho^\beta, a^{\alpha\beta}\}_{zy} + \{a^\alpha, a^\beta\}_{zy} = 0. \quad (2.10)$$

Equation (2.10) is a nonhomogeneous one, whose non-homogeneities are given by the constructed functions a^i . One of the particular solutions of this equation has the following form:

$$B^{\alpha\beta} = \frac{1}{2} \int a^{\alpha\beta}(\lambda) d\lambda,$$

Where

$$a^{\alpha\beta}(\lambda) = [a^\alpha(\lambda), a^\beta(\lambda)]^1$$

By the commutation of two functions f, g we obtain the following expression:

$$[f(\lambda), g(\lambda)]^1 = f(\lambda) \int \frac{g(\lambda') d\lambda'}{\lambda - \lambda'} - g(\lambda) \int \frac{f(\lambda') d\lambda'}{\lambda - \lambda'}$$

Using relations (2.8) and carrying out a number of identical algebraic transformations we get that $\frac{1}{2} \int [a^\alpha(\lambda), a^\beta(\lambda)]^1 d\lambda$ satisfies (2.10). Adding to obtained solution the solution of a homogeneous equation according to scheme (2.8) we get a particular solution of (2.10) dependent on one more function of three variables. The general scheme of reduction is the following: for the function of the n th invariant subspace we have the equation

□

$$X^n + [H_z, X_y^n] + [X_z^n, H_y] + \sum_{k=1}^{n-1} [X_z^k, X_y^{n-k-1}] = 0$$

The assertion of reduction consists of the fact that the particular solution of this equation

$$B^{\alpha_1, \alpha_2, \dots, \alpha_n} = \frac{1}{n!} \int a^{\alpha_1, \alpha_2, \dots, \alpha_n}(\lambda) d\lambda$$

is defined by the use of the previous reduction stages by the formula

$$a^{\alpha_1, \alpha_2, \dots, \alpha_n} = \sum_{s=1}^{n-1} C_{n-2}^{s-1} [a^{\alpha_1, \alpha_2, \dots, \alpha_s}, a^{\alpha_{s+1}, \dots, \alpha_n}]^1. \quad (2.11)$$

Finally, formula (2.11) solves the problem of constructing the solutions of (2.6) in the case of semisimple algebra, moreover the constructed solutions depend on arbitrary functions, the number of which is equal to the sum of the dimension of algebra and the dimension of its invariant subspace with the zero graduate index, and gives the explicit expressions for each function of the invariant subspace with the finite graduate index.

3. RIEMANN-HILBERT PROBLEM METHOD

It is possible to generalize the so-called't Hooft's solutions to the case of arbitrary semisimple Lie algebra and in the special case to find $O(4)$ -invariant solution with topological charge equal to one. The solution depends on r -independent linear self-dual systems, each of which contains $2\omega_\alpha + 1$, where ω_α are indexes of the semisimple algebra. The $O(4)$ -invariant solution, having no singularities in the whole four dimensional space, arises when the solutions of chains of linear systems are simply numerical constants.

From the group of motion of four dimensional space $(x_1, x_2, x_3, x_4) \in R(4)$ let us choose the group $SU(2)$ which transforms the pair complex coordinates y, z ($y = x_1 + x_2; z = x_3 + x_4$) as the components of the two-dimensional (spinor) representation of this group. The components of conjugated spinor $(\bar{z}, -\bar{y})$ and any linear combination of the form $(y + \lambda\bar{z}, z - \lambda\bar{y})$ are transformed at the same way. The infinitesimal operators of this algebra $L_\pm, L_0(H)$ have the form

$$\begin{aligned} L^+ &= y \frac{\partial}{\partial \bar{z}} - \bar{z} \frac{\partial}{\partial \bar{y}}, \\ L^- &= z \frac{\partial}{\partial y} - \bar{y} \frac{\partial}{\partial \bar{z}}, \\ L^0 &= y \frac{\partial}{\partial y} - z \frac{\partial}{\partial \bar{z}} + \bar{z} \frac{\partial}{\partial \bar{z}} - \bar{y} \frac{\partial}{\partial \bar{y}} \end{aligned}$$

The algebra $SL(2, R)$ may be embedded in gauge algebra in many unequivalent ways. Here we shall use the so-called principal embedding, the infinitesimals operators of which are defined as:

$$J_\pm = \sum_{i=0}^r \sqrt{\omega_i} X_i^\pm, \quad H = \sum_{i=0}^r \omega_i h_i$$

where X_i, h_i are the generators of the simple roots and Cartan elements of a semisimple algebra, $\omega_j = \sum_{i=0}^r (k^{-1})_{ji}$ is the set of its indexes, k is the Cartan matrix and r is its rank.

The generators of a semisimple algebra can be decomposed into multiplets, i.e., they may be marked by the quantum numbers (l, m) of irreducible representation of the $SL(2, R)$ algebra. We are interested in the solution of self-dual equations, which are invariant with respect to the total momentum $\vec{S} = \vec{J} + \vec{L}$. For this purpose we need our element F_0 from the algebra which satisfies the reduction condition

$$[F_0, \vec{S}] = 0$$

To construct such an element let us notice that from the components of a spinor we may construct $(2l+1)$ -ordered vectors $\xi_\alpha^l = (y + \lambda\bar{z})^{2l-\alpha} (z - \lambda\bar{y})^\alpha$ ($0 \leq \alpha \leq 2l$) which are transformed according to the $(2l+1)$ -dimensional representation of the algebra $SL(2, R)$. Contracting these vectors with generators of gauge algebra, having the same quantum numbers, we get the invariant F_l^0 connected with the l -multiplet.

For instance, three basic vectors $(z - \lambda\bar{y})^2, (y + \lambda\bar{z})(z - \lambda\bar{y}), (y + \lambda\bar{z})^2$ are transformed according to vector representation of the $SL(2, R)$ algebra and the corresponding invariant has the form:

$$F_0^1 = (z - \lambda\bar{y})^2 J_- + (y + \lambda\bar{z})(z - \lambda\bar{y}) H + (y + \lambda\bar{z})^2 J_+$$

as can be verified by direct calculations.

In general,

$$F_0 = \sum_{i=1}^r c_i F_0^i$$

where summation is over all multiplets of the algebra.

As F_0 is invariant with respect to the total momentum it is always possible to transform it to the coordinate system where

$$y = \bar{y} = 0, \quad z = \bar{z} = \sqrt{R}, \quad R = y\bar{y} + z\bar{z};$$

so F_0 may be presented in the form

$$F_0 = T(\exp(J_- \lambda) \sum_{\alpha=1}^r c_\alpha R^{\omega_\alpha} J_+^\alpha \exp(-J_- \lambda)) T^{-1} \quad (3.1)$$

where

$$T = \exp(-J_+ \frac{\bar{y}}{z}) \exp(J_+ \frac{y\bar{z}}{R}) \exp(H \ln \frac{R}{z})$$

J_+^α is highest vector of α -multiplet, having the properties

$$[H, J_+^\alpha] = 2\omega_\alpha J_+^\alpha, \quad [J_+^\alpha, J_+^\beta] = 0$$

The last commutativity relations of the highest vectors belonging to different multiplets distinguish the principal embedding from the others.

Let us rewrite the self-dual equations in Yang's form

$$G^{-1} G_{\bar{z}} = +f_y, \quad G^{-1} G_{\bar{y}} = -f_z, \quad (3.2)$$

where the elements G and f take values in the gauge group and gauge algebra respectively. To integrate Eq.(3.2) it is necessary to solve the homogeneous Riemann problem

$$e^{F_0} = \Omega_c^+ = \Omega_c^-, \quad (3.3)$$

where are the boundary values of analytical functions, taking values in the gauge group, and are defined outside and inside of the contour c , respectively; F_0 is an arbitrary function of three independent variables $F_0(y + \lambda\bar{z}, z - \lambda\bar{y}, \lambda)$ taking values in the gauge algebra. The boundary condition for (3.2) is

$\Omega^+ \rightarrow 1 + \frac{F}{\lambda}$ when $\lambda \rightarrow \infty$. The point $\lambda = 0$ is

inside and the point $\lambda = \infty$ is outside the contour c . Using the usual methods for the Riemann problem it may be proved that Eqs.(3.2) are fulfilled if we take $G = \Omega^-|_{\lambda=0}$, $f = F$ are taken from the solution of Riemann problem.

If we want to find the solution of the self-dual equations, which are invariant with respect to the total momentum S , we must take F_0 in form (3.1), where c_α are arbitrary functions of λ : $c_\alpha = c_\alpha(\lambda)$.

Here we shall consider the more general case supposing that $c_\alpha = c_\alpha(y + \lambda\bar{z}, z - \lambda\bar{y}, \lambda)$. The same arguments will be used for the function F_0 .

Now we shall solve the Riemann problem for this case.

First of all, we include the element T , which is λ independent, and rewrite (3.3) in the form

$$(\exp \sum c_\alpha J_\alpha^+) e^{-\lambda J^-} \Omega_c^+ = e^{-\lambda J^-} \Omega_c^-$$

From this moment we include the factor R^{ω_α} in c_α : $c_\alpha R^{\omega_\alpha} \rightarrow c_\alpha$.

Let us perform some identical transformations:

$$\begin{aligned} (\exp \sum c_\alpha J_\alpha^+) e^{-\lambda J^-} &= (\exp \sum \tilde{c}_\alpha J_\alpha^+) e^{J^+/\lambda} e^{-\lambda J^-} = \\ &= (\exp \sum \tilde{c}_\alpha J_\alpha^+) M e^{H \ln \lambda} e^{-J^+/\lambda}, \\ \tilde{c}_\alpha &= c_\alpha - \partial_{1\alpha} / \lambda, \quad M J_\alpha^+ M^{-1} = (-1)^\alpha J_\alpha^- . \end{aligned}$$

Taking into account the commutativity of the highest vectors $[J_\alpha^+, J_\beta^+] = 0$ and using the Sokhotsky-Plemeli formulae, we have

$$\begin{aligned} & \left((\exp \sum c_\alpha^+ J_\alpha^-) e^{H \ln \lambda} e^{-J^+/\lambda} \Omega^+ \right)_c = \\ & = \left((\exp \sum c_\alpha^- J_\alpha^-) M e^{-\lambda J^-/\lambda} \Omega^- \right)_c \equiv p(\lambda), \end{aligned} \quad (3.4)$$

where

$$c_\alpha^+(\lambda) = \int \frac{c_\alpha(\lambda') d\lambda'}{\lambda - \lambda'}; \quad (c_\alpha^+(\lambda) - c_\alpha^-(\lambda))_c = \tilde{c}_\alpha(\lambda)$$

All factors of the left-hand side of (3.4) are analytical outside the integration contour and the ones on the right-hand side - inside it. Thus, from the Liouville theorem we may conclude that the function $p(\lambda)$ taking values in the group has in any representation the matrix elements which are polynomial over λ in the whole complex plane.

The asymptotic condition

$$\Omega^+ \rightarrow 1 + \frac{F}{\lambda}$$

allows us to find the coefficients of polynomials of each matrix element and to solve the self-dual equations in the case under consideration.

To make the situation clearer we shall use the method in the simplest case of the $SL(2, R)$ gauge algebra.

Let's parameterize the group element $e^{-J^+/\lambda} \Omega^+$ by Euler's angles:

$$e^{-J^+/\lambda} \Omega^+ = \exp \alpha J_+ \exp \tau H \exp \beta J_-$$

and take the elements J_\pm, H in two dimensional representation. Under these assumptions Eq.(3.4) takes the form:

$$\left(\begin{array}{cc} \lambda e^\tau & \lambda \beta e^\tau \\ \lambda(c_1^+ + \frac{1}{\lambda^2} \alpha) e^\tau & \lambda(c_1^+ + \frac{1}{\lambda^2} \alpha) \beta e^\tau + \frac{1}{\lambda} e^{-\tau} \end{array} \right) = \quad (3.5)$$

$$= p(\lambda) = \begin{pmatrix} \lambda + \tau_0 & \beta_0 \\ c_0 & 0 \end{pmatrix}$$

where we have used the asymptotic expansion of the Cauchy integral at the infinite point

$$\theta = \frac{1}{2\pi i} \int \frac{\theta(\lambda') d\lambda'}{\lambda - \lambda'} = \frac{\theta_0}{\lambda} + \frac{\theta_1}{\lambda^2} + \dots + \frac{\theta_n}{\lambda^n} + \dots ,$$

$$\theta_m = \frac{1}{2\pi i} \int (\lambda')^m \theta(\lambda') d\lambda'$$

and the asymptotical conditions

$$e^{-J^+/\lambda} \Omega^+ \rightarrow 1 + \frac{F - J_+}{\lambda} + \dots$$

i.e.

$$e^\tau \Big|_{\lambda \rightarrow \infty} = 1 + \frac{\tau_0}{\lambda} + \dots ,$$

$$\alpha \Big|_{\lambda \rightarrow \infty} = \sum_{s=0}^{\infty} \frac{\alpha_s}{\lambda^{s+1}} ,$$

$$\beta \Big|_{\lambda \rightarrow \infty} = \sum_{s=0}^{\infty} \frac{\beta_s}{\lambda^{s+1}}$$

From (3.5) we have

$$e^\tau = 1 + \frac{\tau_0}{\lambda} ,$$

$$\alpha = \lambda^2 \left(\frac{c_0}{\lambda + \tau_0} - c_1 \right) = -(c_2 + c_0 \tau_0) + \frac{c_0 \tau_0^2 - c_2}{\lambda} + \dots$$

i.e.

$$\tau_0 = -\frac{c_1}{c_0} , \quad \alpha_0 = -c_2 + \frac{c_1^2}{c_0}$$

In the same way we get $\beta_0 = -\frac{1}{c_0}$ and for f we

have:

$$f = J_+ + \beta_0 J_+ + \tau_0 H + \alpha_0 J_- =$$

$$= J_+ \left(1 - \frac{1}{c_0} \right) - H \frac{c_1}{c_0} + J_- \left(-c_2 + \frac{c_1^2}{c_0} \right)$$

After the necessary transformation $f \rightarrow T^{-1} f T$ and some trivial gauge transformation f turns into the 't Hooft solution in its usual form

$$f = J_+ \frac{1}{\varphi_0} - H \frac{\varphi_1}{\varphi_0} + J_- \left(-\varphi_2 + \frac{\varphi_1^2}{\varphi_0} \right)$$

where $\varphi_0, \varphi_1, \varphi_2$ are the terms of the chain of the self-dual linear equations which are connected with c_0, c_1, c_2 by the relations

$$\varphi_0 = c_0 + \frac{1}{R} ,$$

$$\varphi_1 = c_1 + \frac{y}{\bar{z}} \frac{1}{R} ,$$

$$\varphi_2 = c_2 + \left(\frac{y}{\bar{z}} \right)^2 \frac{1}{R}$$

For the solution of self-duality equation for an arbitrary semisimple algebra using the above approach we refer to [11].

4. DISCRETE SYMMETRY TRANSFORMATION METHOD

Following [12], for the case of a semisimple Lie algebra and for an element f being a solution of (2.2), the following statement takes place:

There exists such an element S taking values in a gauge group that

$$S^{-1} \frac{\partial S}{\partial Y} = \frac{1}{\tilde{F}_-} \left[\frac{\partial \tilde{F}}{\partial Y} , X_M \right] - \frac{\partial}{\partial \bar{Z}} \frac{1}{\tilde{F}_-} X_M \quad (4.1)$$

$$S^{-1} \frac{\partial S}{\partial Z} = \frac{1}{\tilde{F}_-} \left[\frac{\partial \tilde{F}}{\partial Z} , X_M \right] + \frac{\partial}{\partial \bar{Y}} \frac{1}{\tilde{F}_-} X_M$$

Here X_M is the element of the algebra corresponding to its maximal root divided by its norm, i.e.,

$$\left[X_M^+ , X^- \right] = H , \quad \left[H , X^\pm \right] = \pm 2X^\pm ,$$

- \tilde{F}_- - is the coefficient function in the decomposition of \tilde{F} of the element corresponding to the minimal root of the algebra, $\tilde{F} = \sigma f \sigma^{-1}$ and where σ is an automorphism of the algebra, changing the positive and negative roots.

In the case of algebra $SL(3, \mathbb{C})$ we'll consider the case of three dimensional representation of algebra and

the following form of $\sigma = \begin{pmatrix} 0 & 0 & 1 \\ 0 & 1 & 0 \\ -1 & 0 & 0 \end{pmatrix}$.

The discrete symmetry transformation, producing new solutions from the known ones, is as follows:

$$\frac{\partial F}{\partial Y} = S \frac{\partial \tilde{F}}{\partial Y} S^{-1} + \frac{\partial S}{\partial \bar{Z}} S^{-1},$$

3. Let's represent the explicit formulae for transformation of the self-duality equations in the case of SL(2,C) algebra

$$\frac{\partial F}{\partial Z} = S \frac{\partial \tilde{F}}{\partial Z} S^{-1} - \frac{\partial S}{\partial \bar{Y}} S^{-1} \quad (4.2)$$

$$f = \alpha_1 X_1^+ + \alpha_2 X_2^+ + \alpha_{1,2} X_{1,2}^+ + \tau_1 h_1 + \tau_2 h_2 + a_1 X_1^- + a_2 X_2^- + a_{1,2} X_{1,2}^-, \quad (4.3)$$

In connection with the general scheme, first of all, it is necessary to find the solution of the equations (4.1) for the SL(3,C) valued function S for given f , solution of self-duality equation (2.2).

From (3) it is clear that S is upper triangular matrix and can be represented in the following form:

$$S = \exp \beta_1 X_1^+ \exp \beta_{1,2} X_{1,2}^+ \exp \beta_2 X_2^+ \exp \beta_0 H, \quad (4.4)$$

where $H=h_1+h_2$.

After substitution of the last representation of S into (4.1) and taking into account (4.2), we have at every step of the recurrent procedure the following relations

$$\begin{aligned} \beta_0 &= \ln \alpha_{1,2}, \quad \beta_1 = \alpha_2, \quad \beta_2 = \alpha_1 \\ (\beta_{1,2})_Y &= (\alpha_{1,2})_{\bar{Z}} - (\delta_1 + \delta_2)_Y \alpha_{1,2} - (\alpha_1)_Y \alpha_2 \\ (\beta_{1,2})_Z &= -(\alpha_{1,2})_{\bar{Y}} - (\delta_1 + \delta_2)_Z \alpha_{1,2} - (\alpha_1)_Z \alpha_2 \end{aligned} \quad (4.5)$$

As the initial solution we'll take the explicit solution f belonging to the algebra of upper triangular matrixes:

$$f = \alpha_1 X_1^+ + \alpha_2 X_2^+ + \alpha_{1,2} X_{1,2}^+ + \tau_1 h_1 + \tau_2 h_2 \quad (4.6)$$

The component form of self-duality equations for this case is following

$$\begin{aligned} \square \tau_i &= 0, \quad \square \alpha_i = \{\delta_i, \alpha_i\}_{Y,Z}, \quad i=1,2, \\ \square \alpha_{1,2} &= \{\delta_1 + \delta_2, \alpha_{1,2}\}_{Y,Z}, \end{aligned} \quad (4.7)$$

where $\square = \frac{\partial^2}{\partial Z \partial \bar{Z}} + \frac{\partial^2}{\partial Y \partial \bar{Y}}$; $\delta_1 = 2\tau_1 - \tau_2$, $\delta_2 = 2\tau_2 - \tau_1$ and figure brackets of two functions g_1 and g_2 denotes :

$$\{g_1, g_2\}_{Y,Z} = \frac{\partial g_1}{\partial Y} \frac{\partial g_2}{\partial Z} - \frac{\partial g_2}{\partial Y} \frac{\partial g_1}{\partial Z}.$$

The general solution of system (4.7) takes the form

$$\begin{aligned} \tau_i &= \oint_c \tau_i(\lambda) d\lambda, \quad \alpha_i = \oint_c \alpha_i(\lambda) \exp(-\bar{\delta}_i(\lambda)) d\lambda, \\ \bar{\delta}_i(\lambda) &= \oint_c \frac{d\lambda' \delta_i(\lambda')}{\lambda - \lambda'}, \quad i = 1,2, \end{aligned}$$

$$\alpha_{1,2} = \oint_c \alpha_{1,2}(\lambda) \exp(-\bar{\delta}_1(\lambda) - \bar{\delta}_2(\lambda)) d\lambda + \oint_c \alpha_1(\lambda) \exp(-\bar{\delta}_1(\lambda)) d\lambda \oint_c \frac{d\lambda' \alpha_2(\lambda') \exp(-\bar{\delta}_2(\lambda'))}{\lambda - \lambda'} \quad (4.8)$$

Here the circle integration goes over the complex parameter λ and all integrated functions are arbitrary functions of three independent variables $(y + \lambda \bar{z}, z - \lambda \bar{y}, \lambda)$.

By the direct check one can be convinced that (4.8) are the solutions of equations (4.7).

Let's represent two types of Backlund transformation by means of which one can construct new types of solutions of equations (9) from the known solution (10). For solutions of first two equations of (9) this two Backlund transformations are the same:

$$(\alpha_i^k)_{\bar{z}} - (\delta_i)_y \alpha_i^k = (\alpha_i^{k+1})_y - (\alpha_i^k)_{\bar{y}} - (\delta_i)_z \alpha_i^k = (\alpha_i^{k+1})_z, \quad i = 1, 2 \quad (4.9)$$

For solutions of the third equation of the system (4.7) they are different:

$$\begin{aligned} (\alpha_{1,2}^{0,k})_{\bar{z}} - (\delta_1 + \delta_2)_y \alpha_{1,2}^{0,k} - (\alpha_1^k)_y \alpha_2^k &= (\alpha_{1,2}^{0,k+1})_y \\ - (\alpha_{1,2}^{0,k})_{\bar{y}} - (\delta_1 + \delta_2)_z \alpha_{1,2}^{0,k} - (\alpha_1^k)_z \alpha_2^k &= (\alpha_{1,2}^{0,k+1})_z \end{aligned} \quad (4.10)$$

and

$$\begin{aligned} (\alpha_{1,2}^{k,0})_{\bar{z}} - (\delta_1 + \delta_2)_y \alpha_{1,2}^{k,0} + \alpha_1^k (\alpha_2^k)_y &= (\alpha_{1,2}^{k+1,0})_y \\ - (\alpha_{1,2}^{k,0})_{\bar{y}} - (\delta_1 + \delta_2)_z \alpha_{1,2}^{k,0} + \alpha_1^k (\alpha_2^k)_z &= (\alpha_{1,2}^{k+1,0})_z \end{aligned} \quad (4.11)$$

Note that starting, zero step of upper transformations procedure coincides with initial solutions (4.8).

Let's return to the solution of the equation (4.5) at the first step of the recurrent procedure. Comparing (4.5) and (4.11) we came to the conclusion that $\beta_{1,2}^{0,1} = \alpha_{1,2}^{0,1}$.

Finally, knowing all components of matrix S and using (4.2) we can express the solution

$$F = F_1^+ X_1^+ + F_2^+ X_2^+ + F_{1,2}^+ X_{1,2}^+ + F_1^0 h_1 + F_2^0 h_2 + F_1^- X_1^- + F_2^- X_2^- + F_{1,2}^- X_{1,2}^-$$

of self-duality equations at the first step of the recurrent procedure in terms of chains (4.9)-(4.11):

$$\begin{aligned} F_1^0 &= \tau_1 + \frac{\alpha_{1,2}^{1,0}}{\alpha_{1,2}^{0,0}}, \quad F_2^0 = \tau_2 + \frac{\alpha_{1,2}^{0,1}}{\alpha_{1,2}^{0,0}} \\ F_{1,2}^- &= \frac{1}{\alpha_{1,2}^{0,0}}, \quad F_1^- = \frac{\alpha_2^0}{\alpha_{1,2}^{0,0}}, \quad F_2^- = -\frac{\alpha_1^0}{\alpha_{1,2}^{0,0}} \\ F_1^+ &= -\frac{1}{\alpha_{1,2}^{0,0}} \begin{vmatrix} \alpha_1^0 & \alpha_1^1 \\ \alpha_{1,2}^{0,0} & \alpha_{1,2}^{1,0} \end{vmatrix}, \quad F_2^+ = -\frac{1}{\alpha_{1,2}^{0,0}} \begin{vmatrix} \alpha_2^0 & \alpha_2^1 \\ \alpha_{1,2}^{0,0} & \alpha_{1,2}^{0,1} \end{vmatrix}, \quad F_{1,2}^+ = \frac{1}{\alpha_{1,2}^{0,0}} \begin{vmatrix} \alpha_{1,2}^{0,0} & \alpha_{1,2}^{0,1} \\ \alpha_{1,2}^{1,0} & \alpha_{1,2}^{1,1} \end{vmatrix} \end{aligned}$$

-
- | | |
|--|---|
| <p>[1] R.S. Ward, <i>Phil. Trans. R. Soc. Lond.</i>A315, 451 (1985); <i>Lect. Notes Phys.</i>, 1987, 280, 106; <i>Lond. Math. Soc. Lect. Notes Ser.</i>, 1990, 156, 246.</p> <p>[2] L.J. Mason and G.A. J.Sparling. <i>Phys. Lett.</i>, 1989, A137, 29; <i>J. Geom. and Phys.</i>, 1992, 8, 243.</p> <p>[3] S. Chakravarty, M.J. Ablowitz and P.A. Clarkson. <i>Phys. Rev. Lett.</i>, 1990, 1085.</p> <p>[4] I. Bakas and D.A. Depireux. <i>Mod. Phys. Lett.</i>, 1991, A6, 399.</p> <p>[5] M.J. Ablowitz, S. Chakravarty and L.A. Takhtajan. <i>Comm. Math. Phys.</i>, 1993, 158, 1289.</p> <p>[6] T.A. Ivanova and A.D. Popov. <i>Phys. Lett.</i>, 1992, A170, 293.</p> <p>[7] L.J. Mason and N.M.J. Woodhouse. <i>Nonlinearity</i> 1, 1988, 73; 1993, 6, 569.</p> | <p>[8] M. Kovalyov, M. Legare and L. Gagnon. <i>J. Math. Phys.</i>, 1993, 34, 3425.</p> <p>[9] M. Legare and A.D. Popov. <i>Pis'ma Zh. Eksp. Teor. Fiz.</i>, 1994, 59, 845.</p> <p>[10] A.A. Belavin and V.E. Zakharov. <i>Phys. Lett.</i>, 1978, B73, 53.</p> <p>[11] A.N. Leznov and M.A. Mukhtarov. <i>J. Math. Phys.</i>, 1987, 28 (11), 2574; <i>Prepr. IHEP</i>, 1987, 87-90. <i>Prepr. ICTP 163</i>, Trieste, Italy, 1990; <i>J. Sov. Lazer Research</i>, 13 (4), 284, 1992.</p> <p>[12] A.N. Leznov. <i>IHEP preprint-92/87</i>, 1990.</p> <p>[13] A.N. Leznov, M.A. Mukhtarov and W.J. Zakrzewski. <i>Tr. J. of Physics</i> 1995, 19, 416.</p> |
|--|---|

INVESTIGATIONS ON PRESSURE INDUCED PHASE TRANSITION AND DISORDER IN ZnAl_2Se_4

S. MEENAKSHI^a, V. VIJAYAKUMAR^{a+}, A. EIFLER^b, H. D. HOCHHEIMER^c

^a*High Pressure and Synchrotron Radiation Physics Division, Purnima Labs,
Bhabha Atomic Research Centre, Mumbai 400 085, India*

^b*Klebendorfer Strasse 47a, D-04425 Taucha, Germany*

^c*Department of Physics, Colorado State University, Fort Collins, CO 80523, USA*

Results of angle dispersive X-ray diffraction (ADXRD) measurements on the defect chalcopyrite (DCP) compound, ZnAl_2Se_4 , up to 31.5 GPa is presented. The ambient tetragonal phase is retained in ZnAl_2Se_4 up to about 10.5 GPa. The value of the bulk modulus estimated from pressure-volume data is 43.7 GPa in the chalcopyrite phase. The high pressure and the pressure quenched phases have a disordered rock salt and a disordered zinc blende structure with broad X-ray diffraction lines as is the case with the other chalcopyrites. Reverse Monte Carlo (RMC) simulations of the X-ray diffraction data carried out indicate that the disorder in the NaCl phase is due to a partial retention of the four fold coordination in addition to the random mixing of metal ions and vacancies. In the ZnS phase, the disorder is due to the random mixing of metal ions and vacancies.

PACS: 64.30.Jk, 61.50.Ks, 64.60.Cn, 61.43.Bn

Keywords: C. X-ray diffraction, C. High Pressure, A. Semiconductors, A. Optical materials, C. Reverse Monte Carlo simulations

I. INTRODUCTION

The tetrahedral coordination and the covalent bonding found in the diamond structure of group IV elements is retained in the binary ZnS, and the ternary $\text{A}_n\text{B}_{4-n}\text{C}_4$ ($n = 1, 2$ and 3) and the $\text{A}^{\text{II}}\text{B}_2^{\text{III}}\text{C}_4^{\text{VI}}$ materials, but with incremental disorder or ordered vacancies [1]. They form a natural bridge between the perfect and disordered crystals. The large band gap semiconducting ternary materials of the type $\text{A}^{\text{II}}\text{B}_2^{\text{III}}\text{C}_4^{\text{VI}}$ belonging to this category, crystallize in the defect chalcopyrite (DCP) tetragonal structure and have crystallographically ordered arrays of vacancies in the cation (A and B) sublattice [2]. Under pressure these DCP compounds are expected to exhibit high compression and large tunability of physical properties. Several $\text{A}^{\text{II}}\text{B}_2^{\text{III}}\text{C}_4^{\text{VI}}$ compounds have been extensively investigated both theoretically and experimentally for their high pressure behavior [2-13]. Available data indicate that most of them transform to a disordered rock-salt structure under pressure and to a metastable disordered ZnS structure on pressure release [4-8]. This behavior has implications on pressure induced disordering/ amorphization..

Several qualitative and some microscopic models have recently evolved to account for this interesting phenomenon. Martensitic crystal-crystal transformations with increasing pressure yielding a nano-crystalline structure depending on the defect density, compression

rate, and nucleation and growth barriers have recently been proposed. According to another model [14], if one or more flat branches of the phonon spectrum of a material become soft with increasing pressure, then a displacive disorder that can account for the range of the features displayed by many materials that undergo amorphization can occur. The study of amorphization of materials with inbuilt disorder such as DCP materials is hence interesting and can aid in the formulation of general microscopic models of pressure-induced amorphization.

In the present study we supplement our earlier high pressure structural and spectroscopic studies on HgAl_2Se_4 , CdAl_2S_4 , ZnAl_2Se_4 and CdAl_2Se_4 [6,7] with structural investigation and Reverse Monte Carlo (RMC) simulations of disordering under compression on ZnAl_2Se_4 .

II. EXPERIMENTAL DETAILS

ZnAl_2Se_4 was grown using the usual chemical vapor transport (CVT) with iodine as transporting agent [15]. The ambient pressure lattice parameters (Table I) of ZnAl_2Se_4 agree with the literature values. High pressure angle dispersive X-ray diffraction (ADXRD) measurements were carried out on powdered samples obtained by crushing single crystal pieces of ZnAl_2Se_4 .

Table I / Ambient, high pressure, and pressure released lattice parameters for ZnAl_2Se_4 .

Sample	$a_{\text{ambient}} (\text{\AA})$	$c_{\text{ambient}} (\text{\AA})$	$V_{\text{ambient}} (\text{\AA}^3)$	P_{max} (GPa)	High pressure phase (Fm-3m) a (\AA)	Pressure released phase (F-43m) a (\AA)
ZnAl_2Se_4	5.529	10.879	332.569	31.6	4.9868	5.4574

The synchrotron radiation source at Elettra, Trieste, Italy and a Mao-Bell type diamond anvil cell (DAC) was employed for these measurements. Fine powder of ZnAl_2Se_4 along with platinum as the internal pressure calibrant was loaded in a 150 μm hole of a hardened

stainless steel gasket pre-indented to a thickness of 50 μm and centered on a 400 μm diamond anvil indentation. A 4:1 methanol-ethanol mixture was used as the pressure transmitting medium. X-ray diffraction patterns were

collected using an image plate area detector (MarResearch). The sample to image plate distance and the wavelength ($\lambda = 0.688 \text{ \AA}$) were calibrated using LaB_6 as a standard. The X-ray data was collected up to a pressure of 31.5 GPa with a typical exposure time of about 15 to 20 minutes employing beam of size $80 \mu\text{m}$. The scanned two-dimensional diffraction patterns were corrected for imaging plate tilt and converted to intensity versus 2θ plots through radial integration using FIT2D software [16]. The lattice parameters of the sample and pressure calibrant were determined by carrying out full profile refinement using GSAS software [17]. The typical R_p and wR_p factor of the fit was about 2.5% and 4.3% respectively.

III RESULTS AND DISCUSSION

III A X-RAY DIFFRACTION

The evolution of the diffraction pattern for ZnAl_2Se_4 at various pressures is shown in Fig.1.

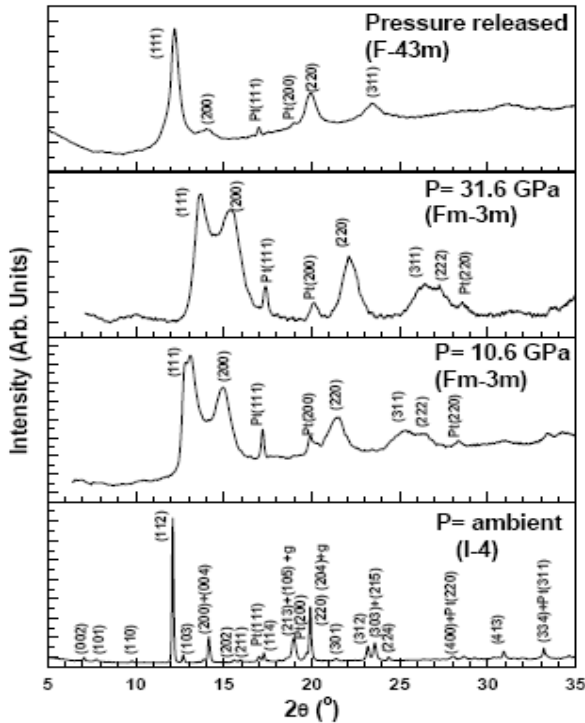


Fig.1 Evolution of the diffraction pattern with pressure for ZnAl_2Se_4 .

It is found that ZnAl_2Se_4 transform to a disordered rock salt (SG: Fm-3m) structure with broad diffraction lines above 10.5 GPa. The disordered NaCl phase is stable up to the highest pressure of the current measurements. Prior to the transition to the disordered phase, there is a mixed phase region where the sharp lines of the tetragonal phase coexist with the broad lines of the NaCl phase. This indicates that the broad diffraction peaks are an intrinsic property of the material in the disordered phase and not due to a pressure gradient. Upon pressure release, the diffraction pattern was different from that of the initial phase as well as from the high-pressure phase. This pattern, again with broad diffraction lines, could be fitted to a disordered zinc blende (SG: F-43m) structure. It may be noted that this type of disordered

phases occur in most of the DCP structured materials under pressure. Table 1 lists the high pressure as well as pressure released lattice parameters for ZnAl_2Se_4 .

The pressure volume (P-V) data for ZnAl_2Se_4 is shown in Fig. 2. The P-V data show a small kink around 4 GPa, although the diffraction pattern at this pressure show no change in the intensity distribution. A similar kink has been observed in the equation of state data of HgAl_2Se_4 [7]. High pressure Raman studies [6] on HgAl_2Se_4 and ZnAl_2Se_4 also show that band width changes occur for most of the bands in the pressure range between 4-6 GPa and these changes were assigned to the two stage order-disorder transition. Because of the low pressure kink and inability to slowly increase the pressure in the low pressure region (in the absence of a ruby pressure measuring setup), the P-V data points below the kinks are few and hence the bulk modulus could only be estimated (43.7 GPa). This indicates that in spite of covalent bonding, the material is very compressible in the DCP phase.

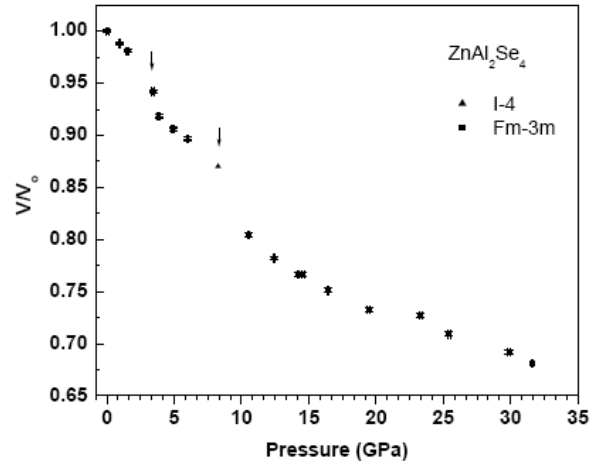


Fig. 2. Equation of state for ZnAl_2Se_4 . \blacktriangle : tetragonal phase (SG: I-4); \blacksquare : disordered rock salt phase (SG: Fm-3m). The arrows indicate the pressures where the PV curve shows discontinuities. The size of the symbol indicate the typical error bars for the volume compression and pressure.

High pressure Raman studies on most of the DCP materials [2,3,6,9] show that the band width decreases for most of the bands in the pressure range between 4-6 GPa before increasing as the transition pressure is approached. Such sharpening of Raman bands prior to a transition is a clear indication that these modes are becoming less dispersive (flat) under pressure. [The collection optics, depending on the aperture, invariably gather signal over a range of scattering vectors. Thus, if the band dispersion decreases, the band will become sharper]. These less dispersive bands are a condition that favors amorphization / disorder [14].

III B REVERSE MONTE CARLO (RMC) SIMULATIONS FOR THE DISORDERED PHASES

While the broad peaks and large background seen in the X-ray diffraction patterns indicate disorder, the systematic absence indicates a NaCl (or ZnS) structure for the high pressure (or pressure cycled) phase. Though the

high pressure pattern is consistent with rocksalt (Fm-3m) phase, the lines are asymmetric and there is an intensity mismatch between the observed pattern and the pattern calculated using GSAS. Also, the intensity ratios vary with pressure. This occurs in addition to the large increase in the background. However, even at the highest pressure, the structure factor is markedly different from that of an amorphous material in that the overall diffraction pattern is preserved, though the lines are broadened. Thus, it appears that under compression, certain structural features of the NaCl structure as well as disordering of atoms determine the behavior of the material.

The general purpose FORTRAN code for reverse Monte Carlo (RMCPOW) [18] modeling of static and dynamic disorder in crystalline materials using powder diffraction data was employed to model the disordered high pressure NaCl and the metastable ZnS phases. The simulation fits the computed total X-ray scattering to the measured powder diffraction. As compared to standard RMC, RMCPOW does not suffer from the truncation error related to the Fourier inversion, but requires a starting crystalline structure. Starting with a super cell of a crystal structure, it partitions the calculated scattering into two, i. e. Bragg and diffuse one. The former is the part coming from the reciprocal lattice (RL) points of the super cell and the latter from the other parts of the reciprocal cell and is present due to movement of atoms

away from RL points and due to the positional disorder within the RL. Such simulations can possibly identify the transition mechanism between the phases involved and look for the existence of any ordering. The X-ray powder patterns collected at 31.3 GPa were employed for carrying out the simulations. A correction due to absorption by diamonds was applied to the disordered patterns before converting them into the required structure factor versus scattering vector form suitable for RMCPOW [18].

The Cu₂MnAl structure (a=6.032Å, Z=4, SG:Fm-3m) [19] can accommodate the chalcopyrite disordered NaCl and ZnS structures as seen in Table II and is a suitable cell from which a super cell for the simulations can be generated. In this structure, the various possible disorder types that may be present in the chalcopyrite, NaCl and ZnS structures under pressure, i. e. disorder in

- i. metal ion position (Type I)
- ii. exchange of metal ions among themselves (Type II) or with vacancies (Type III) or both (Type IV)
- iii. exchange of Se and vacant positions (Type V)

can be easily simulated by allowing flipping of various atoms and vacant positions. In addition, the random displacement of atoms from the crystalline positions can also be simulated.

Table II.

(Cu₂MnAl)₄ structure as a generator of the three structures occurring in chalcopyrites. The positions occupied by atoms in the (Cu₂MnAl) structure listed in Column I can be grouped in to VI types as indicated in Column II. Column III lists half number (with D=1; D=2 gives the other half) of the atom positions of a chalcopyrite structure with C/A=2 and this corresponds to the ZnS structure (column IV). Column V gives positions occupied in a NaCl structure. Thus appropriate occupation of different lattice sites in (Cu₂MnAl)₄ structure yields disordered chalcopyrite, ZnS and NaCl structures.

(Cu ₂ MnAl) ₄	Site Type	AB ₂ C ₄	(ZnS) ₄	(NaCl) ₄
.25 .25 .25 Cu	I	.26 .26 .26/D Se	.25 .25 .25 Se	E
.75 .25 .75 Cu	I	.76 .24 .74/D Se	.75 .25 .75 Se	E
.25 .75 .75 Cu	I	.24 .76 .74/D Se	.25, .75 .75 Se	E
.75 .75 .25 Cu	I	.74 .74 .26/D Se	.75 .75 .25 Se	E
.75.75 .75 Cu	II	E	E	E
.25 .75 .25 Cu	II	E	E	E
.75 .25 .25 Cu	II	E	E	E
.25 .25 .75 Cu	II	E	E	E
.0 .0 .0 Al	III	.0 .0 .0 Zn	.0 .0 .0 Zn	.0 .0 .0 Zn
.0 .5 .5 Al	IV	.0 .5 .5 /D Al	.0 .5 .5 Al	.0 .5 .5 Al
.5 .5 .0 Al	IV	.5 .5 .0 Al	.5 .5 .0 Al	.5 .5 .0 Al
.5 .0 .5 Al	V	.5 .0 .5 /D E	.5 .0 .5 E	.5 .0 .5 E
.5 .0 .0 Mn	VI	E	E	.5 .0 .0 Se
.0 .5 .0 Mn	VI	E	E	.0 .5 .0 Se
.0 .0 .5 Mn	VI	E	E	.0 .0 .5 Se
.5 .5 .5 Mn	VI	E	E	.5 .5 .5 Se

As indicated in Table II, a cubic cell generated from the chalcopyrite structure (in order to do this, only atoms positions in the chalcopyrite phase that corresponds to $c/a = 1$ are considered) and the ZnS structure are identical, except for the positional disorder of the atoms. A comparison of atom positions in the chalcopyrite structure and NaCl structure (Table II, column V) indicates that the transition from the chalcopyrite to the NaCl structure requires a breaking/reconstruction of bonds. The appearance of a disordered NaCl structure (henceforth referred to as Fm-3m structure) is to be viewed in the context of the fact that in sp^3 covalent compounds, a competition between the original tetrahedral coordination and six fold coordination that is compatible with pure p bands topology (three orthogonal bonds/bands) is possible under pressure. The transfer of electrons from s to p orbitals consistent with the well known lowering of higher angular momentum orbitals with respect to the s orbital will favor weakening of covalent bonding and formation of p bands. On the other hand, the better packing requirement should still favor tetrahedral coordination. It may be noted that most of the s-p bonded structures results from the Peierls' distortion of a super cell of a simple cubic cell identical to the NaCl structure (if the separate atomic identity of Na and Cl are ignored), driven by electron filling effects in a hypothetical p-band metal with three one dimensional p bands [20]. Another important feature of Fm-3m structure is, that if atoms also partially occupy the $\pm(1/4, 1/4, 1/4)$ positions (now the actual structure is of a disordered Cu_2MnAl type), it will result in partial tetrahedral coordination as well as in preservation of the NaCl like structure. Similarly, if positions III and VI are partly occupied, then the six fold coordination is partly preserved. Thus, the Fm-3m structures can accommodate partial four fold and six fold coordination and disorder.

In the current simulations, a starting cluster generated from a $6 \times 6 \times 6$ super cell of Cu_2MnAl was employed. The regions where the pressure calibrant lines were present were excluded from the fit. In the starting configuration, the ideal crystal positions for the atoms and vacancies as indicated in Table II were filled to generate the NaCl and ZnS structures. The cell volume was fixed at the value corresponding to the lattice parameter obtained by profile fitting of the corresponding diffraction pattern. The disorder in NaCl and ZnS structures were modeled by allowing atom flips in addition to random movements. Specific details of the flips employed are given in the latter section.

For simulating the disordered NaCl phase, the starting configuration was generated from the coordinates given in Table II (column V) and various types of disorder by atom /vacancy flipping was allowed in the simulation subjected to the constraint of minimum inter particle distance of 2.0 Å. It was observed that unless the inter particle distance was reduced to 2.0 Å good fit could not be obtained. During simulation the scale factor and fit of background to a fourth degree polynomial were refined, but line profile parameters with initial value as that of the pressure calibrant were not refined. It may be noted that the program computes the contribution from incoherent scattering due to disorder and adds it to computed spectra and thus fully accounts for the

increased background and line broadening due to disorder. Simple flipping involving metal atoms and vacancy (Type III) did not give a good fit between the observed and simulated pattern. When in addition to flips involving the metal atoms and vacancies and an exchange of Se with type I and II vacancies was allowed, the observed and calculated patterns gave a good fit as shown in Fig. 3.

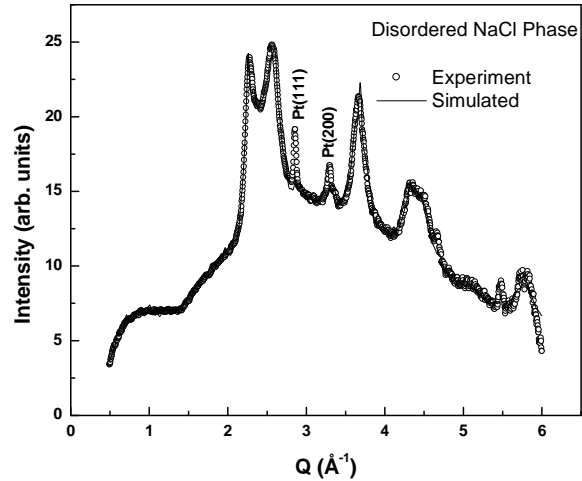


Fig. 3. Comparison of the observed and the simulated pattern using RMCPOW for the disordered NaCl phase.

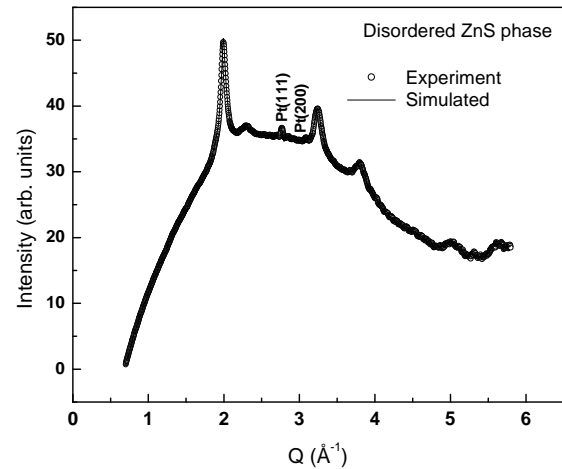


Fig. 4. Comparison of the observed and the simulated pattern using RMCPOW for the disordered ZnS phase.

Atom occupancy in sites I and II implies tetrahedral coordination for some Se atoms. Thus in addition to disorder, there is partial six fold and four fold coordination for Se atoms. This implies that the high pressure phase has a disordered Cu_2MnAl type structure, in which the tetrahedral coordination (and covalent bonding) present in the chalcopyrite structure is partly preserved. It may be noted that under pressure, $GeSb_2Te_4$ with cubic disordered NaCl structure at ambient conditions, undergo further disorder and amorphizes with Ge ions acquiring tetrahedral Te coordination [21].

For simulations of disorder in the ZnS structure, the procedure given above for background, scale factor and

excluded region were followed and the lowest inter particle distance was constrained to be 2.2 Å. With a starting configuration given in Table II, in addition to the normal random motions, atom flips corresponding to type III, IV and V were applied in separate ideal starting cluster. The simulations in which only random motions are allowed and atom flips III between IV were allowed did not converge fast. However runs in which flips between III, IV and V were allowed, the convergence was achieved fast. The computed and measured pattern is given in Fig. 4. The good agreement between the simulated and measured pattern imply that the disorder in ZnS structure involves complete mixing of metal atom and vacant positions. However, the Se atoms need not undergo any atom position flipping other than the normal random displacements.

IV CONCLUSION

High pressure ADXRD measurements on the defect chalcopyrite ZnAl_2Se_4 indicate a structural phase transition beyond 10.5 GPa. The high pressure and the pressure quenched phases have a disordered rock salt and a disordered zinc blende structure with broad x-ray diffraction lines. RMC simulations of the X-ray diffraction data carried out on ZnAl_2Se_4 indicate that the disorder in the NaCl phase is due to a partial retention of the four fold coordination in addition to the random mixing of metal ions and vacancies. In the ZnS phase, the disorder is due to the random mixing of metal ions and vacancies.

+ Retired, Current address:-B-111, SAI VIHAR, SECTOR-15, CBD, NAVI MUMBAI-400614.

-
- [1]. *J.E. Bernard and A. Zunger*, Phys. Rev. **B37** (1988) 6835.
- [2]. *V.V. Ursaki, I.I. Burlakov, I.M. Tiginyanu, Y.S. Raptis, E. Anastassakis and A. Anedda*, Phys. Rev. **B59** (1999) 257.
- [3]. *I.I. Burlakov, Y. Raptis, V.V. Ursaki, E. Anastassakis and I.M. Tiginyanu*, Solid State Commun. **101** (1997) 377.
- [4]. *Grzechnik, V.V. Ursaki, K. Syassen, I. Loa, M. Tiginyanu and M. Hanfland*, J. Solid State Chem. **160** (2001) 205.
- [5]. *D. Errandonea, R.S. Kumar, F.J. Manjon, V.V. Ursaki and I.M. Tiginyanu*, J. Appl. Phys., **104** (2008) 063524.
- [6]. *S. Meenakshi, V. Vijayakumar, B.K. Godwal, A. Eifler, I. Orgzall, S. Tkachev and H.D. Hocheimer*, J. Phys. Chem. Solids **67** (2006) 1660.
- [7]. *S. Meenakshi, V. Vijayakumar, B.K. Godwal, A. Eifler, I. Orgzall, S. Tkachev and H.D. Hocheimer*, J. Phys. Chem. Solids **71** (2010) 832.
- [8]. *J. Marquina, C. Power, P. Grima, M. Morocoima, M. Quintero, B. Couzinet, J.C. Chervin, P. Munsch and J. Gonzalez*, J. Appl. Phys., **100** (2006) 093513.
- [9]. *T. Mitani, T. Naitou, K. Matsuishi, S. Onari, K. Allakhverdiev, F. Gashimzade and T. Kerimova*, Phys. Stat. Sol. (b), **235** (2003) 321.
- [10]. *V.V. Ursaki, I.I. Burlakov, I. M. Tiginyanu, Y. S. Raptis, E. Anastassakis, I. Aksenov and K. Sato*, Jpn. J. Appl. Phys. **37** (1998) 135.
- [11]. *Waskowska, L. Gerward, J. S. Olsen, M. Feliz, R. Liusar, L. Gracia, M. Marques and J.M. Recio*, J. Phys. Condens. Matter, **16** (2004) 53.
- [12]. *K. Allakhverdiev, F. Gashimzade, T. Kerimova, T. Mittani, T. Naitou, K. Matsuishi and S. Onari*, J. Phys. Chem. Solids, **64** (2003) 1597.
- [13]. *M.F. Cabrera and O.F. Sankey*, J. Phys. Condens. Matter, **13** (2001) 1669.
- [14]. *M.H. Cohen, J. Iniguez, and J.B. Neaton*, 2002, Euro. Phys. J. E **9** (2002) 239.
- [15]. *G. Kraus, V. Kramer, A. Eifler, V. Riede, S. Wenger*, Cryst. Res. Technol., **32** (1997) 223.
- [16]. *A.P. Hammersley, S.O. Svensson, M. Hanfland, A.N. Fitch and D. Hausermann*, High Press. Res. **14** (1996) 235.
- [17]. *A.C. Larson, R.B. Von Dreele*, General Structure Analysis System (GSAS), Los Alamos National Laboratory Report LUAR **86** (1994) 748.
- [18]. *Møllergård and R.L. McGreevy*, RMCPOW: Version 2.4, website: <ftp://ftp.studsvik.uu.se/Pub/RMCPOW>
- [19]. *N. Yamada and T. Matsunaga*, J. Appl. Phys. **88** (2000) 7020
- [20]. *J.Y. Raty, J.P. Gaspard, C. Bichara, C. Bergman, R. Bellissent, R. Ceolin*, Physica B **276-278** (2000) 473; *J.K. Burdett, T.J. McLarnan and P. Haaland*, J. Chem. Phys **75** (1981) 5764
- [21]. *D. Lee, S.S. Lee, W. Kim, C. Hwang, M.B. Hossain, N.L. Hung, H. Kim, C.G. Kim, H. Lee, H.N. Hwang, C.C. Hwang, T.Y. Lee, Y. Kang, C. Kim and D.S. Suh*, Appl. Phys. Lett. **91** (2007) 021911

CdTe/CdS SOLAR CELLS PREPARED BY PHYSICAL VAPOR DEPOSITION AND CLOSE-SPACED SUBLIMATION METHODS

N.FATHI¹, R.HAJIMAMMADOV¹, M.SADIGOV¹, E.MIRZOYEV¹,
A. BAYRAMOV¹, G. KHRYPUNOV², N. KLOCHKO², AND T. LI²

¹ *Institute of Physics, Azerbaijan National Academy of Sciences, H. Javid ave. 33, 1143 Baku, Azerbaijan
bayramov@physics.ab.az,*

Phone: +99412 439 1308, Fax: +99412 447 0456

² *National Technical University "Kharkiv Polytechnic Institute", 21 Frunze St., 61002 Kharkiv, Ukraine*

This paper presents comparative analysis of CdTe-based solar cells fabricated by physical vapor deposition (PVD) and close-spaced sublimation (CSS) methods. It was shown that unlike the thermally evaporated CdTe films, no considerable changes after CdCl₂-treatment in the structural properties and surface morphology were observed for the CdTe films obtained by CSS method. The difference between the results on CdCl₂-treatment can be explained by a lower concentration of defects and grain boundary area in CSS deposited CdTe films resulting in lower lattice strain energy which promotes recrystallization and grain growth.

INTRODUCTION

In the photovoltaic material family, cadmium telluride is regarded as one of the most promising material for fabrication of high efficiency polycrystalline CdTe/CdS thin film solar cells [1,2] because of its near-optimum band gap of about 1.46 eV and high optical absorption coefficient in visible range. The maximum efficiency of about 16.5% of the laboratory samples of polycrystalline CdTe based thin film solar cells was achieved by using nanostructured CdS:O window layer and the modified device structure [2]. In spite of the large lattice mismatch between cubic CdTe and hexagonal CdS (nearly 9.7%) the CdTe/CdS solar cells are characterized by essentially high efficiencies caused by interdiffusion at the junction interface removing the lattice mismatch [3]. "CdCl₂ heat treatment" is considered as a key step in CdTe/CdS device processing leading to interdiffusion between CdTe and CdS. It is usually carried out either by means of deposition of CdCl₂ layer onto CdTe surface with following annealing in ambient atmosphere or annealing the structure in CdCl₂ vapor. In the former case the optimum CdCl₂ thickness value varies in the wide range depending on the base layer technology [4]. This paper reports results on the effect of "CdCl₂ treatment" on the output parameters of CdS/CdTe-based solar cells and crystal structure of the base layers deposited on glass substrates by different ways.

EXPERIMENTAL DETAILS

Thin film CdS/CdTe-based solar cells were fabricated by using of two conventional ways. In both cases the superstrate configuration of solar cells on the glass substrates with transparent conductive layer was used. "CdCl₂ treatment" effect on structural properties of CdTe layers was studied in films deposited onto glass substrates.

In the first way, the thin film CdS/CdTe solar cells were prepared on glass substrates covered by transparent 0.5 μm thick ITO. CdS and CdTe layers were deposited sequentially in united cycle by physical vapor deposition at residual pressure of 10⁻⁶ torr from graphite boats at the substrate temperatures 200°C and 300°C, respectively. The thicknesses of the CdS and CdTe layers were 0.35 μm and 4.0 μm, respectively. The obtained device heterostructures were then subjected to "CdCl₂

treatment". CdCl₂ films were deposited by thermal vacuum evaporation onto unheated CdTe surface at the initial vacuum 2·10⁻⁵ torr. The obtained multilayer structures were air-annealed in close box at 430°C during 25 min. After bromine-methanol etching the Cu-Au contacts were formed on their surface.

In a second way borosilicate glass substrates (Corning 7059) with a bilayer transparent SnO₂ (of about 500nm thickness high-conductive and 100 nm thickness low-conductive) were used for CdS/CdTe fabrication. CdS films of 80-100nm thickness were deposited by chemical bath deposition (CBD) method. Cadmium acetate (CdAc₂, 99.99%), ammonium acetate (NH₄Ac, 99.99%), thiourea (NH₂)₂CS, 99+%) and regular ammonium hydroxide (NH₄OH) DI water solution heated up to 90°C was used for CdS deposition. CdTe films were deposited by close-space sublimation (CSS) method to a thickness 6-8 μm. Deposition process was carried out in evacuated chamber with total system pressure of about 16 torr (1 torr oxygen + 15 torr helium) at substrate and source temperatures of 620 °C and 660 °C, respectively. CdCl₂ treatment was carried out using "dry" method. The CdS/CdTe structures were exposed to CdCl₂ vapor at 400 °C for 5-7 min in vacuum chamber in the presence of 100 torr oxygen and 400 torr helium. The samples were then etched in HNO₃:H₃PO₄:H₂O mixture (NP etch) to bare the CdTe surface down to elemental tellurium and a special mixture consisted of graphite paste, Cu_xTe, and HgTe was deposited. The samples were then annealed at 250°C for 25 min in the presence of inert gas. Finally, the silver paste back face electrode was deposited and the samples were annealed at 100°C in air to complete the solar cell device structure [5].

Surface morphology of the CdTe films was studied by Electron Scanning Microscope (SEM) Hitachi S-4000. Atomic force microscopy (AFM) analyses of the samples were performed in multifunctional scanning probe microscope NT-206. X-ray diffraction (XRD) analyses of the films were done in "D8 ADVANCE" (BRUKER) diffractometer using CuKα radiation. I-V parameters of the devices were measured using 100mW/cm² solar simulator. CdTe device prepared by CSS method with NREL confirmed efficiency of 13.7% was used as a reference cell in our measurements.

RESULTS AND DISCUSSION

1. EFFECT OF “CdCl₂ TREATMENT” ON THE OUTPUT PARAMETERS OF CdS/CdTe-BASED SOLAR CELLS AND CRYSTAL STRUCTURE OF CdTe ABSORBERS DEPOSITED BY PHYSICAL VAPOR DEPOSITION

The light I-V characteristics of ITO/CdS/CdTe/Cu/Au solar cells treated at the different CdCl₂ thickness are shown in fig.1. The results on output parameters and diode characteristics of studied devices are summarized in Table 1.

The analysis of the Table 1 shows, that the increase of the CdCl₂ thickness up to 0.35 μm results in the enhance of device efficiency up to η = 10.3% followed by decrease of the diode saturation current density J₀ and series resistance R_s but further increase of CdCl₂ thickness up to 1.2 μm leads to essential decrease of device efficiency with increase of J₀ and R_s. According to [6,7], the “CdCl₂ treatment” of CdTe base layer in the presence of oxygen leads to enhance of majority-carrier

concentration by generation of Cl_{Te}-V_{Cd} acceptors which results in the experimentally observed decrease of device series resistance. On the other hand, at some chlorine concentration on the grain boundary of CdTe, the recrystallization of the base layer above 400 °C occurs due to the presence of low temperature eutectic in the CdTe-CdCl₂ system [1] which may result in the diode saturation current density decrease.

It should be noted that, at first glance, the increase of R_s with the CdCl₂ thickness above 0.35 μm is somewhat strange, however, according to [8], the high concentration of chlorine really leads to the evolution of the electrically active intrinsic point defects in CdTe layers and instead of the acceptor complexes Cl_{Te}-V_{Cd} the isoelectronic complexes 2Cl_{Te}-V_{Cd} are formed. The latter results in the decrease of majority-carrier concentration and therefore the increase of R_s.

The study of the PVD CdTe grain boundary surface by means of the scanning electron microscopy has revealed that “CdCl₂ treatment” results in the enlargement (5-6 times) of the base layer grain size (Fig.2).

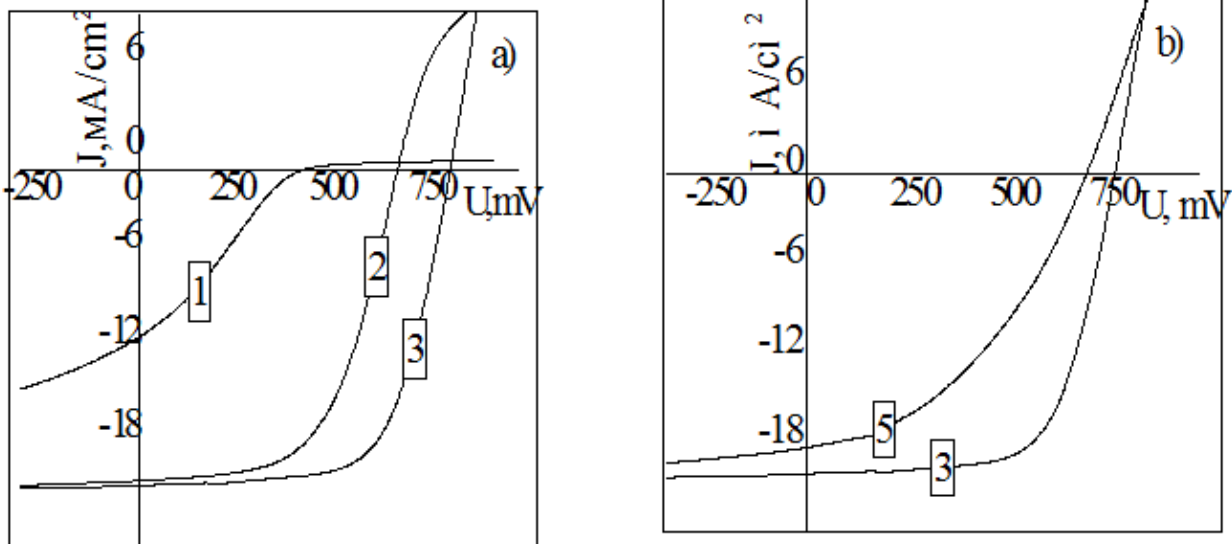
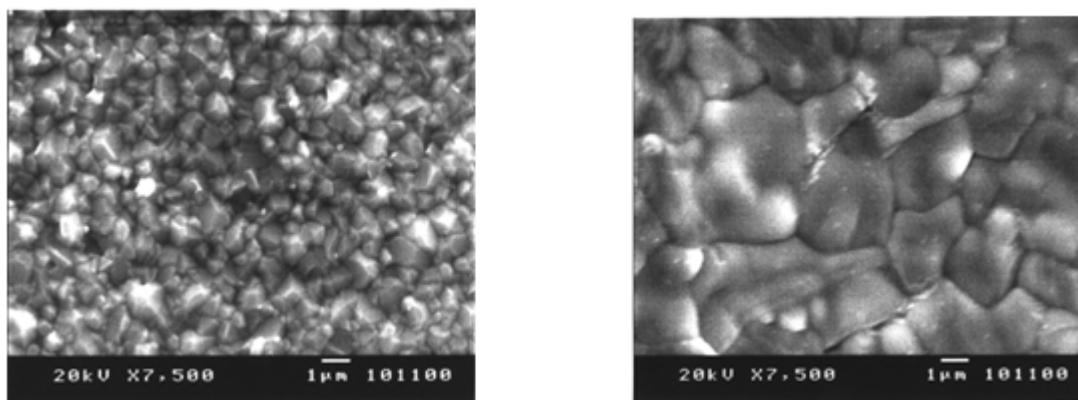


Fig.1 Light I-V characteristics of ITO/CdS/CdTe/Cu/Au solar cells treated at different CdCl₂ thickness: 1 - d=0 μm; 2 - d=0.06 μm; 3 - d=0.35 μm; 5 - d=1.20 μm

Table1.

Output parameters and diode characteristics of ITO/CdS/CdTe/Cu/Au devices

Sample	1	2	3	4	5	
d _{CdCl₂} , μm	0	0.06	0.35	0.68	1.2	
Output parameters	V _{oc} , mV	400	645	773	730	702
	J _{sc} , mA/cm ²	10.7	19.0	20.1	19.0	19.0
	FF	0.28	0.58	0.67	0.58	0.41
	η, %	1.2	7.4	10.3	8.0	5.5
Diode characteristics	R _s , Ohm·cm ²	28	3.8	2.8	3.5	27.5
	R _{sh} , Ohm·cm ²	230	750	720	705	264
	J ₀ , A/cm ²	7.3·10 ⁻³	1.5·10 ⁻⁶	8.2·10 ⁻⁸	2.0·10 ⁻⁷	3.0·10 ⁻⁷
	Diode factor, A	7.0	3.8	2.5	3.0	3.8
	J _{ph} , mA/cm ²	11	19.8	20.2	19.3	19.6



a) before “CdCl₂ treatment”
 b) after “CdCl₂ treatment”
 Fig.2. SEM photomicrograph of CdTe layer deposited by PVD method

According to the results of X-ray diffractometry analysis of the base layers, the single phase CdTe films of stable cubic modification were obtained after “CdCl₂ treatment”. The increase of the CdCl₂ layer thickness from d=0.06 µm to d=0.35 µm diminishes the lattice

parameter of CdTe films. At the same time, the preferential orientation of the grains changes from [111] to [422]. The further increase of the thickness results in the reverse change of the preferential orientation and lattice parameter growth (Table 2).

Table2

Effect of the “CdCl₂ treatment” on the CdTe base layer crystal structure

CdCl ₂ layer thickness, d, µm	0.06	0.35	1.2
Preferential orientation direction	[111]	[422]	[111]
Degree of texture perfection G	1.28	0.58	1.26
Lattice parameter a, Å	6.509	6.496	6.506

According to [9], the lattice parameter of the structurally perfect unstrained CdTe layers is 6,481Å. The two-phase structure, twinning and high concentration of the stacking faults are typical for the CdTe layers textured in [111] direction [10]. These structural defects are easily formed because of insignificant (about 1%) difference in the formation energies of sphalerite and wurtzite crystal lattices, and as a result, the low formation energy of stacking faults in CdTe. Thus, the change of the preferential orientation from [111] to [422] at 0.35 µm CdCl₂ thickness can be evidence of the reduction of crystal defect concentration.

The improvement of crystal perfection up to 0,35 µm is in a good agreement with the conception of the recrystallization mechanism during “CdCl₂ treatment”. According to [11], CdCl₂ acts as a flux during CdTe recrystallization because the phase diagram for CdCl₂-CdTe system at 77% CdCl₂ consists a eutectic with melting temperature of 508°C. The availability of such a low temperature eutectic leads to recrystallization of CdTe under the corresponding thermal treatment of the CdCl₂/CdTe heterosystem. It is clear that the process of the base layer recrystallization begins by means of the creation of the nuclei on the grain boundaries near the cadmium telluride and cadmium chloride interface. The growth of the nuclei of random crystal-lattice orientation at the near thermodynamic equilibrium conditions results not only in the essential grain growth and decrease of preferential orientation degree of the CdTe but also in structure perfection within the grains. The latter causes the reduction of the macrodeformation that eventually

leads to the experimentally registered approach of the CdTe layer lattice parameter to the theoretical one [9].

In accordance with the phase diagram for system CdCl₂-CdTe the cadmium chloride is insoluble in the cadmium telluride. As a result of the grain boundary diffusion, chlorine reaches CdS-CdTe interface that has been experimentally observed in [12]. Thus, excess of CdCl₂ can lead to the recrystallization of CdTe not only near the CdTe-CdCl₂ interface, but also near the CdTe-CdS one. The latter can provoke the reorienting effect of CdS on the CdTe growth and diminish adhesion between CdTe and CdS which leads to enhance of macrodeformation in the base layer.

EFFECT OF “CDCL₂ TREATMENT“ ON THE OUTPUT PARAMETERS OF CdS/CdTe-BASED SOLAR CELLS AND CRYSTAL STRUCTURE OF CdTe DEPOSITED BY CSS METHOD

CdTe and CdS films were deposited onto soda-lime glasses with and without SnO₂ conductive layers. Electrical properties, X-ray diffractions, AFM and SEM images of the films before and after “CdCl₂-treatment” were studied.

Resistivity of n-type CdS films prepared by CBD method was found to be 1.2x10⁴ Ωcm. As-grown CdTe films obtained by CSS method showed p-type conductivity with resistivity about 10⁷Ωcm. “CdCl₂-treatment” in 400 torr He and 100 torr O₂ atmosphere at 400 °C for 7-10 min. (corresponding to CdCl₂-treatment of CdTe solar cells) lowered the resistivity down to 6x10² Ωcm.

CdS films showed the hexagonal wurtzite-type structure (space group P63mc) whose lattice parameters a and c were determined to be 4121 Å and 6716 Å, respectively (Fig.3). On the other hand, the obtained CdTe thin films crystallize in the cubic sphalerite type structure (space group F43m) with a=6485 Å (Fig.4). Both the CdS and CdTe thin films showed a preferential orientations along the [002] and [111] directions, respectively.

Fig.5 and Fig.6 show the AFM image of CdS film and the SEM photomicrograph of “as-grown” CdTe film, respectively.

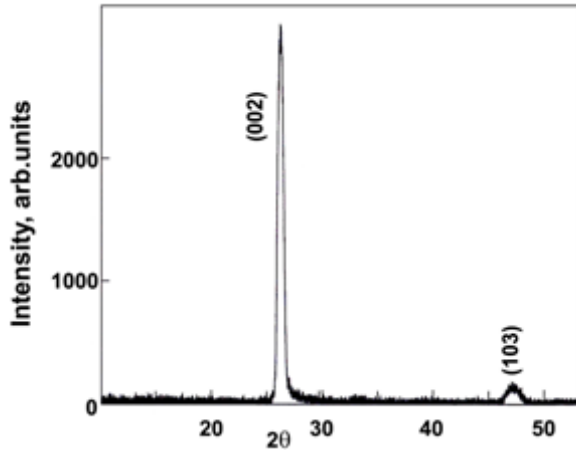


Fig.3. XRD spectrum of CdS film

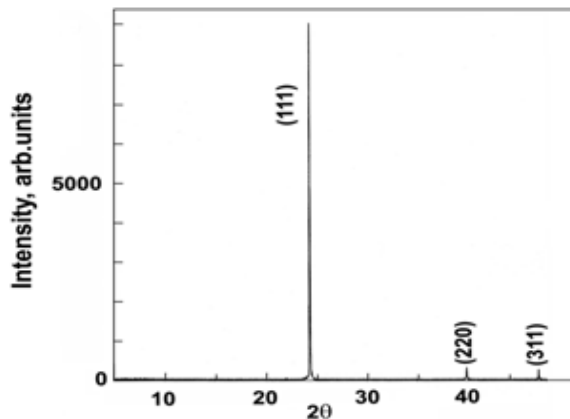


Fig.4. XRD spectrum of CdTe film

As it is seen from the Figure 5, in CdS film the grains with up to 60 nm size can be observed among the tightly packed grains with smaller sizes. The CdTe film consists of grains 2-6 μm in size and is dense. It should be noted that no considerable changes in the structural properties and surface morphology of CdTe films were observed after the “dry” CdCl₂-treatment which is usual for the CdTe films with large grain size obtained by CSS method [13]. Both of CdTe films, “as-grown” and CdCl₂-treated, have a clearly faceted surface morphology and an average grain size of about 3-4 μm.

The difference between the results on CdCl₂-treatment for thermally evaporated and CSS deposited CdTe films can be explained by the fact that CSS films are deposited at much higher temperature (620 °C versus 200 – 300 °C) and therefore contain a lower concentration

of defects. On the other hand, the large grain size of the films leads to a much lower grain boundary area. Low defect concentration and grain boundary area result in lower lattice strain energy, which is the main factor for the crystallization process [13]. As a result the CSS deposited CdTe films do not recrystallize at the temperatures and times used in the CdCl₂ treatment.

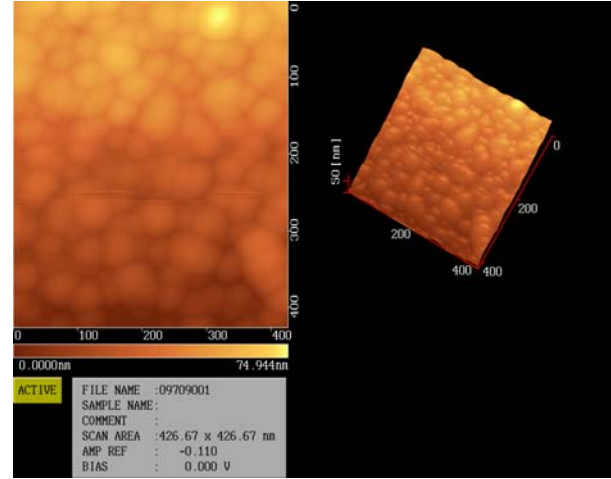


Fig.5. AFM image of CdS film

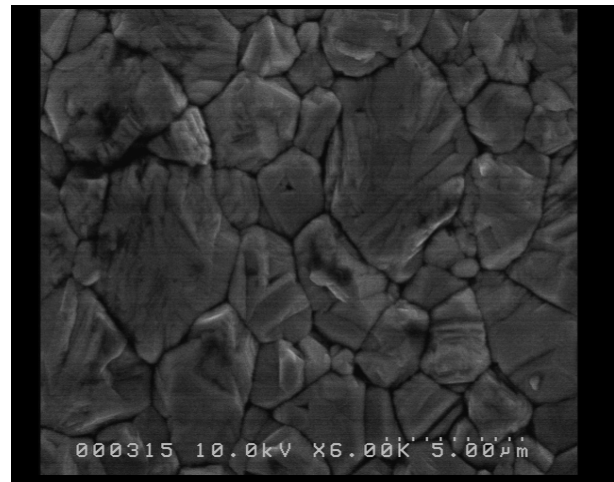


Fig.6. SEM photomicrograph of CdTe

We prepared a series of glass/n-SnO₂/n-CdS/p-CdTe/back contact device structures for solar cell application. The n-CdS/p-CdTe structures were prepared on 4x4 cm² square by-layer Corning7059 glass/n-SnO₂ substrates. After CdCl₂ treatment the substrates were cut into individual 1cm² square pieces and Cu_xTe–HgTe back contacts to the structures were fabricated. I–V parameters of the devices with an area of about 0.98 cm² were measured using 100 mW/cm² solar simulator. The highest efficiency was obtained with the parameters: V_{oc}=773mV, J_{sc}=23.92mA/cm², fill factor FF =68.7%, a total area conversion efficiency of 12.71% (Fig. 7).

It should be noted that the highest efficiency was observed in the cell prepared from the central part of substrate. At the same time, the devices fabricated using the pieces cut from edge part of the substrate exhibited lower efficiencies. The most obvious reason for this is a high density of pinholes emerging on the substrate edges

where the CdTe film quality is essentially lower compared to central part.

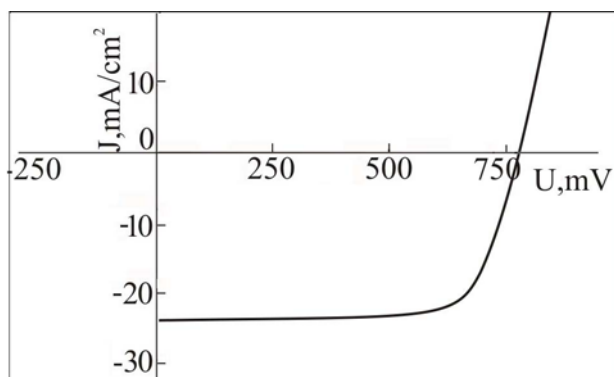


Fig.7. Light I-V characteristics of glass/nSnO₂/nCdS/pCdTe/back contact device

CONCLUSIONS

It was experimentally demonstrated that the maximum efficiency of CdTe based solar cells deposited by physical vapor deposition corresponds to the 0.35 μm CdCl₂ thickness at “CdCl₂ treatment”. The significant grain growth of PVD CdTe film and change of

preferential orientation from [111] to [422] at 0.35 μm CdCl₂ thickness is due to the reduction of the crystal stress caused by high concentration of the defects in this film. The reverse change of the orientation at higher CdCl₂ thickness is caused by the recrystallization of CdTe near the CdTe-CdS interface which provokes the reorienting effect on the CdTe grain growth.

Unlike the thermally evaporated CdTe films, no considerable changes after CdCl₂-treatment in the structural properties and surface morphology were observed for the CdTe films obtained by CSS method. The difference between the results on CdCl₂-treatment can be explained by a lower concentration of defects and grain boundary area in CSS deposited CdTe films resulting in lower lattice strain energy which promote recrystallization and grain growth. As a result the CSS deposited CdTe films do not recrystallize at the temperatures and times used in the CdCl₂ treatment.

ACKNOWLEDGMENTS

The work was supported by STCU under Project 4301

-
- [1]. Moutinho H.R., Hasoon F.S. Abufoltuh F.A., Kazmerski L.L. Investigation of polycrystalline CdTe thin film deposited by physical vapor deposition, close-spaced sublimation, and sputtering, *Journal Vacuum Science Technology*.- 1995.- Vol. 13, №6.- P.2877-2883.
- [2]. Wu X., *Solar Energy*, 77 (2004) 803-814
- [3]. Jensen D. G., McCandless B. E., and Birkmire R. W., 25th Photovoltaic Specialists Conference, 1996, p. 773.
- [4]. Raushenbach H.S., *Solar Cells Array Design*, New York: Litton Education Publishing, 1980, 250 p.
- [5]. Albin D. S., Demtsu S. H., and McMahan T. J. *Thin Solid Films*, 2007. V. 515.- P. 2659– 2668
- [6]. McCandless B.E. Thermochemical and kinetic aspects of cadmium telluride solar cell processing // *Proceedings of the 2001 MRS Spring Meeting*.- 2001.-San Francisco.- H1.6.1-12.
- [7]. Durose K., Boyle D., Abken A., Otley C.J., Nollet P., Degrave S., Burgelman M., Wendt R., Beier J., Bonnetz D. Key aspects of CdTe/CdS solar cells// *Physica Status Solidi*.-2002.-Vol. 229, №2.- P.1055-1064.
- [8]. Valdna J., Hill E. Efficiency limits of CdTe thin film solar cells// 17 European Photovoltaic Solar Energy Conference: Proceeding of the conference.- Munich (Germany).- 2001.- P. 1233-1235.
- [9]. JCPDS. Card № 15-0770.
- [10]. Panchekha P.A., Alaverdova O.G., Gnidash V.I., Heterophase and polytexture of CdTe films condensed from ion-molecular stream, *Ukrainian Physical Journal*, 2000, V.45, № 1, P. 75-80.
- [11]. Zanio N. Cadmium telluride. *Semiconductors and Semimetals*, Vol. 13. - USA: Wiley.-1978.- 280p.
- [12]. Terheggen M., Heinrich H., Kostors G., Batzner D., Romeo A., Tiwari A.N., Romeo N., Bosio A. Transmission electron microscopy of diffusion induced structural and chemical changes in CdTe solar cells // *Thin Solid Films*.-2003.-Vol. 431-432.-P. 262-266.
- [13]. McCandless B. E. and Sites J. R. Cadmium Telluride Solar Cells: *Handbook of Photovoltaic Science and Engineering*, A. Luque and S. Hedegus (eds.) . - USA:New York: Wiley.- 2003.

UV-TRANSMISSION AND FLUORESCENCE PROPERTIES OF POLYMER THIN FOILS FOR USE IN MICROLENS ARRAY FABRICATION

SILVANO DONATI¹, MAO-KUO WEI², JIUN-HAW LEE³, JHIH-HAO CAI²

¹*Università di Pavia, Dipartimento di Elettronica, v. Ferrata 1, 27100, Pavia, Italy*

²*Department of Materials Science and Engineering, National Dong Hwa University, Hualien 974, Taiwan*

³*Graduate Institute of Photonics and Optoelectronics and Department of Electrical Engineering, National Taiwan University, Taipei 106, Taiwan*

silvano.donati@unipv.it

We report measurements of optical transmission and fluorescence of thin foils of PET (PolyEthylene Terephthalate) polymer, data that are unavailable in literature to the best of our knowledge. The foils are those commonly used as substrate and/or lens material in microlens arrays (MLA) designed for use in multi-pixel image photodetectors with the purpose of fill-factor recovery. The wavelength range covered by the measurements is 200 to 800 nm and the thickness of PET foils is 40-80 μm . We find a UV-transmission cutoff of 320-nm for PET and 330-nm for cured epoxy on PET. Fluorescence of the samples is peaked at 385-nm and the wavelength of most effective fluorescence is 340-nm.

1. INTRODUCTION

In recent years, there has been considerable interest in microlens arrays (MLAs) applications, as these optical elements are useful for recovering the fill-factor loss (given by the ratio of photosensitive area A_d to total pixel area A_p) in pixel-board processing image photodetectors [1,2]. An example of MLA (microlens array) fabricated in our laboratory by replica molding [3] for a European Program FET aimed to demonstrate ultrafast imaging SPAD (Single Photon Avalanche Detector) is shown in Fig.1.

Reason for use of an MLA in connection with an image photodetector is that, when we try to allocate processing circuitry in the area surrounding the sensitive area of each pixel of the array, the resulting area loss (and corresponding spectral sensitivity loss) may become intolerably high, and spoil the effective sensitivity of the photodetector [2].

This is a serious hinder to developing novel detectors (3-D, FLIM, ultrafast) with sophisticated circuit processing at the pixel-level [2].

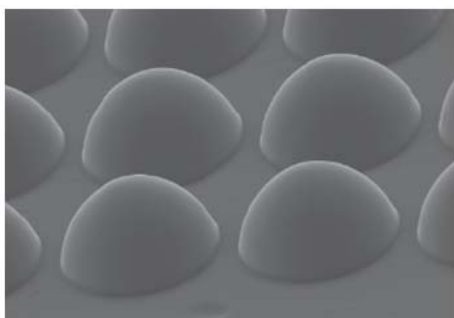


Fig.1 Microphotograph of a MLA made with 32x32 plano-convex lenses made by polymer molding. Pitch is 50- μm and lens diameter is 46- μm , dome height is 22 μm .

A method to recover the fill-factor loss is however using a microlens array (MLA) made of a multiplicity of individual small lenses, coupled to as many pixels, and placed in the focal plane of the imaging objective just in front of the detector array [2,5,6].

Under appropriate conditions, the MLA offers a substantial recovery in sensitivity, equal to the

concentration factor C (defined as the ratio of output-to-input irradiances) [2]. With pixel sizes in the range 20 to 100- μm approximately, the C factor can substantially approach the reciprocal of fill-factor, $1/\mu$, offering an almost complete recovery in sensitivity [4-6].

Recently, MLAs with concentration factors of 20 to 35 have been reported [5-6] for a 32x32 SPAD (Single Photon Avalanche Detector) array of individual 50- μm pixel size in silicon 130-nm CMOS technology.

Of course, the permissible wavelength range for applications is the one offered by the detector spectral response, dependent on the material used, and also on the thicknesses available by the chosen technology. Using silicon as a material, in pin, avalanche photodiode, and SPAD structures, and the standard process of a 350- to 130-nm CMOS-technology, and an epi-layer thickness of a few micrometer, the spectral response ranges from deep UV to near IR (about 320 to 800 nm), see e.g., Fig.7 of Ref.[1], the shortest wavelengths being those of very interesting applications, such as FLIM and fast decaying fluorescence [1,2,8].

About materials to choose from for an MLA sitting just in front of the detector, we need (i) a high optical transmittance in the desired wavelength range, and (ii) minimal fluorescence from UV-excitation in the desired wavelength range.

Close to the UV edge of response, scarce data on fluorescence is available in literature, to our best knowledge, about polymers of interest for MLA fabrication.

In this paper we present the results of measurements, in the range 200 to 800 nm, of the optical transmission and the fluorescence spectra of thin (46-80 μm) foils of polymer, notably PET (PolyEthylene Terephthalate) used as substrates, and of an MAF co-polymer used as moldable lens material.

2. EXPERIMENT AND MEASUREMENTS

The samples were analyzed by a commercial fluorescence spectrophotometer, Cary Eclipse B10, made by Varian Inc. The sample was cut into many stripes and put into the sampling cuvette for testing.

The measuring setup is shown in Fig.2. A high brilliance source, a xenon flash lamp feeds an input monochromator

UV-TRANSMISSION AND FLUORESCENCE PROPERTIES OF POLYMER THIN FOILS FOR USE IN MICROLENS ARRAY FABRICATION

with built-in filters to sort out an input probe beam. After a collimating lens, the beam is passed through the cuvette, in which the cutting polymer foils is located. At the

output, light is passed in a second monochromator with built-in filters. A photomultiplier tube (PMT) detector was used as the detector for the fluorescence measurement.

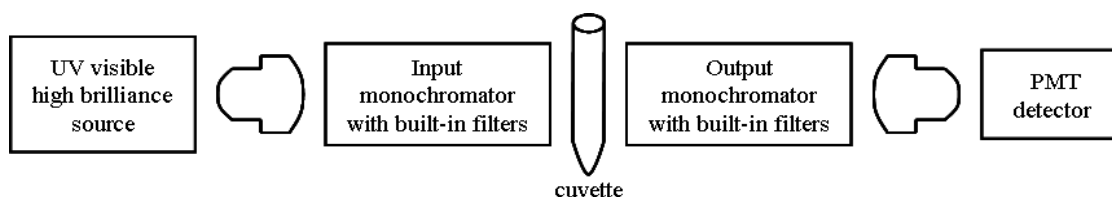


Fig. 2. Schematic for the measurement of fluorescence in thin foils of polymers.

The sample we have measured were PET films, 50- or 80- μm thickness, representative of commonly fabricated MLA, and films of a few-mm thickness in cured MAF, representative of the lens spherical dome molded onto the substrate. The 50- and 80- μm thick PET commercial films were supplied by Goodfellow Ltd. and Chu Lun Stationery Co., respectively. The lens mold film, a copolymer of PMMA and PU, was duplicated on the PET substrate by UV forming process using a PDMS mold with concave microlens array on its surface.

In Fig.3 we plot the transmittance of the 50- and 80- μm films, from 300 to 500 nm wavelength. All graphs are inclusive of the Fresnel at the air/material interface.

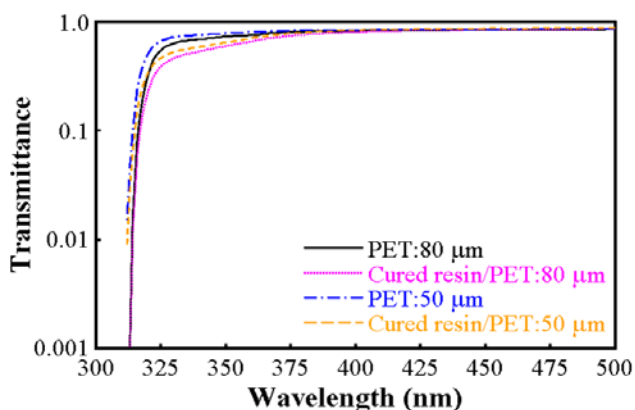


Fig.3. Transmittance of polymer films of replicated microlens arrays with PET substrate. Cured resin/PET is for substrate plus deposited epoxy of the lens body.

As we can see, the transmittance is of all films is consistently close to 90%, above about 450 nm, the small deviation (a few percent) from pure Fresnel loss being attributable to residual scattering of the film. Also, the 50% break point of transmittance is 320 and 325 nm for the 50- and 80- μm thicknesses, whereas the cured resin adds only a minor loss in the range 340-380 nm and moves the 50% cutoff to 330 and 335 nm for the two thicknesses.

About fluorescence, we scanned the 200-600 nm wavelength range by tuning the input monochromator, and measured the spectrum of radiation emitted by the specimen by the output monochromator and PMT detector.

First, operating in direct view (no specimen) we checked the linewidth of excitation, and the results are

reported in Fig.4, showing a half-peak width $\Delta\lambda$ of approximately 15-nm (the monochromator resolution is 10-nm).

Given the field-of-view of the detector and objective lens, the fraction of fluorescent power collected by the readout was about 15%. About fluorescence spectra, results for 80- μm and 50- μm foils of PET are shown in Figs.5 and 6. The most effective wavelength for fluorescence excitation is 340 nm, whereas the fluorescence spectrum has a peak at 385-nm and a significant power content up to about 500...520-nm.

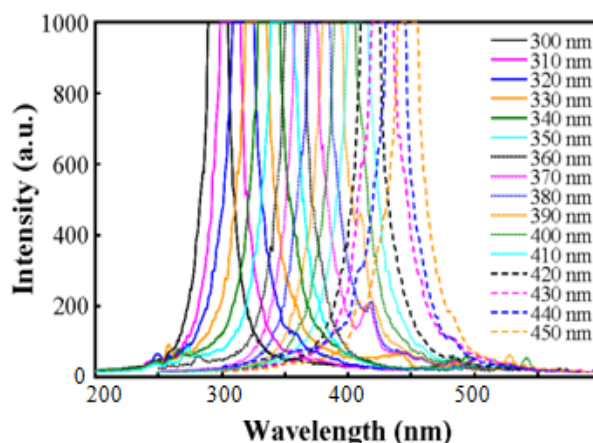


Fig. 4. Spectrum of the UV source used for the excitation of fluorescence different wavelengths.

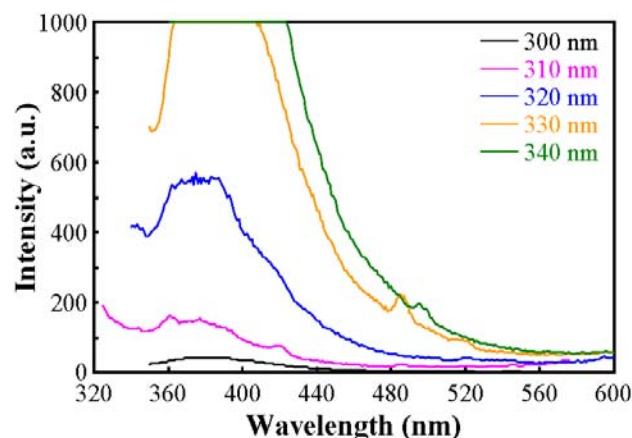


Fig.5. Spectrum of fluorescence of 80- μm PET foil excited at λ from 300 to 340 nm. Scale is expanded to show the low intensity background. Peak of emission is at $\lambda=385$ nm and most effective excitation is at $\lambda=340$ nm

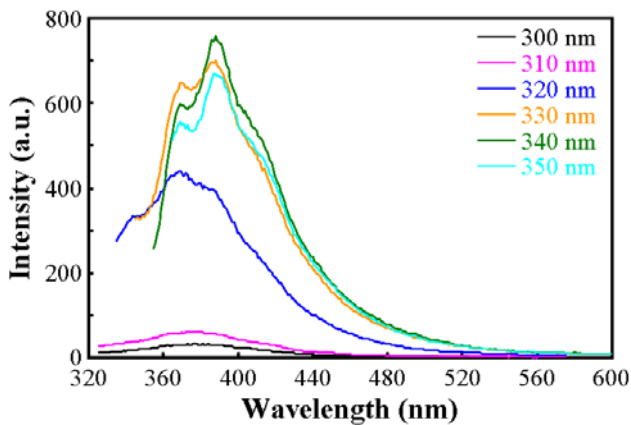


Fig.6. Spectrum of fluorescence of 50- μm PET foil excited at λ from 300 to 340 nm. Peak of emission is at $\lambda=385$ nm and most effective excitation is $\lambda=340$ nm

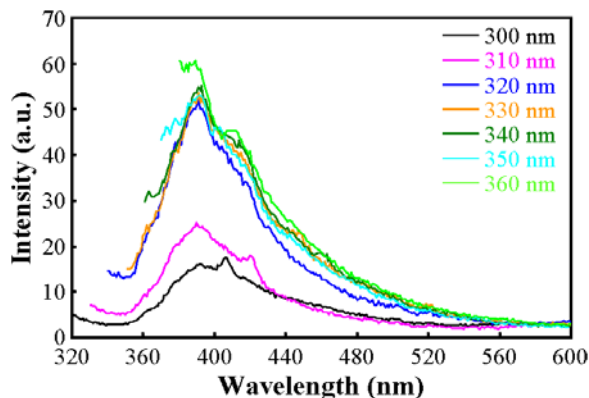


Fig.7. Spectrum of fluorescence of a 50- μm PET foil covered by a $\sim 1\text{-}\mu\text{m}$ layer of MAF moldable polymer, excited at different wavelengths, from 300 to 340 nm. Peak of emission is at $\lambda=385$ nm and most effective excitation is at $\lambda=350$ nm

The most effective wavelength for fluorescence excitation is 340 nm, whereas the fluorescence spectrum

has a peak at 385-nm and a significant power content up to about 500...520-nm.

On comparing the 80- and 50- μm spectra reveals that there is a second smaller peak of fluorescence with emission centered around 365-nm. This peak is concealed by the much larger emission in the thicker foil (Fig.5) and is attributable to an excitation by a deeper UV wavelength.

Adding a $\sim 1\text{-}\mu\text{m}$ layer of MAF polymer onto the 50- μm PET substrate to account for the dome of a typical lens element in an MLA, produces only minor changes in the fluorescence spectrum of the combined layers, as we can see in Fig.7.

3. CONCLUSIONS

From all the above results, we can conclude that MLA replica molded elements using PET substrates can be used, in combination to detectors for spectroscopy measurements, without interfering effects from inadvertently excited fluorescence, in the range of wavelengths from 400-nm to 800 nm (and up to the photoelectric threshold of the detector).

In addition, if we take as good also the photons emitted by fluorescence because λ -converted but detectable as well, then the range of useful wavelengths for PET-based MLAs can be extended to 330 to 800 nm.

ACKNOWLEDGEMENTS

This work has been supported by the EEC within the 6th Framework Program IST FET Open MEGAFRAME ["Million Frame Per Second, Time-Correlated Single Photon Camera"] project (contract No. 029217-2).

Disclaimer: This publication reflects only the authors' views. The EEC Community is not liable for any use that may be made of the information contained herein.

OCIS codes: (220.1770) Concentrators; (230.5160) Photodetectors; (110.280) Image Enhancement

- [1.] C. Niclass, A. Rochas, P.-A Besse, and E.Charbon: "Toward a 3-D camera based on single photon avalanche diode," *IEEE J. Sel. Topics in Quant. Electr.* **10** (2004), pp.796 – 802.
- [2.] E. Charbon, and S.Donati "SPAD Sensors Come of Age", *Optics and Photonics News*, vol.21, No.2, (2010), pp.34-414
- [3.] M.-K. Wei, and I.-L. Sun: "Method to evaluate the enhancement of efficiency in OLED for microlens array," *Optics Express*, **12** (2004), pp.5777-80
- [4.] S.Donati, G.Martini, and M.Norgia: "Microconcentrators to recover fill-factor in image photo-detectors with pixel on-board processing circuits", *Optics Express*, vol.15, 2007, pp. 18066-18074.
- [5.] G.Martini, E.Randone, M.Fathi, and S.Donati: "Uniformity of Concentration Factor and BFL in Microlens Array for Image Detectors Applications" *OSA Proceedings Frontiers in Optics 2009/Laser Science XXV*, San Jose 11-15 Oct 2009, paper FWG5
- [6.] E. Randone, G. Martini, M. Fathi and S.Donati: "SPAD-Array Photoresponse is Increased by a Factor 35 by use of a Microlens Array Concentrator", *Proc. 22nd Ann.Meet. IEEE Photonics Society*, Antalya, 4-8 Oct 2009, paper TuX3.
- [7.] S. Donati, G. Martini, and E. Randone: "Improving Photodetector Performance by means of Micro-optics Concentrators", submitted to *IEEE J. Lightwave Technologies* (2010).
- [8.] M. Gersbachs, R. Trimananda, Y. Maruyama, M. Fishburn, D. Stoppa, F. Richardson, R. K. Henderson, and E.Charbon, "High-frame rate DCPS/FLIM readout system using SPAD-based image sensor," *SPIE Conf. on Optics & Photonics*, Aug.2010 (in press)

GROWTH OF MULTICOMPONENT SOLID SOLUTIONS A³B⁵ CONTAINING ANTIMONY BY METAL-ORGANIC CHEMICAL VAPOR DEPOSITION

G. S. GAGIS¹, V. I. VASIL'EV¹, N.N. MURSAKULOV²

¹*Ioffe Physico-Technical Institute of the Russian Academy of Sciences,
26 Polytekhnicheskaya st., St Petersburg 194021, Russian Federation, e-mail: giman@mail.ioffe.ru*

²*Institute of Physics of Azerbaijan National Academy of Sciences,
33, H.Cavid ave., Az-1143, Baku, Azerbaijan, e-mail: nmursakulov@physics.ab.az*

In present work the technological conditions of metalorganic chemical vapour deposition of narrow-gap (0.35 – 0.5 eV) AlGaInAsSb, AlInAsSb, GaInAsSb and InAsPSb solid solutions with compositions close to InAs were investigated. The epitaxial growth was carried out on AIX200 setup with horizontal reactor. The growth temperature was 600°C, the pressure was 100 mbar. Obtained layers had satisfactory crystalline quality and demonstrated intensive photoluminescence.

Keywords: AlGaInAsSb, AlInAsSb, GaInAsSb and InAsPSb solid solutions, metal-organic chemical vapor deposition, XRD curve (a) and PL-spectra, PL spectra of AlInAsSb solid solutions

1. INTRODUCTION

An interest to optoelectronic devices of mid-infrared (MIR) wavelength range (1.7-5 μm) is caused by their applications for all-semiconductor gas analyzers, capable to control concentration of many toxic gases with absorption lines within MIR range (methane (2.3 μm and 3.3 μm), ethylene (3.17 μm), acetone (3.4 μm and 4.6 μm), nitrogen dioxide (3.9 μm and 4.5 μm), sulfurous anhydride (4.0 μm), carbonic gas (4.27 μm) and carbon monoxide (4.7 μm)).

Moreover, one of the atmosphere transparency windows (3.5-5 μm) falls in this range, which means that such devices are of high interest for free-space telecommunications and lidars. Applications of MIR laser diodes include also spectroscopy, long-range optical communication through fluoride fibers (minimum of losses 3 – 4 μm) and medicine.

2. METHODS AND APPROACHES

Semiconductor materials for MIR range are typically A³B⁵ solid solutions containing antimony and lattice-matched with InAs or GaSb substrates. At present time 1.7 – 3 μm range radiation sources are successfully produced. However, there are problems with obtaining of 3 – 5 μm wavelength range optoelectronic devices. These problems are strong non-radiative Auger processes predominating over radiative recombination in narrow-gap active regions and low efficiency of optical and carriers confinement.

Typical materials for fabrication of 3 – 5 μm wavelength range optoelectronic devices are A³B⁵ solid solutions which are lattice-matched with GaSb. Such device structures contain strained quantum wells GaInAsSb with AlGaInAsSb barriers and AlGaAsSb cladding layers [1, 2, 3]. AlGaAsSb materials with ~90 % aluminium in III-group sublattice provide very high energy barriers for carriers and sufficient effective waveguide.

Interest to materials which can be obtained on InAs substrates increases recently. As active regions InAs and InAsSb are typically used, as cladding layers InAsPSb are utilized [4], in asymmetrical laser structures one of cladding layer is AlAsSb [5]. Also superlattices with

ternary solid solutions quantum wells InAsSb, InAsP, InGaAs are produced [6].

Quaternary and pentanary solid solutions A³B⁵ are attractive materials for fabrication of device structure layers because they cover a wide wavelength range and allow keeping of lattice-matching with substrate.

At present time, multicomponent solid solutions, such as AlGaAsSb, AlInAsSb, AlGaInAsSb, GaInAsPSb are mainly obtained by molecular beam epitaxy (MBE) [2, 3] and liquid phase epitaxy (LPE) [7]. However, for industrial scale device fabrication the metalorganic chemical vapour deposition (MOCVD) technologies are needed.

As our previous investigations shows, narrow-gap solid solutions grown on InAs-substrates have better photoluminescence properties, than their analogs grown on GaSb [8]. In present work the processes of growth of multicomponent solid solutions GaInAsSb, InAsPSb, AlInAsSb, AlGaInAsSb are investigated. The obtained data can be used for device structure fabrication.

3. EXPERIMENT

In epitaxial growth processes InAs(100) substrates undoped as well as doped by tin were used. Prior to growth, the substrates was degreased via boiling in acetone and then was treated in hydrochloric acid (HCl) during 30 seconds and after in etchant HNO₃:HF:H₂SO₄ = 1.5:1:1 during 60 seconds.

Epitaxial growth was carried out on AIX200 apparatus with horizontal reactor at temperature 600 °C and low pressure (100 mbar). The precursors of III group elements was alkyls: trimethylaluminum (TMAI), triethylgallium (TEGa) and trimethylindium (TMIn), V group elements precursors was trimethylantimony (TMSb) and hydrides: arsine (AsH₃) diluted by hydrogen to 10% and 100% phosphine (PH₃). The flux of hydrogen through the reactor was 5.5 L min⁻¹.

To avoid InAs-substrate degradation during heating, arsenic overpressure was provided by blowing through the reactor of 10% arsine (20 cm³ min⁻¹) started at 200 °C and went on up to growth start. After stopping of epitaxial growth, arsine flux was started again and went on during cooling-down to 250 °C.

Growth rate of all epitaxial layers was 3 – 4 μm per hour.

Compositions of the epitaxial layers were measured by X-ray microanalyzer «Camebax».

The spectra of photoluminescence (PL) were investigated on the setup with a closed cycle helium cryostat allowing measurements in wide temperature range from 4 to 350 K. An 980 nm semiconductor laser with adjustable power was used for excitation. The excitation power laid within range 100 – 360 mW. The optical signal was registered with high-aperture spectrometer SDL-1 (LOMO) and a cooled Hg-Gd-Te photoresister («Hamamatsu»).

The images of surfaces morphology of the obtained layers was taken by the electron microscope «CamScan».

Lattice mismatch (LM) f_{\perp} was found from X-ray diffraction (XRD) curves, which were taken by X-ray diffractometer «D8 DISCOVER».

4. RESULTS

GaInAsSb

All samples of GaInAsSb were grown at V/III ratio = 3.6 (the ratio of summa of the partial pressures of V-group elements precursors to summa of the ones of III-group elements precursors). Figure 1 shows the XRD curve (a) and PL-spectra (b) of one of series of the obtained GaInAsSb samples.

Epitaxial layers GaInAsSb having non-perfect (but satisfactory) crystal quality demonstrated intensive PL at room temperature in 3.2 – 3.8 μm wavelength range.

Their LM value f_{\perp} falls in the range from $-1.3 \cdot 10^{-3}$ to $3.8 \cdot 10^{-3}$, full width at half maximum (FWHM) was 46'' – 60'' for substrates and 100'' – 170'' for layers, the compositions of obtained $Ga_{1-x}In_xAs_ySb_{1-y}$ solid solutions laid within the range $0.86 < x < 0.93$, $0.89 < y < 0.91$.

InAsPSb

This solid solutions, lattice-matched with InAs cover wavelength range from 2.5 to 4 μm and can be used as active regions and as cladding layers of radiation sources [9].

At the selected growth temperature (600 °C) the fractions of pyrolyzed arsine and phosphine are 70 % and 3 – 5 % respectively [10].

In the course of present work, the influence of value of phosphine flux H_{PH_3} in MOCVD process on the obtained samples properties was investigated. The fluxes of hydrogen trough alkyl (TMIn, TMSb) source bubblers and flux of arsine (10 % AsH₃) were fixed and adjusted to provide a deficit of V-group components when PH₃ is absent.

Under the provided conditions, the effective incorporation of phosphorous into the crystal lattice was observed at small PH₃ fluxes ($H_{PH_3} = 6 - 20 \text{ cm}^3 \text{ min}^{-1}$), and some saturation occurred at larger values of H_{PH_3} (table 1). This saturation had an effect on dependence of LM value on H_{PH_3} (figure 2, b).

The increasing of crystal perfection of obtained InAsPSb with decreasing of LM value was observed. It appears in narrowing of peaks of XRD curves (table 1, figure 2, a) and narrowing of PL-peaks (figure 3).

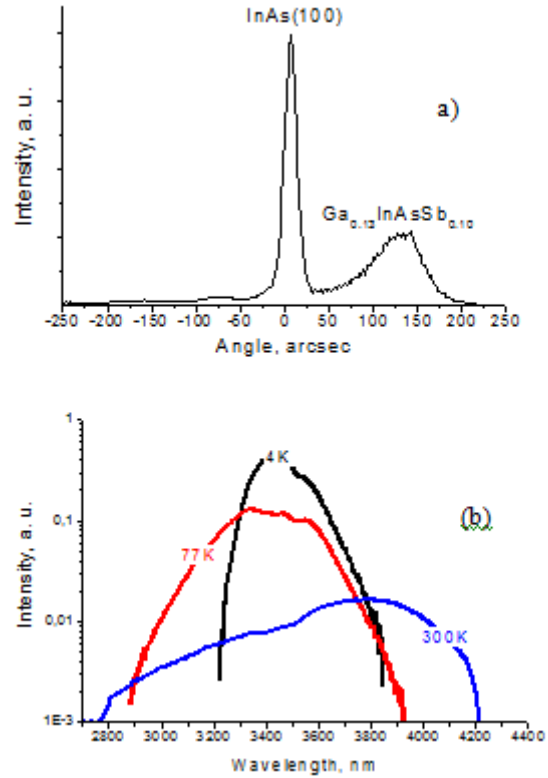


Fig.1. XRD curve (a) and PL-spectra at different temperatures (b) of $Ga_{0.13}In_{0.87}As_{0.90}Sb_{0.10}/InAs(100)$ sample.

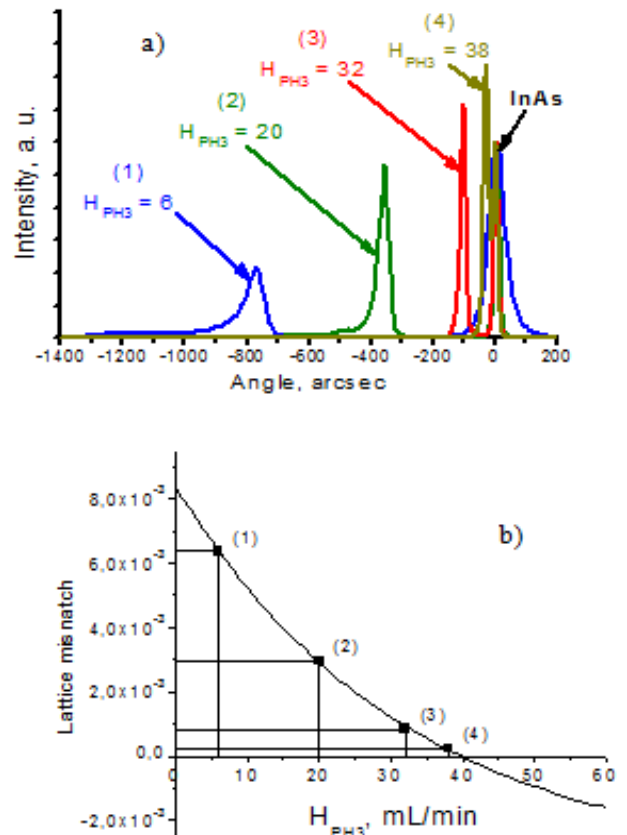


Fig.2. XRD curves for InAsPSb samples grown on InAs(100) substrates (a) and dependence of these InAsPSb LM on H_{PH_3} (b).

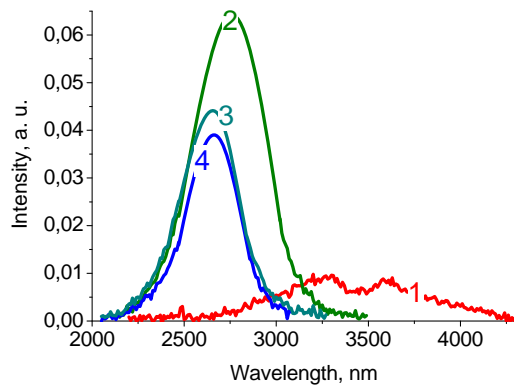


Fig. 3. PL spectra of InAsPSb solid solutions at 300 K. The numbers correspond to samples, listed in table 1.

The morphology of obtained layers surfaces depended on LM between substrate and layer: the larger LM value, the more pronounced relief (figure 4).

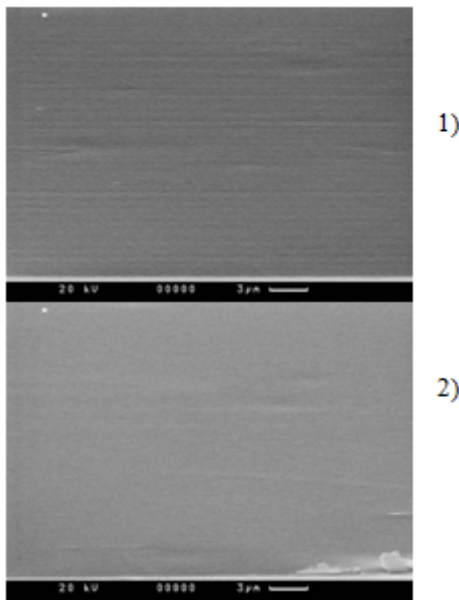


Fig. 4. Images of InAsPSb surfaces taken by electronic microscope “CamScan” for samples with LM $f_L = 6.36 \cdot 10^{-3}$ (1) and $f_L = 2.94 \cdot 10^{-3}$ (2).

In the course of present experiment, sufficiently perfect epilayers of InAsPSb solid solutions was obtained. FWHM of epilayers came down to 14'' that comparable with crystal perfection of substrates.

Accordingly excellent PL and structural characteristics, InAsPSb solid solutions are good materials for active regions of light emitting semiconductor devices.

At present time, solid solutions InAsPSb are popular material for cladding layers of lasers with InAs active region. In this case, maximal energy barrier for electrons makes up 0.08 eV only. Using InAs active region with GaInAsSb cladding layer the barriers for electrons may be some smaller.

Room-temperature devices need in barriers about 0.2 eV for electrons and about 0.1 eV for holes. Thus, other types of materials for cladding layers are needed.

Such materials are A3B5 solid solutions, containing aluminium.

AlGaInAsSb

Narrow-gap (0.35 – 0.5 eV) solid solutions AlGaInAsSb was obtained on InAs substrates using regimes which were selected for growth of GaInAsSb. As our investigations shows, small addition of TMAI into common flow of gases leads to essential decreasing of lattice constant and PL intensity. When LM value was sufficiently large ($\sim 4.4 \cdot 10^{-3}$), PL was not observed. At medium values of LM ($\sim 2 \cdot 10^{-3}$), the PL intensity decreased with Al content value become larger (figure 5).

AlGaInAs

In spite of the fact that containing aluminium solid solutions are difficult for MOCVD growth, but they are important materials for cladding layers of semiconductor lasers, because they allow to create the barriers for electrons more then 0.18 eV and for holes more then 0.09 eV. As our theoretically investigations showed, AlInAsSb quaternary solid solutions can be utilized as cladding layers with active regions InAs and grown in present work GaInAsSb.

The calculations of gallium content influence on properties of AlGaInAsSb showed, than in case of InAs or $Ga_{0.13}In_{0.87}As_{0.90}Sb_{0.10}$ active regions the desirable values of barriers can be obtained using quaternary solid solutions AlInAsSb, what may be preferably then pentanary solid solutions AlGaInAsSb because of more simple selection of growth conditions.

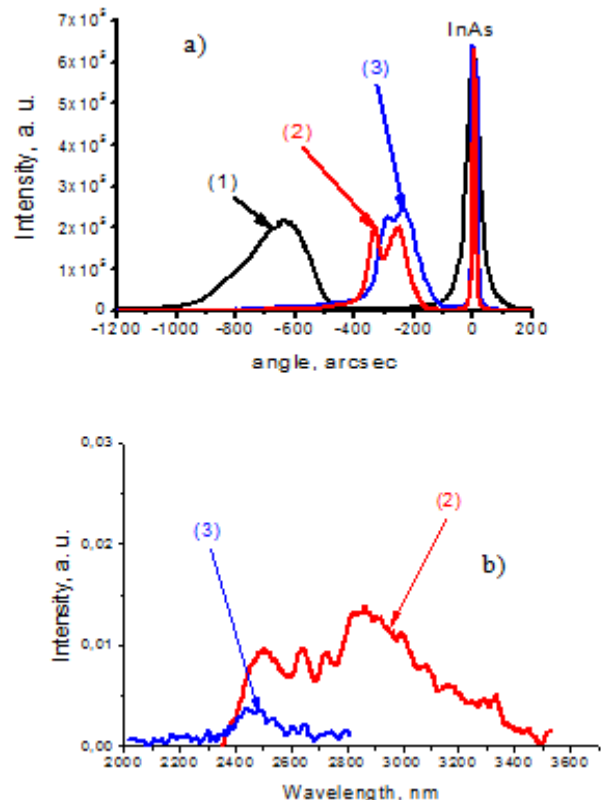


Fig. 5. XRD curves (a) and PL spectra (b) for AlGaInAsSb samples with several content of aluminium.

- (1) - $Al_{0.02}Ga_{0.05}In_{0.93}As_{0.89}Sb_{0.11}$, (2) - $Al_{0.02}Ga_{0.08}In_{0.90}As_{0.91}Sb_{0.09}$,
- (3) - $Al_{0.09}Ga_{0.03}In_{0.88}As_{0.92}Sb_{0.08}$

In the case of active layers which mentioned above, the increasing of aluminium content in solid solution

gives the rising of barriers for both: electrons and holes, but decreases the lattice constant value. The decreasing of arsenic content gives rising of the lattice constant value but decreases the energy barrier for holes and slightly increases one for electrons.

If aluminium and arsenic contents are changed simultaneously so as to provide lattice-matching, the energy barrier change slightly for holes and essentially for electrons.

The figure 6 presents the examples of lattice-matched heterostructures, which can be obtained with $Ga_{0.13}In_{0.87}As_{0.90}Sb_{0.10}$ active regions. For InAsPSb the case of maximal barrier for electrons is showed.

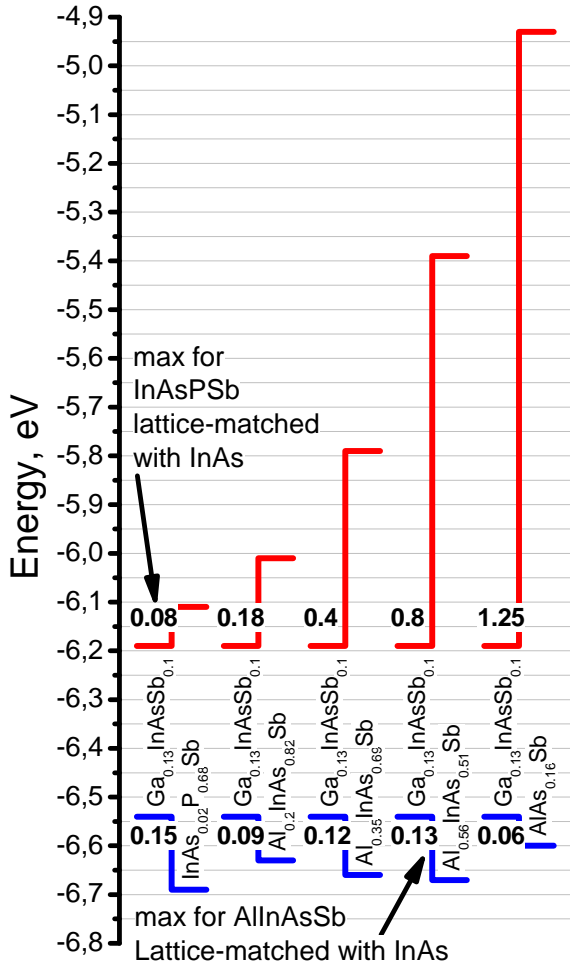


Fig. 6. The examples of heterojunctions between $Ga_{0.13}In_{0.87}As_{0.90}Sb_{0.10}$ and InAsPSb or AlInAsSb lattice-matched with InAs. Band positions was calculated accordingly [11] with bowing parameters from [12] and interpolation scheme, described in [13].

Conditions for growth of AlInAsSb was selected based on regimes which was used for obtaining of mentioned above narrow-gap AlGaInAsSb. The solid solutions with satisfactory crystalline quality (fig. 7) and PL characteristics better than ones of early grown AlGaInAsSb (fig. 8) were obtained.

The increasing of PL intensity was observed with decreasing of LM value (fig. 8).

The dependence of LM on AsH3 flux is nearly linear (fig. 7 a). The dependences of aluminium and antimony contents in corresponding crystalline sublattices on AsH3 flux value are presented on figure 9.

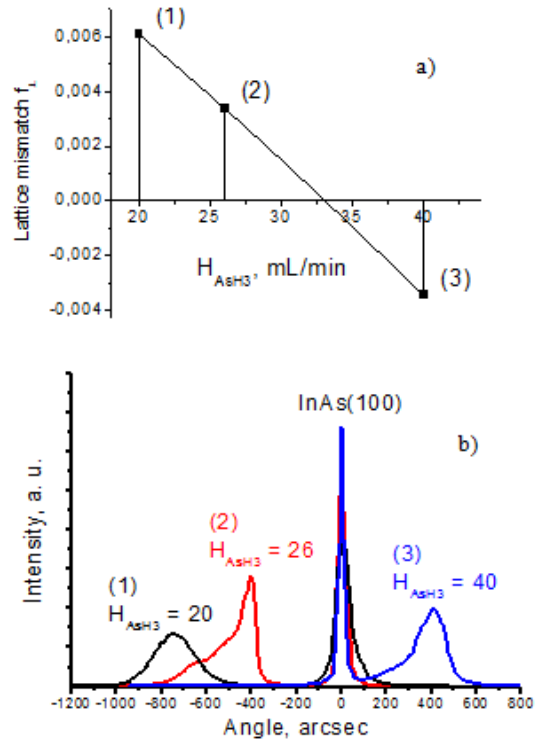


Fig. 7. Dependence of LM on AsH3 flux (a) and XRD curves (b) for AlInAsSb. The fluxes of TMAI, TMIIn and TMSb were fixed.

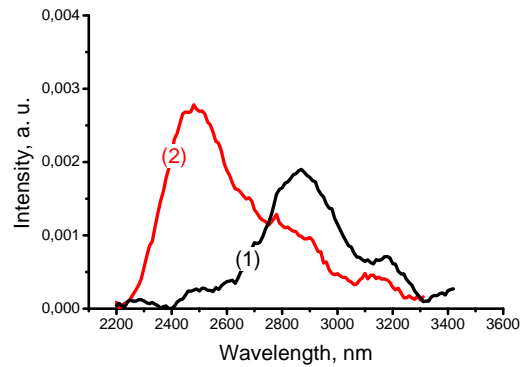


Fig. 8. PL spectra of AlInAsSb solid solutions at 77 K. (1) LM $f_L = 6.08 \times 10^{-3}$, (2) LM $f_L = 3.38 \times 10^{-3}$.

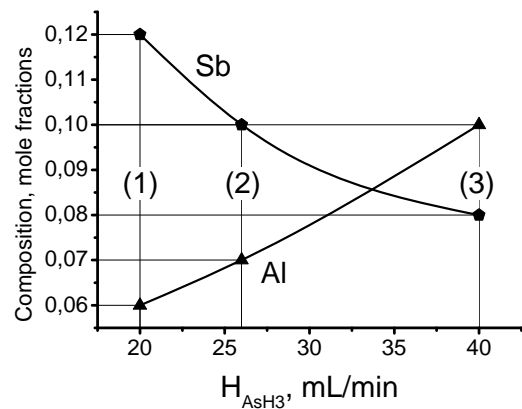


Fig. 9. The dependences of aluminium (Al) and antimony (Sb) content in corresponding crystalline sublattices on AsH3 flux H_{AsH_3} . The fluxes of TMAI, TMIIn and TMSb were fixed.

When TMAI, AsH3 and TMSb fluxes are fixed, the LM value decreases with decreasing of TMIIn flux (figure 10).

The parameters of obtained AlInAsSb samples are listed in table 2, and images of their surfaces are shown in figure 11.

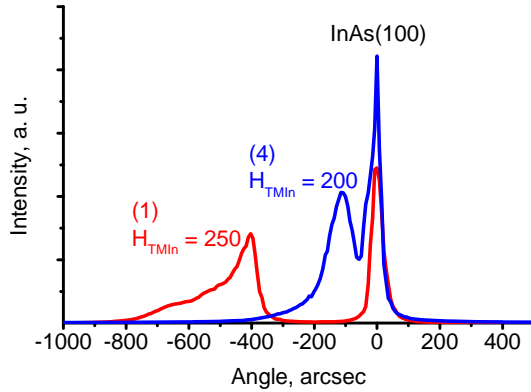


Fig. 10. XRD curves of AlGaInAs solid solutions, obtained at several fluxes of TMIIn H_{TMIIn} at fixed TMAI, AsH₃ and TMSb fluxes.

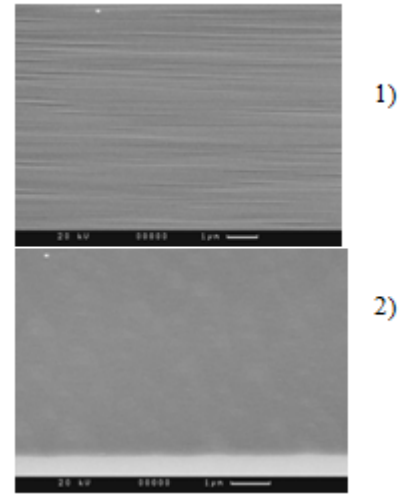


Fig. 11. Images of AlGaInAs surfaces taken by electronic microscope “CamScan” for samples with LM $f_L = 6.08 \times 10^{-3}$ (1) and $f_L = 3.38 \times 10^{-3}$ (2).

Table 1. Properties of obtained samples of InAsPSb/InAs(100)

Sample number	H_{PH3}	V/III	Composition	LM f_L	FWHM of substrate	FWHM of layer
(1)	6	5.3	InAs _{0.68} P _{0.17} Sb _{0.15}	$6.36 \cdot 10^{-3}$	58 ^{''}	59 ^{''}
(2)	20	12.2	InAs _{0.64} P _{0.24} Sb _{0.12}	$2.94 \cdot 10^{-3}$	18 ^{''}	30 ^{''}
(3)	32	18.2	InAs _{0.62} P _{0.25} Sb _{0.13}	$8.29 \cdot 10^{-4}$	15 ^{''}	19 ^{''}
(4)	38	21.2	InAs _{0.61} P _{0.26} Sb _{0.13}	$2.3 \cdot 10^{-4}$	14 ^{''}	13 ^{''}

Table 2. Properties of obtained samples of AlInAsSb/InAs(100)

Sample number	Composition	V/III	LM, f_L
(1)	Al _{0.06} In _{0.94} As _{0.88} Sb _{0.12}	4.6	6.08×10^{-3}
(2)	Al _{0.07} In _{0.93} As _{0.9} Sb _{0.1}	4.9	3.38×10^{-3}
(3)	Al _{0.1} In _{0.9} As _{0.92} Sb _{0.08}	5.8	-3.45×10^{-3}
(4)	Al _{0.08} In _{0.92} As _{0.91} Sb _{0.09}	6	9.52×10^{-4}

5. CONCLUSION

The growth procedures of Ga_{1-x}In_xAs_ySb_{1-y} ($0.86 < x < 0.93$, $0.89 < y < 0.91$), InAs_yP_zSb_{1-y-z} ($0.63 < y < 0.68$, $0.17 < z < 0.26$), Al_uGa_{1-u-x}In_xAs_ySb_{1-y} ($0.02 < u < 0.11$, $0.88 < x < 0.94$, $0.89 < y < 0.92$) and Al_uIn_{1-u}As_ySb_{1-y} ($0.06 < u < 0.1$, $0.88 < y < 0.92$) solid solutions are developed. During epitaxial processes the V/III ratio laid in range 3.6 – 21.2. Obtained solid solutions had satisfactory crystalline perfection and showed the intensive PL. The solid solutions, which not contained aluminium demonstrated PL at room temperature.

As it was discovered, the control of InAsPSb solid solutions properties by the changing of PH₃ flux value is

not very effective. The essential influence of PH₃ flux value on properties of obtained solid solutions can be provided only in conditions of shortage of other V group components.

The variation of AsH₃ flux H_{AsH3} gives the possibilities to strong influence on obtained solid solutions properties: the small changes of H_{AsH3} value results in essential changes of such properties as LM value and solid solution composition.

The quality of obtained layers is mainly depended on LM value that appears in surface morphology, FWHM of XRD curves peaks and PL intensity.

- | | |
|---|---|
| <p>[1]. C. Lin, M. Grau, O. Dier, and M.-C. Amann. Low threshold room-temperature continuous-wave operation of 2.24-3.04 μm GaInAsSb/AlGaAsSb quantum-well lasers. Appl. Phys. Lett. 84, 2004, p. 5088-5090.</p> <p>[2]. M. Grau, C. Lin, O. Dier, C. Laurer, and M.-C. Amann. Room-temperature operation of 3.26 μm GaSb-based type-I lasers with quinary AlGaInAsSb barriers. Appl. Phys. Lett. 87, 2005, p 241104.</p> | <p>[3]. J. A. Gupta, P. J. Barrios, G. C. Aers, P. Waldon and S. Storey. Room-temperature continuous-wave operation of type-I GaSb-based lasers at 3.1 μm. Electron. Lett. 45, 16, 2009, pp. 835-836</p> <p>[4]. S. S. Kizhaev, N. V. Zotova, S. S. Molchanov, and Yu. P. Yakovlev, High power InAsSbP/InAsSb light emitting diodes grown by MOVPE // Abstracts of Mid-infrared Optoelectronics Materials and Devices Fourth International</p> |
|---|---|

- Conference, Montpellier, France, 1-4 April, 2001, p. 106.
- [5]. *D. Wu, B. Lane, H. Mohseni, J. Diaz, and M. Razeghi.* High power asymmetrical InAsSb/InAsSbP/AlAsSb double heterostructure lasers emitting at 3.4 μm . Appl. Phys. Lett. V 74, pp. 1194 – 1196.
- [6]. *R. M. Biefeld, A. A. Allerman, S. R. Kurtz, E. D. Jones, I. J. Fritz, R. M. Sieg.* The growth of infrared antimonide-based semiconductor lasers by metal-organic chemical vapor deposition. Journal of materials science: materials in electronics. V 13, 2002, pp. 649-657.
- [7]. *V. M. Smornov, P. J. Batty, R. Jones, A. Krier, V. I. Vasil'ev, G. S. Gagis and V. I. Kuchinskii.* GaInAsPSb/GaSb heterostructures for mid-infrared light emitting diodes. Phys. Stat. Sol. (a), V 204, 2007, pp. 1047-1050.
- [8]. *G. S. Gagis, V. I. Vasil'ev, A. G. Deryagin, V. V. Dudelev, A. S. Maslov, R. V. Levin, B. V. Pushnyi, V. M. Smirnov, G. S. Sokolovskii, G. G. Zegrya and V. I. Kuchinskii.* Semicond. Sci. Technol. V 23, 2008, p125026 (6pp).
- [9]. *N. N. Mursakulov.* Features of the growth of epitaxial layers of solid solutions $\text{InAs}_{1-x-y}\text{Sb}_y\text{P}_z$ lattice-matched the substrate InAs. Inst/ Phys. Conf. Ser. No 152: Section B: Thin Film growth and Characterization. 11th Int. Conf. on Ternary and Multinary Compounds, ICTMC-11, Salford, 8-12 September (1997), pp: 341-344, 1998 IOP Publishing LTD
- [10]. *Gerald B. Stringfellow;* “Organometallic Vapor-Phase Epitaxy: Theory and Practice”; Departments of Materials Science and Engineering and Electrical Engineering, University of Utah; Academic Press, 1989.
- [11]. *M. P. C. M. Krijn.* Heterojunction band offsets and effective masses in III-V quaternary alloys. Semicond. Sci. Technol. V. 6, (1991), pp. 27-31.
- [12]. *I. Vurgaftman, J. R. Meyer and L. R. Ram-Mohan.* Band parameters for III–V compound semiconductors and their alloys. J. Appl. Phys. V. 89, 2001, pp. 5815-5875.
- [13]. *K. Shim and H. Rabitz.* Electronic and structural properties of the pentanary alloy $\text{Ga}_x\text{In}_{1-x}\text{P}_y\text{Sb}_z\text{As}_{1-y-z}$. J. Appl. Phys. V. 85, 1999, pp 7705-7715.

COMPARISON OF THE VALENCE BAND STRUCTURE PECULIARITIES IN THE $\text{Bi}_{0.84}\text{-Sb}_{0.16}\text{-Sn}_{0.1}$ AND PURE SEMICONDUCTING $\text{Bi}_{1-x}\text{Sb}_x$ ALLOYS

BAKIR TAIROV^{1*} AND ELTAJ YUZBASHOV¹

¹ *Institute of Physics of Azerbaijan National Academy of Sciences, H.Javid pr., 33, Baku, AZ 1143, Azerbaijan*

E-mail address: btairov@physics.ab.az

On the basis of measured low magnetic field galvanomagnetic coefficients both for Sn-doped $\text{Bi}_{0.84}\text{-Sb}_{0.16}\text{-Sn}_{0.1}$ and pure semiconducting Bi-Sb alloys, kinetic parameters of the investigated materials have been determined. It is shown that hole ellipsoids corresponding to the obtained results are less anisotropic ($v_2/v_1=0.05$, $v_3/v_1=0.5$) in comparison with L-hole ellipsoids, where $v_2/v_1=0.009$, $v_3/v_1=0.7$ and their slope is significantly larger ($\phi_h=16$) than L-hole (and L-electron) ones. Therefore peculiarities of the valence band for the $\text{Bi}_{0.84}\text{-Sb}_{0.16}$ alloy and other semiconducting alloys with high content of antimony can not be adequately described by involving dominant contribution of the hole valleys localized in T, H and L points of the Brioullin Zone.

keywords: Bi-Sb alloys, galvanomagnetic properties, energetic zone structure of Bi-Sb alloys

The investigation of Bi-Sb alloys has a great importance both theoretically and practically. Due to high mobility of the charge carriers the semiconducting alloys are one of the best materials for thermoelectric and galvanomagnetic devices. Complexity of the band structure, easily reconstruction of the band structure by small variation of Sb concentration, temperature, pressure resulting in transition between semimetallic, gapless, semiconducting states and other peculiarities of these alloys are of great value to theoretical investigations too. That is why these materials are still being investigated as bulk materials, thin films and nanoscale structures [1-4].

In the present work specific electrical resistance, Hall coefficient, and low magnetic field magnetoresistance tensor components have been measured in n- $\text{Bi}_{1-x}\text{Sb}_x$ single crystals ($0.16 \leq x \leq 0.22$) at the temperature range 77÷300 K and in $\text{Bi}_{0.84}\text{-Sb}_{0.16}\text{-Sn}_{0.1}$ at the temperature 77 K. As a sample the temperature dependence of the low magnetic field magnetoresistance tensor components for the undoped $\text{Bi}_{0.84}\text{-Sb}_{0.16}$ alloy is depicted in the figure 1. On the basis of these measurements, calculations of the kinetic parameters of charge carriers for the $\text{Bi}_{1-x}\text{Sb}_x$ alloys were conducted by using the following 9 formulas connecting kinetic and energetic band parameters with independent coefficients of the low field galvanomagnetic tensor:

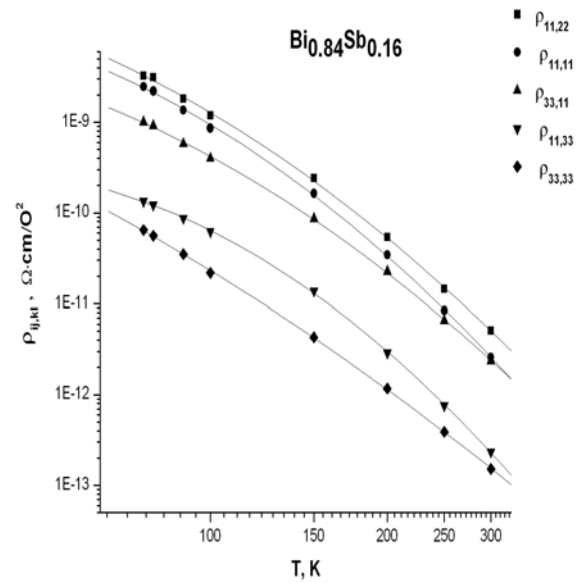


Fig. 1. Temperature dependence of low magnetic field magnetoresistance tensor components for pure single $\text{Bi}_{0.84}\text{-Sb}_{0.16}$ crystal.

$$\sigma_{11,0} = \frac{1}{2} N_e e (\mu_1 + \alpha_1^2 \mu_2 + \beta_1^2 \mu_3) \pm \frac{1}{2} N_g e (v_1 + \alpha_2^2 v_2 + \beta_2^2 v_3) \pm N_g e v_1 \quad (1),$$

$$\sigma_{33,0} = N_e e (\alpha_1^2 \mu_3 + \beta_1^2 \mu_2) \pm N_g e (\alpha_2^2 v_3 + \beta_2^2 v_2) \pm N_g e v_3 \quad (2),$$

$$-\sigma_{231} = -\frac{N_e e}{2c} [\mu_2 \mu_3 + \mu_1 (\beta_1^2 \mu_2 + \alpha_1^2 \mu_3)] \pm \frac{N_g e}{2c} [v_2 v_3 + v_1 (\beta_2^2 v_2 + \alpha_2^2 v_3)] \pm \frac{N_g e}{c} v_1 v_3 \quad (3),$$

$$-\sigma_{123} = -\frac{N_e e}{c} [\mu_1 (\beta_1^2 \mu_3 + \alpha_1^2 \mu_2)] \pm \frac{N_g e}{c} [v_1 (\beta_2^2 v_3 + \alpha_2^2 v_2)] \pm \frac{N_g e}{c} v_1^2 \quad (4),$$

$$\sigma_{11,33} = \frac{N_e e}{2c^2} [(\mu_1 + \beta_1^2 \mu_3 + \alpha_1^2 \mu_2) \mu_1 (\beta_1^2 \mu_3 + \alpha_1^2 \mu_2)] \pm \frac{N_g e}{2c^2} [(v_1 + \beta_2^2 v_3 + \alpha_2^2 v_2) v_1 (\beta_2^2 v_3 + \alpha_2^2 v_2)] \pm \frac{N_g e}{c^2} v_1^3 \quad (5),$$

$$\sigma_{33,11} = \frac{N_e e}{2c^2} (\beta_1^2 \mu_2 + \alpha_1^2 \mu_3) [\mu_2 \mu_3 + \mu_4 (\beta_1^2 \mu_2 + \alpha_1^2 \mu_3)] \pm \frac{N_g e}{2c^2} (\beta_2^2 \nu_2 + \alpha_2^2 \nu_3) [\nu_2 \nu_3 + \nu_1 (\beta_2^2 \nu_2 + \alpha_2^2 \nu_3)] \pm \frac{N_g e}{c^2} \nu_1 \nu_3^2 \quad (6),$$

$$\sigma_{11,11} = \frac{N_e e}{8c^2} [\beta_1^2 \mu_2 (\mu_1 - \mu_3)^2 + \alpha_1^2 \mu_3 (\mu_1 - \mu_2)^2 + 3\alpha_1^2 \beta_1^2 \mu_4 (\mu_2 - \mu_3)^2] \pm \frac{N_g e}{8c^2} [\beta_2^2 \nu_2 (\nu_1 - \nu_3)^2 + \alpha_2^2 \nu_3 (\nu_1 - \nu_2)^2 + 3\alpha_2^2 \beta_2^2 \nu_1 (\nu_2 - \nu_3)^2] \quad (7)$$

$$\sigma_{11,22} = \frac{N_e e}{8c^2} [3\beta_1^2 \mu_2 (\mu_1^2 + \mu_3^2) + 3\alpha_1^2 \mu_3 (\mu_1^2 + \mu_2^2) + \alpha_1^2 \beta_1^2 \mu_4 (\mu_2 - \mu_3)^2 + 2\mu_1 \mu_2 \mu_3] \pm \frac{N_g e}{8c^2} [3\beta_2^2 \nu_2 (\nu_1^2 + \nu_3^2) + 3\alpha_2^2 \nu_3 (\nu_1^2 + \nu_2^2) + \alpha_2^2 \beta_2^2 \nu_1 (\nu_2 - \nu_3)^2 + 2\nu_1 \nu_2 \nu_3] \pm \frac{N_g e}{c^2} \nu_1^2 \nu_3 \quad (8)$$

$$\sigma_{33,33} = \frac{N_e e}{c^2} [\alpha_1^2 \beta_1^2 \mu_4 (\mu_2 - \mu_3)^2] \pm \frac{N_g e}{c^2} [\alpha_2^2 \beta_2^2 \nu_1 (\nu_2 - \nu_3)^2] \quad (9)$$

Here, N_e and N_g concentrations of electrons and holes, respectively;

μ_i and ν_i are components of mobility tensor, correspondingly for electrons and holes; α_1, β_1 and α_2, β_2 are cosines and sines of electron and hole ellipsoids slope angles, correspondingly.

The above mentioned magnetoconductivity tensor components were determined from the experimentally measured magnetoresistivity tensor components according to the following formula:

$$\sigma_{11} = \frac{1}{\rho_{11}} \quad (10)$$

$$\sigma_{33} = \frac{1}{\rho_{33}} \quad (11)$$

$$\sigma_{123} = \frac{R_{123}}{\rho_{11}^2} \quad (12)$$

$$\sigma_{231} = \frac{R_{231}}{\rho_{11} \rho_{33}} \quad (13)$$

$$\sigma_{11,11} = \frac{\rho_{11,11}}{\rho_{11}^2} \quad (14)$$

$$\sigma_{33,33} = \frac{\rho_{33,33}}{\rho_{33}^2} \quad (15)$$

$$\sigma_{11,22} = \frac{\rho_{11,22}}{\rho_{11}^2} + \frac{R_{231}^2}{\rho_{11}^2 \rho_{33}} \quad (16)$$

$$\sigma_{11,33} = \frac{\rho_{11,33}}{\rho_{11}^2} + \frac{R_{123}^2}{\rho_{11}^3} \quad (17)$$

$$\sigma_{33,11} = \frac{\rho_{33,11}}{\rho_{33}^2} + \frac{R_{231}^2}{\rho_{11} \rho_{33}^2} \quad (18)$$

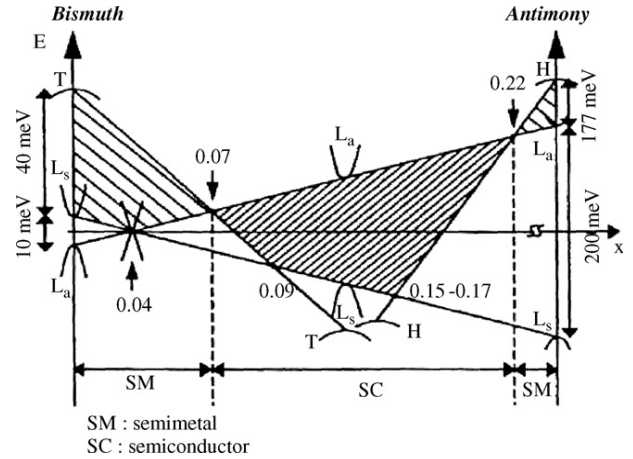


Fig. 2. Band diagram of $\text{Bi}_{1-x}\text{Sb}_x$ alloys as a function of x .

Previous investigations for bismuth rich $\text{Bi}_{1-x}\text{Sb}_x$ ($0 < x \leq 10$) alloys showed that measured values of the low field galvanomagnetic coefficients may satisfactorily be interpreted by choosing an appropriate model of Fermi surface for current carriers; often a two-ellipsoidal model gives acceptable results for the kinetic parameters in that range of antimony content. We chose the range of $0.16 \leq x \leq 0.22$ for $n\text{-Bi}_{1-x}\text{Sb}_x$ single crystals because that interval of the semiconducting alloys is less investigated.

As it is seen from Fig.2 for semiconducting $\text{Bi}_{1-x}\text{Sb}_x$ ($0.16 \leq x \leq 0.22$) alloys there is a region, where all hole valleys (T, H and L_s) may contribute to the transport phenomena. Calculations of kinetic parameters ($N, P, -$ concentration of electrons and holes, respectively; μ_i, ν_i – mobilities of electrons and holes, respectively) for those undoped semiconducting alloys were carried out by using many-ellipsoidal model for Fermi surface of corresponding charge carriers. Particularly the following results concerning hole ellipsoid parameters have been obtained at nitrogen temperatures: $\nu_2/\nu_1=0.05, \nu_3/\nu_1=0.5$. But these results for a hole ellipsoid don't correspond to any of the L, T, H ellipsoids of the Brillouin zone.

To clarify this situation, analogical calculations were performed for $\text{Bi}_{0.84}\text{Sb}_{0.16}\text{Sn}_{0.1}$, where Fermi level lies below conduction band extremum and we deal solely with valence band extremes. In the Table I experimental and calculated components of the conductivity tensor for pure and Sn-doped $\text{Bi}_{0.84}\text{Sb}_{0.16}$ are presented.

Table I. Components of the conductivity tensor for pure and Sn-doped $\text{Bi}_{0.84}\text{Sb}_{0.16}$ alloys at the temperature 77 K.

	0.0 Sn, At. %		0.1 Sn, At. %	
	<i>Exp.</i>	<i>Calc.</i>	<i>Exp.</i>	<i>Calc.</i>
σ_{11} ($\Omega^{-1}\cdot\text{m}^{-1}$)	$5.15\cdot 10^{-1}$	$4.87\cdot 10^{-1}$	4.12	4.00
σ_{33} ($\Omega^{-1}\cdot\text{m}^{-1}$)	$5.70\cdot 10^{-1}$	$6.10\cdot 10^{-1}$	3.52	3.40
σ_{321} ($\Omega^{-2}\cdot\text{m}\cdot\text{C}^{-1}$)	$2.00\cdot 10^{-11}$	$2.06\cdot 10^{-11}$	$2.48\cdot 10^{-7}$	$2.36\cdot 10^{-7}$
σ_{123} ($\Omega^{-2}\cdot\text{m}\cdot\text{C}^{-1}$)	$0.68\cdot 10^{-10}$	$0.60\cdot 10^{-10}$	$0.74\cdot 10^{-7}$	$0.81\cdot 10^{-7}$
$\sigma_{11,33}$ ($\Omega^{-3}\cdot\text{m}^3\cdot\text{C}^{-2}$)	$3.40\cdot 10^{-17}$	$3.90\cdot 10^{-17}$	$0.69\cdot 10^{-14}$	$0.58\cdot 10^{-14}$
$\sigma_{33,11}$ ($\Omega^{-3}\cdot\text{m}^3\cdot\text{C}^{-2}$)	$1.07\cdot 10^{-19}$	$1.43\cdot 10^{-19}$	$1.72\cdot 10^{-14}$	$1.43\cdot 10^{-14}$
$\sigma_{11,11}$ ($\Omega^{-3}\cdot\text{m}^3\cdot\text{C}^{-2}$)	$5.84\cdot 10^{-20}$	$5.10\cdot 10^{-20}$	$0.86\cdot 10^{-14}$	$0.74\cdot 10^{-14}$
$\sigma_{11,22}$ ($\Omega^{-3}\cdot\text{m}^3\cdot\text{C}^{-2}$)	$1.42\cdot 10^{-19}$	$1.56\cdot 10^{-19}$	$1.98\cdot 10^{-14}$	$2.33\cdot 10^{-14}$
$\sigma_{33,33}$ ($\Omega^{-3}\cdot\text{m}^3\cdot\text{C}^{-2}$)	$1.93\cdot 10^{-17}$	$2.00\cdot 10^{-17}$	$0.21\cdot 10^{-14}$	$0.18\cdot 10^{-14}$

Table II. Kinetic parameters of current carriers for pure and Sn-doped $\text{Bi}_{0.84}\text{Sb}_{0.16}$ alloys at the temperature 77 K.

Sn, At. %	φ_e	φ_h	μ_1 ($\text{m}^2\cdot\text{V}^{-1}\cdot\text{s}^{-1}$)	μ_2 ($\text{m}^2\cdot\text{V}^{-1}\cdot\text{s}^{-1}$)	μ_3 ($\text{m}^2\cdot\text{V}^{-1}\cdot\text{s}^{-1}$)	v_1 ($\text{m}^2\cdot\text{V}^{-1}\cdot\text{s}^{-1}$)	v_2 ($\text{m}^2\cdot\text{V}^{-1}\cdot\text{s}^{-1}$)	v_3 ($\text{m}^2\cdot\text{V}^{-1}\cdot\text{s}^{-1}$)	N_e (m^{-3})	N_h (m^{-3})
0.0	5^0	16^0	$9.00\cdot 10^1$	$8.10\cdot 10^{-1}$	$6.30\cdot 10^1$	$3.00\cdot 10^1$	1.50	$1.50\cdot 10^1$	$4.95\cdot 10^{22}$	$4.95\cdot 10^{22}$
0.1	—	16^0	—	—	—	$1.32\cdot 10^{-1}$	$6.60\cdot 10^{-3}$	$6.60\cdot 10^{-2}$	—	$3.50\cdot 10^{24}$

Kinetic parameters of current carriers for pure and Sn-doped $\text{Bi}_{0.84}\text{Sb}_{0.16}$ are depicted in the Table II. It is clear from the table that the obtained results concerning the hole mobility ratios for the doped sample within experimental errors are the same as for pure single crystals.

It is also clear that hole ellipsoids corresponding to the obtained results are less anisotropic in comparison with L-hole ellipsoids, where $v_2/v_1=0.009$, $v_3/v_1=0.7$ and their slope is significantly larger ($\varphi_h = 16$) than L-hole (and L-electron) ones.

Such behavior of hole charge carriers may be explained either by assuming existence of a new type of hole ellipsoids located in some point of the Brillouin zone (fig.3) or by introducing an “effective hole ellipsoid” combined from all contributions of lighthole L band and heavyhole T&H bands.

The final decision about the peculiarities of the valence band requires the knowledge of the precious values of effective masses of the carriers (their temperature dependence too) in all the three bands under consideration, and the temperature dependence of the band gap and consideration of scattering mechanisms of current carriers in Bi–Sb alloys. There is need to carrying out further studies of galvanomagnetic and thermomagnetic effects on pure and acceptor-doped semiconducting single crystals of $\text{Bi}_{1-x}\text{Sb}_x$ as a function of pressure and temperature. In interpreting experimental data on transport phenomena in the many valley crystals a special attention must be paid to choosing of proper scattering mechanisms of current carriers, because intervalley electron-phonon scattering [5] may play a

significant role. Difficulties arising in interpreting of the transport phenomena may be overcome by involving other theoretical models as Pseudo-parabolic model [6].

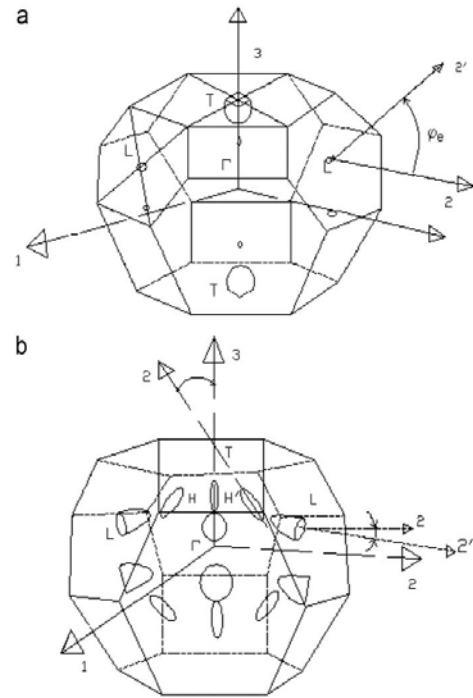


Fig. 3. (a) Fermi surfaces of Bi, electrons are at L- points and holes at T-points. (b) Fermi surfaces of Sb, electrons are at L- points and holes at H-points.

- [1]. *S. Dutta, V. Shubhaa and T.G. Ramesha*: Physica B: Condensed Matter. **405** (2010) No 5, 1239.
- [2]. *J. Heremans, D. L. Parlin, and et.al*: Physical Review B. **48** (1993) No 15, 11329.
- [3]. *D.Choi. A.Balandin, and et.al*: Appl. Phys. Lett. **89** (2006) 1415.
- [4]. *S.Dutta, V. Shubha, T.G. Ramesh, Florita D'Sa*: Journal of Alloys and Compounds. **467** (2009) 305.
- [5]. *Chihiro Hamaguchi*: *Basic Semiconductor Physics* (Springer, 2010). 2nd ed., 248 .
- [6]. *J. Hermans, O.P. Hansen*: J.Phys.C. **12** (1979) No 17, 3483.

ALTERNATIVE II-IV-V₂ AND Zn-III-IV-As₃ COMPOUNDS FOR PHOTOVOLTAIC APPLICATIONS

A. V. KRIVOSHEEVA^{1*}, V. L. SHAPOSHNIKOV¹, V. E. BORISENKO¹, J.-L. LAZZARI²

¹*Belarusian State University of Informatics and Radioelectronics,
P. Browka 6, 220013 Minsk, Belarus*

²*Centre Interdisciplinaire de Nanoscience de Marseille,
CINAM, UPR CNRS 3118, Aix-Marseille Université, Case 913, Campus de Luminy, 13288
Marseille cedex 9, France*

* anna@nano.bsuir.edu.by

The electronic and optical properties of A^{II}-B^{IV}-C^V₂ and Zn-III-IV-As₃ semiconductors are investigated from first principles in order to find the ways of management their band gaps and lattice constants upon variation of its composition. The materials with the best fitting to semiconducting substrates are determined from the whole suite and recommendations upon practical application of such materials on the base of analysis of their reflectance and absorption spectra are given.

INTRODUCTION

Search for alternative and renewable sources of energy requires materials of low cost with new electronic and optical properties. Nowadays photoelectric solar energy converters attract a special attention of world community. Stable II-IV-V₂ compounds weakly lattice mismatched with silicon or gallium arsenide can be potential candidates for photovoltaic devices. Some compounds among II-IV-V₂ and novel Zn-III-IV-As₃ alloys may be materials of interest in order to replace CuInSe₂ or CdTe for thin-film photovoltaic applications. From this point of view, main aspects for a semiconductor are absorption of light and photoelectric or photovoltaic effect [1]. Thus materials for solar cells should possess high absorption coefficient and have large direct band gap (~1.5 eV) to absorb in the range of the visible light. Moreover, if one wants to avoid expensive, rare, dangerous or too toxic elements and their derivatives used for thin-film deposition, it is better not to consider Cd-based and P-containing compounds. Indeed indium, selenium and tellurium are rare elements, cadmium is a heavy and hazardous metal, phosphorous is highly volatile, red-phosphorous burns, and phosphine gas is highly toxic. In this work we present the theoretical analysis of properties of II-IV-V₂ compounds, where II=Be, Mg, Zn; IV=Si, Ge, Sn; V=P, As, and Zn-III-IV-As₃ compounds, where III=Al, Ga; IV=Si, Sn.

The paper is organized as follows: first we analyze number of materials and chose those whose lattice constant is close to the silicon or gallium arsenide substrates. Then we calculate electronic properties, define materials with the preferably large direct band gaps and determine the optical properties of II-IV-V₂ and Zn-III-IV-As₃ semiconductors. For new Zn-III-IV-As₃ materials we also evaluate the changes in optical properties upon replacements of atoms of III and IV groups, from Al to Ga and from Si to Sn, respectively.

METHOD OF CALCULATION

The structural, electronic and optical properties of II-IV-V₂ ternary and Zn-III-IV-As₃ quaternary sp³ compounds were determined by VASP and WIEN2k *ab initio* simulation packages [2, 3] within density functional theory (DFT) using the generalized gradient approximation (GGA) of Perdew and Wang [4]. We

applied projector augmented-wave (PAW) method implemented in VASP code for structural optimization and calculation of lattice parameters. FLAPW method realized in WIEN2k code was used for calculation of band structures and optical properties. According to experiments [5], II-IV-V₂ ternaries are usually formed in body centered tetragonal structure, thus chalcopyrite-type crystal structure with 16 atoms was taken for simulation. Monoclinic lattice with 24 atoms in the unit cell was chosen for all Zn-III-IV-As₃ alloys. It was constructed from the experimentally observed Cu₂SnS₃ monoclinic structure [6] in which group I atoms (Cu) are equally replaced by group II (Zn) and III (Al or Ga) atoms, group VI atoms (S) are replaced by group V atoms (As), and group IV atomic positions are unchanged.

RESULTS

During the relaxation procedure it was revealed that ternary compounds remain in body-centered tetragonal structure while Zn-III-IV-As₃ quaternary alloys are considered to be monoclinic. Stability of compounds was evaluated by the calculation of the enthalpies of formation, which were found to be negative for all of them. Theoretically computed band gaps of II-IV-V₂ compounds in dependence of their lattice constants are presented on Figure 1. As it can be seen, lattice parameters of Zn(Si,Ge)P₂ are matched with silicon substrate, Zn(Si,Ge)As₂ or (Mg,Cd)SiP₂ compounds are found to be close to GaAs ones.

Band structure calculations show all studied compounds to be semiconductors. Most of them have direct-band gap located at the Γ -point with the values ranging from about 0.1 to 1.5 eV (Figure 1). It was found that band gaps for P-based II-IV-V₂ are higher in comparison with corresponding As-based ones. In the row Si-Ge-Sn, the gaps are the largest for Si-containing materials and the modified Becke-Johnson exchange-correlation potentials [8] will be tried in the future for an accurate determination of the band gaps.

However no experimental data are available on the electronic and optical properties of Be- and most of Mg-containing compounds for comparison of the results. Magnesium-containing compounds are found to be direct-gap semiconductors except MgGeP₂ which is quasi-direct gap semiconductor, and experimental data are available

only for MgSiP_2 ($E_g=2.0\text{-}2.26$ eV, direct gap) [9]. For zinc-containing compounds the experimental gaps are: for ZnSiAs_2 $E_g=1.6\text{-}1.8$ eV (direct gap) [10-12], for ZnGeAs_2 $E_g=1.15$ eV (direct), for ZnSiP_2 $E_g=2.0\text{-}2.3$ eV (direct) [13-14], for ZnGeP_2 $E_g=1.8\text{-}2.2$ eV (quasi-direct) [15].

This can be easily explained by the increase of the atom size in the row. One should take into account possible significant underestimation of the band gaps within DFT methods and may expect true gaps ~ 0.5 eV larger than numerically computed. New functionals such the local Perdew-Burke-Ernzerhof exchange-correlation functional, the Heyd-Scuseria-Ernzerhof hybrid functional [7] or the smallest for Sn-containing ones.

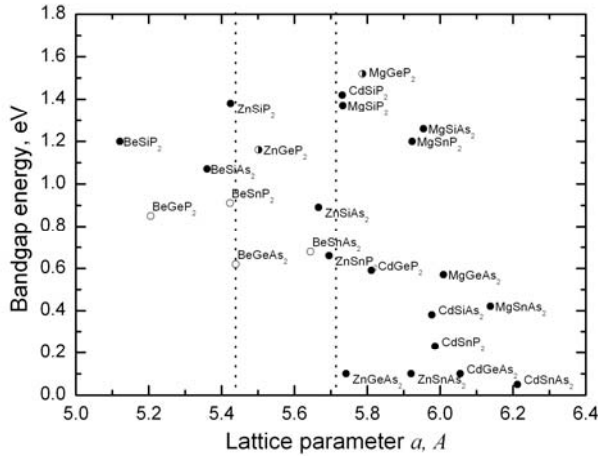


Fig.1. Calculated energy gaps of II-IV- V_2 compounds versus lattice parameters. Filled symbols – direct gap, open symbols – indirect gap, half-filled symbols – quasi-direct gap. Vertical lines correspond to lattice parameters of Si (left) and of GaAs (right).

The averaged reflectance spectra of some most perspective II-IV- As_2 ternaries are presented on Figure 2 in comparison with GaAs and CuInSe_2 . One can see that the shapes of the obtained spectra are similar to the one of GaAs having reflectance greater than 0.4 in the visible range. Otherwise the spectrum shapes of the smaller gaps ternary compounds MgSnAs_2 and ZnSnAs_2 looks approaching the one of CuInSe_2 ; although their reflectance remain higher around 1.5 eV and above.

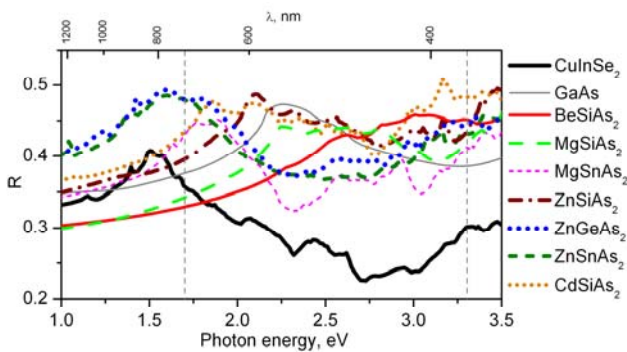


Fig.2 Averaged reflectance spectra of some II-IV- V_2 compounds compared with those of GaAs and CuInSe_2 . Vertical lines correspond to the boundaries of visible spectral range.

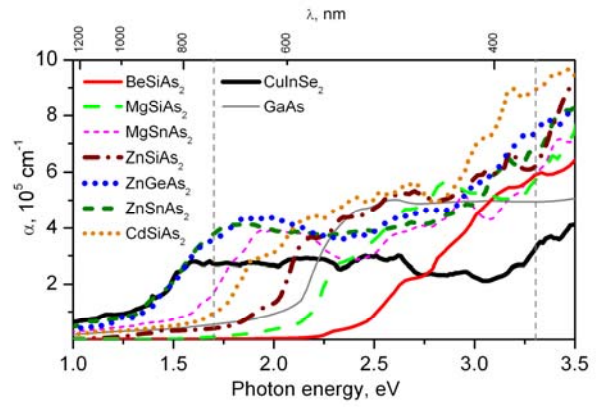


Fig.3. Averaged absorption coefficients of some II-IV- V_2 compounds compared with those of GaAs and CuInSe_2 . Vertical lines correspond to the boundaries of visible spectral range.

In a general way, above their intrinsic absorption edges, the calculated absorption coefficients for investigated II-IV- V_2 compounds are comparable with those for widely used GaAs and CuInSe_2 . The common tendency is that As-containing compounds possess higher α value than P-containing ones. In the row Si-Ge-Sn, the absorption coefficients for Si-containing materials are the lowest while Sn-containing chalcopyrites have the largest α values and the smallest band gaps. Nevertheless the values of α are close to the one of GaAs and $\sim 1.5\text{-}2$ higher than those for CuInSe_2 at photon energies upper 2 eV (Figure 3). Above ~ 1.5 eV, absorption coefficients of BeSnAs_2 , BeGeAs_2 , MgSnAs_2 , ZnSnAs_2 , CdSnAs_2 and CdGeAs_2 compounds demonstrate larger magnitude than those of CuInSe_2 , although both BeSnAs_2 and BeGeAs_2 are indirect-gaps while Cd-containing compounds have predicted small gaps. Unfortunately, most of Be- (and Mg-) containing compounds have not been experimentally synthesized (except MgSiP_2) and measured, probably because Be and Mg are light elements not easy to handle: Be forms very poisonous compounds and Mg metal burns in air. Thus multicolour solar cells with heterostructures close lattice matched to GaAs and built on thin-films of ternary compounds of the Zn-IV- As_2 family appears a promising solution.

Further, we have investigated the new class of Zn-III-IV- As_3 alloys. Here different variants of substitution of group III or IV atoms, namely $\text{ZnAlSi}_{1-x}\text{Sn}_x\text{As}_3$, $\text{ZnGaSi}_{1-x}\text{Sn}_x\text{As}_3$, $\text{ZnAl}_{1-x}\text{Ga}_x\text{SiAs}_3$, and $\text{ZnAl}_{1-x}\text{Ga}_x\text{SnAs}_3$ are considered in order to tune both the lattice constants and the band gaps.

For Al-containing Zn-III-IV- As_3 quaternary alloys band gaps are larger when compared with Ga-containing ones. Similarly, quaternary compounds with Si as IV group element have larger band gaps than those with Sn. All quaternary compounds were found to be stable in simple monoclinic lattice with 24 atoms in unit cell and angle $\beta \approx 108^\circ$. Band structure calculations demonstrate semiconducting nature of all Zn-III-IV- As_3 compounds considered. No experimental data concerning this class of materials are available. Most of the compounds are characterized by a direct band gap band located at the center of the simple monoclinic Brillouin zone with the maximum values of about 1.3 eV for ZnAlSiAs_3 (Figure

4a). Zn-III-Sn-As₃ compounds are practically gap-less. The variation of IV group element from Si to Sn drastically changes the band gap and lattice constants values: the gap values become smaller while *a* lattice constant rises up (Figure 4b), in a way comparable to the respective change of gap (-0.8eV) and lattice (+4.4%) between ZnSiAs₂ and ZnSnAs₂. The change of III group element from Al to Ga does not affect the lattice constant but at the contrary of Al_{1-x}Ga_xAs alloys it lowers the band gap insignificantly (~0.25eV). Indeed this result is not surprising as III elements occupy only 4 atomic sites in the 24 atoms monoclinic cell while they occupy half of the atomic sites in the III-V cubic lattice.

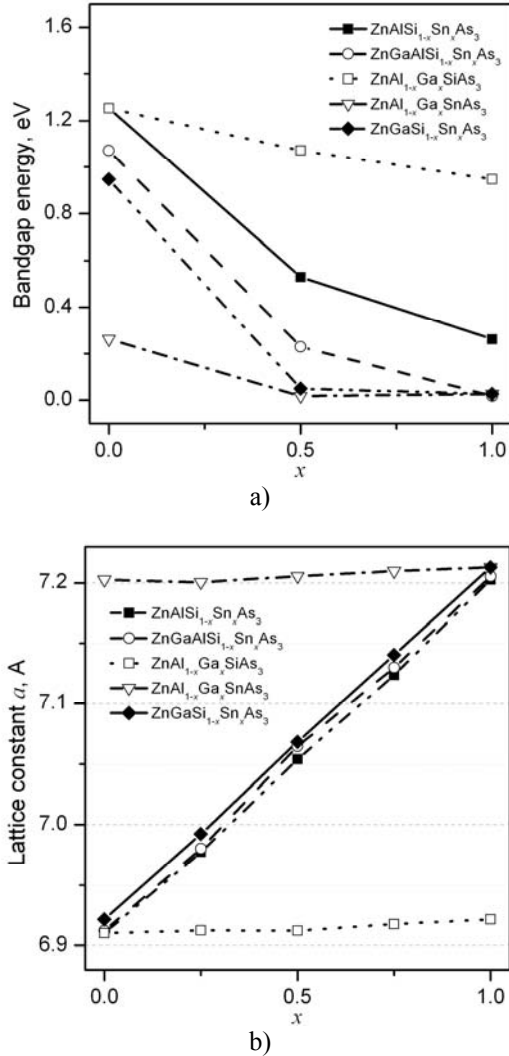


Fig.4. Band gaps (a) and *a* lattice constants (b) of some Zn-III-IV-As₃ compounds. The *c* lattice constants differ not more than 0.2 %.

Absorption coefficients of Zn-III-IV-As₃ demonstrate similar order of magnitude upon different substitutions (Figure 5a, b). Despite the fact that α coefficients of compounds with Sn in IV sites are closer to CuInSe₂ characteristics, especially in the range of low energies, and coefficients of compounds with Si atoms are approaching to GaAs ones, generally absorption coefficients do not show considerable changes when Ga atoms are replaced by Al ones or Sn atoms substitute Si ones.

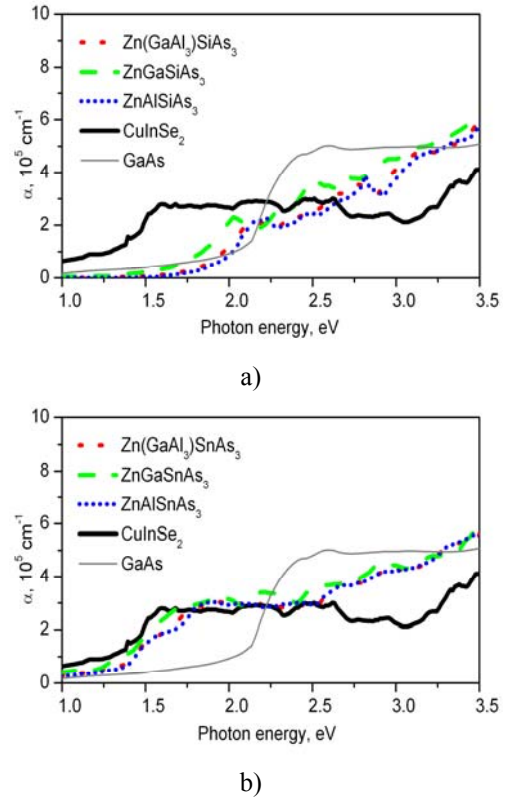


Fig.5. Averaged absorption coefficients of some Zn-III-IV-As₃ compounds with Si (a) or Sn (b) in comparison with CuInSe₂ and GaAs.

SUMMARY AND CONCLUSION

This work is devoted to investigations of II-IV-V₂ and Zn-III-IV-As₃ compounds, which were found to be semiconductors. Ternary compounds exist in a body-centered tetragonal chalcopyrite structure, whereas Zn-III-IV-As₃ quaternaries are found to be stable in monoclinic lattice. Most of the materials (except Be-containing compounds) possess the direct-band gap located at the Γ -point with the gaps ranging from about 0.1 to 1.5 eV. The band gaps in P-containing compounds show to be larger than those in As-containing ones. Nevertheless, among materials of II-IV-V₂ class, arsenic compounds are easier to be obtained experimentally in comparison with phosphorous-based ternaries. The absorption spectra of Zn-III-IV-As₃ compounds are close either to CuInSe₂ or GaAs and do not show considerable changes upon substitution of either III- or IV group elements.

One of the possible ways to increase the quantum efficiency of solar cells is the formation of the multilayered heterostructures consisting of semiconducting materials with different band gaps, like combinations of II-IV-V₂ ternary or Zn-III-IV-As₃ quaternary compounds. From the whole investigated suite of II-IV-V₂ compounds only the Zn-IV-As₂ family seems to be perspective for multicolor heterostructural solar cells as their lattice constants are well matched to GaAs, their band gaps are large enough, their absorption coefficients values are comparable with those of CuInSe₂. Moreover the Zn-IV-As₂ class is composed of rather cheap, abundant and non-toxic elements that make this class of materials potential candidates for photovoltaic applications with ability to replace CuInSe₂.

- [1]. *E. Rosencher, B. Vinter*, Optoelectronics (Cambridge University Press, 2002) 725 p.
- [2]. *G. Kresse, J. Furthmüller*, Phys. Rev. B 54 (1996) 11169.
- [3]. *P. Blaha, K. Schwarz, G. K. H. Madsen, D. Kvasnicka, J. Luitz*, "WIEN2k, An Augmented Plane Wave + Local Orbitals Program for Calculating Crystal Properties" (Karlheinz Schwarz, Techn. Universität Wien, Austria, 2001).
- [4]. *J. Perdew, Y. Wang*, Phys. Rev. B 45 (1992) 13244.
- [5]. *A. Zunger, S. Wagner, P. M. Petroff*: J. Electronic Materials, 22(1) (1993) 3 (and references therein).
- [6]. *M. Onoda, X. Chen, A. Sato, H. Wada*, Crystal structure and twinning of monoclinic Cu_2SnS_3 , Pergamon Materials Research Bulletin 35 (2000) 1563.
- [7]. *J. Paier, R. Asahi, A. Nagoya, and G. Kresse*, Phys. Rev. B 79 (2009) 115126.
- [8]. *F. Tran and P. Blaha*, Phys. Rev. Lett. 102 (2009) 226401 [A. D. Becke and E. R. Johnson, J. Chem. Phys. 124 (2006) 221101].
- [9]. *G. K. Averkieva, A. Mamedov, V. D. Prochukhan, Yu. V. Rud'*: Fiz. Tekh. Poluprovodn. 12 (1987) 1732; Sov. Phys. Semicond. (English Transl.) 12 (1978) 1025.
- [10]. *H. A. Naseem, L. C. Burton, J. E. Andrews*: Thin Solid Films 129 (1985) 49.
- [11]. *T. L. Shay, F. Buehler, T. H. Wernick*: Phys. Rev. B 3 (1971) 2004.
- [12]. *Yu. V. Rud', K. Ovezov*: Fiz. Tekh. Poluprovodn. 10 (1976) 951; Sov. Phys. Semicond. (English Transl.) 10 (1976) 561.
- [13]. *T. Shirakawa, K. Okamura, J. Nakai*: Phys. Lett. 73A (1979) 442.
- [14]. *T. L. Shay, T. H. Wernick*: "Ternary Chalcopyrite Semiconductors" Growth, Electronics, Properties and Applications. Pergamon, 1975.
- [15]. *C. Varea de Alvarez, M. L. Cohen, S. F. Kohn, Y. Petroff, Y.R. Shen*: Phys. Rev. B 10 (1974) 5175.

EFFECTS OF PRESSURE AND TEMPERATURE ON PROPERTIES OF ELECTRONIC-IONIC CONDUCTORS $(\text{GeS})_{1-x}(\text{CuAsS}_2)_x$

NINA MELNIKOVA¹, AHMEDBEK MOLLAEV², OLGA KHEIFETS¹, LUIZA SAYPULAEVA², PETER HOHLACHEV², ABDULABEK ALIBEKOV², ALEXEY FILIPPOV¹, ALEXEY BABUSHKIN¹ AND KIRILL KUROCHKA¹

¹*Ural State University by A.M.Gorki, Ekaterinburg, Russia*

²*Institute of physics of Dagestan Scientific centre of RAS, Makhachkala, Russia*
e-mail: nvm.melnikova@gmail.com, ph: +73432617441, fax: +73432616885

The study of ionic and mixed electronic-ionic conductors in a broad temperature range and at high pressure is of practical and theoretical interest. The present work deals with copper chalcogenides $(\text{GeS})_{1-x}(\text{CuAsS}_2)_x$, $x = 0.1 - 0.6$. The researched materials at normal pressure are mixed electronic-ionic conductors with temperature range of onset of the ionic transport 130 K-200 K. In studied compounds the pressure intervals in which there are essential changes in behavior of electrical properties have been found.

1. INTRODUCTION

The multicomponent chalcogenides of copper and silver are interesting objects for fundamental researches and practical applications because of a possibility to control transport characteristics. A change of external parameters or concentration can be accompanied by a change of conductivity regime from semiconductor to metallic or to fast ionic conductor or by a variation of shares of electronic and ionic conductance [1-3]. The aim of this work is research of electrical properties of the polycrystalline copper chalcogenides $(\text{GeS})_{1-x}(\text{CuAsS}_2)_x$, $x = 0.1 - 0.6$, in the temperature interval 78 K-483 K at atmospheric pressure and under pressures up to 45 GPa at 300 K.

2. MATERIALS FOR INVESTIGATION

The chalcogenides $(\text{GeS})_{1-x}(\text{CuAsS}_2)_x$, $x = 0.1; 0.2; 0.3; 0.4; 0.5$ (structure formula CuGeAsS_3); 0.6 have been prepared by sintering stoichiometric quantities of the elements in evacuated to 10^{-4} Pa and filled helium ($0.5 \cdot 10^5$ Pa) quartz pods. The maximum sintering temperature was 1370 K. The annealing was performed for obtaining of homogeneous materials. The compounds have grey colour and metal shine. X-ray diffraction experiments and qualification of materials have been performed by means with diffractometer *Stadi-P* (monochromatic radiation $\text{CuK}\alpha$). The compounds with $x = 0.1$ and 0.2 are displayed in cubic crystal symmetry with structure of the type a blende. The compounds with $x = 0.3; 0.4; 0.5; 0.6$ are displayed in tetragonal crystal symmetry, with close parameters of an elementary cells. The compounds with $x = 0.3; 0.4; 0.6$ are in the region of homogeneity of CuGeAsS_3 (corresponding to $x = 0.5$). X-ray diffraction results and cell parameters are shown in the Fig. 1 and in table 1.

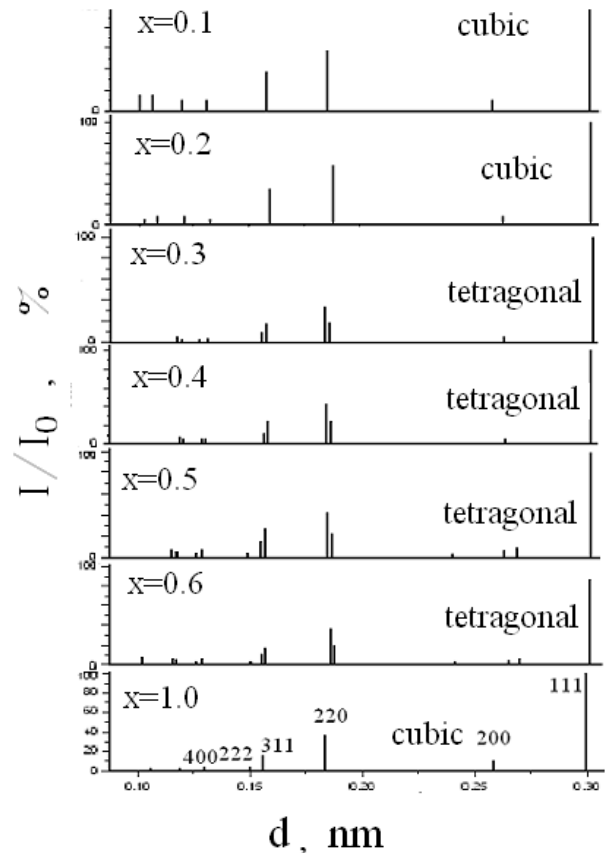


Fig. 1. Line X-ray powder diffraction patterns of the compounds $(\text{GeS})_{1-x}(\text{CuAsS}_2)_x$, $x = 0.1 - 0.6$.

Table 1. Crystal symmetry and cell parameters of compounds $(\text{GeS})_{1-x}(\text{CuAsS}_2)_x$

Compound	x	Crystal symmetry	Cell parameters, nm	Temperature of the melting, K
$(\text{GeS})_{1-x}(\text{CuAsS}_2)_x$	0.1	Cubic	$a = 0.531$	943
	0.2	Cubic	$a = 0.530$	870
	0.3	Tetragonal	$a = 0.376; c = 0.521$	880
	0.4	Tetragonal	$a = 0.376; c = 0.520$	910
	0.5	Tetragonal	$a = 0.3766; c = 0.5212$	915
	0.6	Tetragonal	$a = 0.377; c = 0.520$	900
	1.0	Cubic	$a = 0.518$	688

3. EXPERIMENTAL PROCEDURES

Electrical properties have been investigated by means of impedance spectroscopy in the range of frequencies 0.1-200 kHz and on d.c.

All of the temperature dependent electrical measurements at normal pressure were carried out in the dark and in an evacuated cryostat at temperatures between 78 K and 483 K. To separate ionic and electronic contributions to the current we carried out measurements in a cell with reversible (5CuCl*3RbCl) and blocking (graphite or platinum) electrodes.

High pressure has been generated in the diamond anvil cell (DAC) with anvils of the "rounded cone-plane" (Verechagin-Yakovlev) type made of synthetic carbonado-type diamonds [4]. Anvils made from synthetic diamond consist of dielectric grains of diamond with layers of conducting materials. These anvils are good conductors and allow measurement of the electrophysical properties of samples placed in the DAC. We used these anvils to studying phase transitions in the large groups of metals, dielectrics and semiconductors.

Materials processed by severe plastic deformation are obviously investigated after treatment. It is well known that changes occurring during severe plastic deformation may disappear after processing. We demonstrate the possibility of the application of a diamond anvils cell to study the properties of materials directly at severe plastic deformations.

4. RESULTS AND DISCUSSION

4.1. THE FREQUENCY DEPENDENCES OF ELECTRICAL PROPERTIES

Impedance measurements were carried out to separate the bulk sample properties from the properties at electrode/sample interface.

The dispersion spectra of the compounds were analyzed. All the spectra are characterized by the presence of two clearly distinguished regions – high frequencies (HF) and low frequencies (LF). The equivalent circuit of the cell can be presented as two straightforwardly connected parts, one of which describes the bulk response and the other deals with the electrode processes. At high frequencies the form of the impedance plots may be well approximated by semi-circles which either go through the origin (0,0), with the centers being lower then the abscissa axis in all cases. The corresponding part of equivalent circuit can be approximated by a parallel resistance, and geometrical capacitance and a constant phase element (CPE).

4.2 THE TEMPERATURE DEPENDENCES OF ELECTRICAL PROPERTIES

The temperature dependences of the conductivity $\sigma(T)$, the dielectric permittivity $\varepsilon(T)$ and the loss tangent of a dielectric $\text{tg } \delta(T)$ of the compounds was investigated at a fixed frequencies which belong to the HF region of the impedance measurements. The temperature dependences of the conductivity of all the compounds are of semiconductor type ($\sigma = \sigma_0 \exp(-E_a/kT)$) with different

values of the activation energy at different temperatures (Fig.2). All compounds are the mixed ionic-electronic conductors with temperature of beginning of observable the ionic current 130 K-200 K. The temperature ranges of a beginning of ionic current were determined as a crossing the areas where the slopes of the $\sigma(T)$, $\varepsilon(T)$ and $\text{tg } \delta(T)$ - curves increase rapidly that correspond to the onset of ionic conductivity, since the latter leads to appearance of free charges in the bulk and hence possibility of large polarization. The higher concentration of copper, the more low the temperature region of a beginning of ionic current in the investigated compounds (Table 2). At 300 K the ionic component accounts for 10-25% of the total conductivity in studied materials (for CuGeAsS₃ the ionic component is equal to 15%). The temperature behaviour of the resistivity and dependences resistivity on time at measurement on a direct current in a cell with ion-blocking electrodes can be explained by effects of polarization due to a presence of the ionic conductivity (Fig.3 and Fig.4). At the moment of the cut-in of electric circuit (Fig.4) the total current (ionic and electronic) proceeds through a cell. The conductivity is the sum of ionic and electronic components $\sigma_2 = \sigma_i + \sigma_e$. The value of a current smoothly decreases (accordingly the resistivity increases) in due course to some constant value, corresponding to an electronic component of conductivity, that is connected with formation of a double electric layer at electrode/sample interface. The conductivity thus decreases to σ_e .

Table 2. The temperature ranges of a beginning of ionic current in (GeS)_{1-x}(CuAsS₂)_x

x	T, K
0.1	240-260
0.2	175-230
0.3	140-175
0.4	150-200
0.5	110-130

4.3. THE PRESSURE DEPENDENCES OF ELECTRICAL PROPERTIES

The hodographs of impedance in a studied pressure ranges have the electrode process branch at low frequencies. Presence of these phenomena points to significant share of the ionic conductivity in researched materials (figure 4).

On pressure dependences of resistance and loss angle the maximums and minimums accordingly are visible (Figures 5,6). Analysis of dependences of resistance on pressure had shown, that at certain pressure there is a change of a type of dependence of resistance from pressure (for example for compound with x=0.3 resistance increased up to 29 GPa, then a resistance decreased).

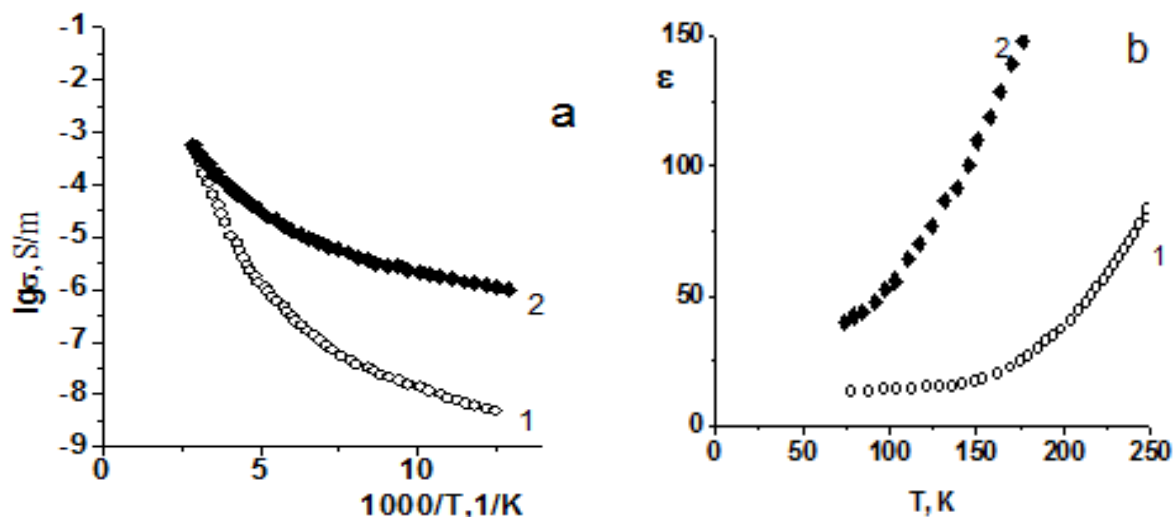


Fig. 2 The temperature dependences of the conductivity (a) and permittivity (b) of the compounds $(\text{GeS})_{1-x}(\text{CuAsS}_2)_x$: 1- $x=0.4$; 2 - $x=0.5$ (CuGeAsS_3). The frequency is 1.592 kHz.

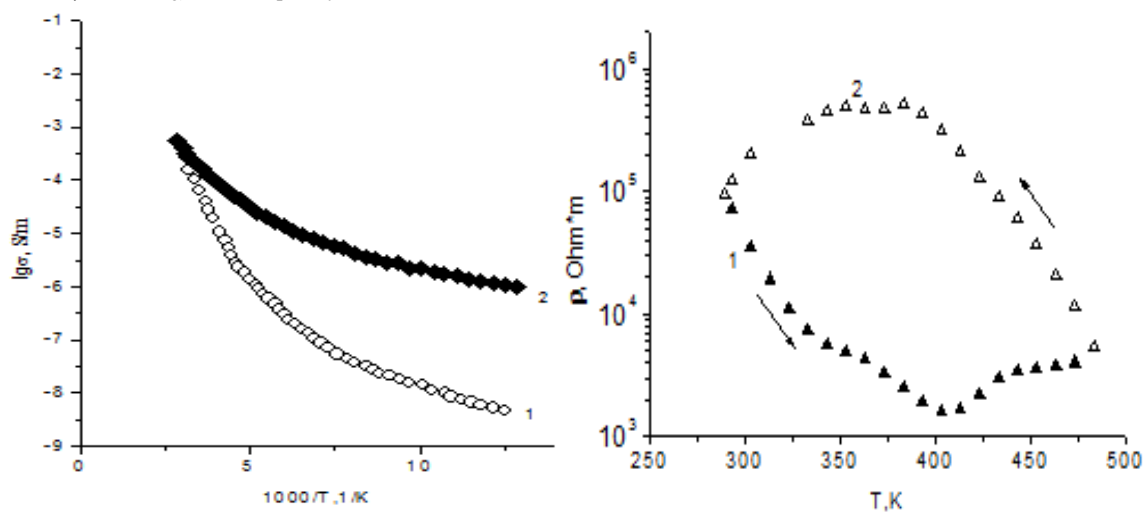


Fig. 3. The temperature dependences of the resistivity of $(\text{GeS})_{1-x}(\text{CuAsS}_2)_x$, $x = 0.2$, in the cell with the ion-blocking electrodes; 1- heating; 2- cooling.

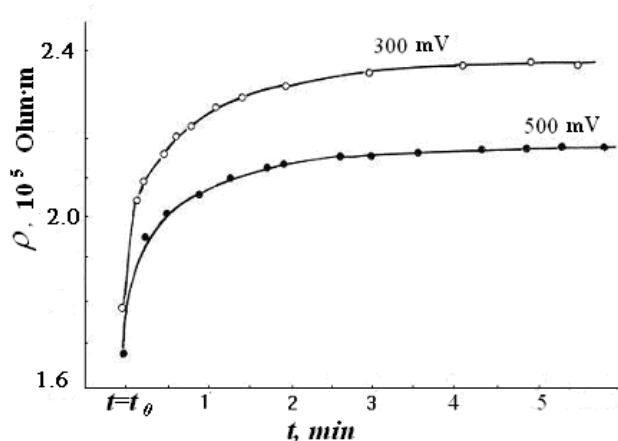


Fig. 4. The dependences of the resistivity from time under specified voltages on cell for $(\text{GeS})_{1-x}(\text{CuAsS}_2)_x$, $x=0.1$.

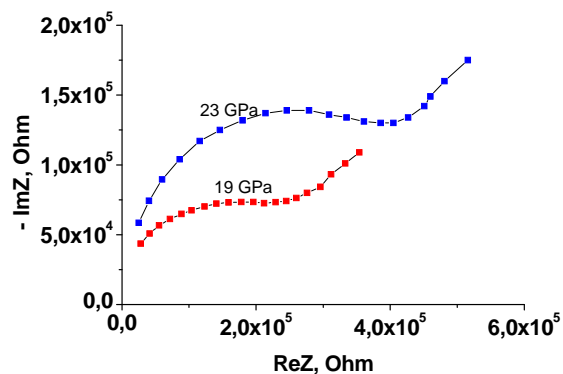


Fig. 4. The hodographs of the impedance of cell with $(\text{GeS})_{1-x}(\text{CuAsS}_2)_x$, $x = 0.1$, at different pressures.

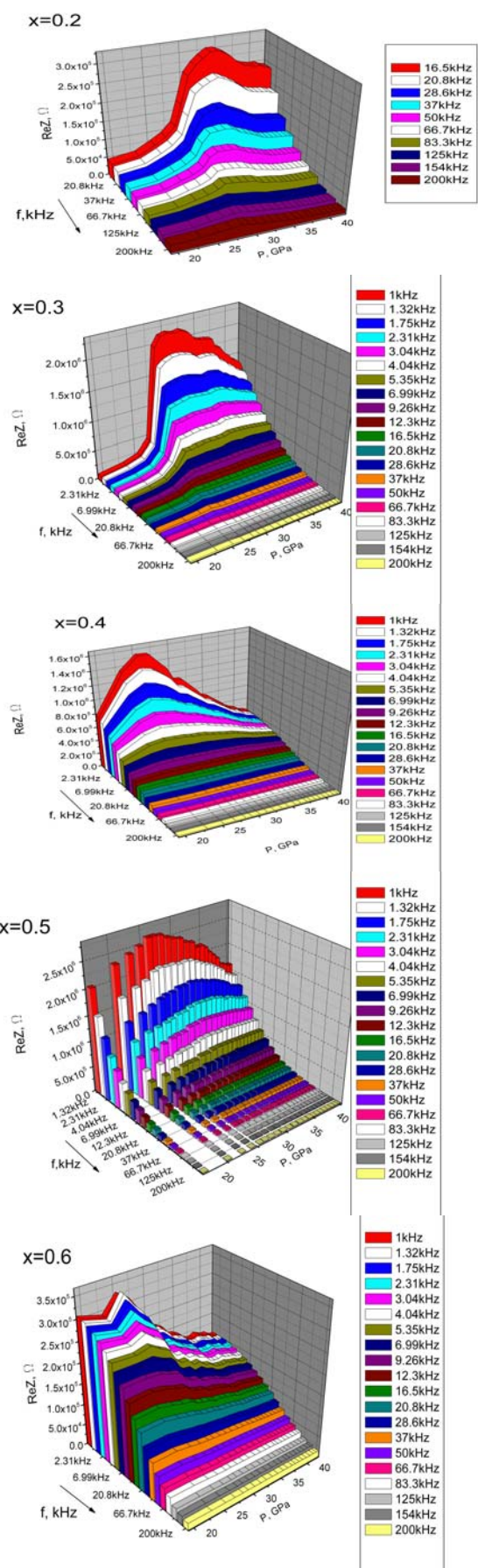


Fig.5 The pressure and frequency dependences of a real part of impedance of a cell with $(\text{GeS})_{1-x}(\text{CuAsS}_2)_x$ at increase of pressure.

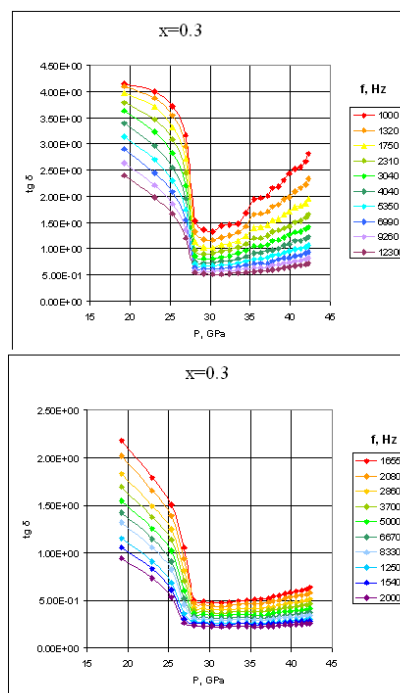


Fig.6 The pressure dependences of tangent of loss angle for $(\text{GeS})_{1-x}(\text{CuAsS}_2)_x$ $x=0.3$ on different frequencies at increase of pressure.

Tangent of loss angle decreased with growth of pressure, at 25-27 GPa the change in velocity of decrease of tangent is observed. At pressure unloading in all compounds the resistance hysteresis was observed. At high frequencies at increase and decrease of pressure resistance and tangent of loss have practically identical values at equal pressures, and the tangent practically returns to values, which were observed before the effect of pressure. The observed hysteresis considerable marked on low frequencies range on baric dependences of resistance and tangent of loss angle.

A maximum on baric dependences of resistance at pressure increase had been observed in investigated region of frequencies in all compounds $(\text{GeS})_{1-x}(\text{CuAsS}_2)_x$. It's may be connected with the effect lattice deformation on ionic mobility. The compression of a lattice can result in mobility decrease of copper ions and, accordingly, in rise of resistance of a sample. At achievement of some pressure there is, probably, a change of a lattice, the resistance starts to decrease.

The results shown that baric region of noticeable changes of electrical properties depends on value x (Fig.7). In studied compounds $(\text{GeS})_{1-x}(\text{CuAsS}_2)_x$ the pressure regions, in which there are essential changes in behavior of electrical properties were found: for $x=0.1$ at 25– 27 GPa, for $x=0.2$ at 29-31 GPa, for $x=0,3$ at 27 - 29 GPa, for $x=0.4$ at 25-27 GPa. In compounds $(\text{GeS})_{1-x}(\text{CuAsS}_2)_x$ ($x=0.5$ and 0.6) the monotonous change of electrical parameters (electroresistance, tangent of loss angle, dielectric constant) with change of pressure is observed on high frequencies. At rise x from 0.1 (cubic lattice) to 0.2 (cubic lattice) this region moved aside higher pressures. At increase x to 0.3 (tetragonal lattice) this region moved aside smaller pressure. At further increase x to 0.4 (tetragonal lattice) the region displaced in the interval of smaller pressure else more. At further

increase x up to 0.5 (tetragonal lattice) this region moved to smaller pressure more strongly, and at $x=0.6$ (the tetragonal lattice) in all investigated interval of pressure on high frequencies monotonic change of electrical properties was observed.

Compounds $(\text{GeS})_{1-x}(\text{CuAsS}_2)_x$ ($x=0.1-0.2$), crystallizing in cubical structure, it is possible to describe as solid solutions CuAsS_2 in GeS . GeS is a hole semiconductor with the distorted cubic (type NaCl) lattice [5]. Addition 10-20 % CuAsS_2 to GeS ($x=0.1, 0.2$) results that the lattice becomes cubic type ZnS. Conductivity becomes of a mixed electronic -ionic type. The motion of ions Cu^+ is possible on defects and tetrahedral emptiness positions. Increase x from 0.1 to 0.2 results in rise of coordination number of copper atoms. The further addition CuAsS_2 ($x=0.3-0.6$), results in formation of a tetragonal lattice. A part of germanium atoms is changed on atoms of copper and arsenic. Copper and arsenic have large effective ionic radiuses as contrasted to by ionic radius of germanium. That's may be reason for in decreasing pressure at which the changes in behavior of electrical properties are watched. Compounds with $x=0.5$ and $x=0.6$ have the greatest concentration of copper. Pressure ranges of change in behavior of electrical properties at low frequencies are 26-27 GPa and 22-26 GPa for $x=0.5$ and $x=0.6$ accordingly. It is possible to explain observable essential changes in behavior of electrical properties exactly on low frequencies to that the electric field role on low frequencies is reduced to initiation of diffusive motion of ions. Ion diffusion is depressed by deformation of a lattice at an increase of pressure. At the high frequencies oscillatory correlated motion of ions becomes prevailing. Diffusion process in contrast with oscillatory correlated motion of ions is more sensitive to pressure influence. Particularities of changes of electrical properties under pressure in investigated compounds $(\text{GeS})_{1-x}(\text{CuAsS}_2)_x$ can be a consequent of phase transition, bound with structural changes of crystal lattice or change of electronic structure.

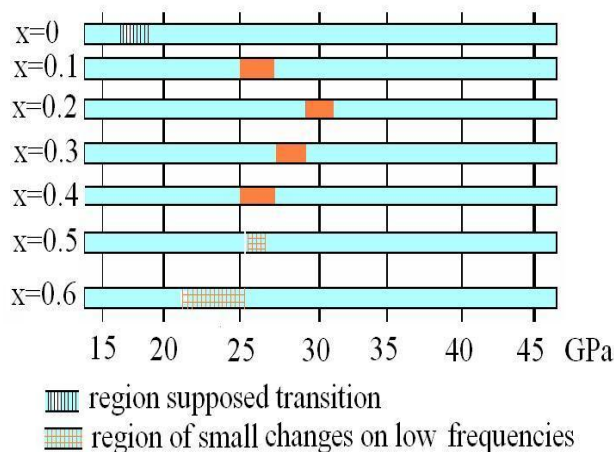


Fig.7. The pressure regions of essential changes in behavior of electrical properties of $(\text{GeS})_{1-x}(\text{CuAsS}_2)_x$. The region of supposed transition for $x=0$ (GeS) was expected in [5].

5 CONCLUSION

Multi-component chalcogenides of copper with general formula $(\text{GeS})_{1-x}(\text{CuAsS}_2)_x$; $x=0.1-0.6$, have been investigated. X-raying experiments and qualification of materials were performed, electric properties in broad temperature range (78-483 K), pressure interval (15-45 GPa) and frequency range (0.1-200 kHz) have been investigated. All materials have been found to have mixed electronic-ionic conductivity. The mobile ions are Cu^+ . Compound CuGeAsS_3 has the most low temperature for the onset of the ionic transport (110-130 K). In studied compounds $(\text{GeS})_{1-x}(\text{CuAsS}_2)_x$ the pressure regions in which there are essential changes in behavior of electrical properties have been found.

ACKNOWLEDGMENTS

The researches were supported in part by Federal program " Scientific and research and educational personnel of the innovation Russia " to 2009-2013 and by RFBR grant No. 09-02-01316.

[1]. Seleznev B.L., Kallion R.V., Bychkov E.A., Vlasov Yu.G., Physics and Chemistry of glass, **17**, 1, 154 (1991).
 [2]. Piarristeguy A., Conde Garrido J.M, Ureña M.A., Fontana M., Arcondo B., J. Non-cryst. Solids **353**, 3314, (2007).

[3]. Alimbarashvily N.A., Kasatkin B.Ye., Borisova Z.U., Neorg. Mater. **10**, 2129 (1974).
 [4]. L.F.Vereshchagin et al. High Temperatures - High Pressures, **6**, 499, (1974).
 [5]. Ignatchenko O.L., Babushkin A.N., Melnikova N.V., Phys. Solid State, **353**(7), 89 (1993)

ELECTRICAL PROPERTIES OF MULTI-COMPONENT COPPER CHALCOGENIDES CuSnAsSe_3 , CuInAsSe_3 AND CuInAsS_3

NINA MELNIKOVA¹, AHMEDBEK MOLLAEV², OLGA KHEIFETS¹,
LUIZA SAYPULAEVA², FAZIL GABIBOV², ABDULABEK ALIBEKOV²,
ALEXEY BABUSHKIN¹, KIRILL KUROCHKA¹

¹*Ural State University by A.M.Gorki, Ekaterinburg, Russia*

²*Institute of physics of Dagestan Scientific centre of RAS, Makhachkala, Russia*

Chalcogenides of copper CuSnAsSe_3 , CuInAsSe_3 and CuInAsS_3 have been investigated. X-raying experiments and qualification of materials were performed, electric properties in broad temperature range (78-400 K), pressure interval (12-45 GPa) and frequency range (10^{-1} - $2 \cdot 10^2$ kHz) have been investigated. Compounds CuSnAsSe_3 and CuInAsSe_3 show ferroelectric properties. From analysis of the pressure and frequency dependences of impedance, dielectric loss angle, resistance and conductance the pressure ranges of the noticeable changes of electrical characteristics were determined.

1. INTRODUCTION

The chalcogenides of copper and silver ABCD_3 , A=Ag,Cu; B=Ge,Sn,Pb,In; C=As,Sb,Bi; D=S,Se, are novel objects for study. These compounds possess the interesting physical features: ferroelectric, piezoelectric, photoelectric, optical [1-5]. The physical characteristics of such materials at high pressure are still not well investigated. We report here some results of the complex studies of physical characteristics of CuSnAsSe_3 , CuInAsSe_3 which show ferroelectric properties and CuInAsS_3 . The temperature dependences of conductivity and permittivity of the last compound are typical for ion conductor (the specific conductivity at 300 K is 0.01 S/m, at 78 - $7 \cdot 10^{-5}$ S/m).

2. EXPERIMENTAL

2.1 SYNTHESIS AND STRUCTURE OF THE COMPOUNDS

The synthesis of compounds was carried out in a regime of a stage heating by means of alloying initial components in the evacuated silica tubes filled superpure argon and deoxygenated with the help of annealing with the titanite sponge. In the process of synthesis, the contents of the ampoules were stirred many times. The resulting ingots, if one-phase, were ground, pelletized, sintered once again, and then taken for X-ray and metallographic analysis. The X-ray diffraction experiments and qualification of materials have been performed by means with diffractometers *Shimadzu XRD 6000* and *Shimadzu XRD 7000* using CuK_α radiation. The structural parameters of the compounds are listed in Table 1.

2.2. ELECTRICAL MEASUREMENTS

Experimental data for the electrical parameters of the sample, i.e., its conductivity, may be greatly affected by processes occurring at the electrode-sample interface (carrier blocking at electrodes, generation and relaxation of space charges, etc.). The contribution of electrode processes to the measured conductivity can be separated out by making variable-current measurements. The method of impedance spectroscopy seems to be the most appropriate in this case. From the frequency dependences of the impedance, one can find the frequency range in which the contribution of the electrode impedance is small. Selecting a frequency from this range, one can determine the temperature or pressure dependences of the

conductivity, permittivity, etc. and the parameters thus measured will characterize the true properties of the material. All the measurements were carried out in a specially constructed cell. For the impedance measurements the ionically blocking or ionically reversible electrodes were used. The value of the ionic conductivity was measured using a Wagner nonsymmetrical cell. Electrical properties at normal and high pressure (12 GPa-45 GPa) were measured by impedance analyzer RLC-2000 in the region of frequencies 0.1-200 kHz.

2.3. THE HIGH-PRESSURE CELL

High pressure up to 50 GPa has been generated in the diamond anvil cell (DAC) with anvils of the "rounded cone-plane" type made of synthetic carbonado-type diamonds. These anvils are good conductors and allow measure the electrical properties of the sample placed in the DAC [6]. The scheme of DAC is shown on Fig.1. Synthetic diamonds (4) have been pressed in bronze holders (3) and then this built-up construction has been subjected to machining to manufacture diamond anvils. Working surfaces of anvils have been polished. Electrode leads from anvils (not shown in the figure) are have been soldered to holders (3). Holders with diamond anvils have been placed within an isolating barrel (textolite or Teflon) (2). They provide the electric isolation of anvils from metal parts of the high-pressure cell. Centering of anvils relative to a axis has been provided by the bush 1 and the cylinder 5. Internal surface of the cylinder and external surfaces of bushes have been grounded to coincide with each other. The rounded anvil (the top on figure) of approximately 1 cm radius has been used in experiments. The contact spot has been about 0.2 mm in diameter. The thicknesses of material tablets after compacting the material with anvils have been 2 - 15 μm . The tablet thickness and diameter are determined by mechanical properties of the compressed material. The error in the measured pressure depends on mechanical properties of compressed material and does not exceed 15 % in a range 15 to 50 GPa.

3. RESULTS AND DISCUSSIONS

Based on the frequency dependences of the impedance of the synthesized compounds the frequency intervals in which it is possible to neglect the influence of electrode processes are determined. The temperature

dependences of the conductivity and permittivity have been studied at the frequencies, which belong to above-mentioned frequency ranges. The temperature dependences of the activation-type conductivity and permittivity of CuSnAsSe_3 , CuInAsSe_3 , CuInAsS_3 are shown in Figs. 2 and 3. The temperature dependences of the permittivity for compounds CuSnAsSe_3 and CuInAsSe_3 are typical of ferroelectrics. The temperature dependences of the permittivity of ferroelectrics usually have a peak at the Curie temperature. Sometimes, the permittivity peaks and remains constant in a certain temperature range (smeared phase transition). In addition, the permittivity of ferroelectrics is, as a rule, high, $\epsilon \geq 1$. The temperature dependence of the conductivity of ferroelectrics is akin to the temperature run of the semiconductor conductivity, i.e., exhibits a change in the energy of activation near the phase transition. Notably, the energy of activation in the ferroelectric range is lower than the energy of activation in the paraelectric range. This change in the energy of activation is associated with conductivity mechanism changing in both phases.

Table 1. Cell parameters, conductivity and dielectric permeability of CuSnAsSe_3 , CuInAsSe_3 and CuInAsS_3

Compound	Symmetry, lattice constants, nm	σ , S/m (300K, 10kHz)	ϵ (300K, 10kHz)
CuInAsS_3	Tetragonal, $a=0.55184$ nm; $c=1.10845$ nm	10^{-2}	40
CuInAsSe_3	Tetragonal, $a=0.57967$ nm; $c=1.15471$ nm	$5 \cdot 10^{-3}$	180
CuSnAsSe_3	Monoclinic, $a=0.5098$ nm, $b=0.8617$ nm, $c=0.7139$ nm, $\beta=94.13^\circ$	$1.6 \cdot 10^{-2}$	300

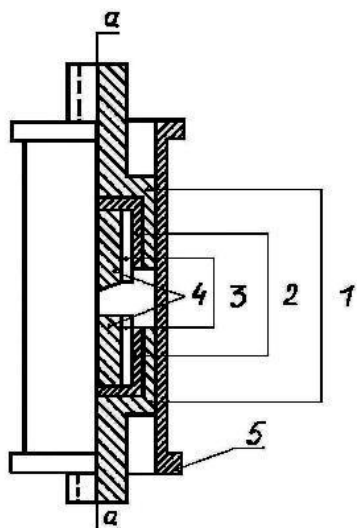


Fig.1. The high-pressure cell: 1 – the bush; 2 – isolating stuff (textolite or teflon); 3 – holders from bronze; 4 – synthetic diamonds; 5 – isolating barrel

From these curves, we determined the temperature ranges of the supposed ferroelectric transition. In CuSnAsSe_3 , both the ferroelectric phase transition and the sharp rise in the permittivity at high temperatures are

observed, which is characteristic of ionic conductors. From the temperature dependences of the conductivity (and its high values), it was concluded that CuSnAsSe_3 and CuInAsSe_3 possess ferroelectric properties. Because of high values of the conductivity, these compounds were categorized as ferroelectric semiconductors. For this reason, we could not analyze the polarization curve (in high-conductivity compounds, dipoles are screened by charge carriers). In CuSnAsSe_3 , both the ferroelectric phase transition and the sharp rise in the permittivity at high temperatures are observed, which is characteristic of ionic conductors. In solid electrolytes at low temperatures, the permittivity either is constant or increases slowly with temperature. As the temperature exceeds the ionic transport temperature, the permittivity sharply grows. In materials with ionic or ionic–electronic conduction, the dc resistivity increases with time because of polarization arising in the cell with the sample. The blocking electrodes delay the ions responsible for charge transfer, and positive ions accumulate near the negative electrode under the action of the electric field, giving rise to a positive ion concentration gradient and a diffusion ion flux in opposition to the drift flux. Under steady conditions, the diffusion and drift fluxes compensate for each other and the electronic current alone passes through the sample. Thus, from the time variation of the resistivity, one can find the ratio between the electronic and ionic components of the conductivity. The dependence of the resistance of CuInAsS_3 from time is typical for ion or electronic – ionic conductors (Fig.4).

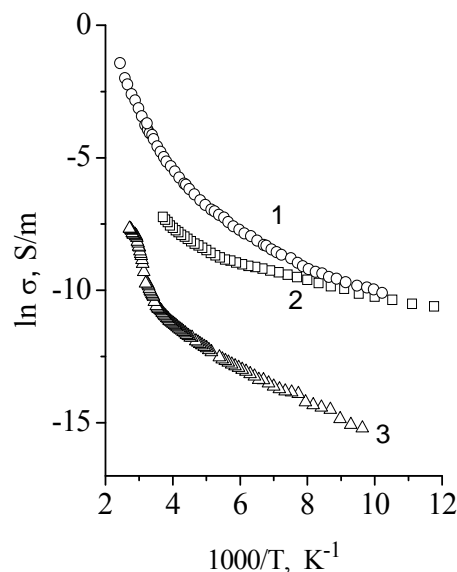


Fig.2. The temperature dependences of the conductivity of CuSnAsSe_3 (1), CuInAsSe_3 (2), CuInAsS_3 (3).

Studies of effects of high pressure on the electrical properties of materials allowed to determine pressure ranges of possible phase transitions. Baric and frequency dependences of a real part of impedance of the cells with samples CuInAsS_3 and CuInAsSe_3 are shown on Fig. 5. These compounds at atmospheric pressure are displayed in tetragonal crystal symmetry with structure of the chalcopyrite type, with close parameters of an elementary cells.

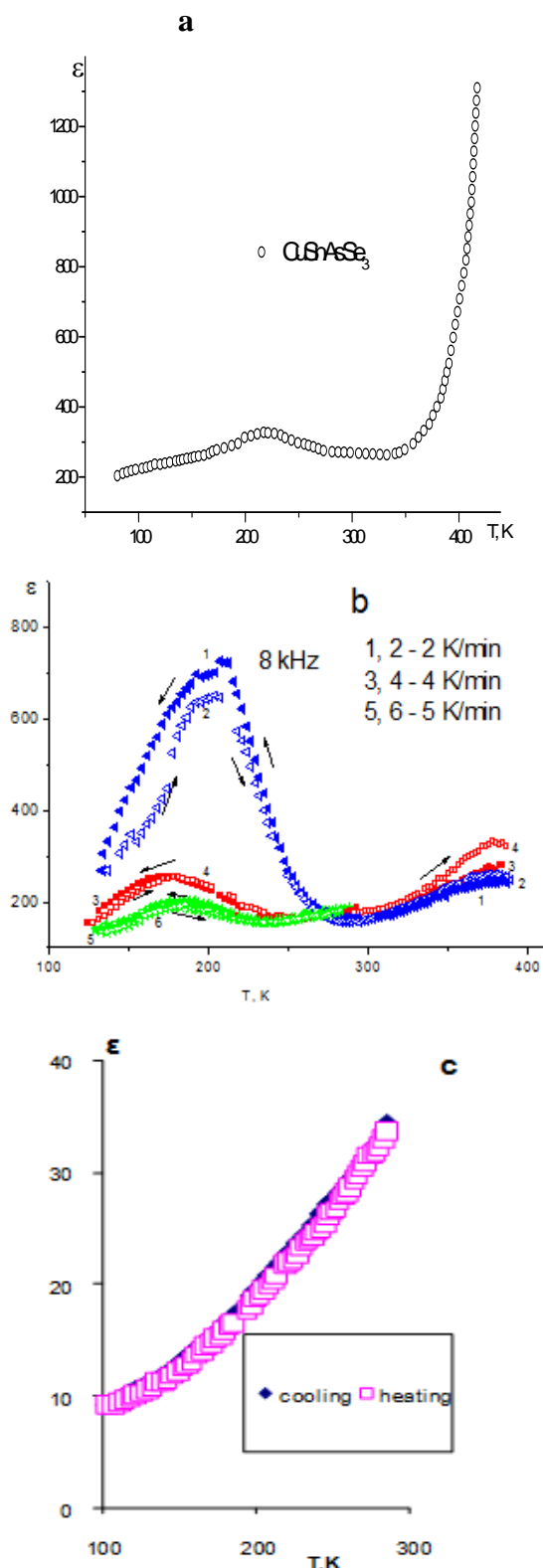


Fig.3. The temperature dependences of the permittivity of CuSnAsSe_3 (a), CuInAsSe_3 (b), CuInAsS_3 (c).

Essential changes of the electric properties have been observed in both CuInAsSe_3 and CuInAsS_3 in the same range of pressures. In compound CuInAsS_3 with ion conduction on baric dependences of resistance (Fig.5a) and of loss angle the maximum and minimum accordingly at the same pressure regions were observed. The compression of a lattice can result in mobility decrease of copper ions and, accordingly, in rise of resistance of a

sample. At achievement of some pressure there is, probably, a change of a lattice, the resistance starts to decrease.

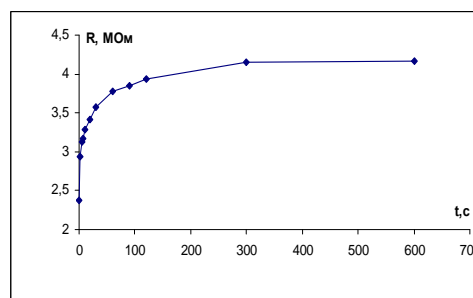


Fig. 4. The dependence of the resistance of CuInAsS_3 from time ($T=293$ K)

In CuInAsSe_3 after 34 GPa a resistance (Fig.5b) sharply decreases and ceases to depend on frequencies, all curves $\text{Re}Z(P)$ practically coincide. If anomalies were observed on baric dependencies of all under study physical parameters in the same pressure intervals on all frequencies than they were interpreted as manifestations of the structured changes. Essential changes of the electric properties have been observed in CuInAsSe_3 and CuInAsS_3 at pressures 34-37 GPa (structured changes in this pressure range can be the same as for CuInSe_2 at 39.2 GPa [7]), in CuSnAsSe_3 at 35-37 GPa and 39-41 GPa. (Fig. 6). The height of column on diagram corresponds to maximal pressure from these ranges (at temperature 300 K).

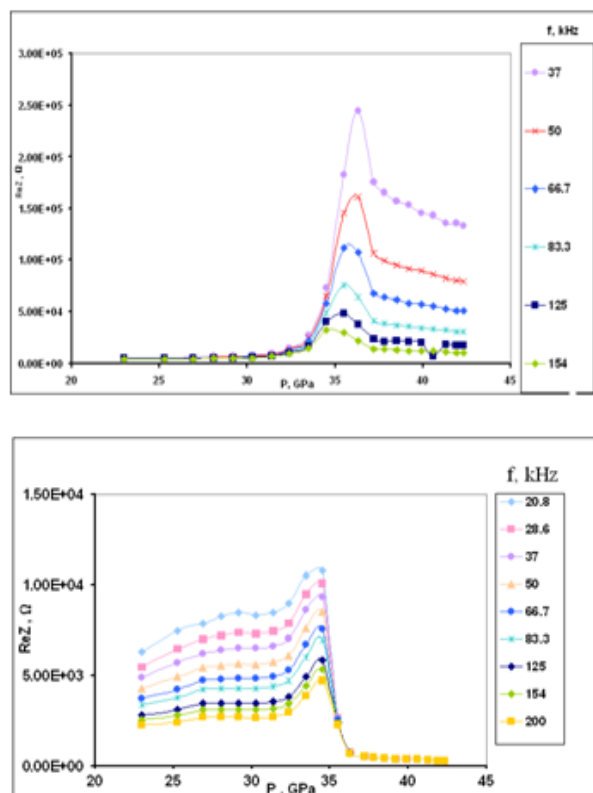


Fig.5. Baric dependences of a real part of impedance of a cell with CuInAsSe_3 and CuInAsS_3 on different frequencies at increase of pressure

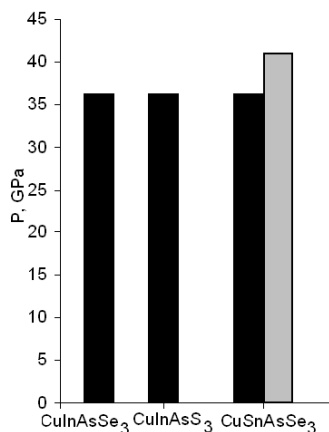


Fig.6. Pressure values of phase transitions in copper chalcogenides.

4. CONCLUSION

The electric properties of the copper chalcogenides CuSnAsSe_3 , CuInAsSe_3 and CuInAsS_3 in broad temperature range (78-400 K), pressure interval (12-45 GPa) and frequency range (10^{-1} - $2 \cdot 10^2$ kHz) have been investigated. Compounds CuSnAsSe_3 and CuInAsSe_3 show ferroelectric properties and the temperature range of the ferroelectric phase

transition is determined. The high permittivity of these compounds allows us to characterize them as new low-temperature ferroelectric semiconductors. The mixed (electronic-ionic) type of conduction in CuInAsS_3 is established (the share of the ionic component of the conductivity is not less 0.43 at 293 K) and the temperature range where ionic transport becomes noticeable are found. From analysis of the pressure and frequency dependences of impedance, dielectric loss angle, resistance and conductance the pressure ranges of the noticeable changes of electrical characteristics were determined. Essential changes of the electric properties have been observed in CuInAsSe_3 and CuInAsS_3 at pressures 34-37 GPa, in CuSnAsSe_3 at 35-37 GPa and 39-41 GPa. Changes can be connected to phase transition at these pressures.

ACKNOWLEDGEMENT

The researches were supported by Federal program "Scientific and research and educational personnel of the innovation Russia" to 2009–2013 and by RFBR grant No. 09-02-01316.

-
- [1]. O. L. Kheifets, L. Y. Kobelev, N. V. Melnikova, L. L. Nugaeva. Electrical properties of solid electrolytes with general formula ABCD_3 (A=Ag,Cu; B=Pb,Sn; C=As,Sb; D=S,Se). Tech. Phys., 2007, 52, p. 86.
- [2]. A.N. Babushkin, O.L. Kheifets., N.V. Melnikova. Effect of high pressures on the electrical properties of AgPbAsSe_3 , AgPbSbSe_3 , CuSnAsSe_3 , CuSnSbSe_3 , AgSnSbSe_3 , CuSnSbS_3 . Proc. Int. Conference "Phase Transitions, Critical and Nonlinear Phenomena in Condensed Matter", Makhachkala, 2007, p. 334-336.
- [3]. N.V. Melnikova, O.L. Kheifets, A.N. Babushkin, A.L. Filippov, Book of Abs. EHPRG 46. Conf., 2008, 87.
- [4]. N.V. Melnikova, L. Kheifets, A.N. Babushkin, L.L. Nugaeva, E.F. Shakirov, Book of Abs. EHPRG 46. Conf., 2008, p. 117.
- [5]. Olga Kheifets, Nina Melnikova, Luisa Saipulaeva, A.G. Alibekov, Ahmedbek Mollaev, Alexey Babushkin, Galina Tikhomirova, Electric properties of AgPbAsSe_3 at pressures up to 45 GPa High Pressure Research, 2009, V. 29, No.2, p.261.
- [6]. L.F. Vereshchagin, E.N. Yakovlev, B.V. Vinogradov, G.N. Stepanov, K.Kh. Bibaev, T.I. Alaeva, V.P. Sakun, High Temperatures - High Pressures, 1974, 6. p. 499.
- [7]. Thiti Bovomratanaraks, Varalak Saengsuwan, Kayorniyod Yoodee, M. I. McMahon Clivia Hejny, Structures and phase transitions of CuInSe_2 at high pressure. Acta Cryst., 2005, A61 p.464 (P.20.03.9).

MAGNETOVOLUME EFFECT AND MAGNETIC PHASE TRANSITIONS IN FERROMAGNETIC SEMICONDUCTOR $\text{Cd}_{1-x}\text{Mn}_x\text{GeAs}_2$ UNDER THE PRESSURE

A. YU. MOLLAEV¹, I. K. KAMILOV¹, R. K. ARSLANOV¹,
T. R. ARSLANOV¹, U. Z. ZALIBEKOV¹, V. M. NOVOTORTSEV², S. F. MARENKIN²

¹*Institute of Physics, Daghestan Scientific Center of the Russian Academy of Sciences,
367003, Makhachkala, Russian*

²*Institute of common and inorganic chemistry of the Russian Academy of Sciences,
Moscow, Russian*

e-mail: a.mollaev@mail.ru

The dependences of relative volume compressibility $\Delta V/V_0$ and relative magnetic susceptibility χ/χ_0 on the pressure $P \sim 7$ GPa are measured at room temperatures in ferromagnetic semiconductor $\text{Cd}_{1-x}\text{Mn}_x\text{GeAs}_2$ with $(0.06 \geq x \geq 0.3)$. There are observed anomalies of magnetic properties in dependences of $\Delta V(P)/V_0$ and $\chi(P)/\chi_0$ at $P \geq 1.6$ and $P \geq 4.1$. The obtained results reveal the occurrence of magnetic phase transitions in all studied polycrystals. Near the critical pressure $P_{SR} \approx 1.6$ GPa takes place a transition from low magnetization state to high magnetization one, and at $P_C \geq 4.1$ GPa happens a transition from magnetic-ordered phase into magnetic-disordered phase. High pressure brings to a considerable decrease in Curie temperature (T_C) with value $dT_C/dP \approx (-14 \div -6.8)$ K/GPa. The calculations for bulk modulus B , carried out by means of scaling expression allows to estimate the values of bulk modulus in magnetic-ordered and magnetic-disordered phases.

I. INTRODUCTION

In the work are presented the experimental results on the relative volume change and relative magnetic susceptibility under the hydrostatic pressure up to 7 GPa and room temperatures, including a region of magnetic transformation.

II. SAMPLES AND METHOD OF EXPERIMENT

The measurements were carried out on polycrystalline samples $\text{Cd}_{0.7}\text{Mn}_{0.3}\text{GeAs}_2$ in "Toroid" high pressure device at the hydrostatic pressure up to $P \geq 7$ GPa in a region of room temperatures. The detail descriptions of a method and a technique of the experiment were given in works [1, 2]. A synthesis of the samples and technological regimes of their growth were described in [3, 4].

The dynamic magnetic susceptibility was estimated by registration of a change in resonant circuit frequency, reel core.

Compressibility was measured by strain-gage method like in [5], the samples were of a cylinder shape with 3 mm in height and 1 mm in diameter.

III. MEASURING RESULTS AND DISCUSSIONS

The results on dependence of relative volume compressibility $\Delta V(P)/V_0$ and relative magnetic susceptibility $\chi(P)/\chi_0$ on a pressure in $\text{Cd}_{1-x}\text{Mn}_x\text{GeAs}_2$ with $(0.06 \geq x \geq 0.3)$ are shown in Figures 1, 2. A usage of strain-gage method in hydrostatic pressure allows to study thoroughly lattice compressibility in a region of magnetic transformation by the experimental decrease in compressibility of the lattice and increase in bulk modulus B , starting from $P > 4.5$ GPa. The bulk modulus increases in a wide range of pressures above 4.5 GPa and is going on gradually arise close to $7 > \text{GPa}$, what indicates that ferromagnetic-paramagnetic transformation occurred at this pressure. measurements of $\Delta V(P)/V_0$. A disappearance of the ferromagnetic state under the pressure manifests as sharp

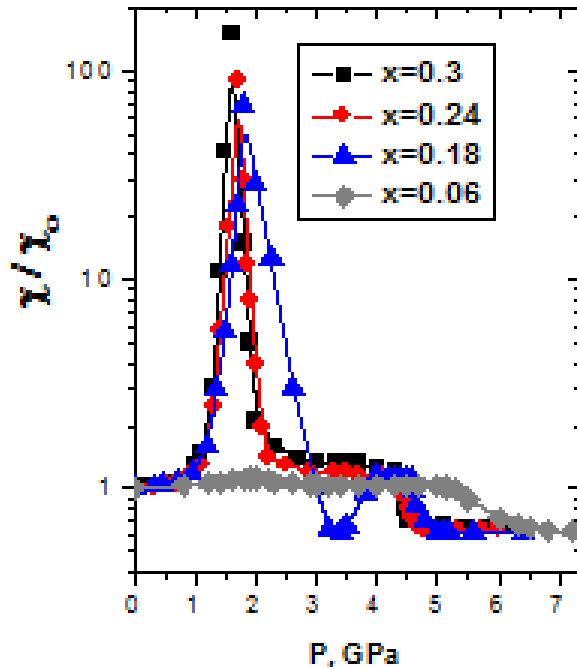


Fig.1. Baric dependence of the magnetic susceptibility for $\text{Cd}_{1-x}\text{Mn}_x\text{GeAs}_2$.

A value of bulk modulus for ferromagnetic phase $B_f = 110-120$ GPa agrees with results in [6] ($B_f = 119 \pm 5$ GPa). A value of bulk modulus for paramagnetic phase $B = 180$ GPa (at $P > 7$ GPa) are also in a good agreement with data in [6], where $B_p = 180 \pm 8$ GPa is mean in pressure ranges from 5 to 12 GPa.

Altogether, it should be noted that ordering of bulk modulus in a region, where the ferromagnetic state disappears, passes smoothly pointing to existence of ferromagnetic and paramagnetic regions in wide pressure ranges.

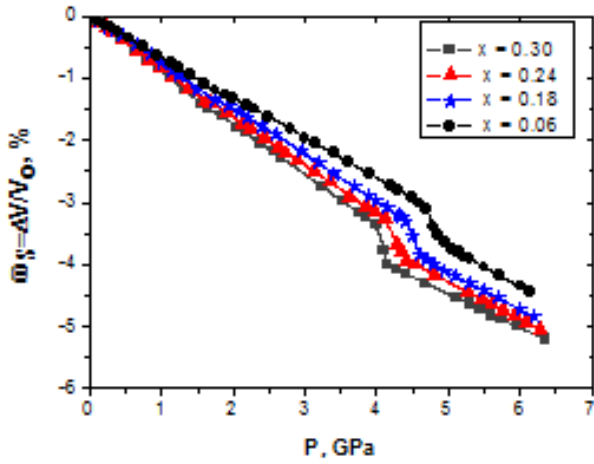


Fig.2. Pressure dependence of the relative volume change of $Cd_{1-x}Mn_xGeAs_2$.

A transition from ferromagnetic state to paramagnetic one is not the first order transition, and a coexistence of phases must be considered as the fluctuation process. Nature of origin of magnetic transformation in magnetic alloys was stated in many works [7, 8], where a temperature dependence of the elastic constants was researched by the ultrasonic method. Thereby, the temperature dependences of bulk modulus are very similar to dependences plotted in Fig. 3. Authors [8, 9] explained the temperature dependence of bulk modulus by heat and volume fluctuations, but not by chemical inhomogeneity of the sample.

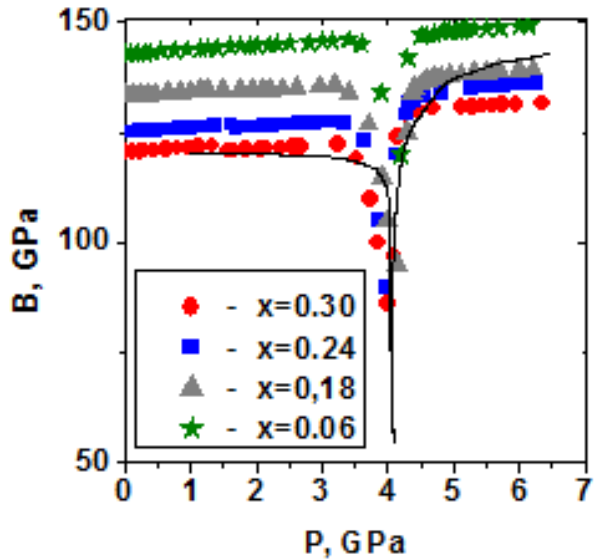


Fig.3. Pressure dependence of the bulk modulus $Cd_{1-x}Mn_xGeAs_2$.

It means that ferromagnetic and paramagnetic regions coexist together. Our results correspond to these ideas. A value of volume magnetostriction ω_s is estimated by means of extrapolation of $\Delta V(P)/V_0$ dependence from high pressure region, i.e. the lattice volume changes owing to spontaneous magnetization of the ferromagnetic phase. The values of ω_s are (0.5÷1.7) % at $T=297$ K for studied samples $Cd_{1-x}Mn_xGeAs_2$ and agree well with results of work [10]. The dependences of volume

compressibility for samples $Cd_{1-x}Mn_xGeAs_2$ with ($x=0.06, 0.18, 0.24$, and 0.30) are presented in Fig. 2. As it is clear from Figure 2, a decrease in volume occurs almost linearly up to $P>4$ GPa, but at $P\geq 1.5$ GPa there is observed a break in curves caused, probably, by magnetic transformation. Metamagnetic effect was revealed in $Cd_{0.9}Mn_{0.1}GeAs_2$ and $Cd_{0.7}Mn_{0.3}GeAs_2$ by researched magnetic properties in [11, 12]. A value of bulk modulus coincides in this pressure ranges (Fig. 3). However, the bulk modulus of $Cd_{1-x}Mn_xGeAs_2$ begins to loose its sharpness at $P>4$ GPa, this smoothing becomes considerable at further increase in pressure. A value of modulus of elasticity at $P>4.1$ GPa is significantly less than initial modulus. The pressure increasing above $P>4.1$ GPa leads to substantial increase in bulk modulus. In general, the dependence of bulk modulus (and compressibility) reveals as a typical λ -anomaly, which happens, obviously, because of magnetic transformation (disappearing of ferromagnetism) at $P\sim 4.1$ GPa. After electronic data processing is derived the scaling expression:

$$B = \frac{a}{b} \left| 1 - \frac{P}{P_c} \right|^{-b} + c \quad (1)$$

used for analysis of critical phenomena. Where $b_f=0.84$, $b_p=0.8$, $P_{cf}=4.04$ GPa and $P_{cp}=4.03$ GPa are critical parameters and critical pressures for ferromagnetic and paramagnetic phases, correspondingly. Similar data were obtained in [16, 19] for $Y_2Fe_{14}B$ and $Nd_2Fe_{14}B$ by ultrasonic changes at high temperatures and pressures.

The dependence of Curie temperature on pressure dT_C/dP in $Cd_{1-x}Mn_xGeAs_2$ can be estimated by the known values of T_C ($T_C=355$ K) [7-13] and a pressure of ferromagnetic-paramagnetic transition P as $dT_C/dP=(T_C-T_{room})/P_C$. The table presents values for magnetic and magnetoelastic properties, where T_C is Curie temperature, P_C is a pressure of magnetic transition ferromagnetic-paramagnetic, P_{SR} is a pressure of spin ordering, ω_s is spontaneous magnetostriction, B is bulk modulus determined from experimental results presented in Fig. 2. The values for B are given in the Table at $T=297$ K and atmospheric pressure.

Table 1. Magnetic and magnetoelastic parameters of $Cd_{1-x}Mn_xGeAs_2$.

No	x	T_C , K	P_C , GPa	dT_C/dP , K/GPa	P_{SR} , GPa	ω_s , %	B, GPa
1	0.06	329 [3]	4,7	- 6.8	1.9	0.5	143
2	0.18	329 [3]	4.3	- 7.5	1.8	0.8	133
3	0.24	355 [3]	4.2	- 13.8	1.7	1.24	125
4	0.30	355 [3]	4.1	- 14.0	1.6	1.7	120

ACKNOWLEDGMENTS:

This work was supported by Program of Presidium of RAS “Thermophysics and mechanics of external energetic influences and physics of high compressed material” and Section of High Compressed Material.

- [1]. *L.G. Khvostantsev, L.P. Vereshagin, A.P. Novikov.* High Temp.-High Press., 1977, v.9, № 6, p.637–639.
- [2]. *A.Yu. Mollaev, R.K. Arslanov, L.A. Saypulaeva, S.F. Marenkin.* Neorg Mater, 2001, v.37, p.4327
- [3]. *S.F. Marenkin, V.M. Novotortsev, K.K. Palkina., et al,* Preparation and Structure of CdGeAs₂ Crystals, Neorg. mater., 2004, v.40, № 2, p.135-137. [Inorg. mater (Engl. Transl.) v.40, № 2, p.93-95]
- [4]. *V.A. Ivanov, T.G. Aminov, V. M. Novotortsev, V. T. Kalinnikov,* Izvestiya Akademii nauk, seriya him., 2004, № 11, p.2255.
- [5]. *O.B. Tsiok, V.V. Bredikhin, V.A. Sidorov and L.G. Khvostantsev,* HiHg. Press. Res. 1992, v.10, p.523.
- [6]. *G. Oomi and N. Mori,* J. Phys. Soc. Jpn. 1981, v.50, p.2917.
- [7]. *M. Shiga and Y. Nakamura,* J. Magn. Magn. Mater, 1990, v.90-91, p.733.
- [8]. *G.P. Renaud and S.G. Steinemann,* Physica B, 1989, v.161, p.75.
- [9]. *G.P. Renaud and S.G. Steinemann,* Physica B, 1988, v.149, p.217.
- [10]. *V.A. Sidorov and L.G. Kvostantsev,* J. Magn. Magn. Mater, 1994, v.129, p.356.
- [11]. *L.S. Lobanovskii V.M. Novotortsev, S.F. Marenkin, V.M. Trukhan, T.V. Shelkovaya,* Pisma v JETF, 2009, v.89, № 37, p.391.
- [12]. *A.Yu. Mollaev, I.K. Kamilov, R.K. Arslanov, T.R. Arslanov, U.Z. Zalibekov, V.M. Novotortsev, S.F. Marenkin,* Pisma v JETF, 2010, v.91, № 9, p.524.
- [13]. *M. Shiga, Y. Kusakaba, Y. Nakamura, K. Makita and M.Sagawa,* Physica B, 1989, v.161, p.206.

THE MAGNETOTRANSPORT AT HIGH PRESSURE IN COMPOUNDS OF $A^{II}B^{IV}C^V_2$ DOPED BY Mn

A. Yu. MOLLAEV¹, I. K. KAMILOV¹, R. K. ARSLANOV¹,
T. R. ARSLANOV¹, U. Z. ZALIBEKOV¹, S. F. MARENKIN², V.M. TRUKHAN³

¹*Institute of Physics, Daghestan Scientific Center of the Russian Academy of Sciences,
367003, Makhachkala, Russian*

²*Institute of common and inorganic chemistry of the Russian Academy of Sciences,
Moscow, Russian*

³*Joint Institute of Solid State Physics and Semiconductors,
National Academy of Sciences of Belarus, Minsk, 220072*

e-mail: a.mollaev@mail.ru

There are researched and revealed the metamagnetic phase transitions in high-temperature ferromagnetic semiconductors p-Cd_{1-x}Mn_xGeAs₂, p-Cd_{1-x}Mn_xGeP₂ and p-Zn_{1-x}Mn_xGeAs₂. In the monocrystal p-Cd_{0.947}Mn_xGeAs₂ there are estimated metamagnetic phase transitions along different crystallographic directions [100] and [001]. It is detected that the crystallographic directions not influence on a position of metamagnet phase transition in a high pressure scale, while a value of the amplitude changes..

I. INTRODUCTION

The present work continues the investigations on high-temperature ferromagnetic semiconductors on the basis of compounds of $A^{II}B^{IV}C^V_2$ doped by magnetic impurities (Mn, Cr, etc). In p-Cd_{1-x}Mn_xGeAs₂ and p-Cd_{1-x}Mn_xGeP₂ were studied the kinetic effects [1-3] and found structural phase transitions. In given work there is researched the magnetotransport and magnetoresistance in p-Cd_{1-x}Mn_xGeAs₂, p-Cd_{1-x}Mn_xGeP₂ and p-Zn_{1-x}Mn_xGeAs₂ at high hydrostatic pressure up to 7 GPa.

II. SAMPLES AND METHOD OF EXPERIMENT

Polycrystalline manganese doped cadmium germanium diarsenide, CdGeAs₂{Mn}, was prepared by reacting presynthesized cadmium diarsenide, manganese powder (99.9% purity), germanium (extra pure grade), and arsenic (extra pure grade). The starting mixture composition was chosen along the CdGeAs₂-MnGeAs₂ join. The mixture (5–10 g) was loaded into a graphitized silica ampule, which was then pumped down to 10–2 Pa, heated (with an isothermal hold at 550°C) to above the melting point of CdGeAs₂ (~670°C), and quenched in order to obtain samples with the highest possible manganese content. The sample preparation procedure was described in detail elsewhere [4-6]. The Mn content of the samples was determined by atomic absorption. Their magnetization was measured as a function of temperature at atmospheric pressure using a SQUID magnetometer. Dynamic magnetic permeability was determined by measuring the frequency change in a resonant circuit incorporating the sample as the core of a toroidal coil. The use of an oscillator based on such a circuit for dynamic magnetic permeability measurements offers a number of advantages: it is convenient for measuring the permeability as a function of frequency, temperature, applied magnetic field, and pressure. The oscillator was fabricated using a K155LN1 integrated circuit. Its frequency varied in the range 2 MHz to 20 kHz when the sample underwent ferromagnetic ordering or a structural transition. The oscillator frequency was monitored with a frequency counter. Magnetic permeability μ was calculated by equating the inductance

of the toroidal coil with N turns around the sample to that evaluated from the resonance frequency of the oscillator:

$$\mu = \frac{\tau^2 \cdot 10^7}{8\pi^2 CN^2 h \ln b/a} \quad (1)$$

Here, C is the capacitance in the resonant circuit; τ is the oscillation period; and a , b , and h are, respectively, the inner radius, outer radius, and height of the toroidal coil. Susceptibility χ was determined from the relation $\mu = 1 + 4\pi\chi$. When the effect was weak, the signal was accumulated for a longer time and then averaged. With this technique, there is no need to take into account the dynamic range of the frequency measurement system. The Hall coefficient R_H and transverse magnetoresistance $\Delta\rho_{xx}/\rho_0$ of polycrystalline Cd_{1-x}Mn_xGeAs₂, Cd_{1-x}Mn_xGeP₂ и Zn_{1-x}Mn_xGeAs₂ were measured as a function of increasing and decreasing pressure near room temperature in a Toroid anvil cell at hydrostatic pressures $P \leq 7$ GPa. The cell was mounted in a solenoid which generated magnetic fields $H \leq 400$ kA/m. The sample was enclosed in an ~80 mm³ Teflon cell fitted with eight wire leads, which allowed the resistivity ρ , Hall coefficient R_H , and transverse magnetoresistance $\Delta\rho_{xx}/\rho_0$ of the sample to be measured simultaneously under pressure. The pressure was monitored with a manganin pressure gage calibrated over the entire pressure range of interest using several phase transitions of Bi. The experimental procedure was described in detail elsewhere [7, 8]. The samples for the ρ , R_H , and $\Delta\rho_{xx}/\rho_0$ measurements were rectangular in shape and $4 \times 1 \times 1$ mm in dimensions. Their homogeneity was checked by four probe ρ and R_H measurements. Electrical contacts were made by lead-tin solder and showed Ohmic behavior as verified by current-voltage measurements.

III. MEASURING RESULTS AND DISCUSSIONS

In figure 1 are presented the baric dependences of the magnetic susceptibility for p-Cd_{1-x}Mn_xGeAs₂, p-Cd_{1-x}Mn_xGeP₂ (fig. 2), and p-Zn_{1-x}Mn_xGeAs₂ (fig. 3). Figure 1 shows that maximum $(\chi/\chi_0)(P)$ shifts towards the

low temperatures from $P=2$ GPa for $x=0.06$ to $P=1.6$ GPa for $x=0.3$ with increasing of manganese percentage in $p\text{-Cd}_{1-x}\text{Mn}_x\text{GeAs}_2$. The maximum amplitude vice versa increases with increasing of manganese percentage. The same behavior is observed for two samples with $x=0.9$ and $x=0.18$ in $p\text{-Cd}_{1-x}\text{Mn}_x\text{GeP}_2$. The studied dependence of relative magnetic susceptibility $(\chi/\chi_0)(P)$ for samples $p\text{-Zn}_{1-x}\text{Mn}_x\text{GeAs}_2$ ($x=0.02$ and 0.04) is presented in Fig. (c), and as is clear the observed scenario is similar to previous materials. When pressure decreases, in all studied samples in $(\chi/\chi_0)(P)$ dependences is observed a hysteresis, which maximums can be used grades.

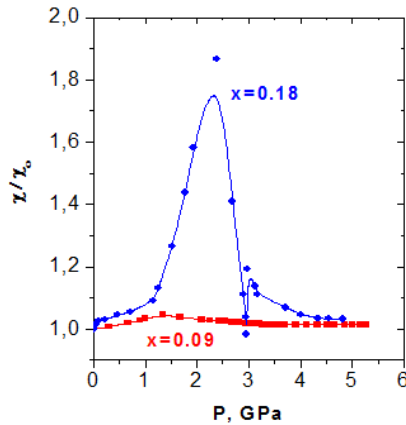


Fig. 1. Baric dependences of the magnetic susceptibility for $p\text{-Cd}_{1-x}\text{Mn}_x\text{GeAs}_2$

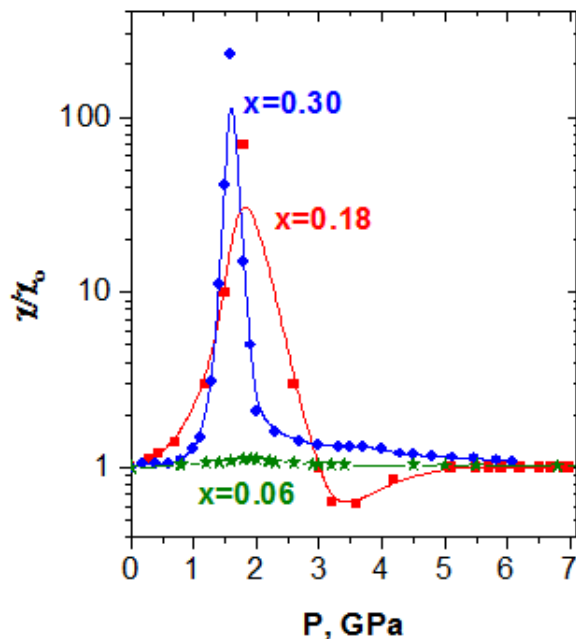


Fig. 2. Baric dependences of the magnetic susceptibility for $p\text{-Cd}_{1-x}\text{Mn}_x\text{GeP}_2$

Throughout the investigations of structural phase transitions in oriented samples [2] in monocrystals $p\text{-Cd}_{0.947}\text{Mn}_{0.053}\text{GeAs}_2$ is presented a dependence of magnetic susceptibility $(\chi/\chi_0)(P)$ for oriented samples $p\text{-Cd}_{0.947}\text{Mn}_{0.053}\text{GeAs}_2$ (Fig. 4). As it is clear from figure the magnetic susceptibility increases at $P_c=1.7$ GPa and achieves the maximum. A position of peaks for magnetic susceptibility in a scale of high pressures for the samples cut out along the axis C [001] and across the axis C [100]

is similar and differs by a height of the peak. The observed maximum in $(\chi/\chi_0)(P)$ dependency can be interpreted as spin-reoriented magnetic phase transition ferromagnetic-antiferromagnetic for what speaks a presence of susceptibility arm after the ferromagnetic-antiferromagnetic transition typical for antiferromagnetic state. Here is observed a considerable hysteresis of $(\chi/\chi_0)(P)$ at pressure release.

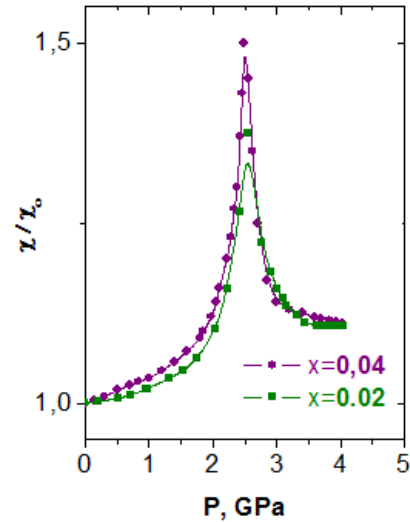


Fig. 3. Baric dependences of the magnetic susceptibility for $p\text{-Zn}_{1-x}\text{Mn}_x\text{GeAs}_2$

In studied samples in a region of the phase transition there is observed a negative magnetoresistance (Fig. 5), which is distinct by a character of $\Delta\rho_{xx}(P)$ dependency for different crystallographic directions. When pressure decreases, the hysteresis observed in $\Delta\rho_{xx}(P)$ dependency.

The estimated experimental data can be used for design for pressure transducers (reference). There are several principles of operations of pressure transducers basing on resistivity, Hall effect, etc. This work offers a pressure transducer based on metamagnetic phase transition.

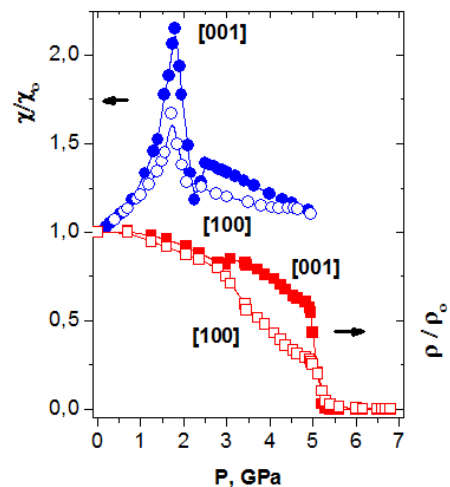


Fig. 4. Dependence of relative magnetic susceptibility $(\chi/\chi_0)(P)$ and specific resistivity $(\rho/\rho_0)(P)$ in different crystallographic orientation for the monocrystalline sample $\text{Cd}_{0.947}\text{Mn}_{0.053}\text{GeAs}_2$

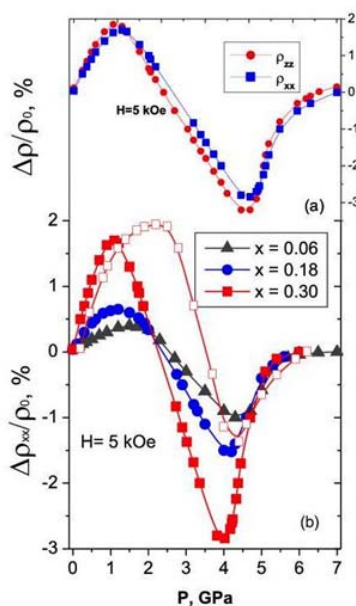


Fig. 5 (a) Dependences of transverse and longitudinal magnetoresistance on the pressure for CdGeAs₂ <Mn> x=0.06-0.3 (b) Dependences of transverse magnetoresistance on the pressure for CdGeAs₂ <Mn> x=0.06-0.3 at pressure increase (dark symbols) and for CdGeAs₂ <Mn> x=0.3 at pressure decrease (light symbols).

The offered transducers are diminutive, practically feasible, as a character indicator is used the magnetic susceptibility of phase transition, which has a sharp peak of high intensity, easily measured, not requires Ohmic contacts. A value of reference pressure can be easily changed varying a percentage of manganese. The data of repes point are presented in the table 1.

Table 1. A value of repes point for the samples Cd_{1-x}Mn_xGeAs₂

№	Samples	X	type	compres	decompres
1	CdGeAs ₂	0.00	p	5.9	2.9
2	Cd _{1-x} Mn _x GeAs ₂	0.003	p	5.7	2.8
3	Cd _{1-x} Mn _x GeAs ₂	0.053	p	5.5	2.7
4	Cd _{1-x} Mn _x GeAs ₂	0.06	p	5.4	2.6
5	Cd _{1-x} Mn _x GeAs ₂	0.18	p	5.2	2.5
6	Cd _{1-x} Mn _x GeAs ₂	0.30	p	4.9	2.4
7	Cd _{1-x} Mn _x GeAs ₂	0.36	p	4.8	2.3

Acknowledgments: This work was supported by Program of Presidium of RAS “Thermophysics and mechanics of external energetic influences and physics of high compressed material” and Section of High Compressed Material.

[1]. A.Yu. Mollaev, I.K. Kamilov, R.K. Arslanov, U.Z. Zalibekov, S.F. Marenkin, Fizika, 2007, v.8, № 1-2, p.320.

[2]. Yu. Mollaev, I.K. Kamilov, R.K. Arslanov, U.Z. Zalibekov, S.A. Varnavskii, S.F. Marenkin, 2009, v.45, № 9, p.1035.

[3]. A. Yu. Mollaev, I. K. Kamilov, R. K. Arslanov, T. R. Arslanov, U. Z. Zalibekov, V. M. Novotortsev, and S. F. Marenkin, JETP Letters, 2010, v.91, № 9, p.524.

[4]. V.M. Novotortsev, V.T. Kalinnikov, L.I. Koroleva, et al., Zh. Neorg. Khim., 2005, v.50, № 4, p.552.

[5]. S.F. Marenkin, V.M. Novotortsev, K.K. Palkina, et al., Neorg.Mater., 2004, v.40, № 2, p.135. [Inorg. Mater. (Engl. Transl.). v.40, № 2, p.93].

[6]. R.V. Demin, L.I.Koroleva, S.F. Marenkin, et al., Pis'ma Zh. Tekh. Fiz., 2004, v.30, № 21, p.81.

[7]. L.G. KhvostansteV, L.P. Vereshchagin, and A.P. Novikov, High Pressure, 1977, v.9, № 6, p.637.

[8]. A.Yu. Mollaev, L.A. Saipulaeva, R.K. Arslanov, and S.F. Marenkin, Neorg. Mater., 2001, v.37, № 4, p.405. [Inorg.Mater. (Engl. Transl.), .37, № 4, p.327].

ABOUT APPLICATION OF *n*-InAs AND *n*-CdAs₂ SAMPLES AS REPER AND CALIBRATOR OF PRESSURE

**A.Yu.MOLLAEV, S.L.SAYPULAEVA, R.K.ARSLANOV,
A.G.ALIBEKOV, N.S.ABAKAROVA**

*Institute of Physics, Dagestan Scientific Center, Russian Academy of Sciences, Makhachkala,
367003, Russia*

e-mail: a.mollaev@mail.ru

In monocrystallin samples *n*-InAs and *n*-CdAs₂ was measured the $\rho(P)$ at the hydrostatic pressures up to 9 GPa and room temperatures with pressure rise and releasing. As a result two reference points were obtained for *n*-InAs, and for *n*-CdAs₂ there were get four reference points in crystallographic direction [001] and three points in [100] direction.

1. INTRODUCTION

Homogeneous semiconductors and semiconductor structures are widely applied as a resistive point continuous transducer of pressure in metrology and also for automation of technological synthesis processes of supersolids and precious-stone raw material at high pressures owing to high susceptibility to external action and variety of properties [1-5].

Physical principles underlying the work of semiconductor resistive continuous transducers of pressure are in a change of electron and phonon spectra under deformation.

The present work is the continuation of researches of perspective semiconductor materials, that were began in the Institute of Physical, Daghestan Scientific Center Russian Academy of Sciences with the aim of forming data bank that can be used either at making pressure transmitters for calibration of high pressure apparatus or as command elements for automatization of processes of synthesis of supersolids and precious stone raw materials [6].

InAs belongs to semiconductors of A₃B₅ type with isotropic electrical properties studied well enough. However, available data for InAs are inconsistent. CdAs₂ is one of least studied semiconductor of A₃B₅ type of crystal heterologal modification whose structural features determine a considerable anisotropy of electrical properties. Data available in literature on investigation of CdAs₂ at high pressure are also insufficient.

I. EXPERIMENT

Mono- and polycrystal *n*- and *p*-InAs samples (with the concentration of carriers $10^{15} - 10^{17} \text{ cm}^{-3}$) and *n*-CdAs₂ monocrystals ($n=10^{14}-10^{15} \text{ cm}^{-3}$) have been investigated that were oriented in different crystallographic directions. Hydrostatic pressure was generated in the high-pressure apparatus of type "toroid" (fig. 1) which was located in the solenoid with magnetic intensity $H \leq 5 \text{ kOe}$.

The measurements were carried out at rise (compression) and fall (decompression) of pressure that was measured by manganine manometer graduated towards reper point [7] in all process of investigations. The error of pressure measurements was about 3 %. Hydrostatic pressure up to $P \leq 9 \text{ GPa}$ was created in teflon capsule whose effective volume was $\approx 80 \text{ mm}^3$ by the methodic described in work [8] that was partially improved.

Monocrystal samples had the form of rectangular parallelepiped with the dimensions of $2.5 \times 0.6 \times 0.5 \text{ mm}$. Polycrystal samples were a kind of circles of cardboard or

paper with the hole of 0.5-1 mm in the central part into which 2-3 mg of semiconductor material is pressed.

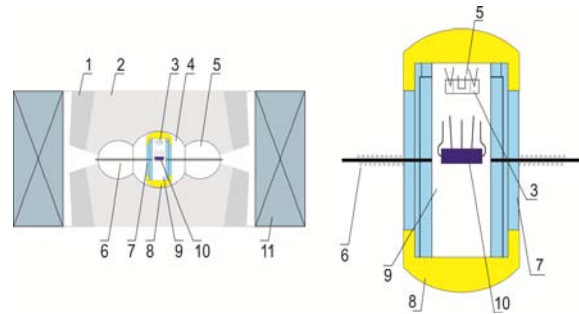


Fig. 1. A device for measuring of baric dependence parameters of solids at high hydrostatic pressure up to 10 GPa: 1 – ring of support; 2 – insert from WC-6M; 3 – manganin pressure pickup; 4 – catlinite insert; 5 – catlinite ring; 6 – electrical leads; 7 – teflon capsule; 8 – copper lid; 9 – cooper lids; 10 – sample; 11 – solenoid.

II. RESULTS AND DISCUSSIONS

The change of electroresistance from pressure which is easily measured with perfect exactness was chosen as indicator of properties.

Performances of the explored samples of arsenide of indium are presented in table 1.

Table 1 Electrophysical properties of the explored samples *n*-InAs

№	$\rho_0, \text{Om}\cdot\text{sm}$	$ R_0 , \text{sm} \cdot \text{C}^{-1}$	$ \mu_H , \text{sm} \cdot \text{V}^{-1} \cdot \text{s}$
1	$1.2 \cdot 10^{-2}$	340.4	28367
2	$1.0 \cdot 10^{-2}$	250	25000
3	$3.7 \cdot 10^{-3}$	76.2	20594
4	$3.2 \cdot 10^{-3}$	63.0	19687
5	$2.4 \cdot 10^{-3}$	26.0	10833

Typical results of measurements of specific electroresistance *n*-InAs in the region of phase transition at hydrostatic pressure up to 9 GPa at compression and decompression are shown in fig.2. Phase transitions that can be used as reper points are observed on curves of baric dependences ρ/ρ_0 from pressure at compression ($P=6.9 \text{ GPa}$) and decompression ($P=2.2 \text{ GPa}$).

Thus the presence of considerable (from several orders) Jumps of electroresistance in the region of phase transition and linear dependence $\lg(\rho/\rho_0)$ in the range of pressures 3-6 GPa allows to use indium arsenical as reper and command element i.e. one semiconductor combines two types of pressure transmitters. The position of phase transition on the scale of high pressures at quasihydrostat-

ic pressure in InAs satisfactory coincides with the data obtained at hydrostatic compression.

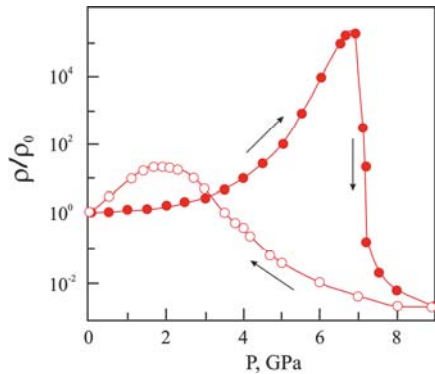


Fig. 2 Dependence of given specific electroresistance in *n*-InAs ($n=2 \cdot 10^{16} \text{ cm}^{-3}$), measured at compression and decompression

Diarsenicum cadmium (CdAs₂) is one of the least studied semiconductor junctions A₂B₅ that crystallized in tetragonal singonia. The peculiarity of its structure is the presence of As-As contacts alongside with Cd-As contacts that form zigzag chain structures stretched along [001] direction what determines considerable anisotropy of electric properties [9]. The samples were made of parallelepiped form and oriented in such way that their edges coincided with [100] and [001] crystallographic directions.

Performances of the explored sample diarsenicum cadmium are presented in table 2.

Table 2 Electrophysical properties of the explored samples *n*-CdAs₂

№	$\rho_0, \text{Om}\cdot\text{sm}$	$ R_0 , \text{sm}^3\cdot\text{C}^{-1}$	$ \mu_H , \text{sm}^2\cdot\text{V}^{-1}\cdot\text{s}^{-1}$	Direction
1	11.2	16892	1508	[100]
2	8.6	21750	2529	[100]
3	7.4	15037	2032	[100]
4	27.0	5840	216	[001]
5	40.0	3289	82	[001]
6	40.0	3500	87.5	[001]

Baric dependences of specific electroresistance $\rho(P)$ for samples of CdAs₂ at compression and decompression are shown in fig.3.

In Fig.3 are presented the dependences of resistivity $\rho(P)$ at compression and decompression for CdAs₂ samples in crystallographic directions [001] (curve 1) and [100] (curve 2). The $\rho(P)$ rises or falls in the dependence of crystallographic directions.

In samples oriented towards [100] direction (curve 2) the specific resistance increases up to $P=2$ GPa, when pressure rises, and then increases up to $P=3.0$ GPa as a result of the phase transition, at $P=3.1$ GPa decreases again up to $P=4.5$ GPa. Two clear peaks are observed in $\rho(P)$ dependence at $P=3.0$ GPa and $P=5.5$ GPa.

A dependence of the specific resistance for *n*-CdAs₂ samples oriented towards [001] direction has more complicated character (Fig.3, curve 1).

When pressure rises, the specific resistance increases, in $\rho(P)$ dependence are observed three peaks at $P=1.8$ and 5.5 GPa. The maximum at $P=5.5$ GPa is interpreted as structural phase transition, which meets in works [10].

A change in resistivity at pressure fall occurs with large hysteresis. When pressure falls, there is also observed phase transition in $\rho(P)$ baric dependences at $P=3.6$ GPa. Value coincidence of initial points of $\rho(P)$ dependences at pressure rise with values of finite points of these curves at pressure fall indicates the reversibility of the phase transition and the lack of splitting and change of phase composition in studied samples. The values of concentration and mobilities before and after phase transition allow to conclude that there is semiconductor-semiconductor phase transition in cadmium diarsenide at $P=5.5$ GPa. The phase transition in CdAs₂ could not be judged more definitely because of lack of X-ray-structural researches at high pressures $P \leq 9$ GPa.

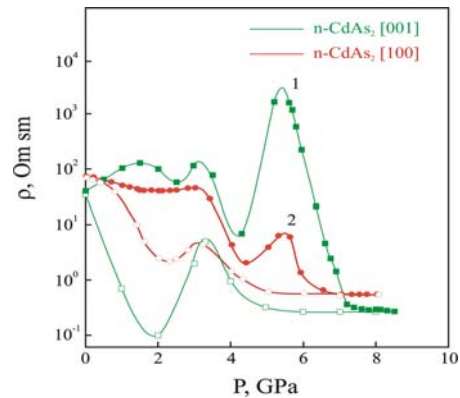


Fig. 3 Dependence of electroresistance in *n*-CdAs₂, measured at compression and decompression in different directions

Thus the presence of maxima at $P=1.8; 3$ and 5.5 GPa at compression, and presence of maximum at $P=3.6$ GPa at decompression allows to recommend *n*-CdAs₂ as a perspective material for making of reference point of pressure.

The obtained data on the reference points for samples *n*-InAs and *n*-CdAs₂ (in directions [001] and [100]) is presented in table 3.

Table 3 Values of pressure in point of phase transition

№	Samples	Direction	Points of phase transition	
			Comp.	Decomp.
1	<i>n</i> -CdAs ₂	[001]	1.8 GPa; 3.0 GPa; 5.5 GPa	3.6 GPa
2	<i>n</i> -CdAs ₂	[100]	3.0 GPa; 5.5 GPa	3.6 GPa
3	<i>n</i> -InAs	—	6.9 GPa	2.2 GPa

From the gained data it is possible to draw the following deduction: *n*-InAs and *n*-CdAs₂ can be recommended as the universal reference points in a wide gamut of pressures.

Acknowledgments: This work was supported by Program of Presidium of RAS “Thermophysics and mechanics of external energetic influences and physics of high compressed material” and Section of High Compressed Material.

-
- [1]. *B.Yu.Tonkov*. Phase transitions of linkings at high pressures. The manual, Metallurgy, Moscow (1988).
- [2]. *A.S.Skoropanov, B.L.Valevsky, V.F.Skums, A.A.Vecher*, Supersolid materials **3**, 61, 1988.
- [3]. *A.S.Skoropanov, B.L.Valevsky, V.F.Skums, A.A.evening, J.N.Rotner, J.S.Maslenko, N.V.Novikov*, FTHP **32**, 25, 1988.
- [4]. *E.M.Ivanov, E.E.Chaputoeich*, The measuring technics **9**, 22, 1972.
- [5]. *J.Z. Jiang, J. Staun Olsen, L. Gerward, S. Steenstrup*, High Pressure Research **22**, 395, 2002.
- [6]. *M.I.Daunov, V.I.Danilov, A.B.Magomedov, A.Yu.Mollaev, S.M.Salikhov*. Sverkhтвердые Materialy, **4**, 7, 1990.
- [7]. *N.A.Bendeliani, L.F.Vereschagin*. Phys. Tekh. Exper., **4**, 218, 1979.
- [8]. *L.G.Khvostantsev, V.A.Sidorov*. Phys. Stat. Sol. (a), **64**, 379, 1991.
- [9]. *S.F.Marenkin, V.A.Morozova*. Neorganicheskie Materialy, **35**, 1190, 1999
- [10]. *V.B.Shipilo, E.M.Plyshevskij, I.M.Belskij*. Physics of gas and solidphase pressures., M: Science, (1978).

PHYSICAL PROPERTIES OF SnS THIN FILMS GROWN BY HOT WALL DEPOSITION

V.F. GREMENOK¹, S.A. BASHKIROV¹, V.A. IVANOV¹, D.M. UNUCHAK²,
V.V. LAZENKA², K. BENTE²

¹*State Scientific and Production Association "Scientific-Practical Materials Research Centre of the National Academy of Sciences of Belarus", P. Brovka str., 19, 220072 Minsk, Belarus
email: gremenok@ifttp.bas-net.by*

²*Institut für Mineralogie, Kristallographie und Materialwissenschaft, University of Leipzig, Scharnhorststr. 20, 04275 Leipzig, Germany*

SnS thin films were grown by hot wall deposition method onto glass substrates at temperatures between 220 and 380 °C. The as-grown films exhibited uniform composition through the film thickness. The atomic ratio of Sn to S is 1.06 (51.5 at. % of Sn and 48.5 at.% of S). The X-ray diffraction studies showed that SnS films were single-phase and had orthorhombic crystal structure with a strong (010) orientation. The SnS layers showed p-type conductivity and exhibited an electrical resistivity of (2 - 6) Ω·cm with an activation energy of (0.12 - 0.13) eV. The thermopower value varied from 240 μV·K⁻¹ to 950 μV·K⁻¹ depending on the deposition parameters. The films exhibited a high absorption coefficient (> 6·10⁴ cm⁻¹) above the fundamental absorption edge with an optical band gap in the range of 1.15 - 1.28 eV. The obtained results were analyzed to evaluate the potentiality of the as-grown SnS films in the fabrication of thin film solar devices.

Keywords: SnS -1: Hot wall deposition – 2: Physical properties – 3

1. INTRODUCTION

During the last decade, investigations of new materials have evoked considerable interest in SnS thin films due to their vast potential for use in thin film solar cells and other optoelectronic devices like holographic recording system, solar control device etc. [1–4]. Layered semiconductor SnS is a IV-VI compound crystallizing in the orthorhombic structure (space-group *Pnma*, GeS structure type) [5, 6]. Their unit cell spans two layers, which stack along the [010] axis of the crystal. In thin film form SnS is usually a p-type semiconductor with different band gap values in the range of 1.07-1.38 eV. The acceptor levels are created by double ionized tin vacancies [7, 8]. Tin sulfide thin films show high absorption coefficient (> 10⁴ cm⁻¹) in the visible range [3]. They contain only relatively less-toxic materials and stable in the slight acidic media [9]. SnS has also a good thermoelectric properties and it may become a good thermoelectric material for future applications [10].

Hot wall vacuum deposition method (HWVD) has been used for thin IV-VI films deposition for some decades [11]. The method showed high efficiency and economy as HWVD is concerned with the film growth under conditions close to thermodynamic equilibrium and with a minimum loss of material [12].

In this paper we report the synthesis of SnS thin films using hot wall vacuum deposition method and the variation of microstructure, electrical and optical properties with respect to substrate temperature.

2. EXPERIMENTAL

Polycrystalline SnS ingots were synthesized by the fusion method. In this method, the reaction between the sulfur vapors and molten tin metal was allowed to take place gradually in evacuated silica glass tube. Stoichiometric mixtures (with an accuracy of 5×10⁻⁴ g) of Sn and S of high purity 99.999% were sealed into evacuated silica tube at the pressure of 10⁻³ Torr. The evacuated tube was then placed into an electric furnace and kept first at 450 °C for 7 days and at 700 °C for 10 days after. In order to avoid explosions due to the sulfur

vapor pressure, the tube was heated slowly (25 °C/h). The tube was gradually cooled with a cooling rate of about 20 °C/h to room temperature in order to obtain polycrystalline SnS ingots.

The main feature of the HWVD system is the heated linear 1.2 cm diameter quartz tube containing source material, which served to enclose and direct the vapor from the source to the substrate. The quartz tube and substrates were heated independently. Thin films were deposited by keeping the quartz tube temperature of around 590 °C [13, 14]. Glass plates were chemically cleaned, rinsed with distilled water and blown dried with compressed air before deposition. The range of substrate temperature was varied from 220 to 380 °C. The substrate was held at a distance of about 1 mm from the open end of the quartz tube. In this way the substrate acts as a lid closing the tube with the help of substrate holder heater. The pressure in the chamber was about 10⁻⁵ Torr during evaporation. Chromel–alumel thermocouples were used to measure the temperatures of quartz tube and the substrate.

The crystal structures of SnS powder and thin films were investigated by X-ray diffraction (XRD) using a Siemens D-5000 diffractometer with CuK_α (λ = 1.5418 Å) radiation. The 2θ - range for the diffractometer was set from 10 to 100° with a step size of 0.038°. The observed phases were determined by comparing the *d*-spacing with the Joint Committee on Powder Diffraction Standard (JCPDS) data files. In order to consider instrumental error, the samples were coated by Si powder suspended in acetone.

The composition and surface morphology of thin films were investigated by electron probe microanalysis (EPMA) using a CAMECA SX-100 with an accuracy of about 2 % and scanning electron microscope JEOL 6400, respectively. Depth profiling was performed by Auger electron spectroscopy (AES) using Perkin Elmer Physical Electronics 590 with simultaneous sputter etching.

Electrical conductivity measurements were carried out using a dc two-probe configuration in a special cryostat. The temperature range was extended from 150 up to 420 K. All measurements were carried out under

vacuum condition of about 5×10^{-4} Torr. The “Leit-C” paste was used as ohmic contact. The ohmic nature of the contacts was checked by recording the current–voltage characteristics. Thermoelectric properties (Seebeck coefficient) of the films were measured at room temperature. The temperature difference between the “hot” and “cold” ends of the samples was $\Delta T = 25$ K.

The optical transmittance was carried out using Varian Cary 50 UV–VIS spectrophotometer in the wavelength range of 500 – 2000 nm with an incident radiation perpendicular to the film.

3. RESULTS AND DISCUSSION

SnS thin films grown at different substrate temperatures were characterized by XRD measurements. All films show strong orientation along [010] direction showing high textured spectra with strong 040 peak. Fig. 1 shows the typical XRD spectrum of the SnS thin film. Tin sulfide pattern (JCPDS # 39-0354) was used as a reference for qualitative analysis of the samples. The cell parameters for orthorhombic structure were evaluated by the following standard equation:

$$\frac{1}{d^2} = \frac{h^2}{a^2} + \frac{k^2}{b^2} + \frac{l^2}{c^2} \quad (1),$$

where d is a interplanar spacing, h, k, l are the Muller’s plane indexes, and a, b, c are the cell parameters.

The obtained films are polycrystalline and single-phase in nature. The grown structure is orthorhombic with cell parameters in the range of $a = 4.270\text{--}4.296$ Å, $b = 11.226\text{--}11.257$ Å, $c = 3.982\text{--}3.991$ Å depending on deposition conditions. The grain size in thin films was calculated from the X-ray (040) line width using the Sherrer’s formula:

$$D = \frac{0.94\lambda}{\beta \cos \theta} \quad (2),$$

where D is the grain size, λ is the wavelength of X-ray radiation, β is the full width at half maximum (FWHM) of the peak, θ is the peak angle. The grain size increases from 35 to 65 nm with the increase of substrate temperature, in agreement with *Devica*’s report [9].

Typical cross-section SEM image of the SnS film is shown on Fig. 2. Deposited films are high densely packed, pinhole and microcracks free. The films show layered structure with the most layers parallel to the substrate surface. The sufficient volume of the film is filled with large grains (about some micrometers). The film thicknesses estimated from the cross-section images of the films are 1 – 5 μm. The SEM studies of as-grown layers demonstrate the strong growth temperature dependence of surface morphology of SnS thin films. A gradual change in crystallites growth from barley like nature to densely packed nature is seen with the increase of substrate temperature. The films grown at high temperature consist of quite large layered crystallites.

These granules are grown randomly with irregular shapes and sizes. The result showed that such a layered structure is a common feature of IV-VI compounds. It also appeared that the grown granules are loosely packed together and form a highly rough surface. The grains are electrically well connected to each other, which is essential for the development of p-n junction. The density of the films is of critical importance, since it will prevent

the diffusion of atoms during the growth of the buffer and window material layers for the production of thin film solar cells.

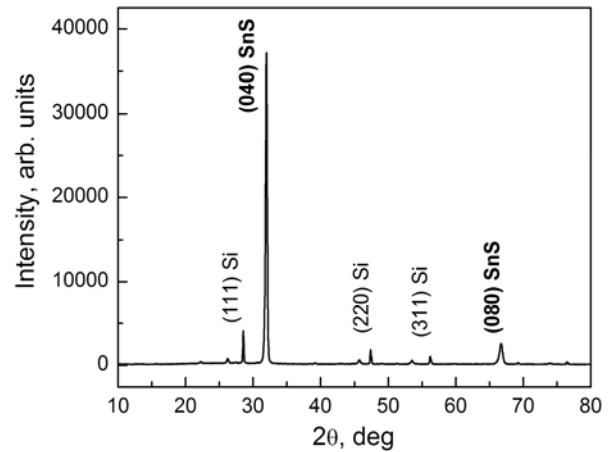


Fig. 1. Typical XRD spectrum of the SnS thin film.

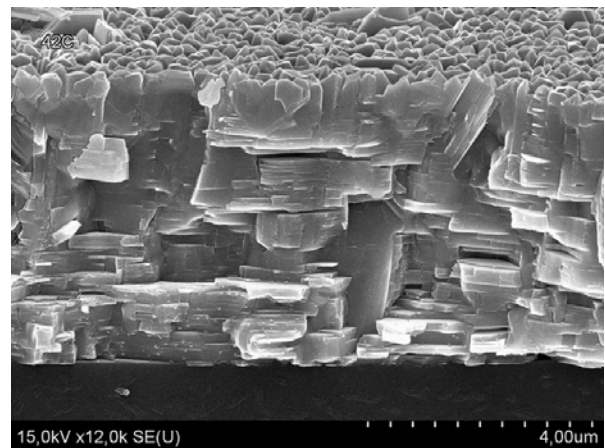


Fig. 2. SEM-image (cross section) of the SnS films.

The elemental composition of the films, observed by EPMA and AES, is close to stoichiometry with small deficiency of sulfur. Fig 3 shows typical EPMA spectrum of SnS thin film. The as-grown films exhibited a composition with the atomic ratio of Sn to S of 1.06 (51.5 at. % of Sn and 48.5 at.% of S). The energy dispersive analysis of all as deposited films showed that the obtained films are homogeneous and the compositions of the films are reproducible. That clearly shows that composition control can be easily achieved using hot wall deposition technique.

The AES depth profile was used to study the concentration of elements in the as-grown SnS films. The data were obtained by sputtering the area of $10 \times 10 \mu\text{m}^2$ with energetic argon ions at a rate of $1000 \text{ \AA}/\text{min}$. The typical depth profile for one representative sample is given in Fig. 4. It shows peak heights at different depths (time) for tin and sulfur elements. The AES depth profiles of films reveal relatively uniform distribution of components across the thin film. This observation supports the XRD data, indicating uniform, single-phase thin film material.

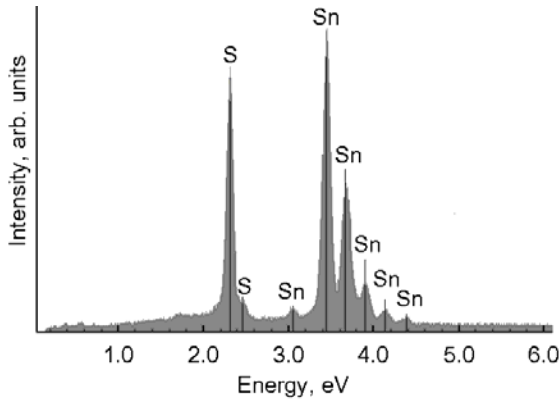


Fig.3. Typical EDAX spectrum of the SnS layers.

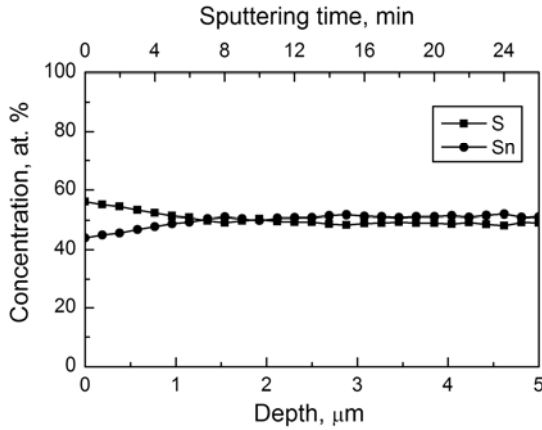


Fig.4. Representative AES depth-profile of the SnS films.

Hot probe measurements indicate p-type conductivity of the as-grown SnS films deposited in the substrate temperature range of 220 – 380 °C. The average Seebeck coefficient and the electrical resistivity at room temperature were $\alpha = 240 - 950 \mu\text{V}\cdot\text{K}^{-1}$ and $\rho = 2 - 6 \Omega\cdot\text{cm}$, respectively.

The temperature dependence of the dark conductivity (σ) was measured in the temperature range of 150 – 420 K. Electrical conductivity of SnS thin films increases with increasing of temperature that exhibits semiconductor behavior. The conductivity activation energy of tin sulfide films was evaluated using the Arrhenius equation:

$$\sigma = \sigma_0 \exp\left(\frac{-\Delta E_a}{kT}\right) \quad (3),$$

where ΔE_a is the electrical conductivity activation energy of the impurity level, which depends on its position in the band gap, σ_0 – proportional constant, k – Boltzmann constant, and T – absolute temperature.

The activation energy of the films calculated from the slope of semilog plot of conductivity (σ) versus $1000/T$ is shown in Fig.5. This plot is linear in a temperature range of 200 – 420 K, indicating the extrinsic nature of the semiconductor.

The extrinsic behaviour is due to the charge carriers liberated from the impurity levels. As-deposited SnS films exhibited activation energy of 0.12-0.13 eV. The activation energy of the SnS films is attributed to shallow acceptor states due to Sn vacancies [7, 15]. These Sn vacancies are characteristics of IV-VI compounds that play a significant role in establishing the p-type conductivity of these compounds.

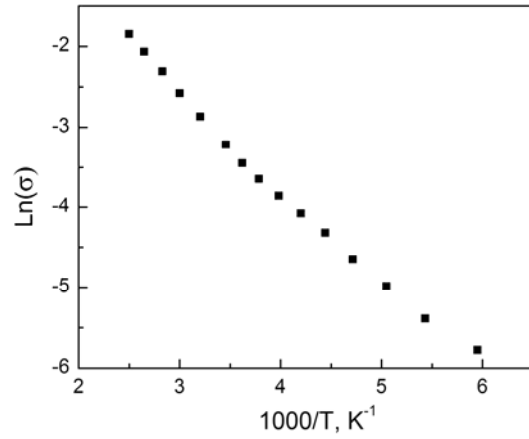


Fig.5. Plot of $\log(\sigma)$ as a function of $1000/T$ for the SnS layers.

Devica *et al.* [9] reported an activation energy of 0.26 eV for thermal evaporation SnS films, Noguchi *et al.* [16] observed the activation energy between 0.28 eV and 0.34 eV in thermal evaporated SnS films. Lopez *et al.* [15] reported activation energy of 0.54 eV for sprayed SnS films. Therefore, the activation energy of the SnS films depends on the film thickness, the preparation technique and the film composition. The nature of the impurities responsible for the different values of activation energy requires further study.

Optical properties of SnS films were studied by the optical transmittance (T) spectra in the range of 500 – 2000 nm using unpolarised light at room temperature. The absorption coefficients α of the films in high absorbing region was calculated using the relation:

$$\alpha = \frac{1}{d} \ln\left(\frac{1}{T}\right) \quad (4),$$

where T is the transmittance value, and where d is the film thickness in cm, evaluated from high magnification cross-sectional SEM images.

The films were highly absorbing with an optical absorption coefficient (α) over 10^4 cm^{-1} near the fundamental absorption edge, so that even thin layers can absorb most of the incident radiation.

The optical energy band gap of the SnS films was estimated using the well-known relationship ($ah\nu$) for direct transitions, given by [17]:

$$(ah\nu) = A(h\nu - E_g)^{1/2} \quad (5),$$

where α is the absorption coefficient, E_g is the optical band gap, $h\nu$ is photon energy and A is a constant.

The typical plot of $(ah\nu)^2$ vs a function of photon energy ($h\nu$) for the SnS films deposited at 220 °C is shown in Fig. 6.

This plot near the fundamental absorption edge is linear, indicating that all optical transitions between valance band and conduction band are direct allowed transitions. The films exhibit the optical band gap in the range of 1.15 - 1.28 eV which increases with a decrease in film thickness. The lower band gap values might be explained by a large number of defects (structural disorders, dislocations) and surface imperfections induced by the rough surface films with larger thickness. The values of the optical energy band gap obtained in this

work are in good agreement with the data reported by the others groups, dealing with SnS materials [9, 18-20].

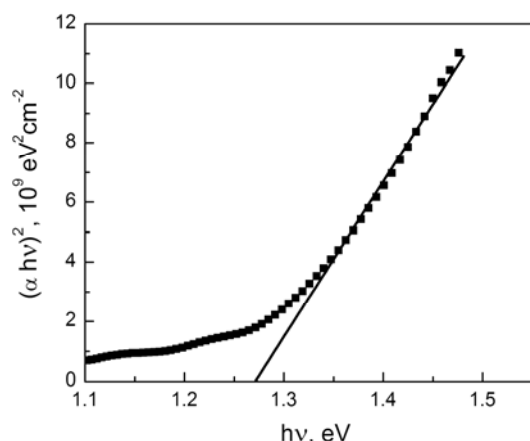


Fig.5. Plot of $(\alpha hv)^2$ as a function of photon energy for the SnS films deposited at 220 °C.

4. CONCLUSION

Tin sulfide films were deposited at different substrate temperatures from 220 °C to 380 °C by hot wall vacuum deposition onto glass substrates. X-ray diffraction measurements showed that as-grown SnS films have a double layered orthorhombic structure with cell

parameters in range of $a = 4.270\text{--}4.296 \text{ \AA}$, $b = 11.226\text{--}11.257 \text{ \AA}$, $c = 3.982\text{--}3.991 \text{ \AA}$. The crystal structure of films remains unaffected by increasing of substrate temperature. According to the SEM investigation, using HWVD method it is possible to produce SnS layers of several microns thick that are pinhole free, conformal to the substrate, and that consist of densely packed large layered crystallites. The electrical measurements showed that the SnS films are non-degenerate semiconductors of p-type conductivity with electrical resistivity about (2 - 6) $\Omega\text{-cm}$, activation energy of 0.12 - 0.13 eV and thermopower in the range of 240 - 950 $\mu\text{V}\cdot\text{K}^{-1}$. The films show absorption coefficients $> 6\cdot 10^4 \text{ cm}^{-1}$ above the fundamental absorption edge with an optical band gap in the range of 1.15 - 1.28 eV, that clearly shows that these films could be used as absorber material in thin film solar cells and the others photovoltaic applications.

ACKNOWLEDGEMENTS

This work has been supported by the Deutsches Zentrum für Luft - und Raumfahrt e.V. and Belarusian Republican Foundation for Fundamental Research. D.M. Unuchak is thankful for financial support of DAAD.

-
- [1] M.G. Bawendi, W.L. Wilson, L. Rothberg, P.L. Carroll, T.M. Jedju, M.L. Teigerwald and L.E. Brus, *Phys. Rev. Lett.* **65**, 623 (1990).
- [2] C.B. Murray, C.R. Kagan and M.G. Bawendi, *Science* **270**, 1335 (1995).
- [3] B. Ghosh, M. Das, P. Banerjee, S. Das, *Solar Energy Materials & Solar Cells*, **92** 1099 (2008).
- [4] Jonathan J. Scragg, Philip J. Dale, Laurence M. Peter, Guillaume Zoppi and Ian Forbes, *Phys. Stat. Sol. B* **245**, 1772 (2008).
- [5] W. Hofmann, *Z. Kristallogr.* **92**, 161 (1935).
- [6] K. Hayashi, A. Kitakaze, A. Sugaki, *Mineralogical Magazine* **65**, 645 (2001).
- [7] M. Ristov, G. Sinadinovski, I. Grozdanov, M. Mitreski, *Thin Solid Films* **173**, 53 (1989).
- [8] M. El-Nahass, *Optical Materials* **20**, 159 (2002).
- [9] M. Devica, N. Koteeswara Reddy, K. Ramesh, K.R. Gunasekhar, *Semicond. Sci. Technol.* **21**, 1125 (2006).
- [10] D.A. Wright, in *Direct Generation of Electricity* edited by K.H. Spring, (Academic Press Inc., London, 1965), chap. 5.
- [11] M. Paić, V. Paić, *J. Mater. Sci.* **7**, 1260 (1972).
- [12] A. Lopez-Otero, *Thin Solid Films* **49**, 3 (1978).
- [13] D.M. Unuchak, K. Bente, G. Kloess, W. Schmitz, V.F. Gremenok, V.A. Ivanov and V. Ukhov, *Phys. Status Solidi C* **6**, 1191 (2009).
- [14] K. Bente, V.V. Lazenka, D.M. Unuchak, G. Wagner and V.F. Gremenok, *Cryst. Res. Technol.* **45**, 643 (2010).
- [15] S. Lopez, A. Ortiz, *Semicond. Sci. Technol.* **9**, 2130 (1994).
- [16] H. Noguchi, A. Setiyadi, H. Tanamura, T. Nagatomo, O. Omoto, *Solar Energy Materials and Solar Cells* **35**, 325 (1994).
- [17] J.I. Pankov, *Optical Processes in Semiconductors*, Academic Press, New York, 1975.
- [18] M. Sugiyama, K. Miyauchi, T. Minemura, K. Ohtsuka, K.I. Noguchi, And H.I. Nakanishi. *Japanese Journal of Applied Physics*, **47**(6), 4494–4495 (2008).
- [19] A. Ortiz, J.C. Alonso, M. Garcia, J. Toriz. *Semicond. Sci. Technol.*, **11**, 243 (1996).
- [20] A. Tanuševski, D. Poelman. *Solar Energy Materials & Solar Cells*, **80**, 297–303 (2003).

GROWTH AND CHARACTERIZATION OF GaInAsSb SOLID SOLUTIONS WITH COMPOSITION NEAR THE MISCIBILITY GAP BOUNDARY

N.N. MURSAKULOV¹, E.V. KUNITSYNA², I.A. ANDREEV², YU.P. YAKOVLEV²,
M. AHMETOGLU³ (AFRAILOV), AND G. KAYNAK³

¹ *Institute of Physics ANAS,*

G. Javid av. 33, AZ1143 Baku, Azerbaijan

nmursakulov@physics.ab.az

² *Ioffe Physical-Technical Institute RAS, 26 Politekhnicheskaya st.,*

194021 St Petersburg, Russia

kunits@iropt9.ioffe.ru

³ *Department of Physics, Uludag University,*

16059 Gorukle, Bursa, Turkey

afrailov@uludag.edu.tr

The growth of the GaSb-related multinary compounds by liquid phase epitaxy has been studied. The high-quality GaInAsSb solid solutions with composition near the miscibility gap boundary have been obtained. These quaternary solid solutions lattice matched with GaSb are competitive for optoelectronic applications in the spectral range of 1.2-2.6 μm . The performance of the photodiodes with GaInAsSb active area is comparable to state-of-the-art results for the devices with photosensitivity maximum at 2.0-2.3 μm .

1. INTRODUCTION

In recent years, the fast development of the infrared (IR) optoelectronic devices has been stimulated by achievements in the epitaxial growth of the III-V semiconductor materials. Lasers, photodiodes, solar cells, TPV devices based on GaSb-related multinary compounds have been suggested for laser diode spectroscopy of gases and molecules, eye-safe laser rangefinding systems, optical fiber communication, ecological monitoring, medicine, energy production and etc. [1-5].

Different epitaxial techniques for growth the high-quality GaSb-related materials have been developed. Such advantages of liquid phase epitaxy (LPE) as simplicity, low cost, the absence of toxic precursors or by-products are of current importance. Moreover, there is a great success in growth of quantum wells (QWs), superlattices and quantum dots by LPE [6], in spite of the fact that application of this technique for nanostructures is limited.

On the other hand, the main drawback of LPE as the thermodynamically equilibrium method is the fundamental thermodynamic limitations on obtaining the III-V materials. Thus, the narrow gap GaIn_xAsSb solid solutions lattice-matched with a GaSb substrate can be grown by LPE with compositions only in the ranges of $0 < x < 0.29$ and $0.74 < x < 1$, which correspond to band gap energy values in the ranges $E_g \sim 0.72\text{-}0.4$ eV and $E_g \sim 0.3\text{-}0.24$ eV, respectively [7]. Unfortunately, a solid phase miscibility gap limits the working wavelength domain of GaInAsSb-based devices.

In this paper we present the important aspects of growth by LPE and characterization of the GaInAsSb solid solutions with composition in the vicinity of the miscibility gap boundary.

2. EXPERIMENT

In this study, for growth from the melts the standard LPE system with the horizontal quartz reactor was used. The reactor was annealed at 950°C under vacuum

conditions for 24 hours and then at 700°C under H₂ flow for 48 hours. After loading the source materials, a graphite boat was annealed in H₂ flow at 720°C for 4 h. Then the system was cooled to room temperature, and the substrate was placed in the boat. The temperature was raised to 640 °C and held for 15 min. The system was then cooled down with the rate of 0.3-0.6 grad/min up to the growth temperature.

The substrates were tellurium-doped GaSb with (100), (111)A and (111)B orientations ($n=(1-5)\times 10^{17}$ cm⁻³, $\mu=4500\text{-}6500$ cm²/V \times s at T=80 K). The GaSb, InAs, InSb binary compounds were used for the melt preparation.

The chemical composition of the alloys was determined by quantitative electron probe microanalysis using a CAMEBAX microanalyzer. The crystalline quality of the grown layers, heterostructure interface abruptness and the surface properties have been studied with X-ray diffraction methods, photoluminescence (PL) spectroscopy, scanning electron microscope (SEM).

3. RESULTS AND DISCUSSION

The liquidus compositions were selected by investigating the melt-solid phase diagrams of the Ga-In-As-Sb systems. The EFLCP (excess thermodynamic functions and linear combinations of chemical potentials) thermodynamical model [8,9] based on the third order virial descending for mean free mole Gibbs energy of the melt onto the mole portion of each component has been used for phase equilibrium diagram calculating.

The basic equation of the EFLCP model for activity coefficients of the melt γ_i has the following form [8]:

Here R is the gas constant, T is the temperature (K), n is the number of components, x_i is the mole fraction of the i-th component of the melt, and α_{ij} , β_{ij} and Ψ_{ijk} are model parameters. All the model parameters have a strong physical meaning. They may be derived from the known data on thermodynamic functions. Our experimental results are in good agreement with our calculations.

$$RT \ln \gamma_i = \sum_{j \neq i}^n \alpha_{ij} x_j^2 + \sum_{j \neq i}^n \sum_{k \neq i}^n (\alpha_{ij} + \alpha_{ik} - \alpha_{jk}) x_j x_k + (2x_i - 1/2) \sum_{j \neq i}^n \beta_{ij} x_j^2 + \sum_{j \neq i}^n \sum_{i \neq k}^n x_j x_k \times \left[(x_j - x_k) \beta_{kj} + x_j (\beta_{ij} + \beta_{ik}) + (1 - 2x_j) \Psi_{ijk} \right]$$

High-quality GaInAsSb solid solutions with composition near the miscibility gap boundary were grown at T=600°C on Te-doped GaSb (100), (111)A and (111)B substrates. The growth rate was 1-4 μm/min. The parameters of these compound semiconductors are presented in Table 1.

Table 1. Room-temperature parameters of the GaInAsSb solid solutions grown by LPE

Composition	Substrate	In content in solid phase	Band gap E _g , eV	Long-wavelength edge λ _{th} , μm
Ga _{0.78} In _{0.22} As _{0.18} Sb _{0.82}	GaSb(100)	0.22	0.53	2.42
Ga _{0.77} In _{0.23} As _{0.20} Sb _{0.80}	GaSb(111)A	0.23	0.512	2.46
Ga _{0.76} In _{0.24} As _{0.21} Sb _{0.79}	GaSb(111)B	0.24	0.504	2.55

In the case of GaSb(100) substrate, the GaIn_xAsSb material with In content of 0.22 was obtained. According to X-ray diffractometry data, the lattice mismatch between the GaInAsSb epitaxial layer and GaSb(100) substrate was as small as (1-3)×10⁻⁴ at T=300K. The full width of half maximum (FWHM) of the diffraction reflection curves were 15 arcsec for the layers and 10 arcsec for the substrates, indicating substrate-layer interface abruptness and high crystalline quality of the grown epitaxial layers. The 80K photoluminescence peak wavelength is 2.075 μm, and the FWHM of PL spectrum is about 17 meV. Such FWHM value results from compositional homogeneity of the material. The width of the Ga_{0.78}In_{0.22}As_{0.18}Sb_{0.82} band gap determined from photoluminescence data was 0.58 eV at T=80K (E_g=0.53 eV at T=300K). These values are accord with calculated miscibility gap boundary at growth temperature of 580-600°C. It was shown earlier that the crystallographic orientation of the GaSb substrate affects on the composition of the GaInAsSb solid solutions [10]. In our experiments, the In content in the solid phase increases from 0.22 to 0.24 as one runs through the series of orientations of the GaSb substrate (100), (111)A, (111)B. As seen from the Table 1, the In content reaches 0.24 for GaSb(111)B substrate.

This effect leads to band gap width decreasing up to E_g=0.50 eV and a shift of the long-wavelength edge of the photosensitivity of the GaSb/GaInAsSb heterostructures (See Fig. 1).

The half maximum wavelength (λ_{50%}) of sensitivity for the heterostructures grown on GaSb(100) substrate (Fig.1, curve 1) is 2.32 μm, the long-wavelength edge (λ_{th}) lies at 2.42 μm. These values are determined by energy gap of the Ga_{0.78}In_{0.22}As_{0.18}Sb_{0.82} active layer (E_g=0.53 eV).

The long-wavelength threshold for the heterostructures on GaSb(111)A is observed at λ_{th}=2.46 μm (Fig.1, curve 2). When substrate is GaSb(111)B, the long-wavelength threshold is red shifted to λ_{th}=2.55 μm (Fig.1, curve 3). Thus, using a GaSb (111)B substrate makes it possible to increase the In content in the solid

phase and to obtain the GaInAsSb with narrower band gap. We suppose that this fact is due to more strong stabilization effect of GaSb substrate with (111) orientation in contrast to GaSb (100) one.

One of the main requirements for the GaInAsSb material from the photodiode point of view is a low carrier density in an active layer.

The Ga_{0.78}In_{0.22}As_{0.18}Sb_{0.82} solid solutions grown on n-GaSb(100) substrate without the buffer layer demonstrate high hole density and low mobility (p=(1-3)×10¹⁷ cm⁻³, μ=300-400 cm²/V×s at T=80 K). To decrease the carrier density in these solid solutions we used such methods as tellurium doping, use of rare-earth elements, and growth from the lead containing melt.

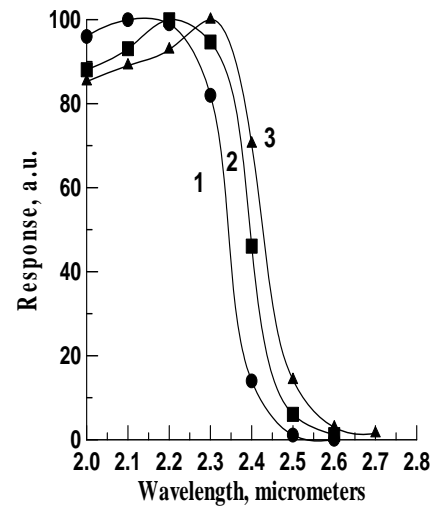


Fig. 1. Spectral photosensitivity distribution of GaSb/GaInAsSb heterostructures grown on the substrates: 1–GaSb(100), 2–GaSb(111)A, 3 – GaSb(111)B.

In this study such method as purification of the materials by rare-earth elements was applied to decrease the carrier density in the GaInAsSb. The rare-earth element holmium of 3N purity was introduced into the melt. The Ho content in the liquid phase was varied from

0.003 to 0.12 at. %. We have found that the hole density in the GaInAsSb material fall by two orders of magnitude (from $(1-3)\times 10^{17}$ to $(2-4)\times 10^{15}\text{cm}^{-3}$, $T=80\text{ K}$) with increasing the Ho content in the melt up to 0.01 at. %. At that, the carrier mobility rises to $2000\text{ cm}^2/\text{V}\cdot\text{s}$. The concentration of shallow acceptors with the activation energy of $E=0.008-0.014\text{ eV}$ decreases. We believe that purification effect is due to the fact that the rare-earth element introduced into the melt actively interacts with residual impurities with the formation of high-melting compounds which precipitate in the melt and are not incorporated into the grown layer [11,12]. The main restrictions on introducing rare-earth atoms into the crystal lattices of III-V materials are the high chemical reactivity and the low solid solubility [13].

The photodiodes with the GaInAsSb active area grown on GaSb(100) substrate demonstrated such threshold as $\lambda_{\text{th}}=2.4\text{ }\mu\text{m}$. However, based on the GaInAsSb solid solutions with composition near the miscibility gap boundary the long-wavelength photodiodes with $\lambda_{\text{th}}=2.55\text{ }\mu\text{m}$ were created on GaSb(111)B substrate. Cross-sectional SEM micrograph of photodiode GaSb/GaInAsSb/GaAlAsSb heterostructure is presented in Fig.2. The monochromatic current sensitivity for the fabricated photodiodes at the $\lambda_{\text{max}}=2.2-2.4\text{ }\mu\text{m}$ is $S_{\lambda}=1.1-1.2\text{ A/W}$, which corresponds to a quantum efficiency of 0.6-0.7 without anti-reflection coatings. The estimated temperature coefficient of the $\lambda_{50\%}$ shift is $1.6\text{ nm}\times\text{K}^{-1}$. The capacitance of the photodiode with the sensitive element diameter of 1.0 mm is 450 pF at the zero bias.

4. CONCLUSIONS

High crystal perfection has been reached for the epitaxial layers of GaInAsSb solid solutions obtained at $T=600^{\circ}\text{C}$ near the miscibility gap boundary. The use of a GaSb(111)B substrate led to the increase of the indium content in solid phase to 0.24. As a result, long-wavelength GaInAsSb-based photodiodes with the photosensitivity threshold of $2.55\text{ }\mu\text{m}$ have been

developed. The proposed technique is to show a great potential for creating the GaInAsSb-based thermophotovoltaic devices and optical sensors for 1.8-3.0 μm spectral range.

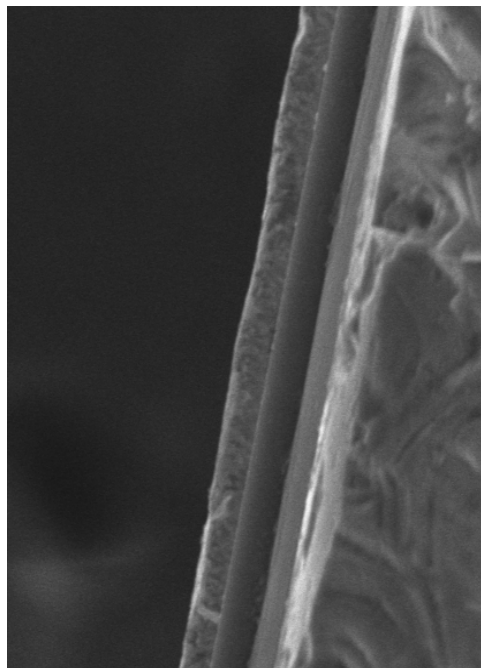


Fig.2. Cross-sectional SEM micrograph of GaSb/GaInAsSb/GaAlAsSb heterostructure. The $2\text{ }\mu\text{m}$ -thick GaInAsSb active layer is dark in the center between GaAlAsSb layer and GaSb substrate.

5. ACKNOWLEDGMENTS.

The work is supported in part by the Russian Foundation of Basic Research (RFBR) through Grant No. 09-08-91224-st, and of the Scientific and Technological Research Council of Turkey (TÜBİTAK) under Grant No: 108T325.

- [1]. O. Cathabard, R. Teissier, J. Devenson, J. C. Moreno, and A. N. Baranov Quantum cascade lasers emitting near $2.6\text{ }\mu\text{m}$, Appl. Phys. Lett. 96, (2010) (141110-1-141110-3).
- [2]. M.P. Mikhailova, I.A. Andreev, E.V. Kunitsyna, and Yu.P. Yakovlev, Sensitivity of a receiver using GaInAsSb/AlGaAsSb SAM avalanche photodiode for long-wavelength optical communication systems in the mid-infrared spectral range, Proc. SPIE 7355 (2009) (735511-1-735511-11).
- [3]. V.M. Andreev "Solar cells for TPV converters" in Next Generation Photovoltaics, Ed. by A. Marti, A. Luque, Inst. Phys. Publish., Bristol, 2003, 246.
- [4]. M.G. Mauk, Survey of Thermophotovoltaic (TPV) Devices, in: A. Krier (Ed.), Mid-infrared Semiconductor Optoelectronics, Springer Series in Optical Sciences, Springer-Verlag, London, 2006, pp. 673-738.
- [5]. M. Ahmetoglu (Afrailov), B. Kucur, I.A. Andreev, E.V. Kunitsyna, M.P. Mikhailova, Yu.P. Yakovlev, Electrical and optical properties of the GaInAsSb-based heterojunctions for infrared photodiode and thermophotovoltaic cell application, Infrared Physics & Technology 53 (2010) 399-403.
- [6]. A.Krier, X.L. Xuang and Z. Labadi, "Liquid Phase Epitaxy of Quantum wells and Quantum dots" in Liquid Phase Epitaxy of Electronic, Optical and Optoelectronic Materials, Ed. By Peter Capper, Michael Mauk, Publish.: Wiley-Interscience, 2007, 227-256.
- [7]. A.N. Baranov, A.A. Guseynov, A.M. Litvak, A.A. Popov, N.A. Charikov, V.V. Sherstnev, and Yu.P. Yakovlev, Obtaining the GaInAsSb near the immiscibility gap boundary, Tech. Phys. Lett. 16 (1990) 177-180.

- [8]. *A.M. Litvak and N.A. Charykov*, New thermodynamical method for calculation of melt-solid phase diagrams, *Zh. Fiz. Khim*, 64, 2331 (1990).
- [9]. *N.A. Charykov, V.V. Sherstnev, and A. Krier*, General theory of multi-phase melt crystallization, *J. Cryst. Growth*, 234 (2002) 762-772.
- [10]. *Baranov A.N., Kuznetsov V.V., Rubtsov E.R., Yakovlev, Guseynov A.A.* Kinetics Of GaInAsSb crystallization from liquid phase, *Zh. Fiz. Khim*, 65, 3228 (1991).
- [11]. *A.T. Gorelenok, A.V. Kamanin, and N.M. Shmidt*, Rare-Earth Elements in the Technology of III-V Compounds and Devices Based on These Compounds, *Semiconductors* 37 (2003), 894-914.
- [12]. *E.V. Kunitsyna, I.A. Andreev, V.V. Sherstnev, T.V. L'vova, M.P. Mikhailova, Yu.P. Yakovlev, M. Ahmetoglu (Afrailov), G. Kaynak, O. Gurler*, Narrow gap III-V materials for infrared photodiodes and thermophotovoltaic cells, *Optical Materials* 32 (2010) 1573-1577.
- [13]. *Jan Grym, O. Prochazkova, J. Zavadil and K. Zdansky* "Role of rare-earth elements in the technology of III-V semiconductors prepared by liquid phase epitaxy" in *Semiconductor Technologies*, Ed. By Jan Grym. Publish.: INTECH, Vukovar, Croatia, 2010, 295-320.

PHONON SCATTERING MECHANISMS IN $\text{Ga}_x\text{In}_{1-x}\text{As}$ SINGLE CRYSTALS

M.I.ALIYEV, I.X.MAMMADOV¹, D.H.ARASLY, R.N.RAHIMOV, A.A.KHALILOVA

Institute of Physics of the Azerbaijan National Academy of Sciences,

33 H.Javid, Az-1143, Baku, Azerbaijan

E-mail: rashad@physics.ab.az ; phone: +(99412)4393315; Fax: +(99412) 447 04 56;

¹*National Academy of Aviation, Bina, Baku, Azerbaijan*

The thermal conductivity of $\text{Ga}_x\text{In}_{1-x}\text{As}$ ($0 \leq x \leq 0.08$ and $0.97 \leq x \leq 1$) single crystals in the temperature range 80-300K has been investigated. Callaway and Holland's model has used to analyze for received experimental results taking into account of all scattering mechanisms. It has been shown that the contribution of transverse phonons to heat transfer in the investigated temperature range is essential.

1. INTRODUCTION

GaAs and InAs binary compounds and ternary compounds on their basis are important materials for ultra speed devices of electronics and optoelectronics. At creation of devices the role of thermal conductivity of materials for computing of their thermal conditions and designing is significance. In literature, experimental data for thermal conductivity of $\text{Ga}_x\text{In}_{1-x}\text{As}$ solid solution are sufficiently scant. In Refs. [1, 2] it was investigated the thermal conductivity of polycrystalline $\text{Ga}_x\text{In}_{1-x}\text{As}$ with compositions of $0.12 < x < 0.85$ at room temperature and with compositions of $0.3 < x < 0.7$ above room temperature. Ohmer et al. [3] measured the thermal conductivity of GaAs-InAs alloys for the concentration of InAs less than 1 % at room temperature. Arasly et al. investigated the thermal conductivity of the $\text{Ga}_x\text{In}_{1-x}\text{As}$ single crystals rich in InAs ($0 \leq x \leq 0.08$) in the temperature range of 300-700K [4] and 80-300K [5] and of single crystals rich in GaAs ($0.97 \leq x \leq 1$) in the temperature range of 80-300K [6]. It should be noted that $\text{Ga}_x\text{In}_{1-x}\text{As}$ solid solutions along with $\text{Ge}_{1-x}\text{Si}_x$ are convenient object for testing different models of the thermal conductivity. Experimental results of thermal conductivity of $\text{Ga}_x\text{In}_{1-x}\text{As}$ solid solutions from Refs.1-3 on the base of models proposed by Abeles, Adachi and Szmulowicz were discussed in Refs.7-9. Our experimental data from Ref.5 were used for examination of Adachi's model [10, 11]. The investigation of the temperature dependence of the thermal conductivity of these single crystals in the wide temperature range and analysis in the framework existing theory enable to determine the intensity of various phonon scattering mechanisms. In the present work results of the thermal conductivity study of $\text{In}_{1-x}\text{Ga}_x\text{As}$ single crystals rich in InAs ($0 \leq x \leq 0.08$) and GaAs ($0.97 \leq x \leq 1$) in the temperature range between of 80 and 300K have been presented.

2. EXPERIMENTAL

$\text{Ga}_x\text{In}_{1-x}\text{As}$ single crystals were grown by the Czochralski method. The samples have electron concentration of $(2 \div 4) \times 10^{17} \text{cm}^{-3}$ and dislocation density of $10^3 \div 10^4 \text{cm}^{-2}$. The thermal conductivity was measured by the stationary longitudinal heat flux method and was proved by the light flash heating method. The thermal conductivity of $\text{Ga}_x\text{In}_{1-x}\text{As}$ at room temperature versus the alloy composition is presented in Fig.1. The data of Abrahams et al. and Ohmer et al. from Ref.1 and 3 also is introduced in Fig.1.

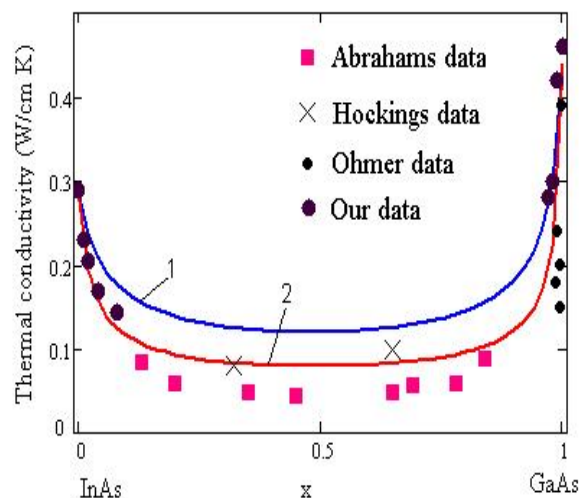


Fig.1. The thermal conductivity of $\text{Ga}_x\text{In}_{1-x}\text{As}$ at room temperature versus the alloy composition: curve 1 was calculated by Klemens [9] model; curve 2 was calculated by Abeles model [7].

In the Fig.2 the temperature dependence of thermal conductivity of $\text{Ga}_x\text{In}_{1-x}\text{As}$ single crystals is represented. It is evident that numerical value of the thermal conductivity with an increase in the content of the second component decreases and its temperature dependence weakens. The obvious dip within the narrow interval of 95 to 115K in the temperature dependence of the thermal conductivity is observed for the solid solution rich in InAs up to $x=0.04$, but with $x>0.04$ it disappears. On the other hand, the obvious dip in the solid solutions, rich in gallium arsenide in the temperature dependence was not observed.

3. DISCUSSION

The electron share of the thermal conductivity (K_{el}) counted in accordance with the Widemann-Franz formula is insignificant and the behaviour in the thermal conductivity is related with phonon processes. The phonon thermal conductivity has been analyzed on the base of well known Callaway model [12] considering different phonon scattering processes:

$$K = \frac{k}{2\pi^2 v} \left(\frac{kT}{\hbar} \right)^3 \int_0^{\theta/T} \frac{\tau_c z^4 e^z}{(e^z - 1)^2} dz, \quad (1)$$

where $z = \frac{\hbar\omega}{kT}$, \hbar is the Planck constant, k is the Boltzmann constant, v is the sound velocity in crystal, θ is the Debye temperature; ω is the phonon frequency, τ_c is the combined relaxation time which expressed as

$$\tau_c^{-1} = \tau_R^{-1} + \tau_N^{-1}, \quad \tau_R^{-1} = \sum_i \tau_i^{-1} \quad (2)$$

where τ_N is the relaxation time of normal process, τ_R is the relaxation time of all resistive processes including the crystal boundary scattering ($\tau_l^{-1} = v/l$, l is size of the sample), the three-phonon Umklapp process, the Rayleigh scattering by point defects and the phonon resonance scattering.

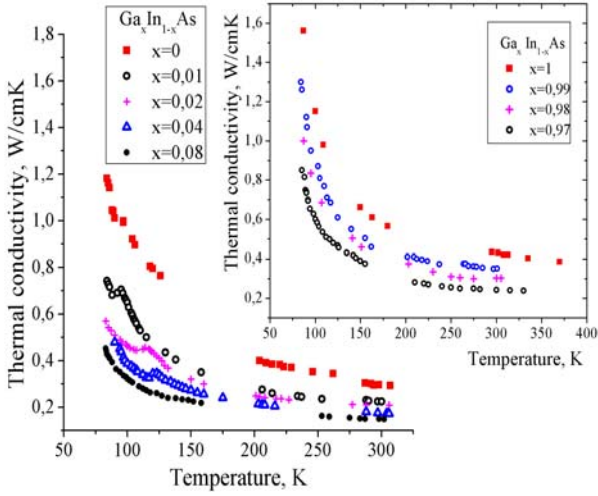


Fig.2. The temperature dependence of thermal conductivity of $Ga_xIn_{1-x}As$ single crystals.

Despite the fact that in Callaway's model [12] nonlinearity of the phonon spectrum dispersion was not taken into account and phonon-phonon interaction for the longitudinal and transverse phonons is not distinguished, this model in the literature has been widely used for processing of the thermal conductivity experimental data.

For the quantitative estimation of processes of phonon scattering by point defects we have first computed the thermal conductivity of $Ga_xIn_{1-x}As$ crystals by formula (1) that takes into account of three-phonon Umklapp and Rayleigh scattering by point defects. In this case the rate of scattering by point defects was determined by Klemens formula [9]. In computations of the disorder parameter the local variations of both densities and elastic properties of defect surroundings, where In and Ga atoms are mutually substituted in $Ga_xIn_{1-x}As$ solid solution, have also been taken into account and their contributions were significant. As seen from Fig.1 (curve1) the simplified Callaway's model does not described the experimental results. To all appearance, the significant quantitative distinction between of calculation and experimental data is connecting with the fact that in expression (2) normal phonon processes are not taken into account.

It is known that three-normal phonon processes themselves don't result directly in finite quantity of the thermal resistivity. N-processes can determine of the

structure of the stationary nonequilibrium phonon distribution. As a result, their role turns out essential in the total momentum relaxation of the phonon systems and renders the important influence on the thermal conductivity magnitude.

The high frequency phonons are strongly scattered by point defects in solid solutions and the interaction between of longitudinal phonons with retention of quasi-impulse, may influence the lattice thermal conductivity at high temperatures ($T > \theta$).

The influence of N-processes on the thermal conductivity at $T > \theta$ in alloys is considered in Refs. 7 and 9. Abeles [7] have proposed a phenomenological approach to a lattice thermal conductivity of disordered semiconductor alloys at high temperatures. His theory was based on the Klemens and Callaway models and successfully used for $In_{1-x}Ga_xAs$ alloys. We calculated the phonon thermal conductivity by the formula (1), where the temperature and frequency dependences of the relaxation time for three-phonon N- and U- processes are taken the same, namely, $\tau_N^{-1} = B_N \omega^2 T$ and $\tau_U^{-1} = B_U \omega^2 T$, the relaxation time for the scattering by point defects is $\tau_d^{-1} = A \omega^4$. For describing the anomaly in the temperature dependence of the thermal conductivity, we include the relaxation time of acoustic phonon resonance scattering into the expression for the resistive relaxation time:

$$\tau_r^{-1} = R \frac{\omega^2 T}{(\omega^2 - \omega_R^2)^2} \quad (3)$$

The computations display that (Fig. 1, curve 2) the normal processes play an essential role in the lattice thermal conductivity of the $In_{1-x}Ga_xAs$ solid solutions and their intensity is greater than that of umklapp processes: $B_N/B_U=2$.

It is known that in the crystals with strong anisotropic phonon spectrum due to differences in dispersion of longitudinal and transverse phonon branch of spectrum, the expressions for the relaxation time and the velocity of sound are essentially differed for phonons at various polarizations. In Ref.13 the total expression for $K(T)$ in the framework Callaway's theory was proposed, which the partial contributions from longitudinal and transverse modes taken into account. Since the acoustic mode of III-V group compounds have the strong dispersion and Debye temperatures for longitudinal and transverse phonon are essentially differed, we also carry out the study of the phonon thermal conductivity in the framework of Holland's two-parameter approximation [14]. At that phonon thermal conductivity is expressed as

$$K = K_L + K_T, \quad (4)$$

where the index l and t is indicate the longitudinal and the transverse phonon contributions to the thermal conductivity, respectively. These components are described by following expressions [12, 13]:

$$K_i = \gamma_i \frac{k^4 T^3}{2 \pi^2 \hbar^3 v_i} \int_0^{\theta_i / T} \tau_{ci} \frac{z^4 e^z}{(e^z - 1)^2} dz \quad (5)$$

where $i=L, T$; γ_i is equal to 1/3 and 2/3 for the longitudinal and the transverse mode, respectively; $z = \frac{\hbar \omega_i}{kT}$, ω_i is the maximum frequency of longitudinal and transverse acoustic phonons at the boundary Brillouin zone; v_i is the group velocity of sound of the corresponding phonons; $v_B^{-1} = \frac{1}{3} [v_l^{-1} + 2v_t^{-1}]$, τ_{ci} is the total relaxation time of the probable scattering mechanism of phonons:

$$\tau_{ci}^{-1}(\omega_i) = \sum_i \tau_i^{-1}(\omega_i) \quad (6)$$

The Rayleigh scattering of phonons, umklapp and normal three phonon processes and phonon resonance scattering we take into account in calculations of the thermal conductivity.

Relaxation expression for three phonon umklapp and normal processes for longitudinal and transverse phonons are differed in the various models. Holland's model is valid in the case when the phonons relaxation frequency for each branch in the phonon spectrum is less than the resistive relaxation frequencies of phonons. According to Ref.13 in this case the relaxation time of three-phonon processes for the longitudinal and transverse phonons takes the following form:

$$\left. \begin{aligned} 1/\tau_L &= B_L^{U,N} \omega^2 T^3 \\ 1/\tau_T &= B_T^N \omega T^4 + B_T^U \frac{\omega^2}{sh(\hbar \omega / kT)} \end{aligned} \right\} \quad (7)$$

In Fig.3 the experimental data (points) with comparison of values of the thermal conductivity K (dashed curve) computed by Formulas (1)-(3) and K_L (dash dot curve); K_T (dotted curve); K_L+K_T (solid curve) by Formulas (4)-(7) for $\text{Ga}_x\text{In}_{1-x}\text{As}$ alloys with $x=0.04$ (a) and $x=0.97$ (b) are plotted.

The intensity of phonon scattering processes is determined by the fitting calculated curves to experimental data.

Approximation parameters are given in Table 1. The sound speed and frequencies data of longitudinal and transverse phonons for the solid solutions were approximated by linear extrapolation on the base of data for the initial compounds.

As seen from figures, at temperatures higher than 200K the contribution of transverse acoustic phonons in the thermal conductivity are main and the Herring's mechanism, i.e. the interaction of different polarized phonons in N- processes prevails. .

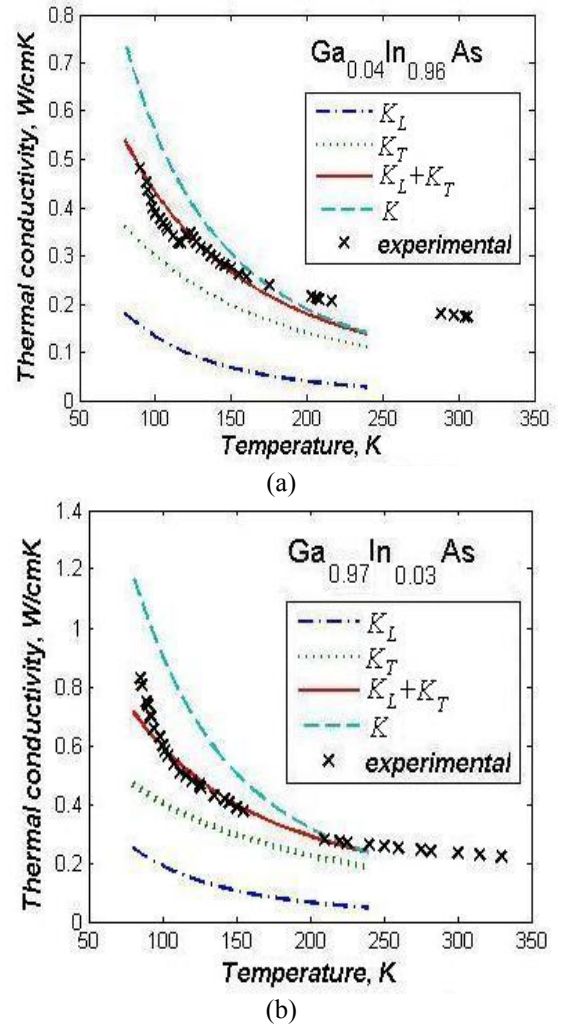


Fig.3. The thermal conductivity of $\text{Ga}_{0.04}\text{In}_{0.96}\text{As}$ (a) and $\text{Ga}_{0.97}\text{In}_{0.03}\text{As}$ (b) alloys; cross is experimental data, K (dashed curve) computed by Formulas (1)-(3) and K_L (dash dot curve), K_T (dotted curve), K_L+K_T (solid curve) by formulas (4)-(7).

Table 1. Parameters used at computation of the phonon thermal conductivity of $\text{Ga}_x\text{In}_{1-x}\text{As}$ with $x=0; 0.04; 0.97$ and 1 (* data was taken from Ref. [15], ** data was taken from Ref. [16]).

	InAs^*	GaAs^{**}	$x=0.04$	$x=0.97$
θ (K)	280	370	284	367
θ_L (K)	187	328	192	323
θ_T (K)	80	114	81	112
v (cm/s) $\times 10^3$	3.09	3.8	3.12	3.78
V_L (cm/s) $\times 10^5$	4.34	5.24	4.38	5.21
v_T (cm/s) $\times 10^5$	2.1	2.48	2.12	2.47
A (s^3) $\times 10^{43}$			7	2.7
$B_L \times 10^{23}$	1.7	1.75	1.2	0.6
$B_T^U \times 10^{18}$	6.5	6.01	9	12
B_N/B_U			2	2
ω_R (s^{-1}) $\times 10^{13}$			1.54	1.4
v/L (s^{-1}) $\times 10^{-6}$			6	6
R ($s^{-3}K^{-2}$) $\times 10^{-29}$			6	5

-
- [1]. *M.S. Abrahams, R.Braunstein, F.D.Rossi* J.Phys.Chem.Solids, 1959, 10, 204.
- [2]. *E.F.Hockings, I.Kudman, T.E.Seidel, E.F.Steigmeier*, J.Appl.Phys., 1966,17, No7, 2879.
- [3]. *C.Ohmer, W.C.Mitchel, G.A.Graves, D.T.Holmes, H.Kuwamoto and P.W.Yu*, J.Appl.Phys., 1988, 64, 2775.
- [4]. *M.I.Aliev, D.H.Arasly, R.E Guseynov*, Fizika i Tekhnika Poluprovodnikov (Semiconductors), 1973, 7, 1846.
- [5]. *D.H.Arasly, R.N.Ragimov, M.I.Aliev*, Sov. Phys. Semiconductor, 1990, 24, 225.
- [6]. *М.И.Алиев, Д.Г.Араслы, Р.Н.Рагимов, А.А.Халилова, И.Х.Мамедов* Fizika 2009,15,2,35.
- [7]. *B.Abeles*, Phys.Rev., 1963 131, 1906.
- [8]. *S.Adachi* J.Appl.Phys., 1983, 54, 1844.
- [9]. *F.Szmulowicz, F.L.Madarasz, P.G.Klemens, J.Diller*, J.Appl.Phys., 1989, 66, 252.
- [10]. *Adachi*, Physical Properties of III-V Semiconductor compounds. Wiley-Interscience, New York, 1992, 296p.
- [11]. *S.Adachi*, J.Appl.Phys. 2007, 102, p 063502(1 -7).
- [12]. *J.Callaway*, Phys.Rev. 1959, 113, 1046-1051.
- [13]. *M.A. Asen-Palmer, N. Bartcovsky, E. Gmlin, M. Cardona*. Phys.Rev.B, 1997, 56, 9431.
- [14]. *M.G.Holland*, Phys.Rev., 1964, 134, 2, A471.
- [15]. *G.Le Guillou and H. J. Albany*, Phys. Rev. B 5, 1972, 2301–2308.
- [16]. *C. M. Bhandari and G. S. Verma* Phys. Rev. ,1965, 140, A2101–A2104.

TERMODYNAMICAL INVESTIGATION OF Yb-S SYSTEM BY EMF METHOD

M.A. MAKHMUDOVA, A.S. ABBASOV

H.B. Abdullayev Institute of Physics of Azerbaijan NAS, Baku, AZ-1141, G. Javid ave., 33

S.Z. IMAMALIYEVA, M.B. BABANLI

Baku State University, Baku, AZ-1148, Z. Khalilov str., 23

The results of thermodynamical investigation of Yb-S system by EMF method are presented in the paper. The relative partial molar functions of ytterbium in alloys and standard integral thermodynamical functions ($\Delta G_{f,298}^0$, $\Delta H_{f,298}^0$, S_{298}^0) of Yb_2S_5 , Yb_2S_3 , Yb_3S_4 and YbS compounds are calculated by combining of measurement results of EMF concentration chains of two types.

The rare-earth element chalcogenides and alloys on their base are perspective functional materials. Many of them have the luminescent properties and photosensitivity. The memory switching effects are found in some of this type compounds. Some of them are used at the production of vacuum photoelements and etc [1,2].

Yb-S system is characterized by formation of Yb_3S_5 , Yb_2S_3 , Yb_3S_4 and YbS [3]. However, the thermodynamical properties of these compounds necessary for development and optimization of the methods of their directed synthesis and growing up in the form of single crystals haven't investigated yet. The standard enthalpy formations

$$(\Delta H_{f,298}^0 = -410 \pm 25 \text{ kJ/mol})$$

is obtained only for YbS [4]. Some thermodynamic functions of YbS and Yb_2S_3 are estimated by means of comparable analysis with thermodynamic sulfide functions of other rare-earth elements in work [5].

In the given paper the investigation results of solid-phase equilibriums in Yb-S system and thermodynamical properties of ytterbium sulfides by EMF method are presented.

EXPERIMENTS AND THEIR RESULTS

The alloys of Yb-Se system are synthesized by direct interaction of stoichiometric quantities of initial simple substances in degasified ($\sim 10^{-2}$ Pa) quartz ampoules at 450-500K. After interaction of the main mass of sulfur the furnace temperature is increased up to 1100K at which the ampoule is kept during twenty hours and further it is treated by continuous graduated annealing at 1000K (100h) and 400K (500h).

For carrying out of experiments the concentration chains of the following types are constructed as in [5]:



The left electrode of the chain (1) is prepared by fixing of metallic ytterbium on molybdenum lead and right electrodes are prepared by pressing of equilibrium alloys Yb-S made in powder form on leads in the form of cylindric tablets having 0,5 gr mass.

The sweet solution KCl with $YbCl_3$ addition is used as electrolyte. Taking under consideration the inadmissibility of the presence of damp and oxygen in electrolyte the glycerol (ЧДА mark) is thoroughly dewatered and degassed by evacuation at temperature ~ 450 K, the waterless, chemically pure KCl and $YbCl_3$ are used.

The techniques of gathering of electrochemical cells

and EMF measurements are described in detail in [6]. The measurements of EMF by (2) type are carried out by usual compensation method with the help of digital voltmeter B-7-27 in 300-380K interval.

However, EMF measurements show the nonequilibrium of chains by (1) type. In measurement beginning during several hours EMF values strongly decrease up to 500-800mV in the comparison with initial ones (~ 1000 - 1500 mV). Though these values are reproducible, they can't be considered as equilibrium ones, so according to previous thermodynamic calculations, they were less than expectable ones in 2-3 times.

Taking into account the above mentioned, the experiments are carried out in two stages. Firstly the concentration chains by the following type:



are constructed.

In the chains of (2) types the ytterbium monosulfide with some sulfur excess (compound $YbS_{1,01}$) is used as left electrode. The equilibrium alloys with different compositions from YbS-S region are used as right electrodes.

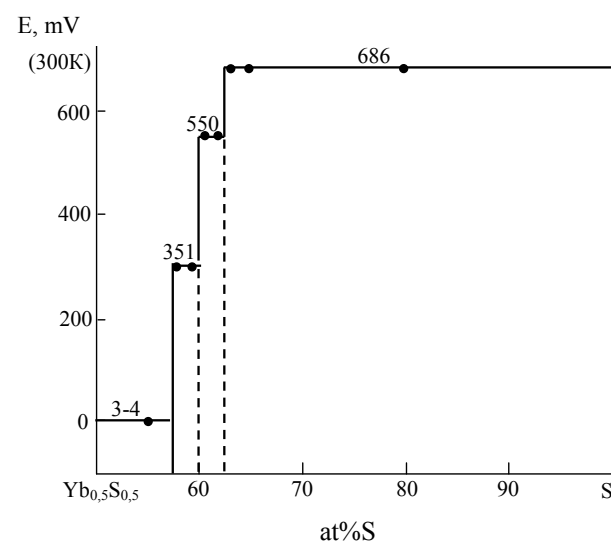


Fig. Dependences of EMF chains of type (2) on the composition in YbS-S subsystem

EMF measurements of chains by (2) type lead to reproducible results. The character of concentration dependence of EMF in YbS-S composition region at

300K (fig) is in total correspondence with phase diagram [3]; EMF values are constant ones in two-phase regions and change spasmodically at the transformation from one phase region into other one, i.e. at stoichiometric compositions of ytterbium sulfides.

The analysis of EMF temperature dependences of chains by (2) type shows their linearity.

The treatment of given EFM measurements with the help of computer program "Microsoft Office Excel 2003" by the method of least squares [7] lead to obtaining of linear equations presented in the table 1 in the following form:

$$E = a + bT \pm t \left[\frac{\delta_E^2}{n} + \delta_b^2 (T - \bar{T})^2 \right]^{1/2}, \quad (3)$$

recommended in [8]. Here \bar{T} is average temperature, K; δ_E^2 and δ_b^2 are dispersions of separate values of EFM and b constant, n is couple number of E and T values; t is Student criteria. $t \leq 2$ at confidence band 95% and $n \geq 2$ [7].

Table 1

Temperature dependences of EFM chains of (1) and (2) types for Yb-S ($T=300-380K$) alloys

№	Concentration chain	Phase region	$E, mB = a + bT \pm t\delta_E(T)$
1	(2)	Yb ₃ S ₅ +S	$649,8 + 0,1201T \pm 2 \left[\frac{0,34}{22} + 3,4 \cdot 10^{-5} (T - 339,4)^2 \right]^{1/2}$
2	(2)	Yb ₂ S ₃ +Yb ₃ S ₅	$572,9 + 0,1834T \pm 2 \left[\frac{0,32}{22} + 3,2 \cdot 10^{-5} (T - 338,8)^2 \right]^{1/2}$
3	(2)	Yb ₃ S ₄ +Yb ₂ S ₃	$310,3 + 0,1364T \pm 2 \left[\frac{0,36}{22} + 3,2 \cdot 10^{-5} (T - 336,8)^2 \right]^{1/2}$
4	(1)	YbS+Yb ₃ S ₄	$935,9 - 0,1785T \pm 2 \left[\frac{0,81}{17} + 10^{-4} (T - 337,9)^2 \right]^{1/2}$

The relative partial thermodynamical ytterbium functions (PThF) in YbS (table 2) and "quasicomponent" YbS from equations 1 and 2 are calculated. It is obvious that the last ones present themselves the difference of corresponding partial molar functions of ytterbium in right and left electrodes of the chains of (2) type:

$$\Delta \bar{Z}_{YbS} = \Delta \bar{Z}_{Yb}(\text{alloy of YbS-S region}) - \Delta \bar{Z}_{Yb}(YbS)$$

where $\Delta Z = \bar{\Delta G}, \bar{\Delta H}, \bar{\Delta S}$.

Table 2

Partial thermodynamical functions of "quasicomponent" of YbS in YbS-S alloys at 298K

Phase region	$-\Delta \bar{G}^*$	$-\Delta \bar{H}^*$	$\Delta \bar{S}^*$
	kJ/mol		J/(mol·K)
Yb ₃ S ₅ +S	198,46±0,15	188,1±1,2	34,8±3,4
Yb ₂ S ₃ +Yb ₃ S ₅	181,67±0,14	165,8±1,1	53,1±3,3
Yb ₃ S ₄ +Yb ₂ S ₃	101,57±0,14	89,8±1,1	39,5±3,3

That's why the corresponding data for YbS which are obtained from EMF measurement data of chains by (2) type by EMF rapid fixation method [6] are necessary for PThF ytterbium calculation.

From obtained equation of EMF temperature dependence (table 1) PThF ytterbium in YbS (table 3, phase region YbS+Yb₃S₄) are calculated.

The substance of this method is in the fact that the

left electrode is not in the cell with right electrode up to the moment of measurement, but in other vessel with the electrolyte at the same temperature.

EMF measurements is carried out in the moment of introduction of left electrode in electrochemical system with right electrode and the maximum value of EMF is fixed. These tests are carried out in the box filled by nitrogen at different temperatures in 300-380K interval.

$\Delta \bar{G}_{Yb}$ can be defined by EMF rapid fixation method for all alloys. However, taking into consideration the difficultness of experiments by means of EMF rapid fixation method and reliability of reversible chains of (2) type, we prefer the above mentioned combined measurement technique of EMF.

PThF ytterbium in alloys YbS-S (table 3) are calculated by summation of data from table 2 with PThF ytterbium for YbS.

From table 3 it follows that ytterbium partial entropy essentially decreases from Yb₃S₅ up to YbS. This well coincides with crystallographic data of ytterbium sulfides, according to which in this direction the crystal lattice symmetry of these compounds increases [1,3].

According to phase diagram, the partial molar functions of ytterbium are thermodynamical characteristics of the certain reactions of potential-formation (substance state is crystalline one) (table 3).

That's why the standard thermodynamical functions of ytterbium sulfide formation can be calculated by means of these equations.

Table 3

Ytterbium partial thermodynamic functions Yb-S alloys at 298K and the potential formatting reactions corresponding to them

Phase region	$-\Delta G_{Yb}$	$-\Delta \bar{H}_{Yb}$	$-\Delta S_{Yb}$	Potential formation reaction
	kJ/mol		J/(mol·K)	
Yb ₃ S ₅ +S	454,0±0,5	449,0±3,2	20,1±9,4	Yb+1,5S=0,333Yb ₃ S ₅
Yb ₂ S ₃ +Yb ₃ S ₅	437,2±0,4	436,7±3,1	1,7±9,2	Yb+3Yb ₃ S ₅ =5Yb ₂ S ₃
Yb ₃ S ₄ +Yb ₂ S ₃	457,1±0,4	360,7±3,1	-12,1±9,2	Yb+4Yb ₂ S ₃ =3Yb ₃ S ₄
YbS+Yb ₃ S ₄	255,5±0,3	270,9±2,0	-51,7±5,9	Yb+Yb ₃ S ₄ =4YbS

Table 4

Standard integral thermodynamic functions of ytterbium sulfides

For example, for thermodynamic formation function of Yb₃S₅ and Yb₂S₃ compounds the following relations take place:

$$\Delta Z_{Yb_3S_5}^0 = 3\Delta \bar{Z}_{Yb}$$

$$\Delta Z_{Yb_2S_3}^0 = 0,2\Delta \bar{Z}_{Yb} + 0,6\Delta Z_{Yb_3S_5}^0$$

for standard entropies:

$$S_{Yb_3S_5}^0 = 3(\Delta \bar{S}_{Yb} + S_{Yb}^0)$$

$$S_{Yb_2S_3}^0 = 0,2(\Delta \bar{S}_{Yb} + S_{Yb}^0) + 0,6S_{Yb_3S_5}^0$$

Besides the own experimental data (table 3) the reference data on standard entropies of elementary ytterbium and sulfur from ref.[4,9] are used for calculation of standard entropies

The obtained results are presented in table 4. The errors are found by the method of error accumulation.

Phase	$-\Delta G_{298}^0$	$-\Delta H_{298}^0$	S_{298}^0
	kJ/mol		J/(mol·K)
Yb ₃ S ₅	1362±2	1347±10	289±28
Yb ₂ S ₃	905±2 1153 [5]	896±6 1172 [5]	186±17 161 [5]
Yb ₃ S ₄	1326±3	1340±11	260±26
YbS	395±1 444 [5]	403±5 452 [5] 410±25 [4]	65±8 69 [5]

In table 4 the scientific literature data are presented. As it is seen, obtained by us values of standard thermodynamic formation functions and standard entropy well coincide with data [4,5] and corresponding functions of Yb₂S₃ essentially differ from given ones in [5].

- | | |
|---|---|
| <p>[1] <i>E.I. Yarembash, A.A. Eliseev.</i> Halkogenidi redkozemelnikh elementov. M.: Nauka, 1975. (in Russian).</p> <p>[2] <i>P.G. Rustamov, O.M. Aliyev, A.V. Eynullayev, I.P. Aliyev.</i> Halkolantanati redkikh elementov. M.:Nauka, 1989, 284s. (in Russian).</p> <p>[3] Binary alloys phase diagrams, Ed. <i>T.B.Massalski</i>, second edition. ASM International, Materials park, Ohio, 1990, v.2, p.1163-1166</p> <p>[4] <i>F.M. Mustafayev, T.X. Azizov, A.S. Abbasov, I.Ya. Aliyev.</i> Termodinamicheskiye svoystva halkogenidov redkozemelnikh elementov. In-t Fizizki AN Azerb. SSR, Preprint №50, Baku, 1977, 10.c. (in Russian).</p> | <p>[5] <i>M.A. Makhmudova, S.Z. Imamaliyeva, A.S. Abbasov, M.B. Babanli.</i> AzTU-nun Elmi əsərləri. Fundamental elmlər, 2010, t.IX (30), №1, c.</p> <p>[6] <i>M.B. Babanli, Yu.A. Yusibov, V.T. Abishev.</i> Metod EDS v termodinamike slojnikh poluprovodnikov veshshestv. Baku: BGU, 1992, 317 s. (in Russian).</p> <p>[7] <i>A.Gordon, R.Ford.</i> Sputnik khimika. M.: Mir., 1976, 541s.</p> <p>[8] <i>A.N. Kornilov, L.B. Stepina, V.A. Sokolov.</i> J. Fiz.khimii, 1972, t.46, №11, c. 2974-2979. (in Russian).</p> <p>[9] <i>O. Kubaschewski, S.V. Alcock, P.J. Spencer.</i> Materials Thermochemistry. Pergamon Press, Oxford, 1993, 350 p</p> |
|---|---|

THE LONGITUDINAL POLARIZATION OF B-BARYON IN SEMI-INCLUSIVE REACTIONS

S.K. ABDULLAYEV, A.I. MUKHTAROV, M.Sh.GOJAYEV

Baku State University, AZ-1148, Z.Halilov str., 23

Semi-inclusive reactions $e^\mp N \Rightarrow e^\mp BX$, $\nu_\mu(\bar{\nu}_\mu)N \Rightarrow \nu_\mu(\bar{\nu}_\mu)BX$, $\nu_\mu(\bar{\nu}_\mu)N \Rightarrow \mu^-(\mu^+)BX$, $\mu^-(\mu^+)(\lambda)N \Rightarrow \nu_\mu(\bar{\nu}_\mu)BX$ are studies in framework of standart model. The expressions for longitudinal polarization of B-baryon are obtained and polarization dependence on kinematic variables x , y , and z is investigated.

1. INTRODUCTION

High energy experiment with polarized beams and targets has opened a new window for revealing QCD dynamics and hadron structures. Ongoing RHIC-SPIN, HERMES and COMPASS experiments are going to provide us with a variety of data disclosing spin distribution inside the nucleon. The Electron Ion Collider (EIC) at BNL is expected to be a more powerful and sensitive tool for the QCD spin physics. In this paper, we study the longitudinally polarized baryons production in polarized semi-inclusive deep inelastic scattering (DIS) off nucleon (they are intensive investigated experimentally at the present time [1-5]):

$$\ell^-(\lambda) + N(h_N) \Rightarrow \ell^- + B(h_B) + X, \quad (1)$$

$$\ell^+(\lambda) + N(h_N) \Rightarrow \ell^+ + B(h_B) + X, \quad (2)$$

$$\nu_\mu + N(h_N) \Rightarrow \nu_\mu + B(h_B) + X, \quad (3)$$

$$\bar{\nu}_\mu + N(h_N) \Rightarrow \bar{\nu}_\mu + B(h_B) + X, \quad (4)$$

$$\nu_\mu + N(h_N) \Rightarrow \mu^- + B(h_B) + X, \quad (5)$$

$$\bar{\nu}_\mu + N(h_N) \Rightarrow \mu^+ + B(h_B) + X, \quad (6)$$

$$\mu^-(\lambda) + N(h_N) \Rightarrow \nu_\mu + B(h_B) + X, \quad (7)$$

$$\mu^+(\lambda) + N(h_N) \Rightarrow \bar{\nu}_\mu + B(h_B) + X, \quad (8)$$

where λ is the lepton spirality, h_N and h_B is the longitudinal polarization of nucleon-target and B -baryon.

The cross-section for the production of a B -baryon in the current fragmentation region are given by

$$\frac{d\sigma(\lambda; h_N; h_B)}{dx dy dz} = \sum_{q, h_q} f_{q(h_q)}^{N(h_N)}(x) \frac{d\hat{\sigma}}{dy} D_{q(h_q)}^{B(h_B)}(z), \quad (9)$$

where $f_{q(h_q)}^{N(h_N)}(x)$ is the distribution function of polarized quarks in the polarized nucleon, $D_{q(h_q)}^{B(h_B)}(z)$ is the fragmentation function of the quark to the detected B -baryon, $d\hat{\sigma}/dy$ is the elementary cross-section. The usual DIS variables x , y and Z defined as:

$$x = \frac{Q^2}{2P \cdot q}, \quad y = \frac{q \cdot P}{k \cdot P}, \quad z = \frac{P_B \cdot P}{P \cdot q},$$

where k , P , P_B and q are the four moments of the initial lepton, the target nucleon, the production B -baryon and the virtual bozon correspondingly.

In sections 2-4 we consider separately the different processes, and derive explicit expressions for the polarization of a final B -baryon in term of elementary dynamics, quark distribution and fragmentation functions.

2. THE POLARIZATION OF B-BARYON IN

$\ell^\mp N \Rightarrow \ell^\mp BX$ REACTION

Let us consider first the processes $\ell^\mp N \Rightarrow \ell^\mp BX$; for them, there exist two possible elementary contributions;

$$\ell^- + q \Rightarrow \ell^- + q, \quad \ell^- + \bar{q} \Rightarrow \ell^- + \bar{q}.$$

Taking under the considerations the exchange of γ and Z^0 , it is easy to make sure, that the spiralities of lepton and quark should be saved separately in subprocess $\ell^- + q \Rightarrow \ell^- + q$. That's why in this process is defined by only four spiral amplitudes F_{RR} , F_{LL} , F_{RL} and F_{LR} , which describe following reactions:

$$\ell_R^- + q_R \Rightarrow \ell_R^- + q_R,$$

$$\ell_L^- + q_L \Rightarrow \ell_L^- + q_L,$$

$$\ell_R^- + q_L \Rightarrow \ell_R^- + q_L,$$

$$\ell_L^- + q_R \Rightarrow \ell_L^- + q_R.$$

The spiral amplitudes in standard model (SM) are defined by expressions

$$F_{\alpha\beta} = \frac{Q_q}{xys} - \frac{g_\alpha^\ell g_\beta^q}{xys + M_z^2} (\alpha, \beta = L; R), \quad (10)$$

where M_z – is mass of Z^0 -bozon, S – is the square of total energy of (N -system in their c.m.s., Q_q – is quark electric charge q , g_R^ℓ and g_L^ℓ (g_R^q and g_L^q) – are right and left neutral weak charges of lepton (quark) with Z^0 -bozon:

$$g_R^\ell = \sqrt{\frac{x_w}{1-x_w}}; \quad g_L^\ell = \frac{-1/2 + x_w}{\sqrt{x_w(1-x_w)}}; \quad (11)$$

$$g_R^q = -Q_q \sqrt{\frac{x_W}{1-x_W}}; \quad g_L^q = \frac{T_3 - Q_q x_W}{\sqrt{x_W(1-x_W)}}. \quad \frac{d\hat{\sigma}}{dy}(\ell_L^- q_R \rightarrow \ell_L^- q_R) = 4\pi\alpha^2 x s (1-y)^2 F_{LR}^2.$$

Here $x_W = \sin^2 \theta_W$ – is the Weinberg's parameter, T_3 – is third projection of the weak isospin of quark q .

Let's reduce the subprocess cross-sections $\ell^- q \Rightarrow \ell^- q$ at the definite values of initial and final particles:

$$\frac{d\hat{\sigma}}{dy}(\ell_R^- q_R \rightarrow \ell_R^- q_R) = 4\pi\alpha^2 x s F_{RR}^2,$$

$$\frac{d\hat{\sigma}}{dy}(\ell_L^- q_L \rightarrow \ell_L^- q_L) = 4\pi\alpha^2 x s F_{LL}^2,$$

$$\frac{d\hat{\sigma}}{dy}(\ell_R^- q_L \rightarrow \ell_R^- q_L) = 4\pi\alpha^2 x s (1-y)^2 F_{RL}^2, \quad (12)$$

$$\frac{d\hat{\sigma}}{dy} = \pi\alpha^2 x s \{ (1+\lambda)(1+h_q)F_{RR}^2 + (1-\lambda)(1-h_q)F_{LL}^2 + (1-y)^2 [(1+\lambda)(1-h_q)F_{RL}^2 + (1-\lambda)(1+h_q)F_{LR}^2] \}, \quad (13)$$

where h_q is spirality of the initial quark.

The differential cross-section of subprocess $\ell^- \bar{q} \Rightarrow \ell^- \bar{q}$ can be obtained from (13) with the help of the elementary changes: $F_{RR} \Leftrightarrow F_{RL}, F_{LL} \Leftrightarrow F_{LR}$.

On the base of formulas (9) and (13), the expression for the differential cross-section of semi-inclusive reaction $\ell^- N \Rightarrow \ell^- BX$ has been obtained [6, 7]:

$$\begin{aligned} \frac{d\sigma^{(-)}(\lambda; h_N; h_B)}{dx dy dz} = & \pi\alpha^2 s x \sum_q \{ [f_q^N(x) D_q^B(z) + h_N h_B \Delta f_q^N(x) \Delta D_q^B(z)] f_1 + \\ & + [f_{\bar{q}}^N(x) D_{\bar{q}}^B(z) + h_N h_B \Delta f_{\bar{q}}^N(x) \Delta D_{\bar{q}}^B(z)] f_2 + \\ & + [h_N \Delta f_q^N(x) D_q^h(z) + h_B f_q^N(x) \Delta D_q^B(z)] f_3 + \\ & + [h_N \Delta f_{\bar{q}}^N(x) D_{\bar{q}}^h(z) + h_B f_{\bar{q}}^N(x) \Delta D_{\bar{q}}^B(z)] f_4 \}, \end{aligned} \quad (14)$$

where

$$\begin{aligned} f_1 &= (1+\lambda)[F_{RR}^2 \pm (1-y)^2 F_{RL}^2] \pm (1-\lambda)[F_{LL}^2 \pm (1-y)^2 F_{LR}^2], \\ f_2 &= (1+\lambda)[F_{RL}^2 \pm (1-y)^2 F_{RR}^2] \pm (1-\lambda)[F_{LR}^2 \pm (1-y)^2 F_{LL}^2], \\ f_q^N(x) &= f_{q(+1)}^{N(+1)}(x) + f_{q(-1)}^{N(+1)}(x), \quad \Delta f_q^N(x) = f_{q(+1)}^{N(+1)}(x) - f_{q(-1)}^{N(+1)}(x), \\ D_q^B(z) &= D_{q(+1)}^{B(+1)}(z) + D_{q(-1)}^{B(+1)}(z), \quad \Delta D_q^B(z) = D_{q(+1)}^{B(+1)}(z) - D_{q(-1)}^{B(+1)}(z), \end{aligned}$$

$f_q^N(x)$ and $D_q^B(z)$ are the usual function of quark distribution in nucleon and quark fragmentation function to B -baryon.

The differential cross-section of semi-inclusive DIS antilepton on nucleon $\ell^+ N \Rightarrow \ell^+ BX$ can be obtained from (14) with the help of the following exchanges:

$$F_{RR} \Leftrightarrow F_{LR}, \quad F_{RL} \Leftrightarrow F_{LL}.$$

We can now compute the longitudinal polarizations $P_B^{(-)}$ and $P_B^{(+)}$ for B -baryon produced in lepton and antilepton initiated DIS scattering processes:

$$P_B^{(\mp)} = \frac{d\sigma^{(\mp)}(\lambda; h_N; h_B = 1) - d\sigma^{(\mp)}(\lambda; h_N; h_B = -1)}{d\sigma^{(\mp)}(\lambda; h_N; h_B = 1) + d\sigma^{(\mp)}(\lambda; h_N; h_B = -1)}, \quad (15)$$

The polarization $P_B^{(\mp)}$ can be evaluated for any lepton (antilepton) and proton spin configuration. When both the lepton ℓ and proton p are longitudinally polarized the polarization becomes

$$P_B^{(-)}(\lambda; h_N) = \frac{\sum_q \{ f_q^N \Delta D_q^B f_3 + f_{\bar{q}}^N \Delta D_{\bar{q}}^B f_4 + h_N [\Delta f_q^N \Delta D_q^B f_1 + \Delta f_{\bar{q}}^N \Delta D_{\bar{q}}^B f_2] \}}{\sum_q \{ f_q^N \Delta D_q^B f_1 + f_{\bar{q}}^N D_{\bar{q}}^B f_2 + h_N [\Delta f_q^N \Delta D_q^B f_3 + \Delta f_{\bar{q}}^N D_{\bar{q}}^B f_4] \}}. \quad (16)$$

For unpolarized protons but longitudinally polarized leptons we have

$$P_B^{(-)}(\lambda = 1) = \frac{\sum_q \{ f_q^N \Delta D_q^B [F_{RR}^2 - (1-y)^2 F_{RL}^2] + f_{\bar{q}}^N \Delta D_{\bar{q}}^B [F_{RL}^2 - (1-y)^2 F_{RR}^2] \}}{\sum_q \{ f_q^N D_q^B [F_{RR}^2 + (1-y)^2 F_{RL}^2] + f_{\bar{q}}^N D_{\bar{q}}^B [F_{RL}^2 + (1-y)^2 F_{RR}^2] \}}, \quad (17)$$

$$P_B^{(-)}(\lambda = -1) = \frac{-\sum_q \{ f_q^N \Delta D_q^B [F_{LL}^2 - (1-y)^2 F_{LR}^2] + f_{\bar{q}}^N \Delta D_{\bar{q}}^B [F_{LR}^2 - (1-y)^2 F_{LL}^2] \}}{\sum_q \{ f_q^N D_q^B [F_{LL}^2 + (1-y)^2 F_{LR}^2] + f_{\bar{q}}^N D_{\bar{q}}^B [F_{LR}^2 + (1-y)^2 F_{LL}^2] \}} \quad (18)$$

while for unpolarized leptons but longitudinally polarized protons we have

$$P_B^{(-)}(h_N) = \left\{ \sum_q [f_q^N \Delta D_q^B (F_{RR}^2 - F_{LL}^2 - (F_{RL}^2 - F_{LR}^2) (1-y)^2) + f_{\bar{q}}^N \Delta D_{\bar{q}}^B (F_{RL}^2 - F_{LR}^2 - (F_{RR}^2 - F_{LL}^2) (1-y)^2) + h_N \Delta f_q^N \Delta D_q^B (F_{RR}^2 + F_{LL}^2 + (F_{RL}^2 + F_{LR}^2) (1-y)^2) + h_N \Delta f_{\bar{q}}^N \Delta D_{\bar{q}}^B (F_{RL}^2 + F_{LR}^2 + (F_{RR}^2 + F_{LL}^2) (1-y)^2)] \right\} \left\{ \sum_q [f_q^N D_q^B (F_{RR}^2 + F_{LL}^2 + (F_{RL}^2 + F_{LR}^2) (1-y)^2) + f_{\bar{q}}^N D_{\bar{q}}^B (F_{RL}^2 + F_{LR}^2 + (F_{RR}^2 + F_{LL}^2) (1-y)^2) + h_N \Delta f_q^N D_q^B \times (F_{RR}^2 - F_{LL}^2 - (F_{RL}^2 - F_{LR}^2) (1-y)^2) + h_N \Delta f_{\bar{q}}^N D_{\bar{q}}^B (F_{RL}^2 - F_{LR}^2 - (F_{RR}^2 - F_{LL}^2) (1-y)^2)] \right\}^{-1}. \quad (19)$$

Finally, the most interesting case is when neither the lepton nor the proton are polarized. In this case the polarization of B -baryon is non-zero only due to parity violating weak contributions and we obtain:

$$P_B^{(-)} = \left\{ \sum_q [f_q^N \Delta D_q^B (F_{RR}^2 - F_{LL}^2 - (F_{RL}^2 - F_{LR}^2) (1-y)^2) + f_{\bar{q}}^N \Delta D_{\bar{q}}^B (F_{RL}^2 - F_{LR}^2 - (F_{RR}^2 - F_{LL}^2) (1-y)^2)] \right\} \left\{ \sum_q (f_q^N D_q^B (F_{RR}^2 + F_{LL}^2 + (F_{RL}^2 + F_{LR}^2) (1-y)^2) + f_{\bar{q}}^N D_{\bar{q}}^B (F_{RL}^2 + F_{LR}^2 + (F_{RR}^2 + F_{LL}^2) (1-y)^2) \right\}^{-1}. \quad (20)$$

The polarizations $P_B^{(\mp)}(\lambda = \pm 1)$, $P_B^{(\mp)}(h_N)$ and $P_B^{(\mp)}$ might be measurable at HERA and numerical estimates will be given in the next Section.

3. THE POLARIZATION OF B - BARYON IN $\mathbf{v}_\mu(\bar{\mathbf{v}}_\mu)\mathbf{N} \Rightarrow \mathbf{v}_\mu(\bar{\mathbf{v}}_\mu)\mathbf{B}\mathbf{X}$ PROCESSES

There are two different kinds of elementary interactions contributing to neutral current neutrino

(antineutrino) processes $\nu_\mu(\bar{\nu}_\mu)N \Rightarrow \nu_\mu(\bar{\nu}_\mu)BX$:

$$\begin{aligned} \nu_\mu(\bar{\nu}_\mu)+q &\Rightarrow \nu_\mu(\bar{\nu}_\mu)+q, \\ \nu_\mu(\bar{\nu}_\mu)+\bar{q} &\Rightarrow \nu_\mu(\bar{\nu}_\mu)+\bar{q}. \end{aligned}$$

$$\begin{aligned} \nu_\mu+q &\Rightarrow \nu_\mu+q, & \nu_\mu+\bar{q} &\Rightarrow \nu_\mu+\bar{q}, \\ \bar{\nu}_\mu+q &\Rightarrow \bar{\nu}_\mu+q, & \bar{\nu}_\mu+\bar{q} &\Rightarrow \bar{\nu}_\mu+\bar{q} \end{aligned}$$

at the definite spiralities of initial and final particles:

As quarks spirality conserves in neglect of its masses, then the elementary subprocess $\nu_\mu+q \Rightarrow \nu_\mu+q$ is defined only by two spiral amplitudes F_{LL} and F_{LR} , which describe following reactions:

$$\begin{aligned} \nu_L+q_L &\Rightarrow \nu_L+q_L, \\ \nu_L+q_R &\Rightarrow \nu_L+q_R. \end{aligned}$$

The spiral amplitudes in SM are defined by following expressions

$$F_{LR} = \frac{g_L^v g_R^q}{xys + M_z^2}, \quad F_{LL} = \frac{g_L^v g_L^q}{xys + M_z^2}, \quad (21)$$

where $g_L^v = \frac{1}{2\sqrt{x_W}(1-x_W)}$.

Let's presents the subprocess cross-sections

$$\frac{d\hat{\sigma}(\nu_\mu q)}{dy} = \pi\alpha^2 xs \left[(1-h_q)(1-h'_q)F_{LL}^2 + (1+h_q)(1+h'_q)(1-y)^2 F_{LR}^2 \right]. \quad (23)$$

The differential cross-section of the elementary subprocess $\nu_\mu+\bar{q} \Rightarrow \nu_\mu+\bar{q}$ can be obtained from formula (23) with the help of the replacements $F_{LL} \Leftrightarrow F_{LR}$.

$$\begin{aligned} \frac{d\hat{\sigma}}{dy}(\nu_L q_L) &= \frac{d\hat{\sigma}}{dy}(\bar{\nu}_R \bar{q}_R) = 4\pi\alpha^2 xs F_{LL}^2, \\ \frac{d\hat{\sigma}}{dy}(\nu_L q_R) &= \frac{d\hat{\sigma}}{dy}(\bar{\nu}_R \bar{q}_L) = 4\pi\alpha^2 xs (1-y)^2 F_{LR}^2, \\ \frac{d\hat{\sigma}}{dy}(\nu_L \bar{q}_L) &= \frac{d\hat{\sigma}}{dy}(\bar{\nu}_R q_L) = 4\pi\alpha^2 xs F_{LL}^2, \\ \frac{d\hat{\sigma}}{dy}(\nu_L \bar{q}_R) &= \frac{d\hat{\sigma}}{dy}(\bar{\nu}_R q_L) = 4\pi\alpha^2 xs (1-y)^2 F_{LR}^2. \end{aligned} \quad (22)$$

The differential cross-section of the elementary subprocess $\nu_\mu+q \Rightarrow \nu_\mu+q$ taking into consideration the spirality of initial and final quarks h_q and h'_q can be presented in the form:

The following expression has been obtained on the base of formulas (9) and (23), for the differential cross-section of semi-inclusive reaction $\nu_\mu+N \Rightarrow \nu_\mu+B+X$ [8]:

$$\begin{aligned} \frac{d\sigma}{dx dy dz} &= \pi\alpha^2 xs \sum_q \left\{ [f_q^N(x) D_q^h(z) + h_N h_B \Delta f_q^N(x) \Delta D_q^B(z)] [F_{LL}^2 + (1-y)^2 F_{LR}^2] + \right. \\ &+ [f_q^N(x) D_q^h(z) + h_N h_B \Delta f_q^N(x) \Delta D_q^B(z)] [F_{LR}^2 + (1-y)^2 F_{LL}^2] + [h_N \Delta f_q^N(x) D_q^B(z) + \\ &+ h_B f_q^N(x) \Delta D_q^B(z)] [(1-y)^2 F_{LR}^2 - F_{LL}^2] + [h_N \Delta f_q^N(x) D_q^B(z) + h_B f_q^N(x) \Delta D_q^B(z)] \times \\ &\left. \times [(1-y)^2 F_{LL}^2 - F_{LR}^2] \right\}. \end{aligned} \quad (24)$$

Neglecting the contribution of antiquarks, we have take following expression for the longitudinal polarization degree of baryon:

$$P_B^{(\nu\mu N)}(h_N) = \frac{\sum_q \{ f_q^N [(1-y)^2 F_{LR}^2 - F_{LL}^2] + h_N \Delta f_q^N [F_{LL}^2 + (1-y)^2 F_{LR}^2] \} \Delta D_q^B}{\sum_q \{ f_q^N [F_{LL}^2 + (1-y)^2 F_{LR}^2] + h_N \Delta f_q^N [(1-y)^2 F_{LR}^2 - F_{LL}^2] \} D_q^B}. \quad (25)$$

If nucleon-target isn't polarized, then longitudinal polarization degree of B -baryon is given by the expression:

$$P_B^{(\nu\mu N)} = \frac{\sum_q \{ f_q^N \Delta D_q^B [(1-y)^2 F_{LR}^2 - F_{LL}^2] \}}{\sum_q \{ D_q^B f_q^N [F_{LL}^2 + (1-y)^2 F_{LR}^2] \}}. \quad (26)$$

Similar formulae hold for $P_B^{(\bar{\nu}\mu^N)}(h_N)$ and for $P_B^{(\bar{\nu}\mu^N)}$.

Neglecting quark masses, one find that there is only one non-zero helicity amplitude for each of the elementary processes in (27):

4. THE POLARIZATION OF B-BARYON IN REACTIONS $\nu_\mu(\bar{\nu}_\mu)N \Rightarrow \mu^-(\mu^+)BX$, $\mu^-(\mu^+)N \Rightarrow \nu_\mu(\bar{\nu}_\mu)BX$

$$F_{LL} = \frac{1}{xys + M_W^2} \cdot \frac{U_{qq'}}{x_W}, \quad (28)$$

Let us consider the neutrino initiated processes $\nu_\mu N \Rightarrow \mu^- hX$, for them there exist four possible elementary contributions:

$$\begin{aligned} \nu_\mu + d &\Rightarrow \mu^- + u, & \nu_\mu + s &\Rightarrow \mu^- + u, \\ \nu_\mu + \bar{u} &\Rightarrow \mu^- + \bar{d}, & \nu_\mu + \bar{u} &\Rightarrow \mu^- + \bar{s}. \end{aligned} \quad (27)$$

where $U_{ud} = \cos \theta_C$, $U_{us} = \sin \theta_C$, θ_C is the Cabibbo angle, M_W is the mass of W -bozon.

Let's give the cross-section of parton processes with definite spiralties of initial and final particles:

$$\begin{aligned} \frac{d\hat{\sigma}(\nu_L q_L \Rightarrow \mu_L^- q_L')}{dy} &= \frac{d\hat{\sigma}(\bar{\nu}_R \bar{q}_R \Rightarrow \mu_R^+ \bar{q}_R')}{dy} = \pi\alpha^2 xs F_{LL}^2, \\ \frac{d\hat{\sigma}(\nu_L \bar{q}_R \Rightarrow \mu_L^- \bar{q}_R')}{dy} &= \frac{d\hat{\sigma}(\bar{\nu}_R q_L \Rightarrow \mu_L^+ q_L')}{dy} = \pi\alpha^2 xs F_{LL}^2 (1-y). \end{aligned} \quad (29)$$

Notice that both neutrino and antineutrino interact only with left polarized quarks and right polarized antiquarks.

$\nu_\mu N \Rightarrow \mu^- BX$ on the base of formulae (9) and (29) has the following expression [9]:

For differential cross-section of semi-inclusive process

$$\begin{aligned} \frac{d\sigma(\nu_\mu N \Rightarrow \mu^- BX)}{dx dy dz} &= \frac{\pi\alpha^2 xs}{2} \sum_{q,q'} F_{LL}^2 \left\{ f_q^N(x) D_{q'}^B(z) + (1-y)^2 f_{\bar{q}}^N(x) D_{\bar{q}'}^B(z) - \right. \\ &- h_N [\Delta f_q^N(x) D_{q'}^B(z) - (1-y)^2 \Delta f_{\bar{q}}^N(x) D_{\bar{q}'}^B(z)] - h_B [f_q^N(x) \Delta D_{q'}^B(z) (1-y)^2 - \\ &\left. - f_{\bar{q}}^N(x) \Delta D_{\bar{q}'}^B(z)] + h_N h_B [(1-y)^2 \Delta f_q^N(x) \Delta D_{q'}^B(z) + \Delta f_{\bar{q}}^N(x) \Delta D_{\bar{q}'}^B(z)] \right\}. \end{aligned} \quad (30)$$

Summing on quark flavors for longitudinal polarization degree of baryon we have expression:

$$\begin{aligned} P_B^{(\nu\mu \Rightarrow \mu^-)}(h_N) &= \left\{ [-f_d^N - Rf_s^N + h_N(\Delta f_d^N + R\Delta f_s^N)] \Delta D_u^B + \right. \\ &+ (1-y)^2 (f_{\bar{u}}^N + h_N \Delta f_{\bar{u}}^N) (\Delta D_{\bar{d}}^B + R\Delta D_{\bar{s}}^B) \left. \right\} \times \\ &\times \left\{ [f_d^N + Rf_s^N - h_N(\Delta f_d^N + R\Delta f_s^N)] D_u^B + (1-y)^2 (f_{\bar{u}}^N + h_N \Delta f_{\bar{u}}^N) (D_{\bar{d}}^B + R D_{\bar{s}}^B) \right\}^{-1}, \end{aligned} \quad (31)$$

$$\begin{aligned} P_B^{(\nu\mu \Rightarrow \mu^+)}(h_N) &= \left\{ [(-f_u^N - h_N \Delta f_u^N) (\Delta D_d^B + R\Delta D_s^B) (1-y)^2 + \right. \\ &+ [f_{\bar{d}}^N + Rf_{\bar{s}}^N + h_N(\Delta f_{\bar{d}}^N + R\Delta f_{\bar{s}}^N)] \Delta D_{\bar{u}}^B \left. \right\} \times \\ &\times \left\{ (f_u^N - h_N \Delta f_u^N) (D_d^B + R D_s^B) (1-y)^2 + [f_{\bar{d}}^N + Rf_{\bar{s}}^N + h_N(\Delta f_{\bar{d}}^N + R\Delta f_{\bar{s}}^N)] D_{\bar{u}}^B \right\}^{-1} \end{aligned} \quad (32)$$

where $R = tg^2\theta_C \approx 0,056$.

Particularly, if the initial nucleon isn't polarized then the longitudinal polarization degrees (31) and (32) have the form

$$P_B^{(\nu\mu \Rightarrow \mu^-)} = \frac{-(f_d^N + Rf_s^N)\Delta D_u^B + (1-y)^2 f_u^N (\Delta D_d^B + R\Delta D_s^B)}{(f_d^N + Rf_s^N)D_u^B + (1-y)^2 f_u^N (D_d^B + RD_s^B)}, \quad (33)$$

$$P_B^{(\bar{\nu}\mu \Rightarrow \mu^+)} = \frac{-f_u^N (\Delta D_d^B + R\Delta D_s^B)(1-y)^2 + (f_d^N + Rf_s^N)\Delta D_u^B}{f_u^N (D_d^B + RD_s^B)(1-y)^2 + (f_d^N + Rf_s^N)D_u^B}. \quad (34)$$

The above mentioned formulae for longitudinal polarization degree (31)-(34) are true in the case of creation of arbitrary B -baryon with spin 1/2. If we specify the final hadron observed, further simplifications are possible. Let's consider the case in which a Λ or Σ^\pm baryon is produced. In this case we can neglect terms which contain both \bar{q} distribution and \bar{q} fragmentation

functions as they are both small, in particular at large x and z . Then we obtain the simple expression for longitudinal polarization degree of Λ -hyperon:

$$P_\Lambda^{(\nu\mu \Rightarrow \mu^-)}(h_N) = P_\Lambda^{(\nu\mu \Rightarrow \mu^-)} = -\frac{\Delta D_u^\Lambda(z)}{D_u^\Lambda(z)}, \quad (35)$$

$$P_\Lambda^{(\bar{\nu}\mu \Rightarrow \mu^+)}(h_N) = P_\Lambda^{(\bar{\nu}\mu \Rightarrow \mu^+)} = \frac{\Delta D_d^\Lambda(z) + R\Delta D_s^\Lambda(z)}{D_d^\Lambda(z) + RD_s^\Lambda(z)}. \quad (36)$$

As it is seen, the longitudinal polarization of Λ° -hyperon is only Z function and doesn't depend on variables χ and γ .

The study of this polarization can give the valuable information about fragmentation function on polarized quark to polarized baryon.

Similar results hold for the $\mu^- N \Rightarrow \nu_\mu BX$ and $\mu^+ N \Rightarrow \bar{\nu}_\mu BX$ processes; the contributing elementary interactions are:

$$\begin{aligned} \mu^- + u &\Rightarrow \nu_\mu + d, & \mu^- + u &\Rightarrow \nu_\mu + s, \\ \mu^- + \bar{d} &\Rightarrow \nu_\mu + \bar{u}, & \mu^- + \bar{s} &\Rightarrow \nu_\mu + \bar{u}, \\ \mu^+ + d &\Rightarrow \bar{\nu}_\mu + u, & \mu^+ + s &\Rightarrow \bar{\nu}_\mu + u, \\ \mu^+ + \bar{u} &\Rightarrow \bar{\nu}_\mu + \bar{d}, & \mu^+ + \bar{u} &\Rightarrow \bar{\nu}_\mu + \bar{s}, \end{aligned}$$

with the same cross-sections as those computed Eqs. (29). The analogue of Eqs. (31) and (32) is now

$$\begin{aligned} P_B^{(\mu^- \Rightarrow \nu\mu)}(h_N) &= \left\{ (-f_u^N + h_N \Delta f_u^N)(\Delta D_d^B + R\Delta D_s^B) + (1-y)^2 \Delta D_u^B [f_d^N + Rf_s^N + h_N(\Delta f_d^N + R\Delta f_s^N)] \right\} \times \\ &\times \left\{ (f_u^N - h_N \Delta f_u^N)(D_d^B + RD_s^B) + (1-y)^2 D_u^B [f_d^N + Rf_s^N + h_N(\Delta f_d^N + R\Delta f_s^N)] \right\}^{-1}, \\ P_B^{(\mu^+ \Rightarrow \bar{\nu}\mu)}(h_N) &= \left\{ -(1-y)^2 \Delta D_u^B [f_d^N + Rf_s^N - h_N(\Delta f_d^N + R\Delta f_s^N)] + (\Delta D_d^B + R\Delta D_s^B)(f_u^N + h_N \Delta f_u^N) \right\} \\ &\times \left\{ (1-y)^2 D_u^B [f_d^N + Rf_s^N - h_N(\Delta f_d^N + R\Delta f_s^N)] + (D_d^B + RD_s^B)(f_u^N + h_N \Delta f_u^N) \right\}^{-1} \quad (38) \end{aligned}$$

and similarly for the analogue of Eqs. (33) and (34).

The obtained expressions for longitudinal polarization degree of baryon are essentially simplified, if we can neglect the antiquark contribution in fragmentation functions:

$$P_\Lambda^{(\mu^- \Rightarrow \nu\mu)}(h_N) = P_\Lambda^{(\mu^- \Rightarrow \nu\mu)} = -\frac{\Delta D_d^\Lambda(z) + R\Delta D_s^\Lambda(z)}{D_d^\Lambda(z) + RD_s^\Lambda(z)}, \quad (39)$$

$$P_\Lambda^{(\mu^+ \Rightarrow \bar{\nu}\mu)}(h_N) = P_\Lambda^{(\mu^+ \Rightarrow \bar{\nu}\mu)} = -\frac{\Delta D_u^\Lambda(z)}{D_u^\Lambda(z)} \quad (40)$$

It is seen, that baryon longitudinal polarization doesn't depend on χ and γ variables in this approximation.

5. NUMERICAL ESTIMATES

In the previous sections we have obtained explicit expressions for the longitudinal polarization of baryons production in semi-inclusive DIS. We now use these

formulae to give predictions in the case of Λ production. The polarization values depend on the SM dynamics, on the quark distribution functions, both polarized and unpolarized, and on the quark fragmentation functions, again both unpolarized and polarized. The later are not so well known and a choice must be made in order to give numerical estimates.

In the literature there are set of distribution functions of quarks in nucleons [9-12]. The distribution functions of valence are see polarized quarks (antiquarks) in nucleons, given in [10] have been considered by us for numeral evaluations of polarizations.

According to the refs [14, 15], the spin functions of quark fragmentation into Λ^0 -hyperon are parameterized in form

$$\Delta D_s^\Lambda(z, Q^2) = z^\alpha D_s^\Lambda(z, Q^2),$$

$$\Delta D_u^\Lambda(z, Q^2) = \Delta D_d^\Lambda(z, Q^2) = N_u \Delta D_s^\Lambda(z, Q^2),$$

and the parameters α and N_u are chosen in three variants

Parameter	Variant 1	Variant 2	Variant 3
α	0.62	0.27	1.66
N_u	0	-0.2	1

In figs. 1-4 we show results for P_Λ for several

processes, with different initial spin configurations, and different kinematical conditions, corresponding to typical experimental setups. Weinberg parameter $\sin^2 \theta_W = 0.232$ is given by us.

The dependence of degree of longitudinal polarization of Λ^0 -hyperon $P_\Lambda^{(+)}(h_N = -1)$ and $P_\Lambda^{(+)}(\lambda = 1)$ in reaction $e^+ p \Rightarrow e^+ \Lambda^0 X$ at energy $\sqrt{s} = 300 \text{ GeV}$ (ep -collider HERA) on x, y, z variables is given on the Figs. 1 and 2. As it is seen, in 1 variant the degree of longitudinal polarization of Λ^0 -hyperon is small and weakly depends on x, y, z . In variant 2 and 3 polarization $P_\Lambda^{(+)}(h_N = -1)$ is positive an negative and with the decrease of $x, y,$ or z , it weakly increase on module.

The analogical behavior is observed for x - y - and z -dependencies of polarization P_Λ in semi-inclusive reactions (3)-(8), for example, the dependence of longitudinal polarization degree $P_\Lambda^{(+)}(h_N = 1)$ in $\nu_\mu p \Rightarrow \nu_\mu \Lambda^0 X$ and $\bar{\nu}_\mu p \Rightarrow \bar{\nu}_\mu \Lambda^0 X$ processes at the energy $\sqrt{s} = 9,6 \text{ GeV}$ (experiment NOMAD in CERN) on $x, y,$ or z variables.

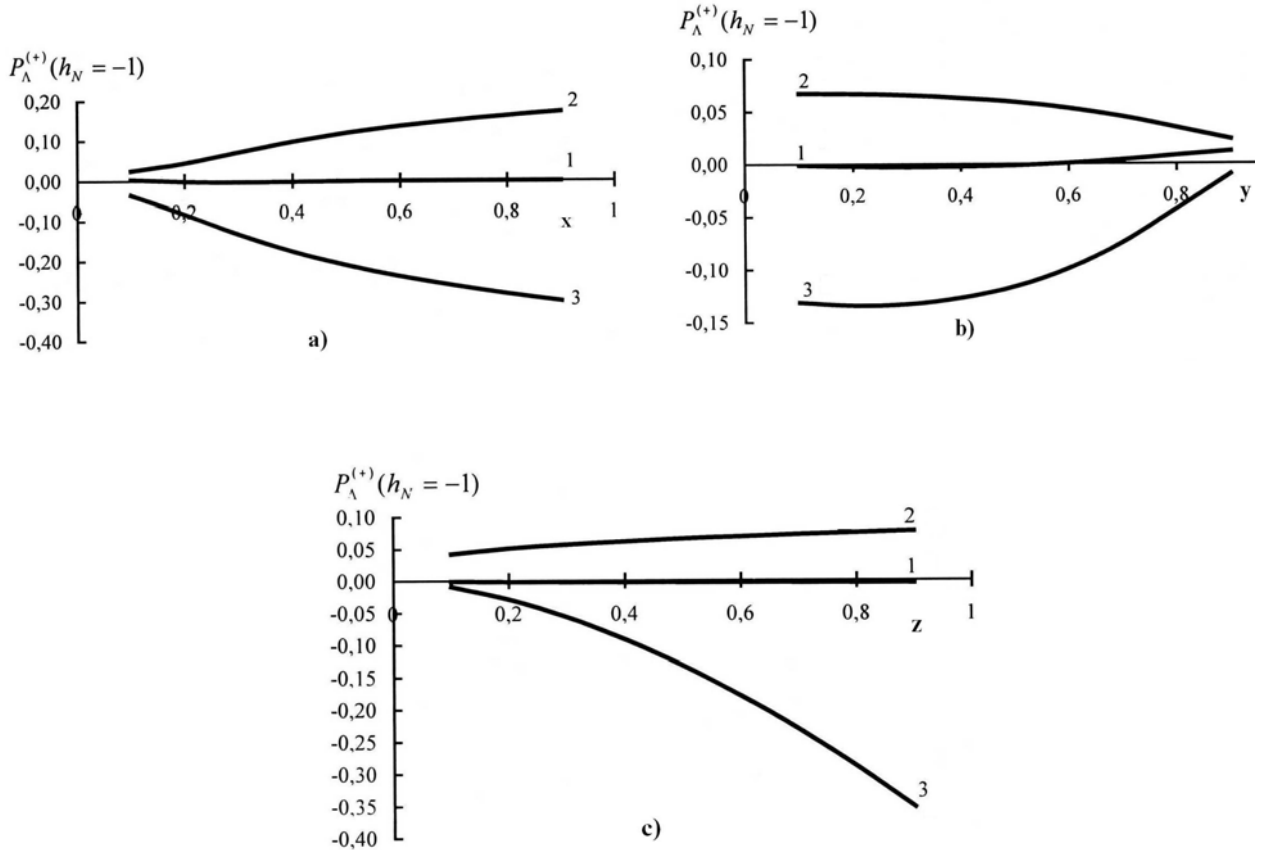


Fig. 1. $P_\Lambda^{(+)}(h_N = -1)$ for Λ^0 -hyperon, as a function of x at $y=0,3, z=0,5$, (a); of y at $x=0,3, z=0,5$, (b) and of z at $x=0,3, y=0,5$ (c).

THE LONGITUDINAL POLARIZATION OF B-BARYON IN SEMI-INCLUSIVE REACTIONS

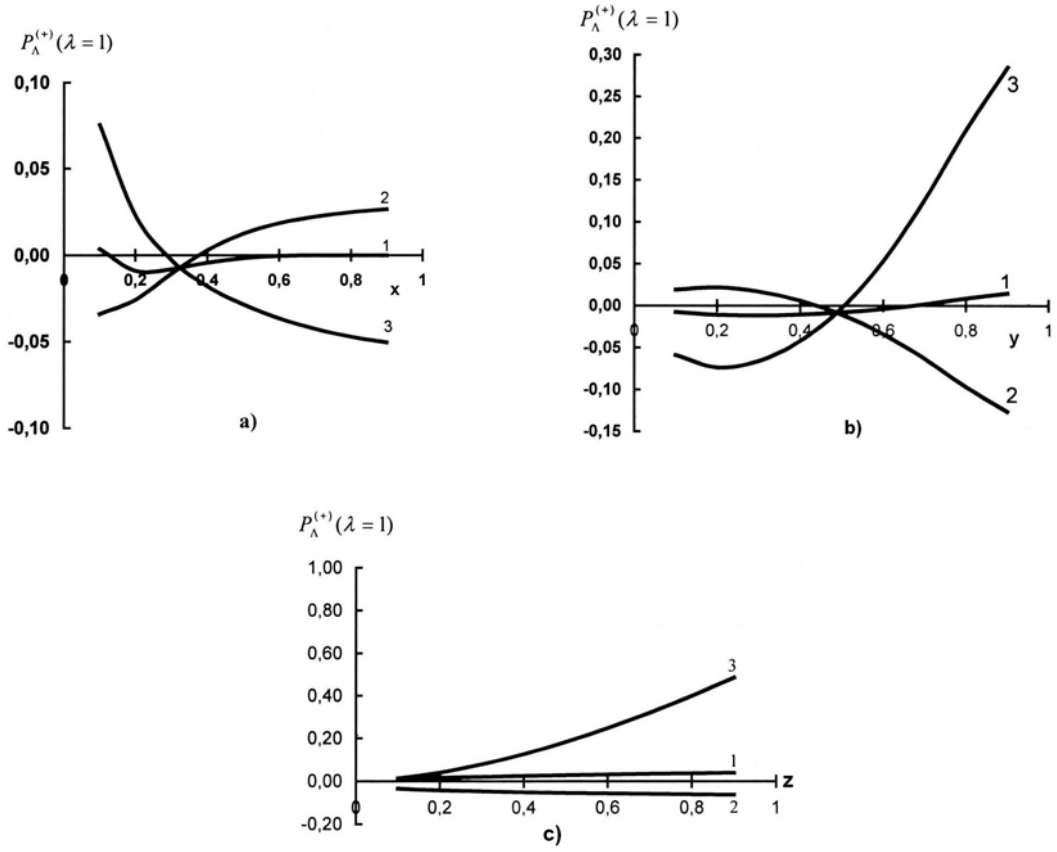


Fig. 2. The dependence of polarization $P_{\Lambda}^{(+)}(\lambda=1)$ on x at $y=0,3, z=0,5$, (a); on y at $x=0,3, z=0,5$, (b) and on z at $x=0,1, y=0,3$, (c).

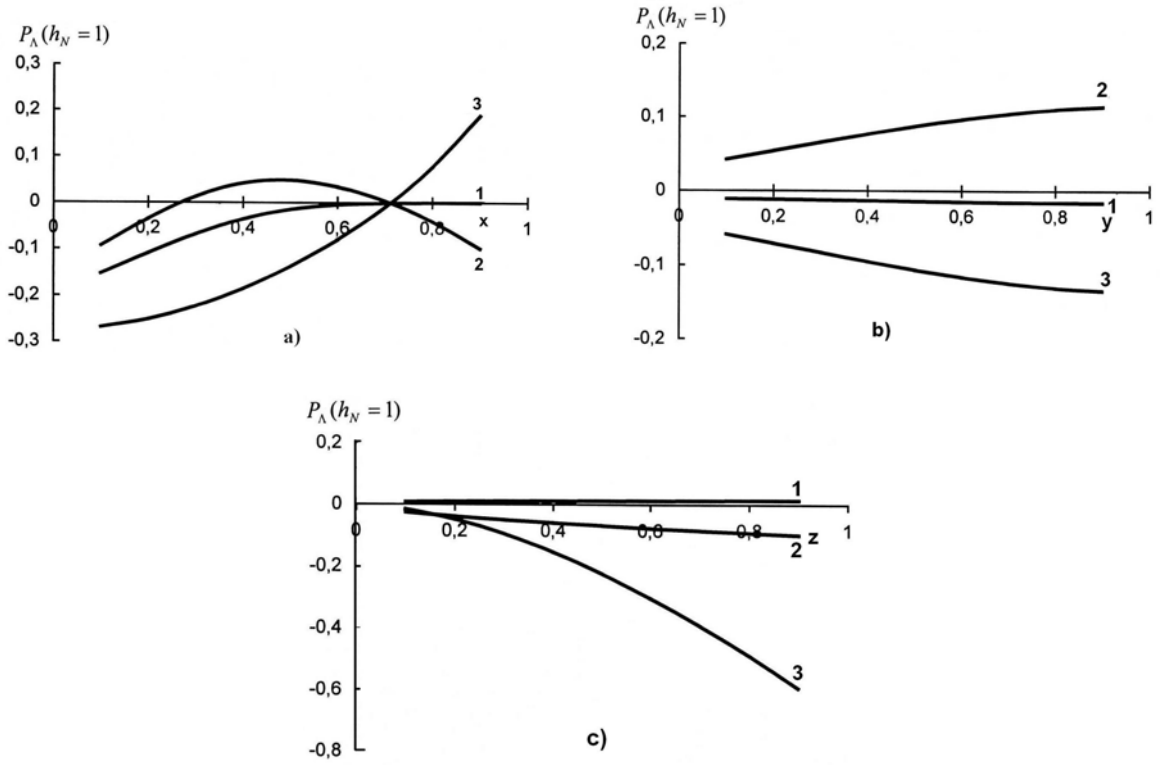


Fig. 3. $P_{\Lambda}(h_N=1)$ for Λ^0 -hyperon in reaction $\nu_{\mu}p \Rightarrow \nu_{\mu}\Lambda^0 X$ as a function of x at $y=0,1, z=0,5$, (a); of y at $x=0,3, z=0,5$ (b) and of z at $x=0,3, y=0,1$ (c).

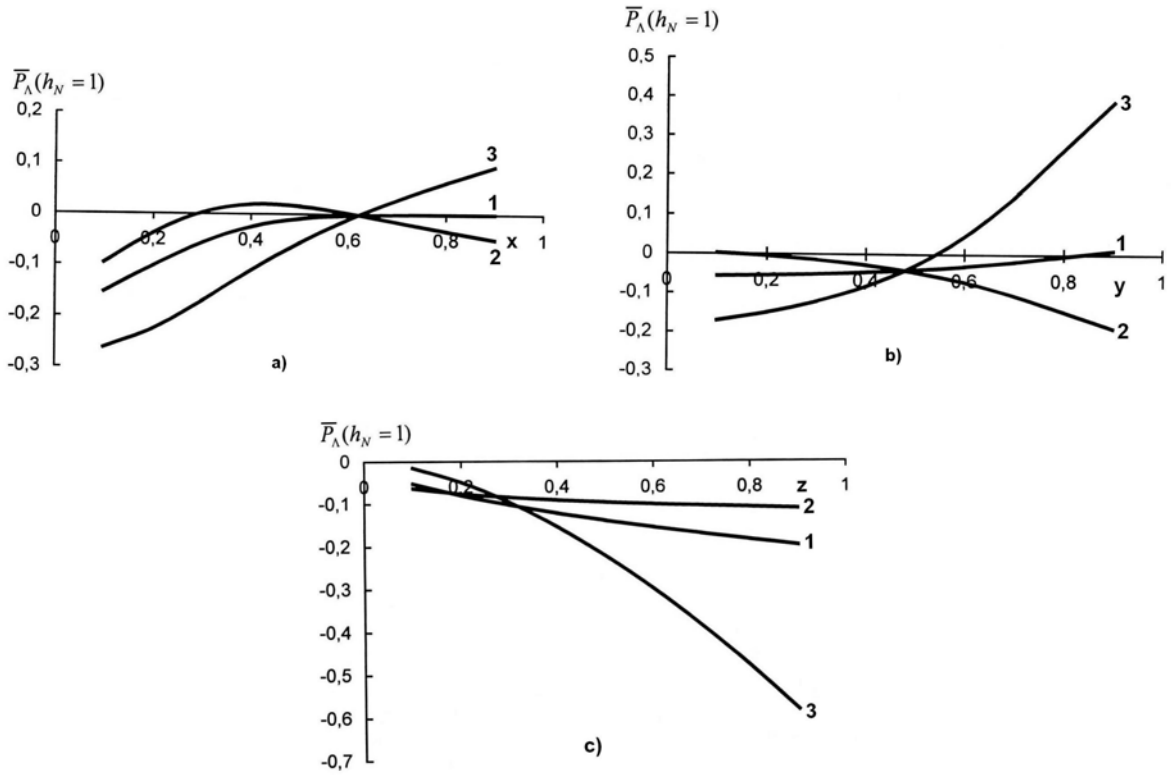


Fig. 4. The dependence of polarization $\bar{P}_\Lambda(h_N=1)$ in reaction $\bar{\nu}_\mu p \Rightarrow \bar{\nu}_\mu \Lambda^0 X$ on x at $y=0,1, z=0,5$ (a); on y at $x=0,3, z=0,5$ (b) and on z at $x=0,1, y=0,3$ (c).

- | | |
|--|---|
| [1] C. Adloff et al., Z. Phys., C 74 (1997), 191. | [9] S.K. Abdullaev, A.I. Mukhtarov. Fizika, 2008, XIV, N1, 14 |
| [2] A. Wagner, Tr. J.of Physics, 22 (1998), 525. | [10] H.Y. Cheng, S.N. Lai, C.Y. Wu. Phys. Rev. D 53 (1996), 2380. |
| [3] A. Airapetian et al., Phys. Lett. B 535 (2002), 85. | [11] J. Blümlein, H. Böttcher, Nucl. Phys. B636 (2002), 225. |
| [4] A. Airapetian et al., Phys. Rev., D 71 (2005), 0122003. | [12] M. Gluck et al. Phys. Rev. D53 (1996), 4775; D 63 (2001), 094005. |
| [5] K. Abe et al., Phys. Rev. Lett, 79 (1997), 26. | [13] M. Hirari, S. Kumano, N. Saito. Phys. Rev. D 69 (2004), 054021. |
| [6] S.K. Abdullaev, M.Sh. Qojayev. News of Baku State University. Series of physico-mathematical sciences. 3(2007), 118. | [14] D. De Florian, M. Stratman, W. Vogelsand. Phys. Rev. D 57 (1998), 5811 |
| [7] S.K. Abdullaev, A.I. Mukhtarov, S.M. Ragimova. Fizika, XI (2005), N3, 53. | [15] Anselmino et al. hep-ph/0106055 V 1 (2001). |
| [8] S.K. Abdullaev, A.I. Mukhtarov, S.M. Ragimova. Fizika, XII (2006), N4, 17. | |

TASK SOLVING METHOD OF WAVE DIFFRACTION ON PLANE SCREENS WITH FRACTIONAL BOUNDARY CONDITIONS

E.I. VELIYEV

*Institute of radiophysics and electronics after A.J.Usikov of Ukrain NAS
acad. Proskura str.,12, Kharkov, 61085, Ukrain*

T.M. AKHMEDOV

*Institute of Mathermatics of Azerbaijan NAS
F.Agayev str., 9, Baku, 1141, Azerbaijan*

The solving method of integral-differential equation of special type to the solution of which the diffraction tasks on plane screens described by fractional boundary conditions (FBC) when the order of fractional derivative α changes between 0 and 1, has been proposed in the given paper. The method is considered on model diffraction two-dimensional tasks which are band and half-plane with FBC. FBC generalize the ideal boundaries which are ideally electric- and magnetic-conducting boundaries which are obtained as the private case at $\alpha = 0$ and $\alpha = 1$ correspondingly. The method is based on use of orthogonal polynomials. Moreover Gegenbauer polynomials are used for the band, the orthogonal polynomials are used in interval $(-1, 1)$ and for half-plane we deal with Laguerre polynomials which are orthogonal ones in interval $(0, \infty)$. The important peculiarity: the given method allows the obtaining the diffraction task solution in obvious form for the one private case $\alpha = 0,5$ is emphasized.

Last time the fractional operators are used in different electrodynamics tasks. The fractional operators are defined as fractalized ones from known operators. For example, the fractal derivatives and integrals are the generalization of the usual derivatives and integrals. Also the operator of fractal rotor which is defined as the fractalized operator from usual rotor operator finds application [1].

In the given paper the two-dimensional diffraction tasks on the boundaries which are described by boundary conditions (BV) containing the fractal derivative:

$$D_n^\alpha U(\vec{r})|_S = 0, \quad (1)$$

The fractal derivative is taken over normal line to the surface. The function U describes the horizontal component of electric or magnetic field. The fractal derivative is defined through Riman-Luivill integral in semi-infinite interval [2]. Let's use one symbol D_y^α taking under the consideration the fractal derivative by y variable on half-axle: $D_y^\alpha \equiv_{-\infty} D_y^\alpha$. BC (1) we call the fractal boundary conditions (FBC).

The introduction of new BC should describe the physical realities from the one hand, but by other one they should allow constructing the effective numerical algorithm of solution obtaining with the given accuracy. The construction of the simple and adequate mathematical models for the description of diffusing surface properties is the one of the common tasks in diffraction tasks.

For FBC (1) the values of fractal order α between 0 and 1 are considered. The extreme values of the fractal order $\alpha = 0$ and $\alpha = 1$ lead to well known ideally electric- (IEC) and magnetic-conducting (IMC) boundaries correspondingly. FBC generalize the ideal boundaries as IEC and IMC. FBC are considered in reflection tasks in refs of E.I.Veliyev and N. Engheta [3-5] in 2003 where the reflection coefficients from

boundaries described by FBC are given. It is shown that the boundary has the reflection coefficient which is equal to zero by modulus, i.e. corresponds to perfect reflecting boundary. Moreover the phase of reflection coefficient is defined by fractal order.

FBC can be compared with known impedance BC (IBC) [6,7] which are well studied by many authors and widely used for modeling of the different objects. IBC are given by the equation:

$$\vec{n} \times \vec{E}(\vec{r}) = \eta \vec{n} \times (\vec{n} \times \vec{H}(\vec{r})), \quad \vec{r} \in S, \quad (2)$$

where \vec{n} is normal line to S surface. IBC are intermediate state between IEC and IMC boundaries [5,6]: the impedance value changes from 0 for IEC up to ∞ for IMC.

The many refs are dedicated to diffraction tasks on impedance boundaries. IBC are successfully used for modeling of reflecting properties of good conductors and also for lattices and others. In each case there are formulas for obtaining of impedance obtaining as metal conducting function, lattice parameters and others. IBC are approximate BC, they have limits for their application and can't describe the reflecting properties of whole surface variation.

The comparison of diffusion properties of boundary with FBC and IBC has been carried out in ref [8].

The further amendment of IBC can be carried out with the use of derivatives of higher (whole) order or generalized BC [7,9,10].

The general methodology of obtaining of detail impedance BC of high order in spectral region is presented in monography D.J.Hoppe and Y.Rahmat-Samii [9]. As it is shown in spectral region one can obtain the detail IBC purely in analytic form. However, not always one can obtain IBC in space region in the obvious form, that's why it is necessary to approximate IBC in spectral region in order to use the reversal Fourier transformation. FBC are the example of non-local BC.

This means that the function value on the boundary depend on field values in the points on the finite distance from the boundary in the difference from classical BC (IEC, IMC, IBC) when the value on the boundary is defined by only field values in the points infinitely close to the boundary. This is connected with use of derivatives of non-integral order instead of usual ones.

The non-local BC in diffusion tasks are widely used in numerical algorithms based on finite-element method or finite-difference method [11,12]. The procedure is based on the consideration of finite region limiting the diffusing object for cutoff of the considered region; moreover the carrying out of new BC which usually have non-local character is need on the boundary of new region. The non-local BC are used for wave equation in parabolic approximation [12]. The non-local BC are effective alternative to traditional use of absorbing layers [12].

The development of effective numerical-analytical solution method of two-dimensional diffraction tasks on the boundaries described by FBC is the aim of the given paper. The proposed method is considered on model tasks of diffusion: on the band and half-plane. The method is based on the presentation of scattered field with the help of fractal derivative from Henkel function of the first type of zero order. This presentation is the result of the application of Green fractal theory considered in refs [13,14].

The solution method of fractal integral-differential equation (FIDE) to the solution of which the series of boundary tasks of diffraction theory is led. The reduction degree is characterized by α parameter which changes in limits $\alpha \in [0,1]$. At values of fractal order $\alpha = 0$ and 1 these equations are led to known integral equations. In the given paper the general method of FEDE solution for any values of $\alpha \in [0,1]$ order which as the private case contains the earlier known solutions, has been proposed. The method essence is in the fact that the required function is found in the form of series by orthogonal polynomials (Gegenbauer polynomials for the band and Lager polynomials for half-plane) with weight function allowing satisfaction to the condition on the edges. The degree of weight function and degree of orthogonal polynomials depend on reduction order α . Rewriting FEDE relatively Fourier images of the required function in the form of coupled integral equations (CIE) and using the properties of breaking integrals of Veber-Shafheyline (in the band case) and also Fourier-presentation for Laguerre polynomials for the task on the half-plane, CIE are led to the solution of infinite system of linear algebraic equations relatively unknown decomposition coefficients. The last ones allow the defining the required coefficients with any before given accuracy on the base of reduction method.

The diffraction tasks of the plane wave on the band with FBC and also half-plane with FBC have been solved on the based of proposed method.

1. THE DIFFRACTION ON THE BAND WITH FBC

Let's consider the two-dimensional diffraction task

of E-polarized plane wave on the band with FBC in the form:

$$D_{ky}^\alpha E_z(x, y) = 0, \quad y \rightarrow \pm 0. \quad (3)$$

The finite-thin band by $2a$ width is situated in plane $y = 0$ and it is infinite one along z axis. The incident field $\vec{E}^i = \vec{z}E_z^i(x, y)$ is described by expression $E_z^i(x, y) = e^{-ik(x \cos \theta + y \sin \theta)}$ where θ is angle of incidence, $k = 2\pi / \lambda$ is wave number. The dependence on time is proposed $e^{-i\omega t}$ and ignored in all formulas. Let's designate the scattered field by the following function: $\vec{E}^s = \vec{z}E_z^s(x, y)$. The complete field $\vec{E} = \vec{z}E_z(x, y)$ is the sum of incident and scattered fields:

$$E_z(x, y) = E_z^i(x, y) + E_z^s(x, y).$$

The task solution, i.e. function $E_z(x, y)$ should satisfies to: 1) Gelmgold equation in whole space besides band surface; 2) the condition of Zommerfeld radiation on infinity for scattered field $E_z^s(x, y)$; 3) Meiksner condition on band edges ($y = 0, x \rightarrow \pm a$) [15, 16]; 4) FBC (3) on band surface $-a < x < a$. For comfort the derivative is taken by dimensionless quantity ky .

Using the fractal Green theorem [13,14,17] let's present the function $E_z^s(x, y)$ through fractal Green function :

$$E_z^s(x, y) \equiv \int_{-a}^a f^{1-\alpha}(x') G^\alpha(x - x', y) dx' \quad (4)$$

where $f^{1-\alpha}(x)$ is unknown function which we will call the density of fractal potential.

In two-dimensional case the fractal Green function G^α in (5) is expressed as fractal derivative of classical Green function:

$$G^\alpha(x - x', y) = -\frac{i}{4} D_{ky}^\alpha H_0^{(1)}(k\sqrt{(x-x')^2 + y^2}),$$

where $H_0^{(1)}(x)$ is Henkel function of first type of zero order.

For private cases of values of fractal order (FO) $\alpha=0$ and $\alpha=1$, the presentation (4) leads to known presentations of potentials of simple and double layers used for diffraction task solutions with BC Dirikhle and Neyman correspondingly [16,18].

Obeying the function $E_z(x, y)$ to FBC in the form of (3) we obtain FEDE by the following form:

$$\lim_{y \rightarrow 0} D_{ky}^\alpha \int_{-a}^a f^{1-\alpha}(x') G^\alpha(x - x', y) dx' = -\lim_{y \rightarrow 0} D_{ky}^\alpha E_z^i(x, y), \quad (5)$$

where the right part of equation is known function and $f^{1-\alpha}(x)$ is unknown function.

Let's introduce the dimensionless quantity $\xi = x/a \in [-1,1]$ and the new function

$\tilde{f}^{1-\alpha}(\xi) \equiv af^{1-\alpha}(a\xi)$. Let's continue the function $f^{1-\alpha}(x)$ by zero outside the function:

$$\tilde{f}^{1-\alpha}(\xi) = \frac{ka}{2\pi} \int_{-\infty}^{\infty} F^{1-\alpha}(\beta) e^{ika\xi\beta} d\beta, \quad F^{1-\alpha}(\beta) = \int_{-1}^1 \tilde{f}^{1-\alpha}(\xi) e^{-ika\xi\beta} d\xi. \quad (6)$$

Using the expressions for fractal Green function we obtain the presentation for scattered field through Fourier image $F^{1-\alpha}(\beta)$:

$$E_z^s = -i \frac{e^{\pm i\pi\alpha/2}}{4\pi} \int_{-\infty}^{\infty} \frac{F^{1-\alpha}(\beta) e^{ik[\beta x + |y|\sqrt{1-\beta^2}]} (1-\beta^2)^{(1-\alpha)/2}}{d\beta}. \quad (7)$$

Now FEDE (5) in Fourier images is led to BIE relatively to unknown function $F^{1-\alpha}(\beta)$:

$$\begin{cases} \int_{-\infty}^{\infty} F^{1-\alpha}(\beta) e^{ika\xi\beta} (1-\beta^2)^{\alpha-1/2} d\beta = -4\pi e^{i\pi/2(1-\alpha)} \sin^\alpha \theta e^{-ika\xi \cos \theta}, & \xi \in [-1,1], \\ \int_{-\infty}^{\infty} F^{1-\alpha}(\beta) e^{ika\xi\beta} d\beta = 0, & |\xi| > 1. \end{cases} \quad (8)$$

Note that BIE (8) for $\alpha=0$ leads to BIC for diffraction task of E-polarized plane wave on IEC infinite-thin band and at $\alpha=1$ BIC describe the diffraction on IMC band. BIE (8) are the more general ones and contain the private cases of BIC considered earlier.

Let's investigate the private case $\alpha=1$ at which the equation (8) has the analytical solution at any value of frequency parameter ka . Indeed, from (8) one can easily obtain the solution in the obvious form:

$$\begin{aligned} \tilde{f}^{0,5}(\xi) &= -2ika \sin^{1/2} \theta e^{-ika\xi \cos \theta + i\pi/4}, \\ F^{0,5}(\beta) &= -4i \sin^{1/2} \theta e^{i\pi/4} \frac{\sin ka(\beta + \cos \theta)}{\beta + \cos \theta}. \end{aligned}$$

Let's consider BIE (8) for general case $0 < \alpha < 1$. The function $\tilde{f}^{1-\alpha}(\xi)$ should satisfy to conditions on the edge at $\xi \rightarrow \pm 1$. Let's obey the function $\tilde{f}^{1-\alpha}(\xi)$ to the condition on the edge by following type:

$$\tilde{f}^{1-\alpha}(\xi) = O\left((1-\xi^2)^{\alpha-1/2}\right) \quad \xi \rightarrow \pm 1 \quad (9)$$

For private cases $\alpha=0$ and $\alpha=1$ conditions on the edge have the form:

$$\tilde{f}^{1-\alpha}(\xi) = \begin{cases} O\left((1-\xi^2)^{-1/2}\right), & \alpha=0 \\ O\left((1-\xi^2)^{1/2}\right), & \alpha=1 \end{cases} \quad \xi \rightarrow \pm 1 \quad (10)$$

The conditions (10) are known Meiksnier conditions on the edge in the diffraction theory task [16].

Let's find the function $\tilde{f}^{1-\alpha}(\xi)$ in the form equally convergent series by Gegenbauer polynomials which is orthogonal one in interval $[-1,1]$:

$$\tilde{f}^{1-\alpha}(\xi) = (1-\xi^2)^{\alpha-1/2} \sum_{n=0}^{\infty} f_n^\alpha \frac{1}{\alpha} C_n^\alpha(\xi) \quad (11)$$

where f_n^α are unknown coefficients. In this case the function $\tilde{f}^{1-\alpha}(\xi)$ satisfies to conditions on the edge (9). Note that Gegenbauer polynomials $C_n^\alpha(\xi)$ in the private cases $\alpha=0$ and $\alpha=1$ are led to Chebishev polynomials of first and second types $T_n(\xi)$, $U_n(\xi)$ [20] correspondingly.

$$\lim_{\alpha \rightarrow 0} \frac{C_n^\alpha(\xi)}{\alpha} = \begin{cases} \frac{2}{n} T_n(\xi), & n \neq 0 \\ 1, & n = 0 \end{cases},$$

$$\lim_{\alpha \rightarrow 1} \frac{C_n^\alpha(\xi)}{\alpha} = C_n^1(\xi) = U_n(\xi). \quad (12)$$

Using Fourier transformation to series (11) we obtain the presentation for function $F^{1-\alpha}(\beta)$ in the series form by Bessel functions:

$$F^{1-\alpha}(\beta) = \frac{2\pi}{\Gamma(\alpha+1)} \sum_{n=0}^{\infty} (-i)^n f_n^\alpha \frac{\Gamma(n+2\alpha)}{\Gamma(n+1)} \frac{J_{n+\alpha}(ka\beta)}{(2ka\beta)^\alpha}. \quad (13)$$

Let's transform the first equation in (8): multiply the both parts on $e^{-ika\xi\tau}$ and integrate by ξ from -1 up to 1. Finally we obtain the following equation:

$$\int_{-\infty}^{\infty} F^{1-\alpha}(\beta) \frac{\sin ka(\beta-\tau)}{\beta-\tau} (1-\beta^2)^{\alpha-1/2} d\beta = -4\pi e^{i\pi/2(1-\alpha)} \sin^\alpha \theta \frac{\sin ka(\tau+\cos\theta)}{\tau+\cos\theta} \quad (14)$$

Substituting the presentation (13) in IC (14) we obtain expression for definition of f_n^α coefficients:

$$\sum_{n=0}^{\infty} (-i)^n \frac{\Gamma(n+2\alpha)}{\Gamma(n+1)} f_n^\alpha C_{kn}^\alpha = \gamma_k^\alpha, \quad k=0,1,2,\dots \quad (15)$$

with matrix coefficients

$$C_{kn}^\alpha = \int_{-\infty}^{\infty} J_{n+\alpha}(ka\beta) J_{k+\alpha}(ka\beta) (1-\beta^2)^{\alpha-1/2} \frac{d\beta}{\beta^{2\alpha}},$$

$$\gamma_k^\alpha = -2\Gamma(\alpha+1)(2ka)^\alpha i^{1-\alpha} \sin^\alpha \theta \frac{J_{k+\alpha}(ka\cos\theta)}{\cos\theta}.$$

After finding the coefficients f_n^α the function of potential density $\tilde{f}^{1-\alpha}(\xi)$ and its Fourier transformation $F^{1-\alpha}(\beta)$ can be found from expressions (11) and (13) correspondingly. One can show that (15) is Fredholm equation of second type and unknown coefficients f_n^α can be found with any earlier given accuracy using the reduction method. The numerical results of the considered task for case of E -polarization are presented in ref [17] where the numerical calculations of band diffusing characteristics with FBC: directional diagram, diameter of inverse section and the density of distribution of surface currents are given.

The case of H -polarization for diffraction task on the band with FBC is considered in ref [19].

II. DIFFRACTION ON HALF-PLANE WITH FBC

In the given part the task of electromagnetic wave diffraction on half-plane with FBC is firstly considered. The method of solution of IC for limited regions developed in previous chapter will be generalized for IC in half-infinite regions to the solution of which the considered task is led.

The many refs are dedicated to solution of diffraction wave task on the half-plane. The method of diffraction task solution with ideally conducting boundary

is considered in [16]. The diffraction task on half-plane is usually solved with the help of Viner-Hoph method. The first application of the method to ideally conducting half-plane can be related to ref of Copson [21] in 1946 and independently Carlson and Heins in 1947 [22]. Senior in 1952 firstly applied Viner-Hoph method to the solution of diffraction task on impedance half-plane [23] and further considered the off-normal incidence [24]. The diffraction tasks on resistive and conducting half-plane and after the different joint half-planes are described in detail in [7].

For serious solution of the considered task the approach which generalizes the results of work [25] for ideally conducting boundaries and contains them as a private case, is proposed. The proposed method allows obtaining expression for finding of unknown coefficients in the decomposition of scattered field in the form of infinite series.

Let's the plane E -polarized wave $E_z^i(x, y) = e^{-ik(x\cos\theta+y\sin\theta)}$ where θ is angle of incidence falls on half-plane ($x > 0$) which is infinite one along Oz axis. The complete field $E_z = E_z^i + E_z^s$ should satisfy to FBC of the following form:

$$D_{ky}^\alpha E_z(x, y) = 0, \quad y \rightarrow \pm 0, \quad x > 0 \quad (16)$$

and also Meiksnor condition on the edge at $x \rightarrow 0$ [15,16].

We will find the diffused field in the form of potential where $f^{1-\alpha}(x)$ is unknown function, G^α is fractal Green function, introduced earlier.

$$E_z^s(x, y) \equiv \int_0^\infty f^{1-\alpha}(x') G^\alpha(x-x', y) dx' \quad (17)$$

Obeying the complete field FBC (16) we obtain FEDE relatively to function $f^{1-\alpha}(x)$ at $x > 0$:

$$\frac{-i}{4} \lim_{y \rightarrow 0} \int_0^\infty D_{ky}^{2\alpha} f^{1-\alpha}(x') H_0^{(1)}(k\sqrt{(x-x')^2 + y^2}) dx' = - \lim_{y \rightarrow 0} \int_0^\infty D_{ky}^\alpha E_z^i(x, y), \quad (18)$$

Let's continue the function $f^{1-\alpha}(x)$ by zero outside the integral $[0, \infty]$ and go into Fourier image:

$$F^{1-\alpha}(\beta) = \int_{-\infty}^{\infty} \tilde{f}^{1-\alpha}(\xi) e^{-ik\beta\xi} d\xi = \int_0^{\infty} f^{1-\alpha}(x) e^{-ik\beta x} dx$$

$$\tilde{f}^{1-\alpha}(\xi) = \frac{k}{2\pi} \int_{-\infty}^{\infty} F^{1-\alpha}(\beta) e^{ik\beta\xi} d\beta,$$

where $\tilde{f}^{1-\alpha}(\xi) \equiv f^{1-\alpha}(\xi)$ ($\xi > 0$), $\tilde{f}^{1-\alpha}(\xi) \equiv 0$ ($\xi < 0$).

Following to proposed method, FEDE is led to IBC system relatively to unknown function $F^{1-\alpha}(\beta)$:

$$\begin{cases} \int_{-\infty}^{\infty} F^{1-\alpha}(\beta) e^{ik\xi\beta} (1-\beta^2)^{\alpha-1/2} d\beta = -4\pi e^{i\pi/2(1-\alpha)} \sin^{\alpha} \theta e^{-ik\xi \cos \theta}, & \xi > 0, \\ \int_{-\infty}^{\infty} F^{1-\alpha}(\beta) e^{ik\xi\beta} d\beta = 0, & \xi < 0. \end{cases} \quad (19)$$

In private case $\alpha = 0,5$ CIC solution (19) has the following analytical type:

$$f^{1/2}(x) = -2 \sin^{1/2} \theta e^{i\pi/4} e^{-ikx \cos \theta},$$

$$F^{1/2}(\beta) = -2 \sin^{1/2} \theta e^{i\pi/4} \frac{\pi}{k} \delta(\beta + \cos \theta). \quad (20)$$

Moreover for diffused field (17) we can obtain the presentation in the obvious form:

$$E_z^s(x, y) = \frac{i}{2k} e^{\pm i\pi\alpha/2} e^{i\pi/4} \sin^{\alpha-1/2} \theta e^{ik(-\cos \theta x + |y| \sin \theta)}$$

Let's go into CIC (19) consideration for general case $0 < \alpha < 1$. The function $\tilde{f}^{1-\alpha}(\xi)$ should satisfy to condition on the edge at $\xi \rightarrow 0$. Let's obey the function $\tilde{f}^{1-\alpha}(\xi)$ to the condition on the edge by the following form:

$$\tilde{f}^{1-\alpha}(\xi) = O(\xi^{\alpha-1/2}), \quad \xi \rightarrow 0 \quad (21)$$

For private cases $\alpha = 0$ and $\alpha = 1$ the conditions on edge have the known form [15,16] for ideally conducting boundaries.

Let's find the function $\tilde{f}^{1-\alpha}$ in the form of equal convergent series by Laguerre polynomials with unknown coefficients f_n^{α} [25]:

$$\tilde{f}^{1-\alpha}(x) = e^{-x} x^{\alpha-1/2} \sum_{n=0}^{\infty} f_n^{\alpha} L_n^{\alpha-1/2}(2x) \quad (22)$$

In this case the function $\tilde{f}^{1-\alpha}$ satisfies to condition on the edge (21). Substituting the series (22) in the first equation (19) we obtain IC:

$$\sum_{n=0}^{\infty} f_n^{\alpha} \int_{-\infty}^{\infty} \left[\int_0^{\infty} e^{-t} t^{\alpha-1/2} L_n^{\alpha-1/2}(2t) e^{-ik\beta t} dt \right] \times e^{ik\xi\beta} (1-\beta^2)^{\alpha-1/2} d\beta = R(\xi), \quad (23)$$

where $R(\xi) = -4\pi e^{i\pi/2(1-\alpha)} \sin^{\alpha} \theta e^{-ik\xi \cos \theta}$ is known function.

Using the formula for Fourier transformation of Laguerre polynomials [26, p.462] we obtain the expression for integral by dt . Finally, IC (23) has the form ($\xi > 0$).

$$\sum_{n=0}^{\infty} f_n^{\alpha} \frac{\Gamma(n+\alpha+1/2)}{\Gamma(n+1)} \times \int_{-\infty}^{\infty} \frac{(ik\beta-1)^n}{(ik\beta+1)^{n+\alpha+1/2}} (1-\beta^2)^{\alpha-1/2} e^{ik\xi\beta} d\beta = R(\xi). \quad (24)$$

For discretization of equation (24) let's integrate the both parts as $\int_0^\infty (\cdot) e^{-\xi} \xi^{\alpha-1/2} L_m^{\alpha-1/2}(2\xi) d\xi$. After transformations we have BCJAY:

$$\sum_{n=0}^{\infty} f_n^\alpha C_{mn}^\alpha = B_m^\alpha, \quad m = 0, 1, 2, \dots, \infty \quad (25)$$

where matrix elements have the form:

$$C_{mn}^\alpha = \frac{\Gamma(n + \alpha + 1/2)}{\Gamma(n + 1)} \int_{-\infty}^{\infty} \frac{(ik\beta + 1)^{m-n-\alpha-1/2}}{(ik\beta - 1)^{n-m-\alpha-1/2}} (1 - \beta^2)^{\alpha-1/2} d\beta$$

$$B_m^\alpha = -4\pi e^{i\pi/2(1-\alpha)} (-1)^{\alpha+1/2} \frac{\sin^\alpha \theta (1 - ik \cos \theta)^m}{(1 + ik \cos \theta)^{\alpha+m+1/2}}$$

One can show that solving BCJAY (25) on the base of reduction method, unknown coefficients f_n^α can be found with any earlier given accuracy. Unknown function

$\tilde{f}^{1-\alpha}(x)$ is defined from (22) that allows defining the diffused field on the base of the presentation (17).

CONCLUSION

In the given paper the solving method of integral-differential equation of special type to solution of which the diffraction tasks on the boundaries described by FBC are led, when the order of fractal derivative α is considered between 0 and 1. The method is considered on model two-dimensional diffraction tasks: band and half-plane with FBC. FBC generalize the ideal boundaries: IEC and IMC which are obtained as private case at $\alpha = 0$ and $\alpha = 1$ correspondingly. The method is based on the use of orthogonal polynomialss. Moreover for the band the Gegenbauer polynomials which are orthogonal ones in interval $(-1, 1)$ and for half-plane we deal with Laguerre polynomials which are orthogonal ones in interval $(0, \infty)$. The important peculiarity is emphasized: the given method allows obtaining the solution of diffraction task in the obvious form for one private case $\alpha = 0, 5$.

-
- [1]. *N.Engheta* Microwave and Optical Technology Letters. 1998. – 17, N 2. - P.86-91.
 - [2]. *S.G.Samko, A.A.Kilbas, O.I. Marichev* Integrali I proizvodnie drobnogo poriadka I nekotorie ih prilogeniia. – Minsk, Nauka I tehnika, 1987. – 688 p.
 - [3]. *M.V.Ivakhnychenko, E.Veliev, T.M.Ahmedov* Journal of electromagnetic waves and applications. – 2007. – 21, N 13. - P.1787-1802.
 - [4]. *E.Veliev, N. Engheta* Mathematical methods in electromagnetic theory: 10th international conference: conf. proc. – Dnieperpetrovsk, 2004. – P.228–230.
 - [5]. *N.Engheta* Mathematical methods in electromagnetic theory: conf. proc. – Kharkiv, 2000. – P.34–40.
 - [6]. *M.A. Leontovich* Investigations on radiowave propagation // Academy of Sciences. – 1948. – Part 2. – P.5–12.
 - [7]. *T.B.Senior, J.L.Volakis* Approximate boundary conditions in electromagnetics. – London : The institution of electrical engineers, 1995. – 353 p.
 - [8]. *M.V.Ivakhnychenko, E.I.Veliev, T.M. Ahmedov* Progress in electromagnetics research C. – 2008. – 2. – P.189–205.
 - [9]. *D.J.Hope, Y.Rahmat-Samii* Impedance boundary conditions in electromagnetics. – Washington, DC: Taylor and Francis, 1995. 196 p.
 - [10]. *M.Idemen* J. Phys. Soc. Jpn.1990.59, N1, P.71–80.
 - [11]. *S.P. Marin* IEEE Transactions on antennas and propagation. 1982. 30, N 6. – P.1045–1049.
 - [12]. *Z.L. Hyaric* IEEE Transactions on antennas and propagation. 2001. 49, N 6. P.916-922.
 - [13]. *E.Veliev, N.Engheta* IEEE AP-S international symposium & USNC/URSI National radio science meeting: 22–27 June 2003: conf. proc. Ohio, USA, 2003. P. 228.
 - [14]. *E.Veliev, T.M. Akhmedov* Dokladi NAN Azerbayjana. – 2005. – v. 41, № 4. – p. 20–27.
 - [15]. *R.Muttra, C.Li* Analiticheskiye metodi teorii volnovodov. –M.: Мир, 1974. – 327p.
 - [16]. *X.Xenl, A.Mauye, K.Vestpfal* Teoriya difraksii.– M.:Mir, 1964. 428p.
 - [17]. *E.I. Veliev, M.V.Ivakhnychenko, T.M. Ahmedov* Progress in electromagnetics research, 2008,79, P.443–462.
 - [18]. *D.Kolton, R.Kress* Metodi inyegralnih uravnenii v teorii rasseiania. M.: Mir, 1987. 311 p.
 - [19]. *T.M. Akhmedov* Dokladi NAN Azerbayjana. – 2006. – v. L X11, № 5-6. – p. 8-18.
 - [20]. *G.Beitmen, A. Erdey* Visshie transtsendentniye funktsii,v.2. M.:Nauka, 1974. – 297 p.
 - [21]. *E.T. Copson* Quart. J. Math. 1946. 17. –P. 19-34.
 - [22]. *J.F.Carlson, A.E.Heins* Quart. Appl. Math., 4. – 1947. – P. 313-329.
 - [23]. *T.B.A. Senior* Proc. Roy. Soc. London, Seria A. – 1952. – 213. – P. 436-458.
 - [24]. *T.B.A. Senior* Appl. Sci. Res., B8. 1959. P. 35-61.
 - [25]. *E.I. Veliev* Journal of electromagnetic waves and applications. 1999. 13, N 10. P. 1439-1453.
 - [26]. *A.P.Prudnikov, Yu.A.Brichkov, O.I.Marichev* Integrali i riadi. M.: Nauka, 1981. 798 p.

SOME PROPERTIES OF THE CENTRAL HEAVY ION COLLISIONS

Z. WAZIR¹, M. K. SULEYMANOV^{1,2,3}, O.B. ABDINOV³, E. U. KHAN¹, MAHNAZ Q. HASEEB¹, M. AJAZ¹, K. H. KHAN¹, SH. GANBAROVA³

¹CIIT, Islamabad (Pakistan),

²JINR, Dubna (Russia)

³Institute of Physics ANAS (Azerbaijan Republic)

Some experimental results are discussed in connection with the properties of the central heavy ion collisions. These experiments indicate the regime changes and saturation at some values of the centrality. This phenomenon is considered to be a signal of the percolation cluster formation in heavy ion collisions at high energies.

1. INTRODUCTION

Study of the centrality dependence of the characteristics of hadron-nuclear and nuclear-nuclear interactions is an important experimental way for obtaining information on phases of strongly interacting matter formed during the collision evolution. L. Wan Hove was first in attempting to use the centrality to get information on the new phases of matter [1] using the data coming from the ISR CERN experiments on pp-interactions. To fix the centrality the particle density (Δn) in given region of rapidity was considered (Δy) -- $\Delta n/\Delta y$. The ISR data shows that by increasing the values of the $\Delta n/\Delta y$ starting from some values of the $\Delta n/\Delta y$ the p_t distribution becomes wider (see fig.1). Wan Hove aimed to explain the fact as a signal on deconfinement [2] in hot medium and formation of the Quark Gluon Plasma (QGP) [3]. In this paper we discuss some properties of central collisions. These are necessary to get the signal on the deconfinement and to identify QGP.

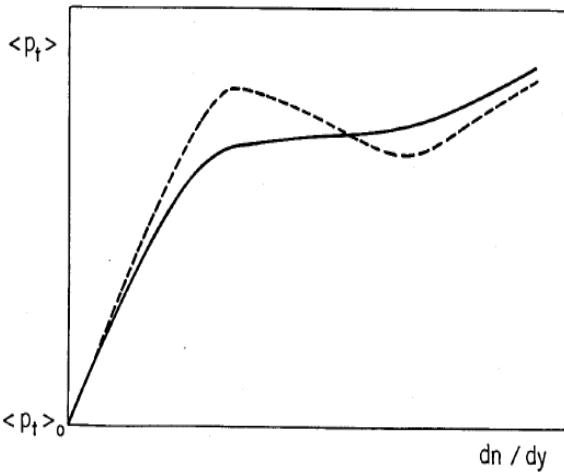


Fig. 1. The dn/dy - dependence of the average values of P_t .

2. SOME PROPERTIES OF CENTRAL COLLISIONS

2.1 HADRON-NUCLEUS COLLISIONS

Fig.2 demonstrates a number of $\pi^{-12}\text{C}$ -interactions (N_{star}) as a function of the number of identified protons N_p [4]. In this experiment N_p was used to fix the centrality. One can see the regime change in the behavior of the values of N_{star} as a function of N_p near the value of $N_p = 4$. The value was used to select the $\pi^{-12}\text{C}$ -reactions with total disintegration of nuclei (central collisions).

As an example of existence of the regime change in proton-nucleus collisions we can show Λ production (see fig.3) as a function of collision centrality for 17.5 GeV/c

p-Au collisions has been measured by BNL E910 [5]. The centrality of the collisions is characterized using a derived quantity v , the number of inelastic nucleon-nucleon scatterings suffered by the projectile during the collision. The open symbols are the integrated gamma function yields, and the errors.

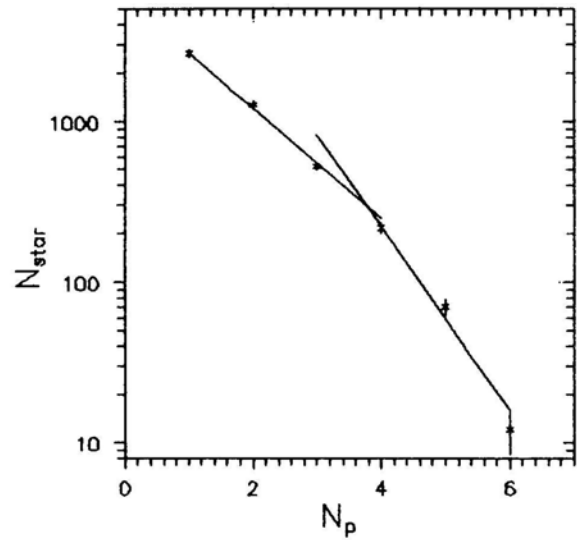


Fig. 2. A number of $\pi^{-12}\text{C}$ -interactions (at $P_\pi=40$ GeV/c) as a function of the N_p .

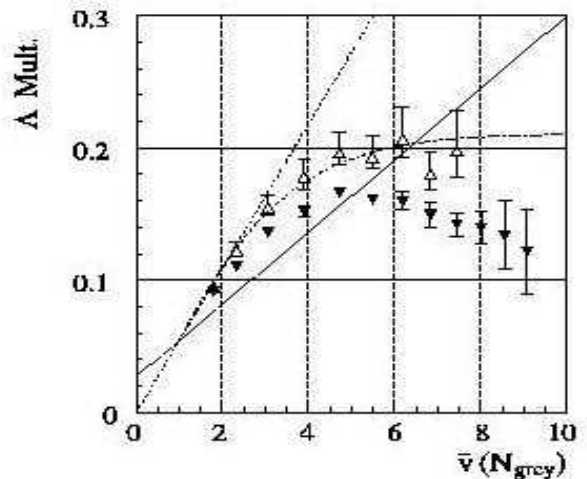


Fig. 3. The Λ yield versus v .

Shown represent 90% confidence limits including systematic effects from the extrapolations. The full symbols are the fiducial yields. The various curves represent different functional scaling. The same results

have been obtained by BNL E910 Collaboration for π^- , K_s^0 - and K^+ - mesons emitted in p+Au reaction.

2.2. NUCLEUS-NUCLEUS COLLISIONS

From Fig.4 one can see the behaviors of the event number as a function of centrality for light nuclei interactions: dC-, HeC- and CC-interaction at 4.2 A GeV/c [6]. There are regime changes again for these interactions. These points of regime change could be used to select the central collisions.

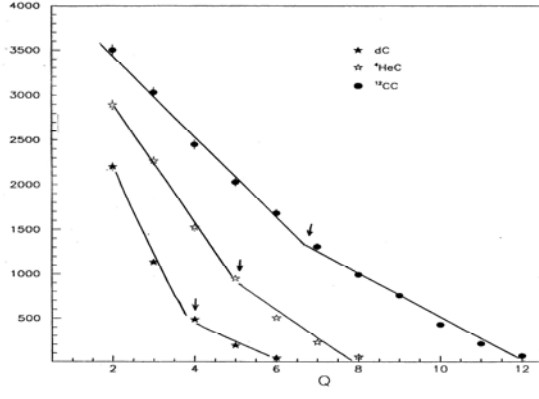


Fig. 4. The number of dC-, HeC- and CC- reactions as a function of centrality at 4.2 A GeV/c.

2.3 HEAVY ION COLLISIONS

Experimental ratios of $\langle K^+ \rangle$, $\langle K^- \rangle$, ϕ , and Λ to $\langle \pi^+ \rangle$ plotted as a function of system size (fig.5). Statistical errors are shown as error bars, systematic errors if available as rectangular boxes. The curves are shown to guide the eye and represent a functional form

$$a - b \exp(-\langle N_{part} \rangle / 40).$$

At $\langle N_{part} \rangle = 60$ they rise to about 80% of the difference of the ratios between $N_{part} = 2$ and 400 [7].

The ratio of the J/ψ to Drell-Yan cross-sections has been measured by NA38 and NA50 SPS CERN (see Fig.6) as a function of centrality of the reaction estimated, for each event, from the measured neutral transverse energy E_t [8]. Whereas peripheral events exhibit the normal behavior already measured for lighter projectiles or targets, the J/ψ shows a significant anomalous drop of about 20 % in the E_t range between 40 and 50 GeV. A detailed pattern of the anomaly can be seen in fig. 6 which shows the ratio of the J/ψ to the Drell-Yan cross-sections divided by the exponentially decreasing function accounting for normal nuclear absorption. Other significant effect which is seen from this picture is a regime change in the E_t range between 40 and 50 GeV both for light and heavy ion collisions and saturation.

Recent data obtained by STAR RHIC BNL[9] on the behavior of the nuclear modification factors of the strange particles as a function of the centrality in Au+Au- and p+p-collisions at $\sqrt{s_{NN}} = 200$ GeV is shown in Fig.7. One can see regime change and saturation for the behavior of the distributions. To fix the centrality the values of participants (N_{part}) was used.

Recent results from RHIC on heavy flavor production [10] show nuclear modification function (R_{AA}) distributions for Au+Au and Cu+Cu collisions (see Fig.8) as a function of centrality. A number of participants

(N_{part}) were used to fix the centrality. We can see again the regime change and saturation in the behavior of the distributions.

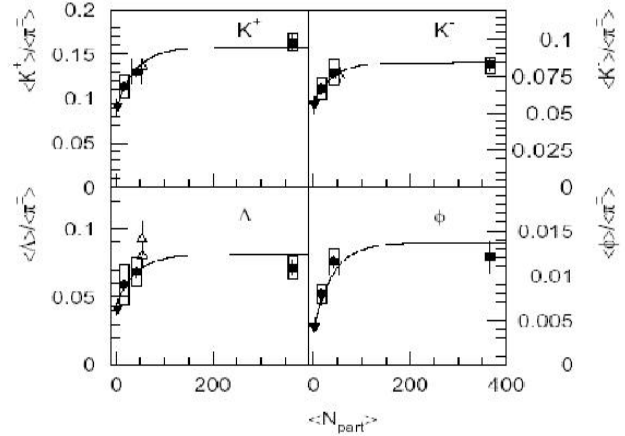


Fig.5 The experimental ratios of $\langle K^+ \rangle$, $\langle K^- \rangle$, ϕ , and Λ to $\langle \pi^+ \rangle$ plotted as a function of system size (∇ p+p, C+C and Si+Si, \bullet S+S, \blacksquare Pb+Pb).

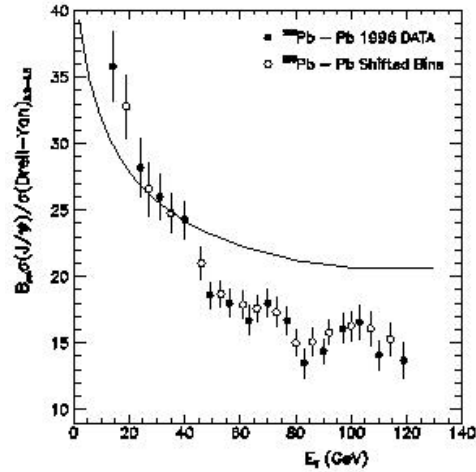


Fig.6. The ratio of the J/ψ to Drell-Yan cross-sections as a function of centrality.

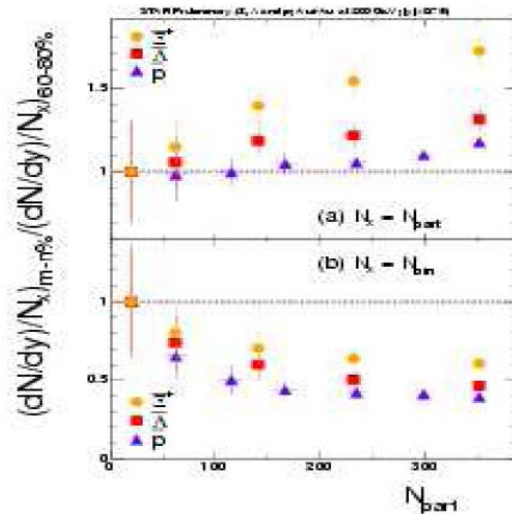


Fig.7. The nuclear modification factors of the strange particles as a function of centrality.

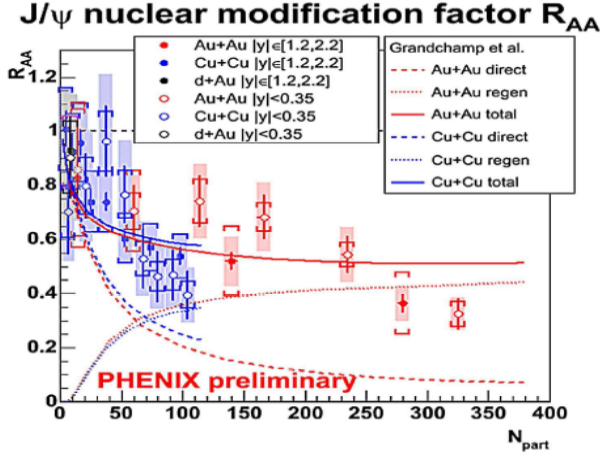


Fig.8. The values R_{AA} as a function of N_{part} for heavy flavor coming from RHIC.

3. DISCUSSION

The points of regime change appear for the behavior of some characteristics of events as a function of centrality as some critical phenomena for hadron-nuclear, nuclear-nuclear interactions and for ultrarelativistic ion collisions. The phenomenon observed in the wide range of energy and almost for all particles (mesons, baryons, strange particles and heavy flavor particles). After point of regime change the saturation is observed. The simple models (such as wounded-nucleon model and the cascade model) which are usually used to describe the high energy hadron-nuclear and nuclear-nuclear interactions could not explain the results. To explain this result it is necessary to suggest that the dynamics of the phenomena is same for hadron-nuclear, nuclear-nuclear and heavy ion interactions and is independent of the energy and mass of the colliding nuclei. The responsible mechanism to describe the above mentioned phenomena could be statistical or percolation ones because phenomena have a critical character. In Ref. [11] complete information was presented about using statistical and percolation models to explain the experimental results coming from heavy ion physics. However, it is known that the statistical models give more strong A -dependences than percolation mechanisms. That is why we believe that the responsible mechanism to explain the phenomena could be percolation cluster formation [12]. Big percolation cluster may be formed in the hadron-nuclear, nuclear-nuclear and heavy ion interactions independent of the colliding energy. But the structure and the maximum values of the reached density and temperature of hadronic matter could be different for different interactions depending on the colliding energy and masses within the cluster. Ref. [13] shows that deconfinement is expected when the density of quarks and gluons become so high that it no longer makes sense to partition them into color-neutral hadrons, since these would strongly overlap. Instead we have clusters much larger than hadrons, within which color is not confined; deconfinement is thus related to cluster formation. This is the central topic of percolation theory, and hence a connection between percolation and deconfinement [13] seems very likely. So we can see that the deconfinement could occur in the percolation cluster. Ref. [13] explains the charmonium suppression as a result of deconfinement in cluster.

Experimental observation of the effects connected with formation and decay of the percolation clusters in heavy ion collisions at ultrarelativistic energies and the study of correlation between these effects could provide the information about deconfinement of strongly interacting matter in clusters. We suggest two effects to identify the percolation cluster formation. One is the nuclear transparency effect and other light nuclear production.

In Ref. [14] percolation cluster is a multibaryon system. Increasing the centrality of collisions, its size and masses could increase as well as its absorption capability and we may see saturation. So after point of regime change the conductivity of the matter increases and it becomes a superconductor [13] due to the formation of percolation clusters. In such systems the quarks must be bound as a result of percolation.

The critical change of transparency could influence the characteristics of secondary particles and may lead to their change. As collision energy increases, baryons retain more and more of the longitudinal momentum of the initial colliding nuclei, characterized by a flattening of the invariant particle yields over a symmetric range of rapidities, about the center of mass - an indicator of the onset of nuclear transparency. To confirm the deconfinement in cluster it is necessary to study the centrality dependence in the behavior of secondary particles yields and simultaneously, critical increase in transparency of the strongly interacting matter.

Appearance of the critical transparency could change the absorption capability of the medium and we may observe a change in the heavy flavor suppression depending on their kinematical characteristics. It means that we have to observe the anomalous distribution of some kinematical parameters because those particles which are from area with superconductive properties (from cluster) will be suppressed less than the ones from noncluster area. So the study of centrality dependence of heavy flavor particle production with fixed kinematical characteristics could provide the information on changing of absorption properties of medium depending on the kinematical characteristics of heavy flavor particles.

In Ref. [15] it was suggested that the investigation of the light nuclei production as a function of the centrality could give the clue on freeze-out state of QGP formation, which may be used as an additional information to confirm the percolation cluster formation near the critical point. There are two types of light nuclei emitted in heavy ion collisions: first type are the light nuclei which get produced as a result of nucleus disintegration of the colliding nuclei; while the second ones are light nuclei which are get comprised of protons and neutrons (for example, as a result of coalescence mechanism) which were produced in heavy ion interactions. In an experiment we can separate these two types of nuclei from each other using the following ideas: the yields for first type of nuclei have to decrease, by some regularity, with centrality of collisions. On the other hand, formation of the clusters could be a reason of the regime change in the behaviour of light nuclei yields as a function of centrality in the second type.

- [1] *L. Wan Hove*. Preprint TH.3391-CERN, 1982, CERN.
- [2] *M. K. Suleymanov et al.* Nuclear Physics B (Proc. Suppl.) , vol. 177–178 , pp. 341–342, 2008; E-print:nucl-ex/0706.0956, 2007.
- [3] *M. Gazdzicki and S. Mrowczynski*.Z.Phys., C54,127, 1992.
- [4] *O. B. Abdinov et al.* JINR RC, 1996, No 1[75]-96 pp. 51.
- [5] Ron Soltz for the E910 Collaboration, J. Phys. G: Nucl. Part. Phys., 27, pp. 319–326, 2001.
- [6] Preprint JINR 1-12114, 1979; 1-12424, 1989, P1-98-292,; *M. K. Suleimanov et al.*, Phys.Rev.C, 1998, 58, pp. 351.
- [7] *C. Alt, et al.* Phys.Rev.Lett. 94, 2005, 052301.
- [8] *C. Abreu et al.*, Phys. Lett. B 1999, 450, p. 456; *M. C. Abreu et al.*, Phys. Lett. B, 1997, 410, p. 337; *M. C. Abreu et al.* Phys. Lett. B, 1997, 410, p. 327; *M. C. Abreu et al*, NA50 Collaboration, Phys. Lett. B, 2001, 499, pp. 85-96.
- [9] Christelle Roy for STAR Collaboration POS (HEP), 2005, 141.
- [10] *A. P. Suaide*, Brazilian Journal of Physics, vol. 37, no. 2C, June 2007, 731-735.
- [11] Claudia Höhne, GSI Darmstadt, Probing QCD with High Energy Nuclear Collisions, Hirschegg, 2005.
- [12] *Helmut Satz* arXiv: hep-ph/0212046, 2002; *Janusz Brzychczyk*, arXiv:nucl-th/0407008. 2004; *C. Pajares*, arXiv:hep-ph/0501125, 2005.
- [13] *H. Satz*, arXiv:hep-ph/0007069, 2000.
- [14] *K. Suleymanov et al.*, Acta Phys. Polon. Supp.1, 405-406, 2008.
- [15] *M. K. Suleymanov et al.*, nucl-ex/0804.3133, 2008.

INFLUENCE OF ACETIC ACID ON THE PROCESS OF STAIN POROUS SILICON FORMATION AT OXIDANT INSUFFICIENCY

F.A. RUSTAMOV, N.H. DARVISHOV, M.Z. MAMEDOV,
E.Y. BOBROVA, H.O. QAFAROVA

*Baku State University, Institute for Physical Problems., Semiconductor Physics Division,
AZ-1148, Z. Khalilov, 23, Baku, Azerbaijan*

The influence of acetic acid on the process of stain porous silicon formation at oxidant insufficiency has been investigated. The process of porous formation has been estimated to be appreciably changed in concentration of acetic acid above 5%. This resulted in improvement of both reproducibility and lateral homogeneity of nanoporous silicon films. All obtained samples exhibit intensive photoluminescence in visible spectra at room temperature.

1. INTRODUCTION

Nanoporous silicon is a promising material due to its capabilities of use in Si – based optoelectronic integrating circuits [1, 2]. Nanoporous Si exhibits fairly intensive red – orange photo – and electroluminescence in visible spectra in contrast to Si itself [3,4]. The investigations show large perspectives in the use of nanoporous silicon layers as antireflecting coating for solar elements [5,6]. The layers of nanoporous Si are obtained both by electrochemical and pure chemical etching. In case of anodization the Si substrate is a supplier of holes needed for PS layers formation, but in chemical etching the ones are generated in solution during the HNO₃ dissociation. In electrochemical etching it is necessary to apply the external voltage, whereas in chemical etching anode and cathode processes occur locally on the Si substrate surface. That nanoporous Si layers obtained by pure chemical etching are rather thin but possess a significant porosity of about 70-80%. While a mechanism of porous silicon formation is identical in both cases, the chemical stain etching doesn't need applied voltage, so the problem of contacts no longer arises. Moreover in this method even very thin layers of porous Si (20 – 200 nm) are luminescence, so the problem of cracking no longer arises too [1,7,8].

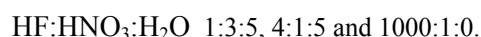
The reaction of Si and electrolyte is electrochemical, since it runs with the participation of holes and electrons of semiconductive material. The silicon surface plays a part of multielectron galvanic element consisting from a large number of connected with each other microelectrodes – anode and cathodes (between them local surface current develops). Areas of surface with the large number of distorted bonds (the grain's interfaces, hillocks and peaks on the polish surface) have the most negative potential, play a role of anodes and dissolve in the solvent. The anode reaction, proceeding with electron yield, leads to Si oxidation, covalent bonds distortion and building up holes and free electrons, migrating along the surface to cathode areas. The areas with less distorted structure having more positive electrode potential are the cathodes. These cathodes do not dissolve but only transfer the anode's electrons to molecules and ions of etchant to favor the oxidation – reduction.

In this, at the energy – homogeneous surfaces the redox and dissolution reactions really occur at the same place, apart from each other and with same rate. But at the energy – nonhomogeneous surfaces these reactions run apart from each other with different rates and are spatially separated.

It is known that Si etching reaction in HF/HNO₃ solutions is autocatalytic and runs according to this scheme [1]:



Thus, depending on type and value of original Si wafers conductivity and etchant composition the incubation period can range from few second to 30 min. The process is followed by H₂ evolution, which affects the morphology and lateral homogeneity of obtained samples. In electrochemical etching methanol, ethanol or 2-propanol are added to HF to increase the wettability the PS surface, to minimize H₂ yield and prevent against bubbles adhesion. It isn't desirable to add these alcohols in the solution during the chemical etching in HF/HNO₃ mixture since it enters into reaction with the etchant [9]. Usually at stain etching an acetic acid (CH₃COOH) is used for this purpose. It has low surface tension and so increases the wettability of hydrophobic Si surface [1.2]. At the present time for obtaining the porous silicon by pure chemical etching the following etchants compositions are mainly used:



The selections of the composition are determined by the substrate conductivity, incubation period, reproducibility, lateral homogeneity, luminescence and antireflection properties. In etchant solution 1000:1, i.e. for lack of oxidant, the PS formation process is controlled by rate of Si oxidation by nitric acid. In this case spontaneous reaction occurs whatever the type and conductivity of silicon wafers and it is characterized by good reproducibility and more thick layers of PS [10-12].

The given work is aimed at investigation of the question: how does the addition of acetic acid affect the morphology and luminescence properties of porous Si in HF/HNO₃ solution in regime of lack of oxidant.

2. EXPERIMENT

In the present work the porous Si layers were fabricated by stain etching on the monocrystalline p-Si wafers with (100) orientation and 20 Ω.cm resistivity, polished on each side. As etchant were used a solutions of hydrofluoric (49%) and nitric (65%) acids in proportion of 1000:1 and 1200:1 with various amount of acetic acid to be added. The etching was run only on the one side of wafers in teflon cell. The etched area is 1 cm². The use of

chemically resistant seal has made possible to carry out the etching on only one side of wafer and remove boundary influence. Before the beginning of etching the wafers were washed in organic solvents in order to remove the organic contaminations. At first, the wafers were immersed in acetone for around five minutes and washed in bidistilled water. Then ones were immersed in propanol and were washed in water again. The wafers were finally immersed in 5% aqueous solution of HF to remove of natural oxide layer from silicon surface and after washing in water were blown by N₂ jet.

The chemical etching was run at daylight illumination at room temperature during 1 – 15 min. After etching the samples were washed in bidistilled water, then in propanol and were dried by N₂ jet.

Morphology of *por*-Si and porous layer thickness have been inspected by interference microscope MII-4 and SEM. Photoluminescence spectra have been investigated under room temperature. The PL was excited by xenon lamp DKSL -1000, transmitted through monochromator SPM-2 and was recorded by monochromator IKS-12 in geometry “on reflection”. Signal was recorded by cooled photoelectric multiplier FEU-83. Photoluminescence spectra have been corrected on sensibility of spectrometric system.

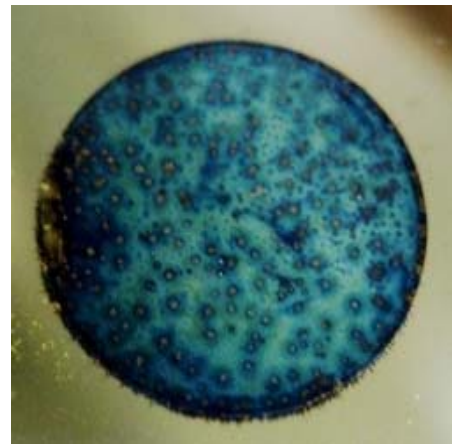
3. RESULTS AND DISCUSSION

Experiments demonstrated that in 1000:1 solution (although the incubation period is 60 sec) the *por*-Si formation process is followed by abundant hydrogen gas evolution. As result there are many nonetched areas on the surface of obtained samples (fig.1a). The incubation period increases to 120 sec with increasing acetic acid concentration to 20%. The reaction runs slowly, but H₂ evolution decreases. Interference bands on the samples surface points to lateral nonhomogeneity over the layer thickness (fig.1b). Reproducibility of samples obtained under these etching conditions is very good. The increasing CH₃COOH content effects on rate and duration of reaction (reaction rate decelerates and it's duration decreases). In further increase of acetic acid concentration the incubation period essentially increases, many nonetched areas appear and reproducibility essentially gets worse.

In solution of 1200:1 the incubation period was about 30 sec, but the porous formation process proceeded very slowly although without marked H₂ bubbles evolution. The addition of acetic acid (5 – 10%) remarkable affects the *por*-Si formation process. Reaction begins over the entire surface at the same time. With increasing of etching time the colour of the surface changes wave-like, manifesting all rainbow colours. It is indicated of homogeneous thickness growth of obtained porous silicon. The observed scene resembles Si surface oxidation process. During ~60 sec the process runs **without the bubbles evolution and the lateral homogeneous** of samples with mirror-like surface are obtained in this case (Fig.1c). The *por*-Si layer thickness more increases with increasing of etching time, but in so doing bubbles begin to rise and distort the sample homogeneity.

The investigations of samples morphology at SEM demonstrate that in all cases nanoporous silicon is formed

and has red cathodoluminescence under electron irradiation.



a)



b)



c)

Fig.1. Stain PS in HF:HNO₃: CH₃COOH. (a) 1000:1:0, (b) 1000:1:100, (c) 1200:1:100.

The emission and excitation spectra of porous silicon have been investigated under room temperature too. Excitation was induced by the wave of 350 nm. All samples have rather intense red - orange luminescence visible with naked eye at daylight illumination at room temperature.

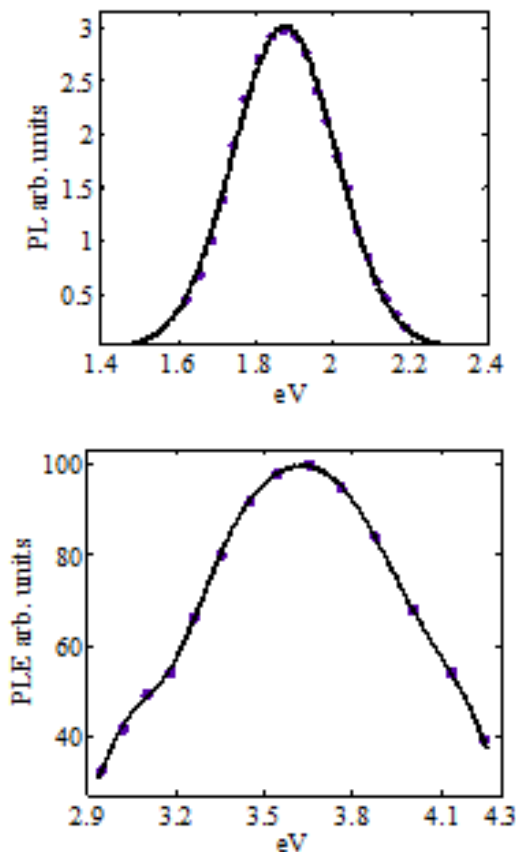


Fig2. Photoluminescence (a) and excitation (b) spectra of stain PS

A photoluminescence spectra does not change during exposure of the samples at the ambient laboratory

atmosphere by the month. With increasing of etching time the maximum of emission spectra of fresh prepared samples shifts from 1.7 to ~1.9 eV and rather good is extrapolated by one Gaussian (fig.2a). The halfwidth of spectrum is about ~0.31 eV. Excitation spectrum was taken at 650 nm (Fig.2b).

It is known that the composition and concentration of etchant strongly affect both the process of etching and morphology of obtained samples. Depending on concentration of HF:HNO₃ : CH₃COOH solutions the etching can lead to either polishing surface or the por-Si formation. In microelectronics these solutions are usually used for final polishing of Si wafers surface. The addition of acetic acid helps to reduce the effective oxidation of Si to supply the holes needed for reaction. It is clear from the investigation that such complex action of acetic acid results in perfecting lateral homogeneity of samples and quenching of H₂ bubbles appearance and doesn't change the incubation period. The decrease of reaction rate has made possible to obtain the homogeneous layers of various thickness and with various maximum of photoluminescence. The homogeneity of porous silicon does not deteriorate with increasing time of etching. Good extrapolation of emission spectra by one Gaussian and form of excitation spectra points to the radiation proceeding only via one recombination center related to quantum confinement effect and its half-width indicates the dispersion of nanocrystalline sizes.

The work was carried out by support of "50+50" program of Baku State University.

-
- [1]. L.T. Chanham. Properties of porous silicon. EMIS Data Review Series No. 18, London, 1997, 424pp.
 - [2]. V. Lehmann. Electrochemistry of Silicon. New York: Willey VCH, 2002, p.277.
 - [3]. L.T. Chanham. *Appl. Phys. Lett.* 57, 1990, 1046.
 - [4]. V. Lehmann, U. Gosele. *Appl. Phys. Lett.* 58 (1991) 856.
 - [5]. M. Lipinski, P. Panek, E. Bielanska, J. Weglowska, H. Czternastek. *Opto-Electron. Rev.* 8(4), 2000, 418
 - [6]. B. Gonzalez-Diaz et al. *Mater.Sci.Eng. B*, 150-160, 2008, 295
 - [7]. S.D. Campbell, L.A. Jones, E. Nakamichi, F.X. Wei, L.D. Zajchowski. *J. Vac. Sci. Technol. B* 13(3), 1995, 1184
 - [8]. J.Xu, J. Steckl. *J. Vac. Sci. Technol. B* 13(3), 1995, 1221
 - [9]. M. Nahidi, K.Ü. Kolasinski. *J.Electrochem. Soc.*, 153(1), C19-C26, 2006
 - [10]. L.Schirone, G.Sotgiu, M.Montecci. *J. Luminescence* 80, 1999, 163.
 - [11]. E. A. Старостина, В.В. Старков, А.Ф. Вяткин. *Микроэлектроника*, 31, 2, 2002, 104
 - [12]. B. Gonzalez-Diaz et al. *Sensors and Actuators. A* 150, 2009, 97
 - [13]. Sh.M. Efendiev, N.G. Darvishov. *Phys. Stat. Sol.(a)*. 86, 1984, 105.

ON INTERACTION OF MACROMOLECULES WITH THE MOLECULES OF SOLVENT IN THE SYSTEM POLYETHYLENEGLYCOL – WATER

H.F. ABBASOV

Baku State University, AZ-1148, Z.Halilov str., 23

The refraction properties of the diluted water solutions of polyethylene glycols with different molecular mass have been investigated. Equation Lorenz- Lorenz has been used for explanation experimental results and the contributions to the general polarization of both the free molecules of water and the hydrated macromolecules of polymer were considered. The influence of KOH on the solubility of polyethylene glycol was studied by dielectric spectroscopy, also.

It is well known that at the optical frequencies the contribution to the polarization of medium gives only the electrons, which are oscillated under the electric field of light wave [1, 2]. In this case for the homogeneous medium equation Lorenz- Lorenz is carried out [3]:

$$\frac{n^2 - 1}{n^2 + 2} = \frac{N\alpha}{3} \quad (1)$$

where, n - the refractive index of medium, N - concentration, α is the polarizability of the molecules of substance.

Assuming the additivity of polarizability, formula (1) can be written as follows for the diluted aqueous solutions of polymers:

$$\frac{n^2 - 1}{n^2 + 2} = \frac{(N_{w0} - k \cdot N_p) \cdot \alpha_w}{3} + \frac{N_p \cdot \alpha_p}{3} \quad (2)$$

where, k is the interaction parameter, which determines the number of molecules of water connected with one macromolecule, n - refractive index of solution, N_{w0} - the number of molecules of water per unit of volume of clean solvent, α_w - the polarizability of not connected with the macromolecules of the polymer molecules of water, N_p - the number of macromolecules of the polymer per unit of solution volume and α_p - the polarizability of the hydrated macromolecules, respectively.

In equation (2) the first component in the right side reflects the polarization of the free molecules of water, not taking part in the hydration, and the second component - the polarization of the macromolecules of polymer, kN_p indicates the number of molecules of water connected with the macromolecules in the unit volume of solution. Let us note that the polydispersion of the macromolecules of polymer is not taken into account in given case, we assume that the polymer is monodisperse. Formula (2) can be rewritten as follows:

$$\frac{n^2 - 1}{n^2 + 2} = \frac{N_{w0}\alpha_w}{3} + \frac{N_p(\alpha_p - k\alpha_w)}{3} \quad (3)$$

The number of molecules of the polymer per unit of volume of solution can be represented as follows:

$$N_p = \frac{N_{TotP}}{V} = \frac{v_p N_A}{V} = \frac{m_p N_A}{M_p V} = \frac{cm N_A}{M_p V} = \frac{c \rho N_A}{M_p} \quad (4)$$

where, N_{TotP} is the total number of macromolecules in the solution, m_p, M_p, c are the mass, the molar mass and the concentration of polymer in the solution, respectively, m, ρ, V are the mass, density and the volume of solution, respectively, N_A is Avogadro constant, v_p - the number of moles of polymer in the solution. After substituting expression (4) in formula (3), and having also replaced $(N_w \alpha_w)/3$ on $(n_w^2 - 1)/(n_w^2 + 2)$ we will obtain:

$$\frac{n^2 - 1}{n^2 + 2} = \frac{n_w^2 - 1}{n_w^2 + 2} + \frac{c \rho N_A}{3 M_p} \cdot (\alpha_p - k \alpha_w) \quad (5)$$

In this formula the refractive index of pure water is designated through n_w , which can easily be measured experimentally.

In the first rough approximation it is possible to show α_p as the volume of the hydrated macromolecule, which strictly depends on the conformation of the macromolecule:

$$\alpha_p \approx v_p \approx \frac{m_{0p} + km_w}{\rho} \approx (M_p + kM_w) \cdot \frac{1}{\rho N_A} \quad (6)$$

where, m_{0p} is the mass of polymer macromolecule, m_w - the molecular mass of water.

Taking into account (6) in formula (5) we will obtain:

$$\frac{n^2 - 1}{n^2 + 2} = \frac{n_w^2 - 1}{n_w^2 + 2} + \frac{c}{3} \left[1 + \left(\frac{M_w}{M_p} - \frac{\rho N_A}{M_p} \alpha_w \right) k \right] \quad (7)$$

We measured the concentration dependence of the refractive index of the diluted aqueous solutions of polyethylene glycols with different molecular weights. Obtained data are represented in Fig. 1 through the $(n^2 - 1)/(n^2 + 2) - c$ diagram. As shown in the figure this dependence is linear up to the certain concentration, where the interaction parameter of macromolecules with the water molecules does not depend on the polymer concentration. As the concentration increases, the

coefficient k , and solution density ρ become dependent on C .

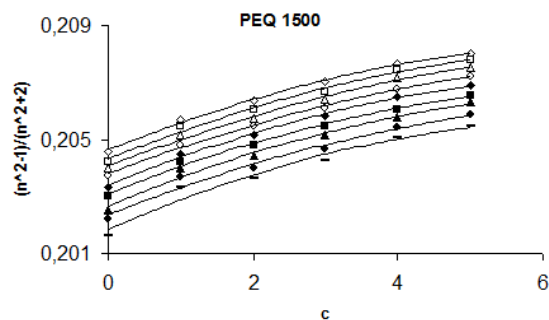


Fig. 1. Concentration dependence of $(n^2 - 1)/(n^2 + 2)$ for the aqueous solution of polyethylene glycol with molecular weight 1500

Dependence of the coefficient k from C is caused by the fact that when the interaction of the macromolecules with each other begins to occur, the conformation of macromolecules changes: balls get more unpacked with the increase in the concentration of macromolecules and attract more water molecules, which is expressed as the change in the angular coefficient (Fig. 1). Solution density grows proportionally with the polymer concentration, as a result of which, the coefficient in front of k in equation (7) decreases as C increases, which also leads to the decrease of slope angle in the indicated dependence. Occurrence of interaction starting from a certain concentration and a change in the structure of aqueous solution were confirmed by our studies on aqueous solutions of polyethylene glycols tested by the low-frequency dielectric spectroscopy method [4, 5].

The influence of KOH on the solubility of polyethylene glycol was studied by dielectric spectroscopy [6, 7, and 8]. Effect of third component on the solubility of the substance in water depends on the polarity or non-polarity introduced into the solution component, and this dependence can be established by investigating the permittivity of the solution [9]. Molecules are introduced into the solution of salt, bases, acids, etc. under the influence of water molecules dissociated on ions and around these ions formed hydrate layer of polar water molecules.

At this time the no polar solute molecules are available in the water pushing from all sides gather in one place, resulting in the dielectric constant of the solution

increases, the solubility of no polar substances weakens. On the contrary, in the case of polar substances molecules of these substances are actively involved in solvation of ions, the solubility of polar substances is growing; the dielectric constant of the solution is increased.

Figure 2 identifies the dependence of the dielectric constant of aqueous solution of polyethylene glycol and KOH on the concentration of KOH. As can be seen up to a certain concentration of KOH solution permittivity

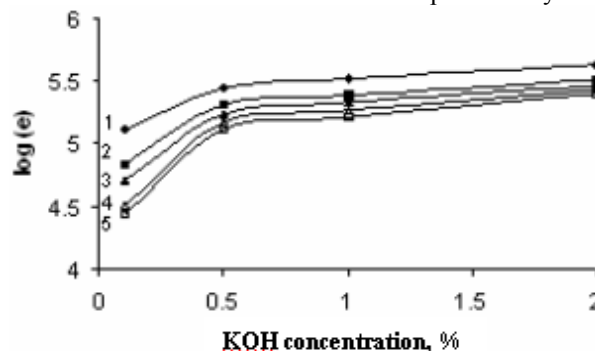


Fig. 2. The dependence of the dielectric constant of aqueous solution of polyethylene glycol and KOH on the concentration of KOH

increases, and then reaches saturation. This fact can be explained as follows. Dissociation of KOH in water is separated on ions and around these ions occurs hydrate shell. Up to a certain concentration of KOH the hydrate shell is created by the free water molecules. As a result, no polar macromolecule polyethylene glycol crowding get together, i.e. solubility of polyethylene glycol under the action of KOH is deteriorating. At a certain critical concentration of all available in the free solution water molecules have already become involved in the hydration. With further increase of the concentration of KOH hydrate shell around the ions can formed through job-related in the clusters of water molecules, but it requires more energy compared with free water molecules. Therefore, from a certain critical concentration of KOH has little effect on the solubility of PEG in water.

Given these considerations on the critical concentration the ratio of free water molecules to the number of bound water molecules can be measured in the solution.

- [1] P.T. Oreshkin "Physics of semiconductors and dielectrics", 1977, Moscow "Higher school", 448 s.
- [2] C.J.F Bottcher. and P. Bordewijk, Theory of electric polarization. Elsevier, Amsterdam, 1992
- [3] G.S. Landsberg, "Optics", the publishing house "Science", Moscow, 1976, s. 926.
- [4] E.A. Masimov, H.F. Abbasov. "About structural changes in the aqueous solutions", Russian international conference on the chemical thermodynamics "RCCT-2007", Suzdal, 2007
- [5] E.A. Masimov, H.F. Abbasov. "Structural changes in the diluted aqueous solutions of polyethylene glycol", XV All-Russian conference, "Structure and the dynamics of molecular systems", [Yalchik] - 2008, June 30 - July 4, 2008.
- E.A. Masimov, H.F. Abbasov. Baku University news, BSU, № 2, 2007, p.21-40.
- E.A. Masimov, H.F. Abbasov. J. of Qafqaz University, № 23, 2008, p.59-61
- E.A. Masimov, H.F. Abbasov, XV Vserossiyskaya konfer.«Struktura i dinamika molekulyarnikh sistem»,Yalchik – 2008, 30 iyunya – 4 iyulya, 2008g.
- E.A. Masimov, H.Sh. Hasanov. "Thermodinamics of biological systems", Baku, 2007, 411 p.

ON THE FINITE-DIFFERENCE ANALOGUE OF THE LINEAR SINGULAR OSCILLATOR AND ITS $su(1,1)$ DYNAMICAL SYMMETRY ALGEBRA

S.M. NAGIYEV¹, E.I. JAFAROV¹, R.M. IMANOV²

¹ *G.B. Abdullayev Institute of Physics, Azerbaijan National Academy of Sciences*

Javid av. 33, AZ-1143, Baku, Azerbaijan

² *Physics Department, Ganja State University*

A. Camil str. 1, AZ-2700, Ganja, Azerbaijan

We consider the finite-difference analogue of the linear singular oscillator. It can be solved both analytically and by using group-theoretical approach. Its wave functions being eigenfunctions of the finite-difference Hamiltonian are expressed in terms of the continuous dual Hahn polynomials. The dynamical symmetry of this problem is $su(1,1)$ Lie algebra. Raising and lowering operators also have finite-difference form and they are generators of this algebra.

INTRODUCTION

Quantum singular oscillator in the non-relativistic approach thanks to its specific properties quite different than properties of the usual non-relativistic harmonic oscillator, has been used for enormous applications in various fields of modern physics and technologies.

It is known that the linear singular oscillator problem in the non-relativistic quantum mechanics is governed by the Hamiltonian [1]

$$H_N = \hbar\omega \left(-\frac{1}{2} \partial_\zeta^2 + \frac{1}{2} \zeta^2 + \frac{g_0}{\zeta^2} \right), \quad (1)$$

where $\zeta = \sqrt{m\omega/\hbar}x$ is a dimensionless position and $g_0 = mg/\hbar^2$.

The linear singular oscillator being one of the exactly solvable problems of the non-relativistic quantum mechanics has been extensively used in many applications. There are a lot of quantum mechanical and field theory problems leading to solution of Schrödinger equation with Hamiltonian (1).

In the interval $0 < \zeta < \infty$ the eigenfunctions of the Hamiltonian (1) are expressed in terms of the associated Laguerre polynomials:

$$\psi_n^{nonrel}(\zeta) = c_n^{nonrel} \zeta^{d+\frac{1}{2}} e^{-\frac{\zeta^2}{2}} L_n^d(\zeta^2), \quad (2)$$

$$d = \frac{1}{2} \sqrt{1+8g_0}.$$

Eigenvalues of operator H_N corresponding to (2) have the following form:

$$E_n^{nonrel} = \hbar\omega(2n + d + 1), \quad n = 0, 1, 2, 3, \dots \quad (3)$$

The purpose of this paper is to construct and investigate an exactly solvable finite-difference analogue of the linear singular oscillator (1). Our construction is based on the relativistic quantum mechanics that has been developed in a number of published works [2-9].

THE FINITE-DIFFERENCE LINEAR SINGULAR OSCILLATOR

In the framework of this relativistic approach, the transformation between one-dimensional configuration x - and p -representations is performed as follows:

$$\Psi(x) = \frac{1}{\sqrt{2\pi\hbar}} \int d\Omega_p \xi(p, x) \Psi(p). \quad (4)$$

As one observes, this transformation is rather different than the similar transformation in the canonical non-relativistic quantum mechanics because of its expansion in terms of the matrix elements of the representation of the Lobachevsky space motion group

$$\xi(p, x) = \left(\frac{p_0 + p}{mc} \right)^{ix/\lambda}. \quad (5)$$

Corresponding Lobachevsky space is realized as a hyperbola in the (p_0, p) plane through $p_0^2 - p^2 = m^2 c^2$, for the positive $p_0 > 0$ branch.

We consider the finite-difference analogue of the linear singular oscillator, which is described by the following Hamiltonian:

$$H = \hbar\omega \left\{ -\frac{1}{\delta^2} \cosh(i\delta\partial_\zeta) + \left[\frac{1}{2} \zeta(\zeta + i\delta) + \frac{g_0}{\zeta(\zeta + i\delta)} \right] e^{i\delta\partial_\zeta} \right\}, \quad (6)$$

where $\delta = h\sqrt{m\omega/\hbar}$ and h is a step of the finite-difference differentiation. In the framework of the non-relativistic quantum mechanics one can select h as Compton wavelength of the particle, i.e. $h = \lambda = \hbar/mc$.

The correct limit, where (6) reduces to (1) can be easily shown, i.e. it is obvious that $H \rightarrow H_N$ in the limit $\delta \rightarrow 0$ (or $h \rightarrow 0$).

SYMMETRY ALGEBRA

The eigenfunctions of Hamiltonian (6) obeying the boundary conditions $\psi(0) = 0$ and $\psi(\infty) = 0$ are explicitly given by [10]

$$\psi_n(\zeta) = c_n (-\zeta/\delta)^{(\alpha)} \delta^{2\zeta/\delta} \times \Gamma(\nu + i\zeta/\delta) \cdot S_n\left(\zeta^2/\delta^2; \alpha, \nu, \frac{1}{2}\right), \quad (7)$$

where

$$\alpha = \frac{1}{2} + \frac{1}{2} \sqrt{1 + \frac{2}{\delta^4} (1 - \sqrt{1 - 8g_0\delta^4})}, \quad (8)$$

$$\nu = \frac{1}{2} + \frac{1}{2} \sqrt{1 + \frac{2}{\delta^4} (1 + \sqrt{1 - 8g_0\delta^4})},$$

and the continuous dual Hahn polynomials are

$$S_n(x^2; a, b, c) = (a+b)_n (a+c)_n \times {}_3F_2\left(\begin{matrix} -n, a+ix, a-ix \\ a+b, a+c \end{matrix} \middle| 1\right). \quad (9)$$

The functions

$$\left(-\frac{\zeta}{\delta}\right)^{(\alpha)} = i^\alpha \frac{\Gamma(\alpha + i\zeta/\delta)}{\Gamma(i\zeta/\delta)}$$

And

$$\delta^{2\zeta/\delta} \Gamma(\nu + i\zeta/\delta)$$

are related to the behavior of the wavefunction $\psi(\zeta)$ (7) at the points $\zeta = 0$ and $\zeta = \infty$, respectively.

c_n is the normalization constant and it can be easily computed from the orthogonality relation for wavefunctions (7). It has the following form:

$$c_n = \sqrt{\frac{2}{\Gamma(n+\alpha+\nu)\Gamma\left(n+\alpha+\frac{1}{2}\right)\Gamma\left(n+\nu+\frac{1}{2}\right) \cdot n!}}.$$

The energy spectrum corresponding to Hamiltonian (6) has the following form:

$$E_n = \hbar\omega(2n + \alpha + \nu), \quad n = 0, 1, 2, \dots \quad (10)$$

From the limit relation

$$\lim_{\delta \rightarrow 0} \frac{1}{n! \delta^{2n}} S_n\left(\zeta^2/\delta^2; \alpha, \nu, 1/2\right) = L_n^d(\zeta^2), \quad (11)$$

one can easily verify that in the limit $\delta \rightarrow 0$, eigenfunctions (7) coincide with the non-relativistic linear singular oscillator wavefunctions (2).

Energy spectrum (10) also has a correct non-relativistic limit, i.e.

$$E_n - \hbar\omega/\delta^2 \rightarrow E_n^{nonrel} = \hbar\omega(2n + d + 1).$$

Combining all these results, one can say that we constructed a finite-difference analogue of the linear singular oscillator. Eigenvalues and eigenfunctions of this problem are determined and it is shown that they have correct non-relativistic limit.

$SU(1,1)$ DYNAMICAL SYMMETRY GROUP

As in the non-relativistic limit, the simplicity of the obtained energy spectrum (10) allows that solution by group-theoretical methods is also possible.

One can show that Hamiltonian (6) can be factorized as follows:

$$H = \frac{\hbar\omega}{\delta^2} [b^+ b^- + \delta^2(\alpha + \nu)], \quad (12)$$

where b^\pm are the following finite-difference operators:

$$b^- = \frac{1}{\sqrt{2}} \left[e^{-\frac{i}{2}\delta\partial_\zeta} - \delta^2 e^{\frac{i}{2}\delta\partial_\zeta} (\nu + i\delta\zeta) \left(1 + \frac{\alpha}{i\delta\zeta}\right) \right],$$

$$b^+ = \frac{1}{\sqrt{2}} \left[e^{\frac{i}{2}\delta\partial_\zeta} - \delta^2 (\nu - i\delta\zeta) \left(1 - \frac{\alpha}{i\delta\zeta}\right) e^{\frac{i}{2}\delta\partial_\zeta} \right].$$

Commutation relations of these operators lead to the following expression:

$$[b^+, b^-] = \frac{1}{2} \delta^2 \left(1 + \frac{\alpha\nu}{\delta^2 \zeta^2 + \frac{1}{4}} + \delta^2 \Delta e^{i\delta\partial_\zeta} \right), \quad (13)$$

where

$$\Delta = \alpha + \nu - \frac{1}{4} + \alpha\nu \left[-\frac{(\alpha-1)(\nu-1)}{\zeta(\zeta+i\delta)} + \frac{\alpha\nu}{\left(\zeta + \frac{i}{2}\delta\right)^{(2)}} \right].$$

By using the explicit expression of b^- , one can introduce the new finite-difference B^- operator of the following form:

$$B^- = i\delta\zeta \left[\sqrt{2}e^{-\frac{i}{2}\delta\zeta} b^- - \frac{\delta^2}{\hbar\omega} H + \delta^2(\alpha + \nu) \right] + \frac{1}{2} \frac{\delta^2}{\hbar\omega} H - \frac{1}{2} \frac{\delta^2}{\hbar^2\omega^2} H^2 + \delta^2\alpha\nu. \quad (14)$$

It is possible to check that that B^- is the lowering operator:

$$[H, B^-] = -2\hbar\omega B^-. \quad (15)$$

The taking into account that we can obtain raising operator B^+ as complex conjugate of B^- , one can compute their commutation:

$$[B^-, B^+] = \frac{\delta^4}{\hbar\omega} H \left\{ 1 + \frac{2}{\delta^4} \left[\left(\delta^2 \frac{H}{\hbar\omega} \right)^2 - 1 \right] \right\}. \quad (16)$$

From (16), one observes that in order to construct closed Lie algebra of the finite-difference analogue of the linear singular oscillator, we need to introduce new pair of finite-difference operators:

$$\begin{aligned} K^- &= B^- f^{-\frac{1}{2}}(H), \\ K^+ &= f^{\frac{1}{2}}(H) B^+, \end{aligned} \quad (17)$$

where

$$f(H) = \delta^4 \left[\frac{H}{\hbar\omega} + \alpha - \nu - 1 \right] \left[\frac{H}{\hbar\omega} + \nu - \alpha - 1 \right].$$

Now, one can see that operators K^- , K^+ and

$$K_0 = \frac{1}{2\hbar\omega} H \quad \text{satisfy the commutation relations [11]}$$

$$[K_0, K^\pm] = \pm K^\pm, \quad [K^-, K^+] = 2K_0,$$

on the space of basis elements $\{\psi_n(\zeta)\}_0^\infty$, i.e.

$$[K^-, K^+] \psi_n(\zeta) = 2K_0 \psi_n(\zeta), \quad (18)$$

which determines the algebra of Lie group $SU(1,1)$. Also, the Casimir operator in this case is equal to

$$K^2 = K_0(K_0 - 1) - K^+ K^- = \frac{\alpha + \nu}{2} \left(\frac{\alpha + \nu}{2} - 1 \right) \quad (19)$$

Consequently, eigenvalues of the operator $H = 2\hbar\omega K_0$ are restricted below and are equal to

$$E_n = \hbar\omega \varepsilon_n = \hbar\omega(2n + \alpha + \nu), \quad n = 0, 1, 2, 3, \dots$$

whereas, eigenfunctions $\psi_n(\zeta)$ form the basis of the irreducible representation $D^+\left(\frac{\alpha + \nu}{2}\right)$ of the $SU(1,1)$ group.

Operators K^- and K^+ act to the wavefunctions $\psi_n(\zeta)$ as follows:

$$\begin{aligned} K^- \psi_n(\zeta) &= \kappa_n \psi_{n-1}(\zeta), \\ K^+ \psi_n(\zeta) &= \kappa_{n+1} \psi_{n+1}(\zeta), \end{aligned} \quad (20)$$

where, $\kappa_n = \sqrt{n(n + \alpha + \nu - 1)}$.

In this paper, in the framework of finite-difference approach, we constructed new kind of exactly solvable quantum mechanical model, which has similar properties with non-relativistic quantum linear singular oscillator. Its wavefunctions are expressed in terms of the continuous dual Hahn polynomials and the dynamical symmetry group is $SU(1,1)$. It has been shown that under special limit $\delta \rightarrow 0$, the finite-difference analogue easily reduces to the similar non-relativistic problem, which wavefunctions are expressed through the associated Laguerre polynomials.

-
- | | |
|--|---|
| <p>[1]. <i>L.D. Landau, E.M. Lifshitz</i>, Quantum Mechanics: Non-relativistic Theory (Oxford: Butterworth-Heinemann) 1997.</p> <p>[2]. <i>A.A. Logunov, A.N. Tavkhelidze</i>, Nuovo Cim. 29 380 (1963).</p> <p>[3]. <i>V.G. Kadyshovsky, R.M. Mir-Kasimov, N.B. Skachkov</i>, Nuovo Cim A 55 217 (1968).</p> <p>[4]. <i>N.M. Atakishiyev, R.M. Mir-Kasimov, S.M. Nagiyev</i>, Ann. der Phys. 42 25 (1985).</p> <p>[5]. <i>E.D. Kagramanov, R.M. Mir-Kasimov, S.M. Nagiyev</i>, Phys. Lett. A 140 1 (1989).</p> <p>[6]. <i>S.M. Nagiyev</i>, J. Phys. A 21 2559 (1988).</p> | <p>[7]. <i>K.S. Jhung, K.H. Chung, R. S. Willey</i>, Phys. Rev. D 12 1999 (1975).</p> <p>[8]. <i>K.A. Milton, I.L. Solovtsov</i>, Mod. Phys. Lett. A 16 2213 (2001).</p> <p>[9]. <i>R.A. Frick</i>, Europ. Phys. J. C 28 431 (2003).</p> <p>[10]. <i>S.M. Nagiyev, E.I. Jafarov, R.M. Imanov</i>, J. Phys. A 36 7813 (2003).</p> <p>[11]. <i>S.M. Nagiyev, E.I. Jafarov, R.M. Imanov</i>, Europhys. Lett. 76 175 (2006).</p> |
|--|---|

DETERMINATION OF PHOTO- AND ELECTROLUMINESCENCE SPECTRA OF $Pb_{1-x}Mn_xSe$ AND $Pb_{1-x}Mn_xTe$ THIN FILMS

Sh.M. ABBASOV, R.M. MAMISHOVA, T.I. KERIMOVA, G.T. ISMAYILOVA
Institute of Radiation Problems, Azerbaijan National Academy of Sciences

I.R. NURIYEV
Institute of Physics, Azerbaijan National Academy of Sciences

R.A. IBRAHIMOVA
Institute of Cybernetics, Azerbaijan National Academy of Sciences

In the given work photo and electroluminescence properties of $Pb_{1-x}Mn_xSe$ and $Pb_{1-x}Mn_xTe$ thin films by the mathematically modeled method of molecular beams epitaxial on BaF_2 substrates were studied. It was established that band gap width of epitaxial layers expanded by the change in Mn amount.

In the present work the dependence of band gap on $Pb_{1-x}Mn_xSe$ thin films' composition was determined out of photoluminescence spectra. The magnitude of exchange interaction was estimated in magnetic field due to the experiments on photo-and electroluminescence for $PbMnSnSe$ crystals.

The structural perfection of the films was controlled by electronographic, electromicroscopic and X-ray diffraction methods. Epitaxial films were grown by the mathematically modeled method of molecular beam condensation in vacuum 10^{-4} Pa.

Optimal conditions ($v_k=8\div9$ Å/sec; $T_n=663\div673$ K) of manufacturing epitaxial films with a perfect crystal structure ($W_{1/2}=80\div100\%$), growth plane (111), lattice parameter $a=6.10\div6.05$ Å and charge carrier mobility $\mu_{77K}=2.53\cdot 10^4$ cm²/V·sec were determined.

It was established that structurally perfect $Pb_{1-x}Mn_xSe$ films with different (n,p) conduction types and specified electrophysical properties can be obtained by regulating the temperature of compensating Se source.

As far as we know, it's necessary to manufacture films with a clean and smooth surface without switching the second phase for making various photosensitive epitaxial structures. For this purpose additional compensating source Se was used in the process of film growth. The application of this source resulted in manufacturing $Pb_{1-x}Mn_xSe$ films with a clean and smooth surface without switching the second phase.

Photoluminescence excitation was realized by an impulse YAG laser ($h\nu_0\approx 1.17$ eV). Pumping intensity equaled to $\sim 10^5$ W/cm². The measurement was carried out on reflection geometry at 77.4 K. The measurement of luminescence was conducted in magnetic field on Whoyt configuration, at the same time magnetic field was parallel to a crystallographic direction [100]. Radiation spectra were recorded with the help of a lattice monochromator and two radiation detectors on Ge(Au) and Ge(Cu) base. Band gap E_g was determined along the long-wave edge of radiation spectra. The accuracy of E_g determination depended on a concrete sample and equaled to 0.1÷0.2%. Within energy region of 0.15 eV where magnitooptical measurements were carried out spectral resolution was 0.15÷0.20 MeV. High spectral resolution allowed observing material heterogeneity according to the

composition (up to $\Delta x\sim 10^{-4}$) as well as luminescence intensity during scanning on the sample surface. The regions with maximal photoluminescence intensity were selected for conducting measurements.

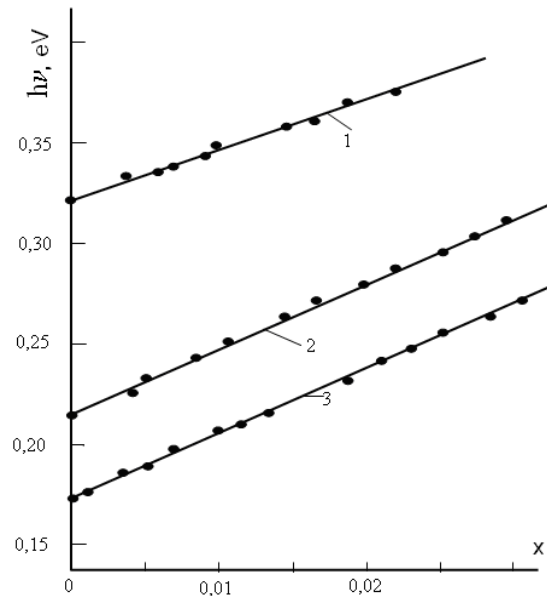


Fig.1. Dependence of band gap E_g on $Pb_{1-x}Mn_xS$ (1), $Pb_{1-x}Mn_xTe$ (2), $Pb_{1-x}Mn_xSe$ thin films composition (3): $T = 77$ K.

In fig.1 the dependence of radiation quantum energy on the compositions of three thin films - $Pb_{1-x}Mn_xS$ ($0\leq x\leq 0.014$), $Pb_{1-x}Mn_xTe$ ($0\leq x\leq 0.05$), $Pb_{1-x}Mn_xSe$ ($0\leq x\leq 0.04$) was shown. It becomes evident that the dependence $E_g(x)$ can be considered linear one in the given region. The inclination dE_g/dx is practically the same at 77 K temperature and equals to 3.2, 3.4 and 3.8 eV/fraction x correspondingly for $Pb_{1-x}Mn_xS$, $Pb_{1-x}Mn_xTe$, $Pb_{1-x}Mn_xSe$. For two samples with high manganese (Mn) composition- $Pb_{0.95}Mn_{0.05}Te$, $Pb_{0.96}Mn_{0.04}Se$ the radiation quantum energy was considerably lower (correspondingly 273 and 267 MeV at 77 K) than appropriate linear inclination values dE_g/dx .

It should be mentioned that radiation quantum energy for binary crystals (without manganese) grown by Bridgman method is more than band gap energy measured on qualitative epitaxial layers with charge carrier concentration of $\sim 10^{17} \text{ cm}^{-3}$. In dependence with the sample, charge carrier concentration and excitation level this difference reaches $\sim 10 \text{ MeV}$.

It is conditioned by relatively low quantum yield in the crystals grown by Bridgman method. In this connection high excitation level is required which leads to Burstein shift and crystal heating, i.e. to radiation quantum energy increase. It means that conservative values E_g (within 10 MeV) are acquired for Bridgman crystals with manganese (Mn). However, it has weak effect on inclination magnitudes [2].

During manganese introduction the number of the observed transitions obviously decreases due to low radiation quantum yield of the material [3, 4]. Thereby, during Mn introduction into $A^{IV}B^{VI}$ type semiconductor the band gap rises with x growth, and at low values x ($x \leq 0.02$) this dependence becomes linear. Besides, Mn introduction violates mirror symmetry of energy bands in magnetic field because of the fact that the contribution of exchange interaction to g -factor is more for holes than for electrons. It's necessary to use epitaxial layers for carrying out more accurate photoluminescence measurements, as Bridgman crystals have low radiation quantum yield and considerable composition heterogeneity.

-
- [1]. *I.I. Lyapiline, I.M. Cidilkovskiy*. Progress in Physical Science (PPS), 1985, v. 146, iss. 1, p. 35-72.
- [2]. *D.G. Andrianov, N.M. Pavlov, A.S. Savelyev, V.I. Phystule, G.P. Ciskarishvili* – Physics and Technology of Semiconductors (PTS), 1980, v. 14, iss. 6, p. 1202-1212
- [3]. *Sh.M. Abbasov, G.T. Agaverdiyeva, T.I. Kerimova, I.R. Nuruyev, R.M. Sadicohv*. "Physic" N1-2, V.12, "Science" 2006. p.60-61.
- [4]. *Sh.M. Abbasov, I.R. Nuruyev, T.B. Tagiyev, G.T. Agaverdiyeva, T.I. Kerimova, G.T. Ismayilova*. Semiconductor Physics, Quantum Electronics & Optoelectronics, 2007. v.10, iss 2. p. 26-28.

THERMODYNAMIC INVESTIGATION OF Yb-S SYSTEM BY EMF METHOD

M.A. MAKHMUDOVA, A.S. ABBASOV,

H.B. Abdullayev Institute of Physics of Azerbaijan NAS, Baku, AZ-1141, G. Javid ave., 33

S.Z. IMAMALIYEVA, M.B. BABANLI

Baku State University, Baku, AZ-1148, Z. Khalilov str., 23

The results of thermodynamic investigation of Yb-S system by EMF method are presented in the paper. The relative partial molar functions of ytterbium in alloys and standard integral thermodynamic functions ($\Delta G_{f,298}^0$, $\Delta H_{f,298}^0$, S_{298}^0) of Yb_2S_5 , Yb_2S_3 , Yb_3S_4 and YbS compounds are calculated by combining of measurement results of EMF concentration chains of two types.

The rare-earth element chalcogenides and alloys on their base are perspective functional materials. Many of them have the luminescent properties and photosensitivity. The memory switching effects are found in some of this type compounds. Some of them are used at the production of vacuum photoelements and etc [1,2].

Yb-S system is characterized by formation of Yb_3S_5 , Yb_2S_3 , Yb_3S_4 and YbS [3]. However, the thermodynamic properties of these compounds necessary for development and optimization of the methods of their directed synthesis and growing up in the form of single crystals haven't investigated yet. The standard enthalpy formations

($\Delta H_{f,298}^0 = -410 \pm 25$ kJ/mol) is obtained only for YbS [4]. Some thermodynamic functions of YbS and Yb_2S_3 are estimated by means of comparable analysis with thermodynamic sulfide functions of other rare-earth elements in work [5].

In the given paper the investigation results of solid-phase equilibriums in Yb-S system and thermodynamic properties of ytterbium sulfides by EMF method are presented.

EXPERIMENTS AND THEIR RESULTS

The alloys of Yb-Se system are synthesized by direct interaction of stoichiometric quantities of initial simple substances in degasified ($\sim 10^{-2}$ Pa) quartz ampoules at 450-500K. After interaction of the main mass of sulfur the furnace temperature is increased up to 1100K at which the ampoule is kept during twenty hours and further it is treated by continuous graduated annealing at 1000K (100h) and 400K (500h).

For carrying out of experiments the concentration chains of the following types are constructed as in [5]:



The left electrode of the chain (1) is prepared by fixing of metallic ytterbium on molybdenum lead and right electrodes are prepared by pressing of equilibrium alloys Yb-S made in powder form on leads in the form of cylindric tablets having 0,5 gr mass.

The sweet solution KCl with $YbCl_3$ addition is used as electrolyte. Taking under consideration the inadmissibility of the presence of damp and oxygen in electrolyte the glycerol (ЧДА mark) is thoroughly dehydrated and degassed by evacuation at temperature $\sim 450K$, the waterless, chemically pure KCl and $YbCl_3$ are used.

The techniques of gathering of electrochemical cells and EMF measurements are described in detail in [6]. The measurements of EMF by (2) type are carried out by usual compensation method with the help of digital voltmeter B-7-27 in 300-380K interval.

However, EMF measurements show the nonequilibrium of chains by (1) type. In measurement beginning during several hours EMF values strongly decrease up to 500-800mV in the comparison with initial ones ($\sim 1000-1500mV$). Though these values are reproducible, they can't be considered as equilibrium ones, so according to previous thermodynamic calculations, they were less than expectable ones in 2-3 times.

Taking into account the above mentioned, the experiments are carried out in two stages. Firstly the concentration chains by the following type:



are constructed.

In the chains of (2) types the ytterbium monosulfide with some sulfur excess (compound $YbS_{1,01}$) is used as left electrode. The equilibrium alloys with different compositions from YbS-S region are used as right electrodes.

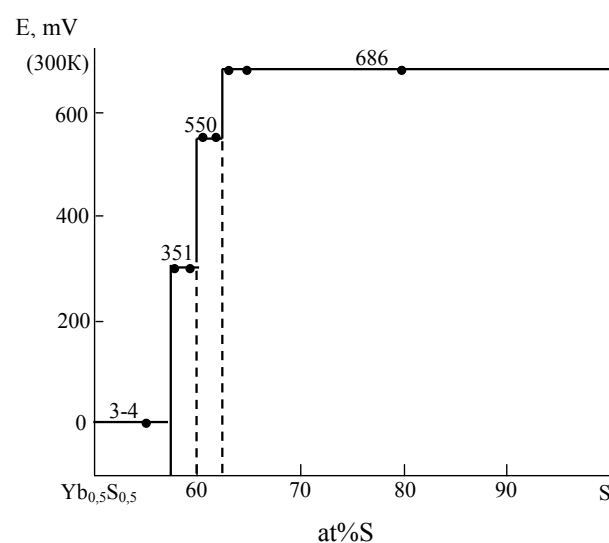


Fig. Dependences of EMF chains of type (2) on the composition in YbS-S subsystem

EMF measurements of chains by (2) type lead to reproducible results. The character of concentration

dependence of EMF in YbS-S composition region at 300K (fig) is in total correspondence with phase diagram [3]: EMF values are constant ones in two-phase regions and change spasmodically at the transformation from one phase region into other one, i.e. at stoichiometric compositions of ytterbium sulfides.

The analysis of EMF temperature dependences of chains by (2) type shows their linearity.

The treatment of given EFM measurements with the help of computer program "Microsoft Office Excel 2003" by the method of least squares [7] lead to obtaining of linear equations presented in the table 1 in the following

form:

$$E = a + bT \pm t \left[\frac{\delta_E^2}{n} + \delta_b^2 (T - \bar{T})^2 \right]^{1/2}, \quad (3)$$

recommended in [8]. Here \bar{T} is average temperature, K; δ_E^2 and δ_b^2 are dispersions of separate values of EFM and b constant, n is couple number of E and T values; t is Student criteria. $t \leq 2$ at confidence band 95% and $n \geq 2$ [7].

Table 1

Temperature dependences of EFM chains of (1) and (2) types for Yb-S ($T=300-380K$) alloys

No	Concentration chain	Phase region	$E, mB = a + bT \pm t\delta_E(T)$
1	(2)	Yb ₃ S ₅ +S	$649,8 + 0,1201T \pm 2 \left[\frac{0,34}{22} + 3,4 \cdot 10^{-5} (T - 339,4)^2 \right]^{1/2}$
2	(2)	Yb ₂ S ₃ +Yb ₃ S ₅	$572,9 + 0,1834T \pm 2 \left[\frac{0,32}{22} + 3,2 \cdot 10^{-5} (T - 338,8)^2 \right]^{1/2}$
3	(2)	Yb ₃ S ₄ +Yb ₂ S ₃	$310,3 + 0,1364T \pm 2 \left[\frac{0,36}{22} + 3,2 \cdot 10^{-5} (T - 336,8)^2 \right]^{1/2}$
4	(1)	YbS+Yb ₃ S ₄	$935,9 - 0,1785T \pm 2 \left[\frac{0,81}{17} + 10^{-4} (T - 337,9)^2 \right]^{1/2}$

The relative partial thermodynamic ytterbium functions (PThF) in YbS (table 2) and "quasicomponent" YbS from equations 1 and 2 are calculated. It is obvious that the last ones present themselves the difference of corresponding partial molar functions of ytterbium in right and left electrodes of the chains of (2) type:

$$\Delta \bar{Z}_{YbS} = \Delta \bar{Z}_{Yb}(\text{alloy of YbS-S region}) - \Delta \bar{Z}_{Yb}(YbS)$$

where $\Delta Z = \Delta \bar{G}, \Delta \bar{H}, \Delta \bar{S}$.

Table 2
Partial thermodynamic functions of "quasicomponent" of YbS in YbS-S alloys at 298K

Phase region	$-\Delta \bar{G}^*$	$-\Delta \bar{H}^*$	$\Delta \bar{S}^*$ J/(mol·K)
	kJ/mol		
Yb ₃ S ₅ +S	198,46±0,15	188,1±1,2	34,8±3,4
Yb ₂ S ₃ +Yb ₃ S ₅	181,67±0,14	165,8±1,1	53,1±3,3
Yb ₃ S ₄ +Yb ₂ S ₃	101,57±0,14	89,8±1,1	39,5±3,3

That's why the corresponding data for YbS which are obtained from EMF measurement data of chains by (2) type by EMF rapid fixation method [6] are necessary for ytterbium PThF calculation.

From obtained equation of EMF temperature dependence (table 1) ytterbium PThF in YbS (table 3, phase region YbS+Yb₃S₄) are calculated.

The substance of this method is in the fact that the left electrode is not in the cell with right electrode up to the moment of measurement, but in other vessel with the electrolyte at the same temperature.

EMF measurements are carried out in the moment of introduction of left electrode in electrochemical system with right electrode and the maximum value of EMF is fixed. These tests are carried out in the box filled by nitrogen at different temperatures in 300÷380K interval.

$\Delta \bar{G}_{Yb}$ can be defined by EMF rapid fixation method for all alloys. However, taking into consideration the difficultness of experiments by means of EMF rapid fixation method and reliability of reversible chains of (2) type, we prefer the above mentioned combined measurement technique of EMF.

Ytterbium PThF in alloys YbS-S (table 3) are calculated by summation of data from table 2 with PThF ytterbium for YbS.

From table 3 it follows that ytterbium partial entropy essentially decreases from Yb₃S₅ up to YbS. This well coincides with crystallographic data of ytterbium sulfides, according to which in this direction the crystal lattice symmetry of these compounds increases [1,3].

According to phase diagram, the partial molar functions of ytterbium are thermodynamic characteristics of the certain reactions of potential-formation (substance state is crystalline one) (table 3). That's why the standard thermodynamic functions of ytterbium sulfide formation

can be calculated by means of these equations. For example, for thermodynamic formation function of Yb₃S₅ and Yb₂S₃ compounds the following relations take place:

$$\Delta Z_{Yb_3S_5}^0 = 3\Delta \bar{Z}_{Yb}$$

$$\Delta Z_{Yb_2S_3}^0 = 0,2\Delta \bar{Z}_{Yb} + 0,6\Delta Z_{Yb_3S_5}^0$$

for standard entropies we have:

$$S_{Yb_3S_5}^0 = 3(\Delta \bar{S}_{Yb} + S_{Yb}^0)$$

$$S_{Yb_2S_3}^0 = 0,2(\Delta \bar{S}_{Yb} + S_{Yb}^0) + 0,6S_{Yb_3S_5}^0$$

Table 3

Ytterbium partial thermodynamic functions in Yb-S alloys at 298K and the potential formatting reactions corresponding to them

Phase region	$-\Delta \bar{G}_{Yb}$	$-\Delta \bar{H}_{Yb}$	$\Delta \bar{S}_{Yb}$	Potential formation reaction
	kJ/mol		J/(mol·K)	
Yb ₃ S ₅ +S	454,0±0,5	449,0±3,2	20,1±9,4	Yb+1,5S=0,333Yb ₃ S ₅
Yb ₂ S ₃ +Yb ₃ S ₅	437,2±0,4	436,7±3,1	1,7±9,2	Yb+3Yb ₃ S ₅ =5Yb ₂ S ₃
Yb ₃ S ₄ +Yb ₂ S ₃	457,1±0,4	360,7±3,1	-12,1±9,2	Yb+4Yb ₂ S ₃ =3Yb ₃ S ₄
YbS+Yb ₃ S ₄	255,5±0,3	270,9±2,0	-51,7±5,9	Yb+Yb ₃ S ₄ = 4YbS

Besides the own experimental data (table 3) the reference data on standard entropies of elementary ytterbium and sulfur from ref.[4,9] are used for calculation of standard entropies

The obtained results are presented in table 4. The errors are found by the method of error accumulation.

In table 4 the scientific literature data are presented. As it is seen, obtained by us values of standard thermodynamic formation functions and standard entropy well coincide with data [4,5] and corresponding functions of Yb₂S₃ essentially differ from given ones in [5].

Table 4

Standard integral thermodynamic functions of ytterbium sulfides

Phase	$-\Delta G_{298}^0$	$-\Delta H_{298}^0$	S_{298}^0
	kJ/mol		J/(mol·K)
Yb ₃ S ₅	1362±2	1347±10	289±28
Yb ₂ S ₃	905±2	896±6	186±17
	1153 [5]	1172 [5]	161 [5]
Yb ₃ S ₄	1326±3	1340±11	260±26
YbS	395±1	403±5	65±8
	444 [5]	452 [5]	69 [5]
		410±25 [4]	

- | | |
|---|---|
| <p>[1] <i>E.I. Yarembash, A.A. Eliseev.</i> Halkogenidi redkozemelnikh elementov. M.: Nauka, 1975. (in Russian).</p> <p>[2] <i>P.G. Rustamov, O.M. Aliyev, A.V. Eynullayev, I.P. Aliyev.</i> Halkolantanati redkikh elementov. M.:Nauka, 1989, 284s. (in Russian).</p> <p>[3] Binary alloys phase diagrams, Ed. <i>T.B.Massalski</i>, second edition. ASM International, Materials park, Ohio, 1990, v.2, p.1163-1166</p> <p>[4] <i>F.M. Mustafayev, T.X. Azizov, A.S. Abbasov, I.Ya. Aliyev.</i> Termodinamicheskiye svoystva halkogenidov redkozemelnikh elementov. In-t Fizizki AN Azerb. SSR, Preprint №50, Baku, 1977, 10.c. (in Russian).</p> | <p>[5] <i>M.A. Makhmudova, S.Z. Imamaliyeva, A.S. Abbasov, M.B. Babanli.</i> AzTU-nun Elmi əsərləri. Fundamental elmlər, 2010, t.IX (30), №1, c.</p> <p>[6] <i>M.B. Babanli, Yu.A. Yusibov, V.T. Abishev.</i> Metod EDS v termodinamike slojnikh poluprovodnikov veshshestv. Baku: BGU, 1992, 317 s. (in Russian).</p> <p>[7] <i>A.Gordon, R.Ford.</i> Sputnik khimika. M.: Mir., 1976, 541s.</p> <p>[8] <i>A.N. Kornilov, L.B. Stepina, V.A. Sokolov.</i> J. Fiz.khimii, 1972, t.46, №11, c. 2974-2979. (in Russian).</p> <p>[9] <i>O. Kubaschewski, S.V. Alcock, P.J. Spencer.</i> Materials Thermochemistry. Pergamon Press, Oxford, 1993, 350 p</p> |
|---|---|

THE TEMPERATURE, FREQUENCY AND VOLTAGE DEPENDENT CHARACTERISTICS OF Al-TiW-Pd₂Si/n-Si STRUCTURE USING *I-V*, *C-V* AND *G/ω-V* MEASUREMENTS

I.M. AFANDIYEVA

*Institute for Physics Problems, Baku State Universit,
Z. Khalilov str.,23, AZ 1148, Baku, Azerbaijan*

In this study, we have investigated the behavior of forward and reverse bias current-voltage (*I-V*), capacitance-voltage (*C-V*) and conductance-voltage (*G/ω-V*) characteristics of Al-TiW-Pd₂Si/n-Si Schottky diodes fabricated by the magnetron sputtering method. Experimental results show that ideality factor *n* and zero-bias Schottky barrier height Φ_{B0} are strong function of temperature. The forward (*I-V*) characteristics are analyzed on the basis of the standard thermionic emission model and the assumption of a Gaussian distribution of the barrier height. The values of Schottky barrier heights $\bar{\Phi}_{B0}$ and zero-bias standard deviation σ_0 have been calculated as 0.535 eV and 0.069V, respectively. The interface states density (N_{ss}) profile in the band gap of semiconductor has been calculated. Besides, on the basis of (*C-V*) and (*G/ω-V*) characteristics of Al-TiW-Pd₂Si/n-Si structures over a wide frequency range of 5 kHz–5 MHz series resistance (R_s) distribution profile have been investigated. The *C-V-f* and *G/ω-V-f* characteristics of studied structures show fairly large frequency dispersion especially at low frequencies due to N_{ss} in equilibrium with the semiconductor.

Dielectric properties and electrical conductivity of Al-TiW-Pd₂Si/n-Si structures in the frequency range of 5 kHz–10 MHz and voltage range of (-4 V) to (10 V) have been investigated in detail by using experimental *C-V* and *G/ω-V* measurements. Experimental results indicate that the values of ϵ' show a steep decrease with increasing frequency for each voltage. It can be concluded that the interfacial polarization can be more easily occurred at low frequencies, and the majority of interface states at metal semiconductor interface, consequently contributes to deviation of dielectric properties of Al-TiW-Pd₂Si/n-Si structures. The reason is explained in term of displacement of atoms at the fabrication of silicides and the presence of hexagonal emptiness in crystal lattice of Si (111).

INTRODUCTION

Metal-semiconductor (MS) contact is one of the most widely used rectifying contacts in the electronics industry [1-3]. Due to the technological importance of Schottky barrier diodes (SBDs) which are of the most simple of the MS contact devices, a full understanding of the nature of their electrical characteristics is of greater interest [1-5]. In this respect, the formation of silicide compounds at metal-Si interface is of current interest because of the potential device applications [6-10]. Knowledge of the basic parameters of contact structures on the basis silicide/Si and its dependence on temperature, frequency and geometrical sizes is important for understanding the formation mechanism of Schottky barriers. While Schottky barriers (SBs) have been investigated for a long time, the uniform structure has been assumed in the proximity of the metal/semiconductor interface [11]. However, nonideal characteristics are considered to be due to nonuniformity in the barrier height (BH) [12].

In this paper Al-TiW-Pd₂Si/n-Si Schottky diodes have been investigated using *I-V*, *C-V* and *G/ω-V* measurements. The reason for choosing this structure is threefold:

First, we wish to investigate the contact of platinum silicides /Si fabricated with the diffusion barrier (TiW). To prevent the disadvantage of Al diffusion to n-Si, the TiW amorphous alloy between Pd₂Si and Al was deposited as a diffusion barrier.

Second, decreasing of geometrical sizes of diodes increases the probability of fluctuation. In this respect the study of diodes areas of which changes from $1 \times 10^{-6} \text{ cm}^2$ to $14 \times 10^{-6} \text{ cm}^2$ is interesting.

Third, in the literature there is information about different results of study of contact structures silicides/Si(100) and silicides/Si (111) [7-10]. However in this papers don't take into account peculiarities the crystallographic structure of Si(111).

On the other hand it is known that crystal lattice of Si(111) contains hexagonal emptiness, areas of which are about $14,6 \times 10^{-2} \text{ nm}^2$ [13]. On the base of this result has been concluded that, the presence of these emptiness increases the probability of formation of inhomogeneities, patches and particular distribution of interface states.

All these factors facilitate our prototype study of the Al-TiW-Pd₂Si/n-Si structure.

EXPERIMENTAL DETAILS

The Al-TiW-Pd₂Si/n-Si structures were fabricated on 3inc diameter n-type (P-doped) single crystal silicon wafer with (111) surface orientation, $0.7 \Omega \text{ cm}$ resistivity and $3.5 \mu\text{m}$ thickness by use the method of planar technology [14-18]. It is known, Pd₂Si has loose structure and Al using as metal electrodes has high diffusion ability and it can lead to degrade contact's quality. In our previous study, we studied electrical characteristics of Al-TiW-Pd₂Si/n-Si and Al-TiW-PtSi/n-Si Schottky diodes (SD) with the amorphous alloy TiW as diffusion barrier between Pd₂Si or PtSi and Al [14-18]. To prevent the disadvantage of Al diffusion to n-Si, the TiW alloy played the role of the diffusion barrier between Pd₂Si and Al was deposited on Pd₂Si /n-Si wafer. Thus, the produced chip contains 14 diodes with the areas of changing $1 \times 10^{-6} \text{ cm}^2$ to $14 \times 10^{-6} \text{ cm}^2$. Only the results of diode with the area of $8 \times 10^{-6} \text{ cm}^2$ are presented in this paper. The *I-V*, *C-V* and *G/ω-V* measurements were performed by the use of a Keithley 220 programmable constant current source, a Keithley 614 electrometer and an HP 4192 LF impedance analyzer. The temperature dependence of *I-V-T* measurements was performed in a Janes VPF-475 cryostat with a Lake Shore model 321 auto-tuning temperature controllers in a vacuum of $5 \times 10^{-4} \text{ Torr}$. All measurements were carried out with the help of a microcomputer through an IEEE-488 ac/dc converter card.

RESULTS AND DISCUSSIONS

Usually, the first characterization obtained on a Schottky diode which considered series resistance R_s is to draw the current-voltage ($I-V$) curve. This plot is generally assumed to follow the thermionic model [2]:

$$I = I_0 \exp\left[\frac{q(V - IR_s)}{nkT}\right] \left\{ 1 - \exp\left[-\frac{q(V - IR_s)}{kT}\right] \right\} \quad (1)$$

q being the electronic charge, k the Boltzman's constant, T absolute temperature, V the voltage applied to the junction, n a ideality factor higher than unity, R_s series resistance and I_0 the saturation current and expressed as

$$I_0 = AA^*T^2 \exp\left(-\frac{q\Phi_{B0}}{kT}\right), \quad (2)$$

where A is the contact area, A^* is the effective Richardson constant (the theoretical value is $264 \text{ A/cm}^2\text{K}^2$ for (111) orientation n-type Si [2], Φ_{B0} is the zero bias BH. However, the current-voltage ($I-V$) characteristics of real Schottky diodes usually deviate from the ideal thermionic emission-diffusion (TED) model. Recently, these deviations have been explained by assuming the presence of the barrier height inhomogeneities [19,20].

The $I-V$ characteristics of Al-TiW-Pd₂Si/n-Si Schottky diodes at various temperatures are shown in Fig.1. At first we analyze the experimental $I-V$ data by the well known thermionic emission equation at forward and reverse bias ($V \geq 3kT/q$) [1,21]. As shown in Table 1 the value of forward current ratio to reverse current changes from 4,67 to 50,5 at $\pm 0.25\text{V}$ and from 7,8 to 126 at $\pm 1.5\text{V}$, respectively with increasing the temperature from 300 to 400K. Straightening improves with increasing temperature, especially at high voltage.

Table 1.

The values of forward current ratio to reverse current at 0.25V and $\pm 1.5\text{V}$ in the temperature range of 300 - 400K.

T, K	I_{forw}/I_{rev} ($V=0,25 \text{ V}$)	I_{forw}/I_{rev} ($V=1,5 \text{ V}$)
300	4,67	7,80
320	5,26	6,88
340	11,1	18,1
360	16,7	30,9
380	3,32	86,6
400	50,5	126

The ideality factor n is introduced to describe the deviation of the experimental $I-V$ data from the ideal TED model using the definition

$$n = \frac{q}{kT} \left(\frac{dV}{d(\ln I)} \right) \quad (3)$$

The zero-bias barrier height Φ_{B0} ($= \Phi_B(I-V)$) is determined from the extrapolated I_0 and is given by

$$\Phi_{B0} = \frac{kT}{q} \ln \left[\frac{AA^*T^2}{I_0} \right] \quad (4)$$

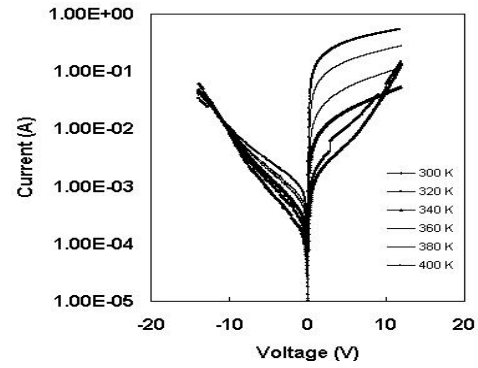


Fig. 1. The experimental $I-V$ characteristics of the Al-TiW-Pd₂Si/n-Si Schottky barrier diodes at various temperatures.

The experimental values of n and Φ_{B0} for the Al-TiW-Pd₂Si/n-Si Schottky barrier diode were determined from Eq.(3) and (4), respectively, are strong function of temperature [15,22] (Fig.2).

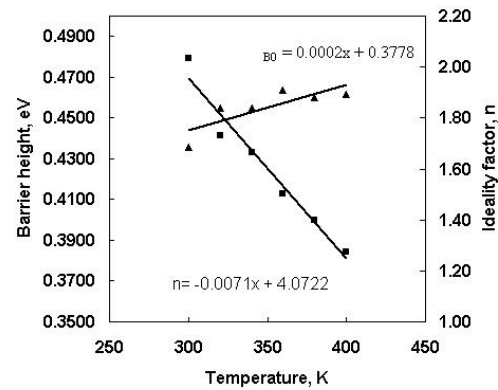


Fig. 2. Schottky barrier height and ideality factor derived from the fitting as a function of temperature for Al-TiW-Pd₂Si/n-Si.

To evaluate the BH we used different methods and obtained results shown in the Table 2. According to [4,23] on the basis the linear correlation between the experimental zero-bias SBH and ideality factor the value of BH Φ_{Bn} at $n=1$ has been obtained. Besides, we use the Richardson plot of saturation current I_0 . Likewise, a Richardson constant (A^*) value of $15,46 \text{ Acm}^{-2}\text{K}^{-2}$ and potential barrier height $\Phi_{ac} = 0,369 \text{ eV}$ for the Al-TiW-Pd₂Si/n-Si Schottky diode were determined from the intercept at the ordinate and slope of the experimental $\ln(I_0/T^2)$ versus $1000/T$, respectively [16]. However, the Richardson constant (A^*) value is much lower than the known value of $264 \text{ Acm}^{-2}\text{K}^{-2}$ for n-Si (111). This result is attributed to inhomogeneous interfaces and barrier heights, because there is a linear relationship between the barrier height and ideality factor [4,15,23].

Table 2.

The values of various diode parameters obtained from I-V characteristics of Al-TiW-Pd₂Si/n-Si Schottky barrier diode

T,K	Φ_{B0} (eV)	Φ_{bf} (eV)	Φ_{B0} (eV) (T=0)	Φ_{B0} (eV) (n=1)	Φ_{Rich} (eV)	$\bar{\Phi}_{BG}$ (eV)	σ_0 (V)	$\bar{\Phi}_{BGm}$ (eV)	A^* (Acm ⁻² K ⁻²)	A^*_{mod} (Acm ⁻² K ⁻²)
300	0,436	0,638	0,378	0,483	0,369	0,535	0,069	0,510	15,46	121,96
400	0,462	0,508								

The BH obtained under a flat-band condition Φ_{fb} is considered to be a real fundamental quantity. Unlike the case of the zero-bias barrier height, the electrical field in a semiconductor is zero under the flat –band condition. This eliminates the effect of the image force lowering that would affect the I-V characteristics, and removes the influence of lateral inhomogeneity [24].

To explain the commonly observed abnormal deviation from classical thermionic emission theory, some authors [25,26] have considered a system of discrete region of low barrier imbedded in a higher background uniform barrier. This abnormal behaviour can be explained by assuming a Gaussian distribution of the barrier height with a mean $\bar{\Phi}_{BG}$ and standard deviation σ_0 , which can be given as [25,26]:

$$\Phi_{B0} = \bar{\Phi}_{BG} - \frac{q\sigma_0^2}{2kT} \quad (5)$$

Thus, the plot of $\bar{\Phi}_{BG}$ versus $q/2kT$ should be a straight line that gives $\bar{\Phi}_{BG}=0.535$ eV and $\sigma_0 = 0,069V$ from the intercept and slope, respectively (fig.3). The lower value of σ_0 corresponds to more homogeneous BH. It was seen that the value of $\sigma_0 = 0,069V$ is not small compared to the mean value of $\bar{\Phi}_{BG} = 0,535eV$, indicating the presence of interface inhomogeneities. Nevertheless, this inhomogeneity and potential fluctuation dramatically affect low temperature I-V characteristics.

To explain the abnormal behavior of the plot $\ln(I_0/T^2)$ versus $1/T$ and Richardson constant which deviates from the known value, equation for Richardson plot can be rewritten by taking into account Gaussian distribution of the BH and standard deviation:

$$\ln\left(\frac{I_0}{T^2}\right) - \left(\frac{q^2\sigma_0^2}{2k^2T^2}\right) = \ln(AA^*) - \frac{q\Phi_{B0}}{kT} \quad (6)$$

The modified Richardson plot (6) gives $\bar{\Phi}_{BGm}$ and A_m^* as 0,510 and 121,96Acm⁻²K⁻², respectively (Fig4).

It is known that interfacial parameters such as density of interface states and the thickness of interface layer can influence both the electrical and dielectric behavior of metal-semiconductor structures [27,28].

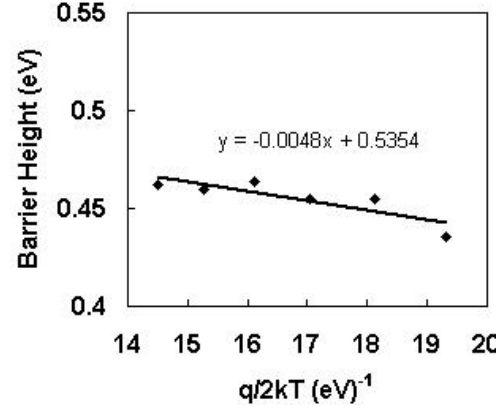


Fig. 3. Zero-bias apparent barrier height versus $1/T$ curves of the Al-TiW-Pd₂Si/n-Si Schottky diode according to the Gaussian distribution of the barrier height.

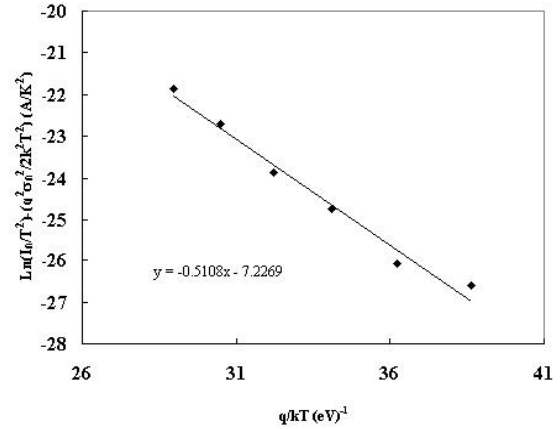


Fig.4. Modified Richardson $\ln\left(\frac{I_0}{T^2}\right) - \left(\frac{q^2\sigma_0^2}{2k^2T^2}\right)$ vs. $1/T$

plot for the Al-TiW-Pd₂Si/n-Si Schottky diode according to the Gaussian distribution of the barrier height.

In this respect, the profile of distribution of surface state density has been calculated as a function of (E_c-E_{ss}) identical Card and Roderick [21]:

$$N_{ss}(V) = \frac{1}{q} \left[\frac{\varepsilon_i}{\delta} (n(V) - 1) - \frac{\varepsilon_0}{W_D} \right] \quad (7)$$

Where E_c is bottom of the conduction band, E_{ss} is the energy of the interface states, δ is the thickness of interfacial insulator layer, W_D is the width of the space

charge region, ϵ_i and ϵ_s are the permittivity of the dielectric layer and the semiconductor, respectively. In our previously study δ and W_D were obtained ($\delta = 0.381 \text{ nm}$, $W_D = 0.385 \mu\text{m}$). As shown in Fig 5, the exponential growth of the N_{ss} from midgap towards the bottom of conduction band is very apparent. The density distribution curve of the interface states is in the range ($E_c - 0.54$) to ($E_c - 0.64$) eV.

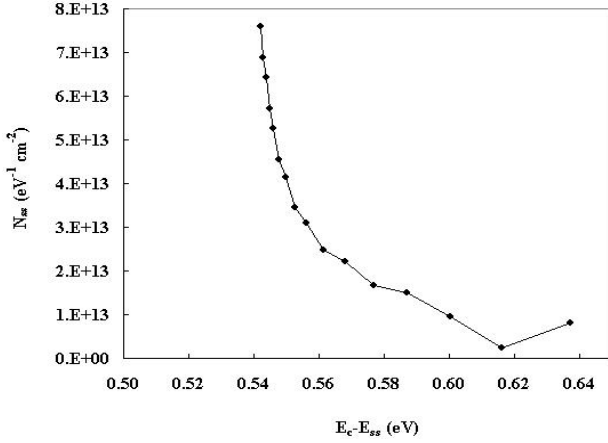


Fig. 5. The energy distribution profile of the N_{ss} with obtained from the forward bias I-V characteristics of the Al-TiW-Pd₂Si/n-Si structure at room temperature.

The forward and reverse bias capacitance–voltage ($C-V$) and conductance–voltage ($G/\omega - V$) characteristics of Al-TiW-Pd₂Si/n-Si structures have been investigated over a wide frequency range of 5 kHz–10 MHz. with a small ac signal of 20 mV_{rms} peak to peak amplitude at room temperature. Fig 6 (a and b) shows that the rapid decreasing of both C and G/ω with frequency, respectively at the positive biases. These changes occur especially at the low frequencies and depletion regions while the high-frequency capacitance and conductance remain almost constant.

As a result, we can say that in the low frequencies surface states can follow the ac signal and yield an excess capacitance and conductance, which depends on the frequency. But at the efficiently high frequencies ($f > 100 \text{ kHz}$), the interface states cannot follow the ac signal. In addition the values of conductance give peaks at low frequencies and this anomalous peak has a tendency to disappear at high frequencies. Such behavior indicates that there are various kinds of interface states with different life times and they can follow an ac signal at low frequency, but cannot follow at high frequencies.

In this study, the frequency and voltage dependent series resistance R_s of Al-TiW-Pd₂Si/n-Si structures according to a method presented by Nicollian and Brews [27] has been calculated from the $C-V$ and $G/\omega - V$ measurements at each frequency:

$$R_s = G(G^2 + (\omega C)^2)^{-1} \quad (8)$$

Where ω is the angular frequency.

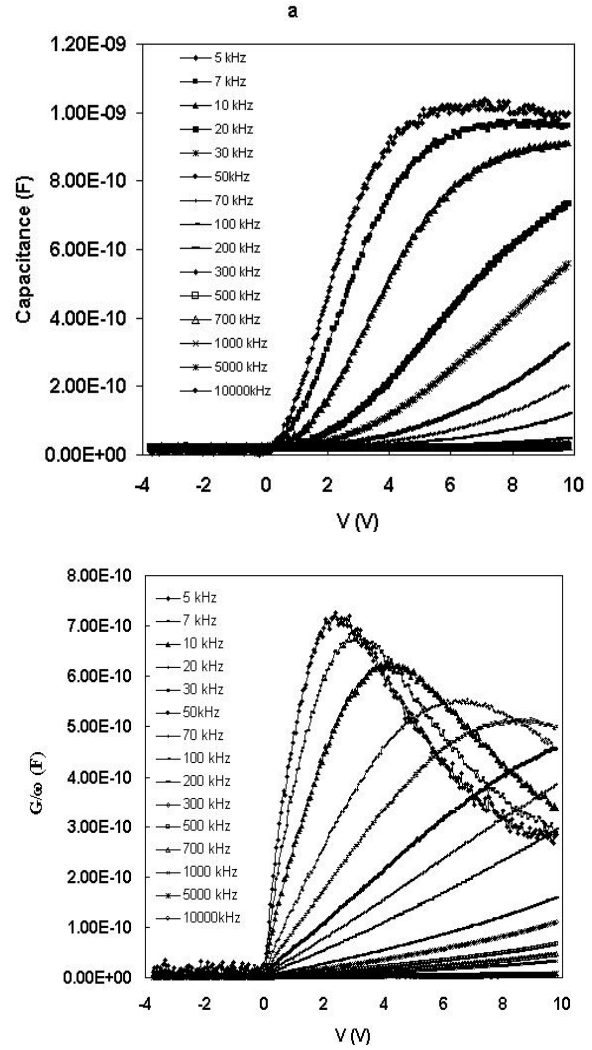


Fig. 6. (a) The measured capacitance $C(V, f)$ and (b) conductance $G/\omega(V, f)$ for Al-TiW-Pd₂Si/n-Si structure at room temperature.

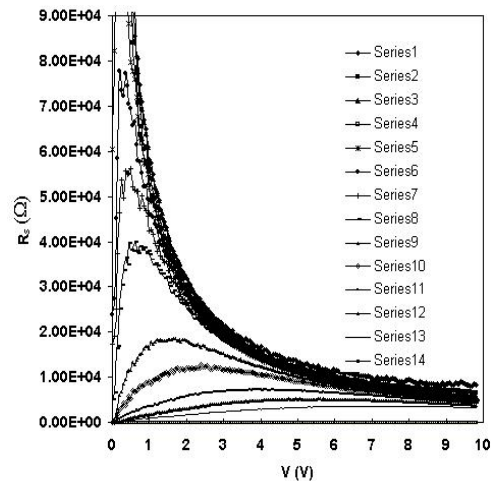


Fig.7. The R_s - V plots at various frequencies for Al-TiW-Pd₂Si/n-Si structure at room temperature.

As seen in Fig. 7, the series resistance gives a peak between about 0–1V depending on frequency and disappears at sufficiently high frequencies. From Fig. 8a,b,c it is clearly seen that the series resistance,

capacitance and conductance are dependent both frequency and voltage and changes from region to region. The results indicate the presence of the low frequency dispersion of the resistance, capacitance and conductance for the investigated structure. Such frequency dependence is observed in the literature [28, 29, 30].

It can be concluded that the values of R_s are significant only in the downward curvature of the forward bias $I-V$ characteristics at high bias voltage, but the values of N_{ss} are significant in both the low and high bias voltages. In conclusion, the ignoring the interface state density (N_{ss}) and series resistance (R_s) of device can lead to significant errors in the capacitance–voltage ($C-V$) and conductance–voltage ($G/\omega-V$) characteristics.

Besides, by using experimental $C-V$ and $G/\omega-V$ measurements dielectric properties and electrical conductivity of Al-TiW-Pd₂Si/n-Si structures in

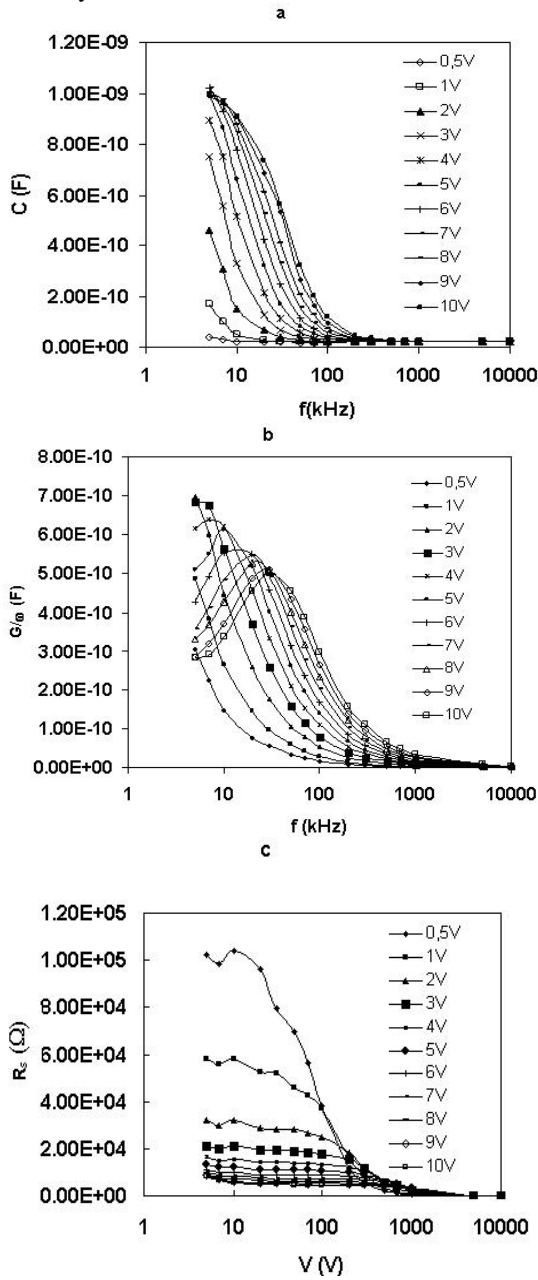


Fig.8. The frequency dependence of (a) the $C(V_g)-f$, (b) $G/\omega(V_g)-f$ and (c) $R_s(V_g)-f$ of the Al-TiW-Pd₂Si/n-Si structure at room temperature.

the frequency range of 5 kHz–10 MHz and voltage range of (-4 V) to (10 V) at room temperature have been investigated in detail.

It is known that the complex permittivity can be written as:

$$\varepsilon^* = \varepsilon' - \varepsilon'' \quad (9)$$

where ε' and ε'' are the real and imaginary of complex permittivity, and i is the imaginary root of -1. The complex permittivity formalism has been employed to describe the electrical and dielectric properties. In this respect the connection between complex permittivity and C and G described as:

$$\varepsilon^* = \frac{C}{C_0} - i \frac{G}{\omega C_{0i}} \quad (10)$$

Where $\omega = 2\pi f$ is the angular frequency of the applied electric field, C_0 and C_{0i} are capacitance of an empty capacitor and C_{0i} the maximal capacitance of the structure corresponds to the insulator capacitance, respectively [32].

The real and imaginary parts of the complex permittivity described by the relations [33]

$$\varepsilon' = \frac{C}{C_0} = \frac{C d_i}{\varepsilon_0 A} \quad \text{and} \quad \varepsilon'' = \frac{G}{\omega C_i} = \frac{G d_i}{\varepsilon_0 \omega A} \quad (11)$$

where d_i is the interfacial insulator thickness, ε_0 is the permittivity of free space charge, A is the rectifier contact area of the structure.

The loss tangent ($\tan \delta$) can be expressed as follows [33]:

$$\tan \delta = \frac{\varepsilon''}{\varepsilon'} \quad (12)$$

Fig. 9 shows the dependence of the real part of dielectric constant (ε') of the Al-TiW-Pd₂Si/n-Si structure on the voltage at various frequencies. It is noticed that the values of ε' increase with decreasing frequency and tend to be frequency independent at low voltages. The decrease in ε' with increasing frequency may be attributed to the polarization decreasing with increasing frequency and then reaches a constant value due to the fact that beyond a certain frequency of external field the electron hopping cannot follow the alternative field. The dispersion in ε' with frequency can be attributed to Maxwell–Wagner type interfacial polarization, i.e. the fact that inhomogeneities give rise to a frequency dependence of the conductivity because charge carries accumulate at the boundaries of less conducting regions, thereby creating interfacial polarization [33].

Figs. 10 and 11 show the voltage dependence of dielectric loss (ε'') and the loss tangent $\tan \delta$ of the Al-

THE TEMPERATURE, FREQUENCY AND VOLTAGE DEPENDENT CHARACTERISTICS OF Al-TiW-Pd₂Si/n-Si STRUCTURE USING I-V, C-V AND G/ω-V MEASUREMENTS

TiW-Pd₂Si/n-Si structure at various frequencies. As can be seen in these figures, the values of ϵ'' and $\tan \delta$ are strongly dependent on both frequency and applied bias voltage. The ϵ'' -V and $\tan \delta$ -V characteristics have a peak especially at low frequency. The peak values of ϵ'' -V and $\tan \delta$ -V have decreased with increasing frequency and the peak positions strongly shift towards negative bias region.

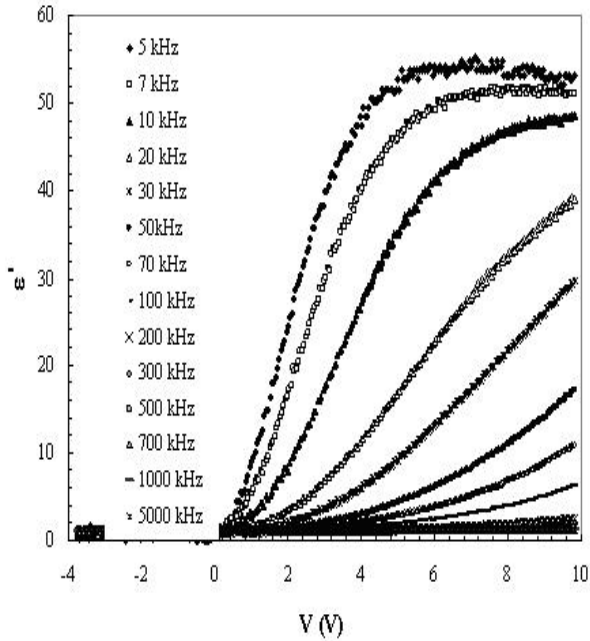


Fig.9. The variations of the dielectric constant vs. applied voltage for various frequencies of Al-TiW-Pd₂Si/n-Si structure at room temperature.

The peak behavior of the ϵ'' and $\tan \delta$ depend on a number of parameters such as doping concentration, interface state density, series resistance of diode and the thickness of the interfacial insulator layer [34].

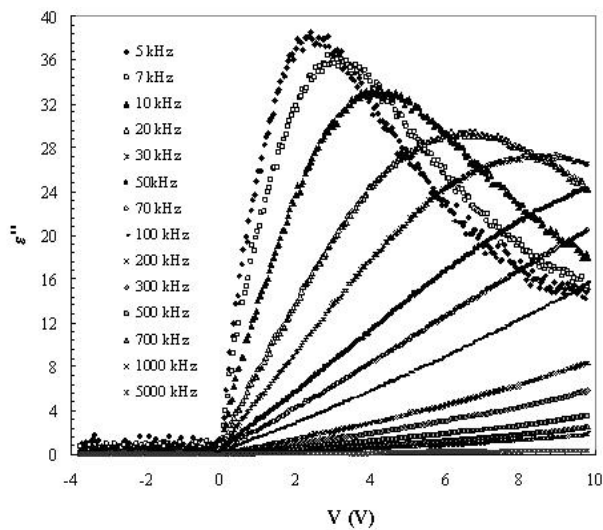


Fig.10. The variations of dielectric loss vs. applied voltage for various frequencies of Al-TiW-Pd₂Si/n-Si structure at room temperature.

It is well known that the capacitance and conductance are extremely sensitive to the interface properties and series resistance [27]. This occurs because of the interface states that respond differently to low and high frequencies. Similar results have been reported in the literature [35,36] and they ascribed such a peak to only interface states. The frequency dependence of the ϵ' , ϵ'' and $\tan \delta$ (Fig.9-Fig.11) of Al-TiW-Pd₂Si/n-Si structure obtained from the measured capacitance and conductance were found a strong function of applied voltage especially at low frequencies.

As shown in Fig.12a, the values of ϵ' show a steep decrease with increasing frequency for each voltage. Besides, the values of ϵ' show a broad peak, and its intensity increases with decreasing voltage and shifts the lower frequency side. It is clearly seen in Fig 12, that the values of ϵ' , ϵ'' and $\tan \delta$ of Al-TiW-Pd₂Si/n-Si are almost independent of voltage at high frequencies. In principle, at low frequencies, all the four types of polarization processes, i.e. the electronic, ionic, dipolar, and interfacial of surface polarization contribute to the values of ϵ' and ϵ'' . In addition, at high frequencies the values of ϵ' become closer to the values of ϵ'' due to the interface states (N_{ss}) cannot follow the ac signal at enough high frequency ($f \geq 500\text{kHz}$) [28,34].

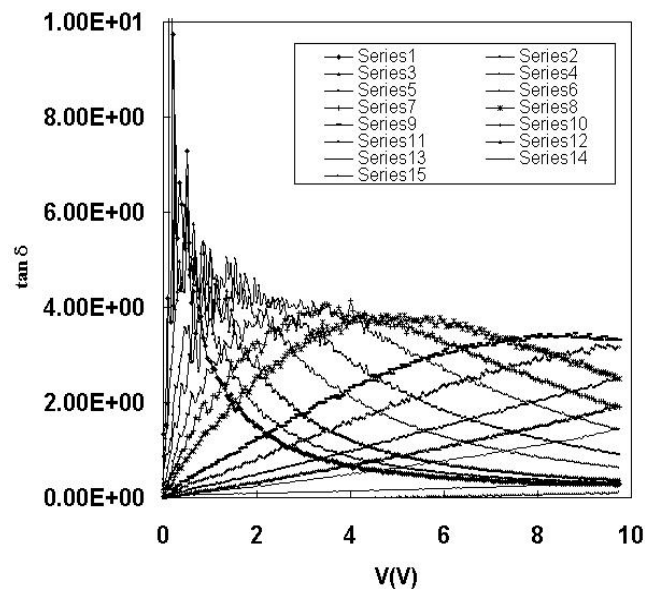


Fig.11. The variations of tangent loss vs. applied voltage for various frequencies of Al-TiW-Pd₂Si/n-Si structure at room temperature.

The electrical conductivity (σ_{ac}) of the dielectric material can be given by the following equation [31,32]:

$$\sigma_{ac} = \epsilon'' \omega \epsilon_0 \quad (13)$$

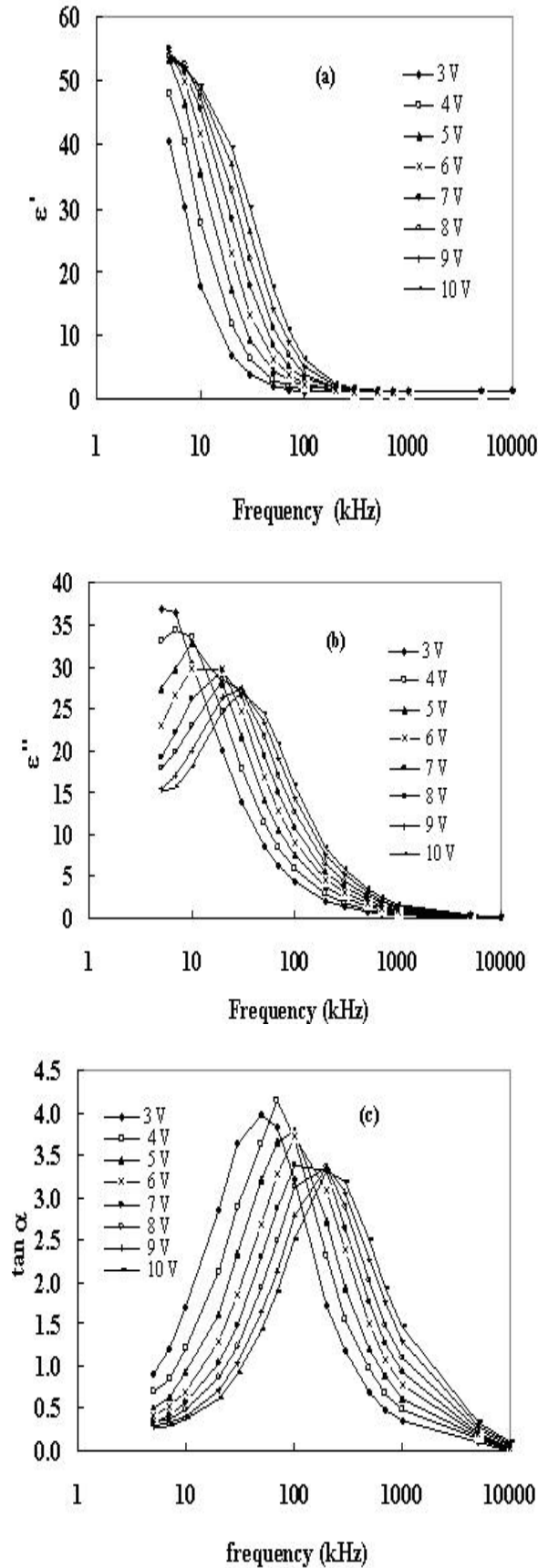


Fig.12. Frequency dependence of the (a) ϵ' , (b) ϵ'' and (c) $\tan \delta$ for various applied voltage of Al-TiW-Pd₂Si/n-Si structure at room temperature.

The behaviour of ac electrical conductivity (σ_{ac}) of the Al-TiW-Pd₂Si/n-Si structure at different voltage is presented in Fig. 13. It is noticed that the electrical conductivity generally increases with increasing frequency at low frequencies

Up to 30 kHz, and after that frequency it is independent of frequency for each voltage. This electrical contribute to the dielectrically loss, which becomes infinity at zero frequency and not important at high frequencies [28]. The increase the electrical conductivity lead to an increase of the eddy current which in turn increases the energy loss $\tan \delta$. This behaviour can be attributed to a gradual decrease in series resistance with increasing frequency [28].

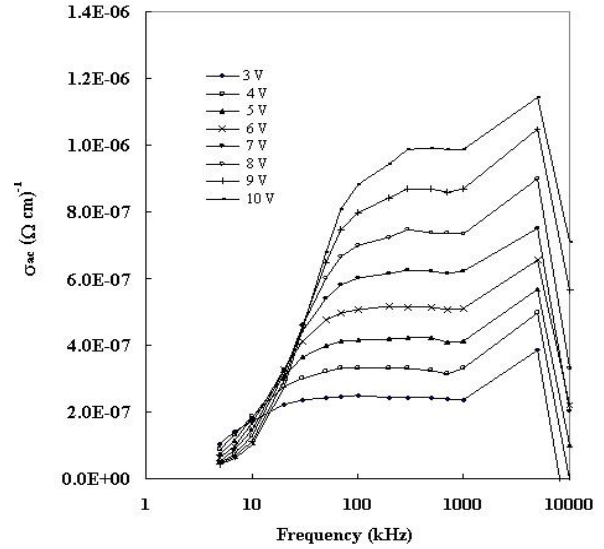


Fig.13. Frequency dependence of ac electrical conductivity (σ_{ac}) for various applied voltage of Al-TiW-Pd₂Si/n-Si structure at room temperature. vs frequency for Al-TiW-Pd₂Si/n-Si structure at room temperature.

Analysis of the complex permittivity (ϵ^*) data in the complex impedance (Z^*) formalism ($Z^* = 1/i\omega C_0 \epsilon^*$) is commonly used to separate the bulk and the surface phenomena and to determine the bulk dc conductivity of the material [17,37,38]. On the other hand, many authors prefer to describe the dielectric properties of devices on the basis metal-semiconductor contact by using the electric modulus (M^*) formalize. The complex impedance or the complex permittivity ($\epsilon^* = 1/M^*$) data are transformed into the M^* formalism using the following relation:

$$M^* = i\omega C_0 Z^* \quad (14)$$

or

$$M^* = \frac{1}{\epsilon^*} = M' + jM'' = \frac{\epsilon'}{\epsilon'^2 + \epsilon''^2} + j \frac{\epsilon''}{\epsilon'^2 + \epsilon''^2} \quad (15)$$

The real component M' and the imaginary component M'' are calculated from ϵ' and ϵ'' .

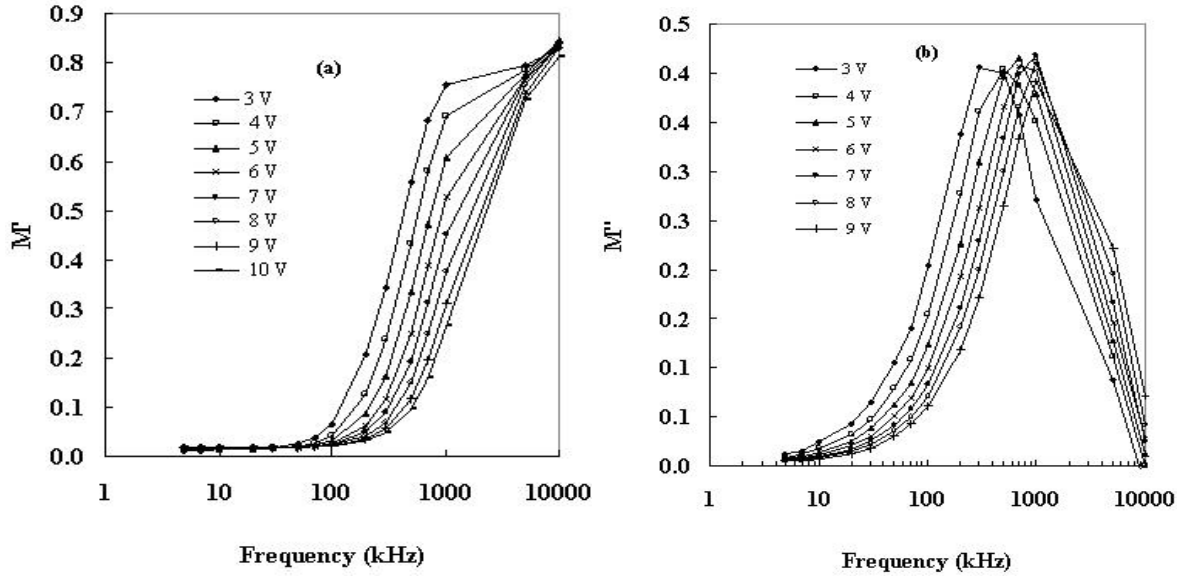


Fig.14. (a) the real part M' and (b) the imaginary part M'' of electric modulus M^* .

As is shown in Fig.14(a) for each bias voltage, M' reaches a constant value at higher frequency. In other words, M' reaches a maximum constant value corresponding to $M_\infty = 1/\epsilon_\infty$ due to the relaxation process. At low frequencies, the values of M' approach zero, confirming the removal of electric polarization. The variation of M'' with frequency at various bias voltages in Fig.14b reveals that as frequencies increases M'' increases and takes a peak value at each bias voltage between 200kHz and 1MHz. The position of peak shifts to higher frequency with increase gate voltage.

All above noted peculiarities may be due to the spatial inhomogeneous barrier heights, potential fluctuation at the interface and contribution of surface states. On the base of this result has been concluded that the displacement of atoms from the equilibrium positions, the deformation of a lattice of contact materials, changes of band structure of materials and the presence of emptiness in crystal lattice of Si(111) areas of which are about $14,6 \times 10^{-2} \text{ nm}^2$ increased the probability of formation of inhomogeneities, patches and particular distribution of interface states.

CONCLUSIONS

In a novel Al-TiW-Pd₂Si/n-Si structure a thin amorphous film was deposited on Pd₂Si/n-Si to form the diffusion barrier to prevent the disadvantage of Al diffusion to n-Si. In this paper Al-TiW-Pd₂Si/n-Si Schottky diode with the area $8 \times 10^{-6} \text{ cm}^2$ has been investigated using *I-V*, *C-V* and *G-V* measurements. It was shown that the *I-V* characteristics of the Al-TiW-Pd₂Si/n-Si SBD in the temperature range of 300-400 K were found to be a strong function of temperature. The satisfactory explanation of the *I-V* characteristics of the Al-TiW-Pd₂Si/n-Si structure in the temperature range of 300-400 K can be made on the basis of TE with Gaussian distribution of the barrier height of $\overline{\Phi}_{B0} = 0.535 \text{ eV}$ and

zero-bias standard deviation $\sigma_o = 0.069 \text{ V}$, the density of N_{ss} distribution profiles as a function of energy ($E_c - E_{ss}$) obtained from the *I-V* data by taking into account the bias dependence of the n and Φ_b .

As is known, the distribution of the barrier height is caused by inhomogeneities that are present at the interface. In this respect, the forward and reverse bias (*C-V-f*) and (*G/ω-V-f*) characteristics of the Al-TiW-Pd₂Si/n-Si diodes have been obtained at room temperature. The results show that surface states can easily follow the ac signal at low frequencies and yield an excess capacitance, which depends on the relaxation time of the surface states and the frequency of ac signal. Besides, it can be concluded that the values of R_s are significant only in the downward curvature of the forward bias *I-V* and *C-V* characteristics at high bias voltage, but the values of N_{ss} are significant in both the low and high bias voltages. An analysis of experimental results have shown that the values of ϵ' show a steep decrease with increasing frequency for each voltage while the values of ϵ'' show a peak, and its intensity increasing with decreasing voltage and shift towards the lower frequency side. The values of ϵ' , ϵ'' , $\tan \delta$, M' and M'' in Al-TiW-Pd₂Si/n-Si structure are strongly depend on both the frequency and applied bias voltage.

In conclusion, the ignoring the interface state density N_{ss} and series resistance (R_s) of device can lead to significant errors in the characteristics of diodes. The inhomogeneity of BH and deviate of characteristics from standard model could be explain by deformations of a lattice of contacted materials, which results in changes of band structure of material and the presence of hexagonal emptiness in crystal lattice of Si(111).

THE TEMPERATURE, FREQUENCY AND VOLTAGE DEPENDENT CHARACTERISTICS OF Al-TiW-Pd₂Si/n-Si STRUCTURE USING I-V, C-V AND G/ω-V MEASUREMENTS

- [1]. *V.I.Strikha*. Theoretical bases of metal–semiconductor contact work. Kiev, Naukova Dumka, 1974 [in Russian].
- [2]. *S.M. Sze*. Physics of Semiconductor Devices. New York, Willey, 1981.
- [3]. *E.V. Buzanyova*. Microstructures of integrated electronics. Moskow, Radio i svyaz, 1990. (in Russian).
- [4]. *R.T. Tung*. Matter Sci.Eng. 2001.R.351.
- [5]. *P.N.Krylov*. Vestnik Udmurtskogo Universiteta, Fizika. 2006;4:125 [in Russian].
- [6]. *B.Pellegrini* Solid-State. Electr. 1975;18: 417.
- [7]. *S.Zhu, R.L.Van Meirhaeghe, C.Detavernier, F.Cardon, G.P. Ru, X.P. Qu, B.Z. Li*. Solid- State Electron. 2000, 44, 663.
- [8]. *S.Zhu, C.Detavernier, R.L.Van Meirhaeghe, F.Cardon, G.P.Ru, X.P.Qu, B.Z. Li*. Solid-State Electron. 2000, 44, 1807.
- [9]. *S.K. Pandey, S.Kumar, S.N.Chatterjee, U.Kumar, Ch.P. R.Chatterjee, T.C. Goel*. Physica B, 2007, 388, 404.
- [10]. *Ş.Karataş, Ş.Altındal, A.Türüt., A.Özmen*. Appl. Surf. Sci. 2003, 217, 250.
- [11]. *E.H.Rhoderick, R.H.Williams*. Metal-Semiconductor Contacts, 2nd Edition. Oxford: Clarendon Press., 1978.
- [12]. *J.H.Werner, H.H.Güttler*, J.Appl.Phys. 1993, 73, 1315.
- [13]. *B.K.Vainshtein, A.A.Chernov, L.A.Shuvalov*, Modern crystallographie, Moskow, Nauka, 1979 [in Russian].
- [14]. *I.M.Afandiyeva, Sh.G.Askerov, L.K. Abdullayeva, Sh.S. Aslanov*. Solid State Electron. 2007, 51, 1096.
- [15]. *I. Dökme, Ş. Altındal, I.M. Afandiyeva*, Semiconductor Science and Technology, 2008, 23 (035003)1.
- [16]. *I.M.Afandiyeva, I.Dökme, Ş.Altındal, L.K.Abdullayeva, Sh.G.Askerov*. Microelectr. Engineering. 2008, 85, 365.
- [17]. *I.M. Afandiyeva, I.Dökme, Ş.Altındal, M.Bülbül, A.Tataroğlu* Microelectr. Engineering. 2008;85:247.
- [18]. *I.M. Afandiyeva* Journal of Qafqaz University. 2006,17, 56 [in Russian].
- [19]. *G.P.Ru, R.L.Van Meirhaeghe, S.Forment, Y.L.Jiang, X.P.Qu, S.Zhu, B.Z.Li*. Solid-State Electron. 2005,49, 606.
- [20]. *V.W.L. Chin, M.A.Green, J.W.V. Storey*. Solid-State Electron , 1990, 33, 299.
- [21]. *H.C.Card, E.H. Rhoderich*. J.Phys.D. 1971, 4, 1589.
- [22]. *Ş.Altındal, I.Dökme, M.Bülbül, N.Yalcin ,T.Serin*. Microelectr.Eng. 2006, 83, 499.
- [23]. *R.F.Schmitsdorf, T.U.Kampen, W.Mönch*. Sur.Sci.1995, 324, 249.
- [24]. *A.Gümüş, A.Türüt, N.Yalcin*. J.Appl.Phys. 2002,91,245.
- [25]. *S.Chand, Kumar*, J. Appl. Phys. 1996, 80, 288.
- [26]. *R.Tung*, 2001, Mater.Sci.Eng. R 351.
- [27]. *E.H Nicollian, J.R.Brews*, MOS Physics and Technology. New York: Wiley; 1982.
- [28]. *A.Tataroğlu, Ş.Altındal, M.Bülbül*, Microelectronic Engineering. 2005, 81, 140.
- [29]. *J.Domaradzki, K Nitsch*. Thin Solid Films. 2007, 515, 3745.
- [30]. *S.Kochowski, K.Nitsch, B.Paszkievicz, R.Paszkievicz, M.Szydlowski* Appl.Surf.Sci. 2004; 235:389.
- [31]. *P.T.Oreshkin*, Physic of semiconductors and dielectrics, Moskow, Visshaya shkola, 1977 [in Russian].
- [32]. *M.S Mattsson, G.A Niklasson., K.Forgsgren, A.Harsta*, J.Appl.Phys., 85(4) (1999) 2185.
- [33]. *M.Popesku, J.Bunget*. Physics of solid dielectrics, Elsevier, Amsterdam, 1984.
- [34]. *S.P. Szu, C.Y Lin*, Mater.Chem.Phys, 82 (2003)295.
- [35]. *I.Dökme, Ş.Altındal*, Physica B. Condens.Mat. 2007, 391, 59.
- [36]. *I.Yucedag, Ş.Altındal, A.Tataroğlu*, Microelectron.Eng. 2006 84, 180.
- [37]. *K.Prabakar, S.K Narayandass, D.Mangalaraj*, Phys. Stat.Sol. (a) 2003,199, 3, 507.
- [38]. *M.D. Migahed, M. Ishra, T.Fahm., A. Barakat*, J. Phys. Chem. Solids, 65 (2004) 1121

DEEP AND SHALLOW ACCEPTOR LEVELS IN SOLID SOLUTIONS $\text{Pb}_{0,98}\text{Sm}_{0,02}\text{S}$

H.A. HASANOV, R.Sh. RAHIMOV

Academy of the Ministry of National Security named after Heydar Aliyev
Baku State University, Z. Khalilov str., 23

The acceptor states forming in forbidden band the “deep” $\varepsilon_a \sim 0,085\text{eV}$ and “shallow” $\varepsilon_a \sim 0,025\text{eV}$ energy levels are revealed on the base of Hall effect investigations in $\text{Pb}_{0,98}\text{Sm}_{0,02}\text{S}$ solid solutions.

INTRODUCTION

It is well known that the metal vacancies the energy levels of which take place between permitted energies of valency band, are the main acceptor centers in the led salts and solid solutions on their base [1,2]. The aim of the given paper is founding of character of acceptor levels in single crystals $\text{Pb}_{0,98}\text{Sm}_{0,02}\text{S}$ with low concentrations of charge carrier (up to level 10^{16}cm^{-3}).

EXPERIMENT AND DISCUSSION OF OBTAINED RESULTS

In the given paper the deep and shallow acceptor levels are found at investigation of Hall effect in $\text{Pb}_{0,98}\text{Sm}_{0,02}\text{S}$ solid solution with character low concentrations of charge carriers in crystals [3].

The investigations are carried out on several decades of samples in concentration interval $2 \cdot 10^{16} \div 1 \cdot 10^{18}\text{cm}^{-3}$. Statistic character of investigations allows us to group all investigated crystals on signatures of Hall coefficient temperature dependences into 3 groups each of which is presented by character curve on the fig.1. Let's pay attention on two peculiarities of these dependences. The first one is that Hall coefficient for all crystals increases with temperature decrease, moreover the important fact is that relation R_{77}/R_{300} for samples with least concentrations is in interval from 10 up to 100 (R_{77} is Hall coefficient at 77K and R_{300} is Hall coefficient at 300K). The second one is that dependences $R_x(T)$ for all crystals are non-monotonous, though both character and the non-monotonocity for called groups of the samples have individual peculiarity. The monotonicity breaking takes place in temperature interval $\sim 150 \div 190\text{K}$.

The character of temperature dependences $R_x(T)$ shows that the investigated materials have acceptor centers with nonzero activation energy unlike binary compounds and many solid solutions on $\text{A}^{\text{IV}}\text{B}^{\text{VI}}$ base. Besides, the big variation interval of R_x value in both in the region of low temperatures and high ones allows us to conclude that we deal with more than one acceptor level of considered type. This fact is confirmed by the quantitative analysis the results of which are shown on the fig.2; the dependence character of $R_x(T)$ from one sample of one of crystal groups are shown by curve on the fig.1. The calculation of temperature dependences of hole concentration (and Hall coefficient, correspondingly) is carried out on the base of well-known equations of electroneutrality and expression for hole concentration in Kane's dispersion law approximation:

$$p = \Delta + N_a \left(1 - \frac{1}{1 + \frac{1}{2} \exp(-\varepsilon_a^* - \eta^*)} \right) \quad (1)$$

$$p = \frac{(2m_d \kappa_0 T)^{3/2}}{3\pi^2 \hbar^3} \zeta_{3/2,0}^0(\eta, \beta) \quad (2)$$

where N_a and ε_a^* are concentration and activation energy of acceptor centers correspondingly, Δ has difference mean between hole concentrations and possible donor centers which are hypothetically not frozen out at the most low temperatures. Effective mass of state density m_d is taken the same one as earlier at mobility calculations: $m_d(T) = 0.14 \cdot (T/77)^{0.6} m_0$.

As it is seen from fig.2, if we take under consideration only one acceptor level with nonzero activation energy, then only small section of curve $R_x(T)$ is described more correctly. Moreover, we suppose the existence of “shallow” level for explanation of low-temperature curve section and the existence of “deep” level for explanation of high-temperature curve section.

The average activation energy value $\varepsilon_a = 0,025\text{eV}$ of big amount samples of this crystal group at which one can successfully describe the low-temperature of $R_x(T)$ curve sections and for high-temperature curve sections we have $\varepsilon_a = 0,085\text{eV}$. The high-temperature $R_x(T)$ curve sections in two other sample groups represented by curves 2,3 on the fig.1 are well described at $\varepsilon_a = 0,085\text{eV}$.

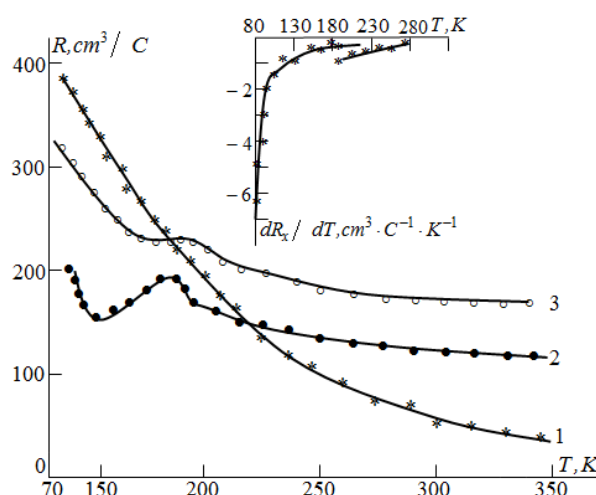


Fig.1. Character temperature dependences of Hall coefficient for different groups of $\text{Pb}_{0,98}\text{Sm}_{0,02}\text{S}$ crystals. The temperature dependence of first derivative dR_x/dT for first crystal group presented by curve 1 of the main figure is given in the insertion.

The nature of revealed acceptor centers hasn't been known yet. One can only propose the fact that they are connected with intrinsic crystal defects because the investigated crystals have been grown up from high-clean initial materials. Probably they present themselves the difficult complexes the appearance of which we connect with tendency of investigated material to self-compensation [3].

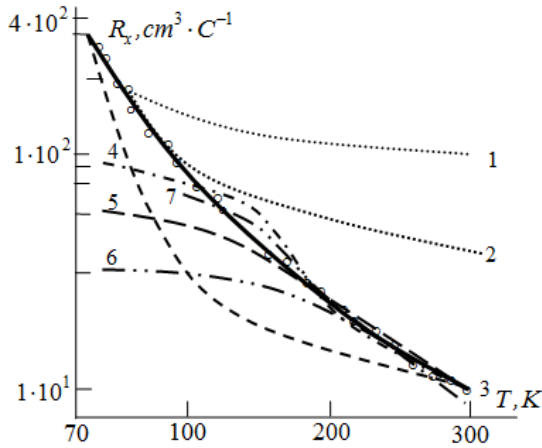


Fig.2. Temperature dependence of Hall coefficient. The points are experimental results. The full lines are calculative curves, calculated by (1) and (2) formulas at following activation energy values ε_a (eV): 1-0.02, 2-0.03, 3-0.04, 4-0.08, 5-0.089, 6-0.1. 7 is curve corresponding to simultaneous action of two acceptor levels with 0.025eV and 0.085eV activation energies.

At least, the crystals close to composition to solid solutions of $Pb_{0.98}Sm_{0.02}S$ one don't reveal the compensated material characters at the investigation and we don't observe the similar acceptor levels. By other hand, the activation energy of "deep" level revealed by us is well correlated with activation energy of acceptor centers in strongly doped by compensating impurities of PbS crystals which are rich of sulfur [4]. Comparing our data with work data [4], one can suppose that compensation processes in complex systems on the lead base lead to formation of acceptor centers creating "deep" levels in forbidden band independently on the fact that the intrinsic components interact between each other or with impurities.

CONCLUSION

We have investigated the nature of revealed acceptor levels and question on simultaneous action of two acceptor levels or transformation of one acceptor complexes (or their part) into other ones during temperature change require the more detail consideration. Our investigation allow us to describe theoretically all temperature dependence $R_x(T)$ for first group crystals (curve 7 of fig.2), but we can't explain the dependence $R_x(T)$ for crystal group presented by curve 3 on the fig.1 without additional suppositions. If we suppose that the transformation (full or partial) of some complexes into another ones take place during temperature change, then at least such behavior of $R_x(T)$ becomes quite explainable from qualitative analysis point of view. For the final solving of the given question the additional investigations are necessary, in particular the theoretical calculations of energy states of intrinsic defect complexes in $A^{IV}B^{VI}$. In future such investigation will be supposed.

- [1]. V.I. Kaydanov, U.I. Ravich. PPS, 145, 51 (1985) (in Russian).
 [2]. B.A. Volkov, O.A. Pankratov. JETF, 88, 280 (1985) (in Russian).
 [3]. H.A. Hasanov The questions of special radioelectronics, vol. 2, p.114, (2008) (in Russian).
 [4]. E.A. Guriyeva, P.P. Konstantinov, L.V. Prokofyev et al. FTP, 40, 7, 783 (2006) (in Russian)

BAND STRUCTURE CALCULATION OF GeS COMPOUND BY LCAO METHOD AND DEEP LEVELS OF Ge_S AND S_{Ge} ANTISTRUCTURAL DEFECTS INVESTIGATION

Z.A. DJAHANGIRLI

Institute of Physics of Azerbaijan NAS, G.Javid ave., 33, Az-1143, Baku, Azerbaijan

The energy structure GeS containing the defects of Ge_S and S_{Ge} is investigated by method of Green function by self-consistency method. The change of state density caused by defect, the origin and orbital composition of electron states in forbidden band, their charge state are discussed.

Last years the essential progress in the investigation of deep defect levels in semiconductors [1-5] has been made. These investigations present the big interest in understanding of their electrophysical properties which play the important role in applied physics and instrument making. The cluster methods, method of extended elementary cell and method of Green function are the one of the more popular study methods of electric states of different defects. It is known that in cluster method the cluster dimensions and the choice of boundary conditions influence on results of calculation of energy states of deep defect levels. The peculiarity of method of Green function in comparison with cluster methods is in defect tractability as disturbance of infinite periodic lattice of crystal [6-8].

The investigation results of electric states of antistructure defects of Ge_S and S_{Ge} in GeS by method of Green function in approximation of strong bond by the use of Sletor orbitals. For definition of Green function of ideal crystal one firstly consider the infinite volume crystal, eigen functions and eigen values of which are defined using three-dimensional translation symmetry by the method of linear combinations of atom orbitals (LCAO).

THE CALCULATION OF BAND STRUCTURE BY LCAO METHOD

The main idea of the strong bond method is that the eigen states of free atoms are used in the capacity of basis functions in expansion of wave functions. In particular, Bloch sum in LCAO method is expressed in the form [9]:

$$\psi_m^{(j)}(\vec{k}, \vec{r}) = \sum_{\vec{R}} e^{i\vec{k}\vec{R}} \varphi_m(\vec{r} - \vec{R} - \vec{\tau}_j) \quad , \quad (1)$$

where \vec{R} are translation lattice vectors, $\vec{\tau}_j$ are basis vectors of atoms. If one decompose $\psi_m^{(j)}(\vec{k}, \vec{r})$ on plane waves with vectors of reciprocal lattice \vec{G}

$$\psi_m(\vec{k}, \vec{r}) = \sum_{\vec{G}} \alpha_m(\vec{k} + \vec{G}) e^{i(\vec{k} + \vec{G})\vec{r}} \quad . \quad (2)$$

The expansion coefficients are defined as

$$\alpha_m(\vec{k} + \vec{G}) = \Omega^{-1} \int e^{-i(\vec{k} + \vec{G})\cdot(\vec{r} + \vec{\tau}_j)} \varphi_m(\vec{r}) d\vec{r} \quad (3)$$

Then for overlap integrals one can obtain the following expressions:

$$S_{mn}(\vec{k}) = \langle \psi_m(\vec{k}, \vec{r}) | \psi_n(\vec{k}, \vec{r}) \rangle, \quad (4)$$

or

$$S_{mn}(\vec{k}) = \sum_{\vec{G}} \alpha_m^*(\vec{k} + \vec{G}) \alpha_n(\vec{k} + \vec{G})$$

Taking under consideration the equations (2), (3) and (4) the substitution of equation (1) into Schrödinger equation for ideal crystal leads to usual eigenvalues equation in matrix form with matrix elements of Hamiltonian

$$H_{mn}(\vec{k}) = \sum_{\vec{G}\vec{G}'} \alpha_m^*(\vec{k} + \vec{G}) \alpha_n(\vec{k} + \vec{G}') [(\hbar^2 / 2m) \delta_{\vec{G}\vec{G}'} + V(\vec{G} - \vec{G}')], \quad (5)$$

where $V(\vec{G} - \vec{G}')$ is Fourier transform of crystalline potential.

The desired eigenvalues are obtained by standard methods by the way of solution of secular equation. Hamiltonian matrix elements H_{mn} and overlap integrals S_{mn} are found with usage of Sletor orbitals centered in six neighbor atoms

$$\varphi(\vec{r}) = r^n e^{-\alpha r} Y_{lm}(\theta, \phi). \quad (6)$$

For orbitals of *s*- and *p*- type we have:

$$\varphi_s(\vec{r}) = r e^{-\alpha r} \quad , \quad (7)$$

$$\varphi_x(\vec{r}) = x r e^{-\alpha_2 r}, \quad \varphi_y(\vec{r}) = y r e^{-\alpha_2 r}, \quad (8)$$

$$\varphi_z(\vec{r}) = z r e^{-\alpha_2 r},$$

and five Bloch functions of d-type are as follows:

$$\varphi_{xy}(\vec{r}) = x y e^{-\alpha_2 r}, \quad \varphi_{xz}(\vec{r}) = x z e^{-\alpha_2 r}, \quad (9)$$

$$\varphi_{zy}(\vec{r}) = z y e^{-\alpha_2 r} \quad ,$$

$$\varphi_{(x^2-y^2)}(\vec{r}) = (x^2 - y^2) r e^{-\alpha_2 r} \quad \text{and et.al.} \quad (10)$$

$$\alpha = (2\pi / a) \lambda \quad (11)$$

Further Fourier transforms are calculated of Sletor orbitals

$$\int e^{-\vec{k}^* \vec{r}} \varphi_s(\vec{r}) d\vec{r} = -8\pi \frac{-3\alpha^2 + \vec{k}^2}{(\alpha^2 + \vec{k}^2)^3} \quad (12)$$

$$\int e^{-\vec{k}^* \vec{r}} \varphi_p(\vec{r}) d\vec{r} = 32i\pi \frac{-5\alpha^2 + \vec{k}^2}{(\alpha^2 + \vec{k}^2)^4} \vec{k} Y_{p,m}(\Theta, \Phi) \quad (13)$$

$$\int e^{-\vec{k}^* \vec{r}} \varphi_d(\vec{r}) d\vec{r} = -192\pi \frac{\alpha \vec{k}^2}{(\alpha^2 + \vec{k}^2)^4} Y_{d,m}(\Theta, \Phi) \quad (14)$$

where Θ , Φ are spherical angles of \vec{k} vector.

The matrix elements of H_{mn} , S_{mn} one can obtain in analytical form if one can use the explicit form of Fourier transforms of Sletor orbitals and this leads to essential simplifying of calculative process.

As the definition of localized state position in forbidden band is the main task of the given work, it is necessary to reproduce the right value of energy gap width obtained by more detail methods. To this effect the calculation of band structure by the method of pseudopotential on the base of plane waves has been carried out.

The nonlocal pseupotentials from first principles are constructed by circuit supposed by Bachelet G.B. and others [10]. The exchange-correlated potentials are calculated by Seperli and Alder circuits parameterized by Perdu and Cunger. The calculations by both methods give the identical results as for valence bands so for conduction band. By the way of increase of basis functions the convergence of results has been checked. The calculations show that increase of basis number centered on more distant neighbors doesn't lead to essential shifts of energy levels.

The bond structure of GeS compound calculated by LCAO method with basis use of базисов s -, p - and d -type λ_{Ge} , $\lambda_S = 1.5$ for s -, 1.8 for p - and d - type and detail method of pseudopotential on the basis of plane waves. The analysis of origin of bond states on the basis of linear combination method of atom orbitals shows that four isolated situated low valence bands are connected with s -states of S atoms. The following group of valence states near 6-8 eV mainly consists in s -states of cation with some deposition of p -states of anion. Finally, the uppstet group consisting in twelve bands occurs from Ge states with some small deposition of p -states of S atom. The origin analysis of valence bands are well agreed with experiment results by photoelectron emission [11].

It is known that Hamiltonian matrix elements in method of empirical strong bond are selected so that reproduce the some experimental data (for example, extended gap width) and further, the bond structure of volume crystal is calculated and moreover, the valence band is satisfactory described. In the comparison with empirical strong bond in our calculations the matrix

elements are calculated in analytical form. That's why the conduction band is well agreed with previous detail pseudopotential calculations [12] on the basis of plane waves. In calculations by the strong bond method the number of basis functions is essentially less than number of basis functions used in pseudopotential method that leads to essential gain of computer time without accuracy loss.

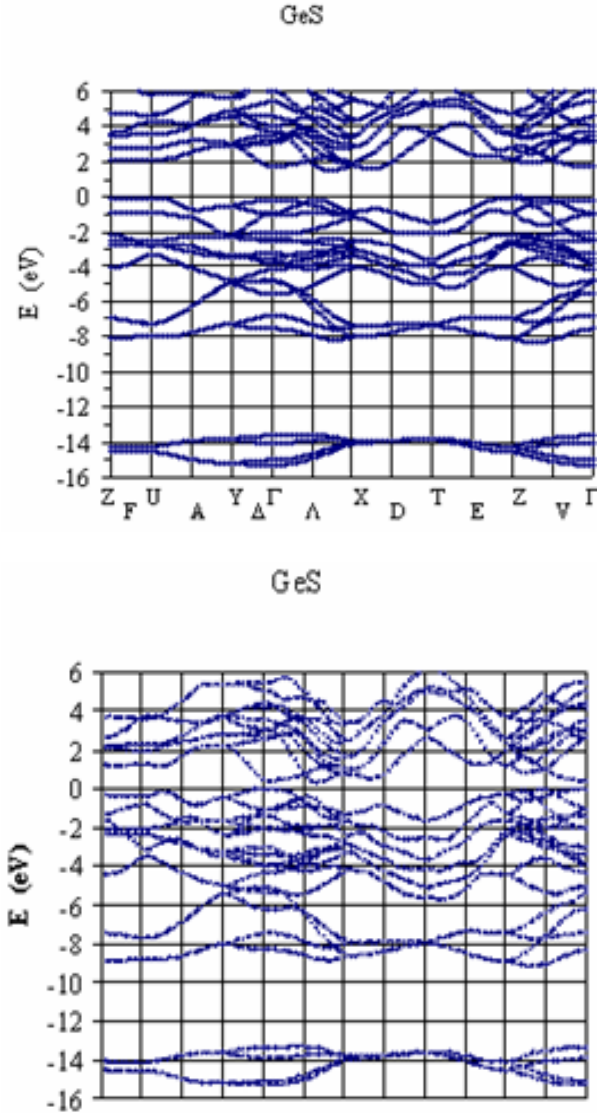


Fig. 1. The band structure GeS calculated by pseudopotential method (upper fig.) and strong bond (lower fig.) one.

GREEN FUNCTION METHOD

Let's H^0 is one-electron Hamiltonian of ideal crystal, U is disturbance potential, introduced by fact. Then one can find the electron spectrum of disturbed Hamiltonian $H = H^0 + U$ solving the following equation:

$$(H^0 + U) | \Psi \rangle = E | \Psi \rangle \quad (15)$$

The formal solution of equation (15) leads to Lippman-Shvinger equation:

$$|\Psi\rangle = |\Psi_0\rangle + G^0 U |\Psi\rangle, \quad (16)$$

where $|\Psi_0\rangle$ is general solution of homogeneous equation $(E - H^0)|\Psi_0\rangle = 0$, and $G^0 U |\Psi\rangle$ is private solution of heterogeneous equation. Green function G^0 of unperturbed system is defined by following way:

$$G^0(E) = \frac{1}{E + i0 - H^0}. \quad (17)$$

Then the state density of ideal system is:

$$N^0(E) = -\frac{1}{\pi} \text{Im Sp} G^0(E). \quad (18)$$

When eigenvalues of E don't coincide with any energy from spectrum H^0 , the solutions spatially localized near defect can exist. In this case the formula (15) can be led to the following form:

$$(1 - G^0 U) |\Psi\rangle = 0 \quad (19)$$

Then the existence condition of bound states corresponds to:

$$D(E) = \det(1 - G^0(E)U) = 0 \quad (20)$$

Let's present the operators $G^0(E)$ and U in matrix form:

$$G^0(E) = \lim_{\varepsilon \rightarrow 0^+} \sum_{n, \vec{k}} \frac{|n, \vec{k}\rangle \langle n, \vec{k}|}{E + i\varepsilon - E_{n, \vec{k}}}. \quad (24)$$

Let's compose ψ on orthonormal basis φ_α

$$\psi = \sum_{\alpha} C_{\alpha} \varphi_{\alpha} \quad (25)$$

and let's express the matrix elements $G^0(E)$ and U in the same basis

$$G_{\alpha\alpha'}^0(E) = \sum_{n, \vec{k}} \frac{\langle \alpha | n, \vec{k}\rangle \langle n, \vec{k} | \alpha'\rangle}{E - E_{n, \vec{k}}^0}, \quad (26)$$

where $E_{n, \vec{k}}^0$ are eigenvalues of H^0 , i.e. of ideal crystal.

Then (19) becomes the linear algebraic equation:

$$\sum_{\alpha'} [\delta_{\alpha\alpha'} - \sum_{\alpha''} G_{\alpha\alpha''}^0(E) U_{\alpha''\alpha'}] C_{\alpha} = 0, \quad (27)$$

which has the non-zero solutions only in that case if:

$$\det \|\delta_{\alpha\alpha'} - \sum_{\alpha''} G_{\alpha\alpha''}^0(E) U_{\alpha''\alpha'}\| = 0. \quad (28)$$

As the defect potential has the local character then the formula (28) strongly simplifies. When the eigenvalues of E is in the region of continuous spectrum of Hamiltonian H^0 , the resonances appear. The integral information about resonances is defined from total change of density of states:

$$\Delta N(E) = \frac{1}{\pi} \frac{d\delta(E)}{dE}, \quad (23)$$

where

$$\delta(E) = -\text{arctg}[\text{Im} D(E) / \text{Re} D(E)].$$

Let's chose Sletter orbitlas φ_α localized in atom centers in the capacity of basis. As the disturbance potential U is strongly localized then the matrix element $U_{\alpha''\alpha'}$ calculated with the use of Sletter orbitals is differed from zero only for closest neighbours where the potential overlaps with both orbitals.

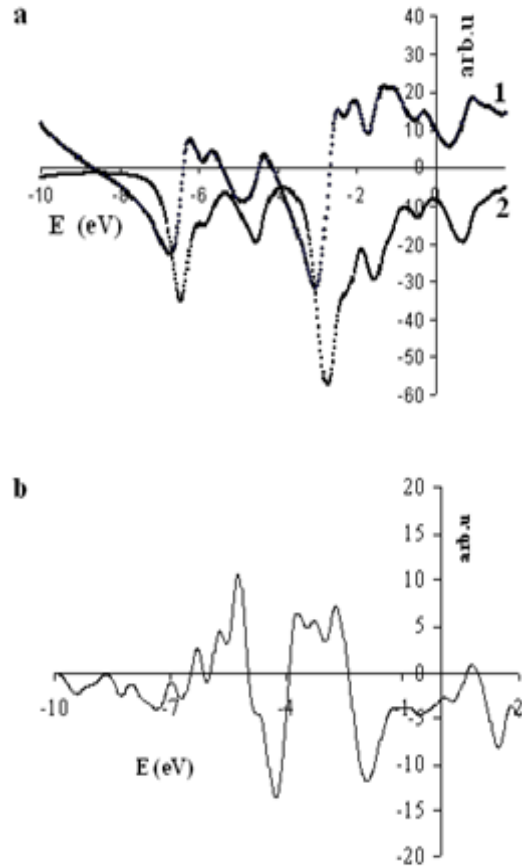


Fig. 2. **a** is imaginary (1) and real (2) parts of Green function, **b** is change of state density $\Delta N(E)$.

Theoretical-group analysis shows that point group C_{1h} Ge_s and S_{Ge} of antistructural defects consist in elements: $\{E\}$ is single element; $\{\sigma_v\}$ is reflection plane perpendicular to x-axis and passing through defects (the axes are chosen as in [13]). The both presentations are one-dimensional and all defect states are nondegenerate ones. According the point symmetry the defect states

either symmetrical ones or antisymmetrical ones relatively the reflection plane.

The change of state density caused by antistructural defect Ge_S , the imaginary and real part of Green function are presented on the fig.2.

The antistructural defects Ge_S and S_{Ge} form the deep levels in forbidden band at $E_V + 0.37$ eV and at $E_C - 0.16$ eV correspondingly. The local state in fundamental forbidden band for GeS is occupied by two electrons and is the donor and for S_{Ge} the bound state isn't occupied and acts as acceptor. The wave functions of both deep levels are exponentially decreased at removal from defects.

The analysis of wave functions of localized states in fundamental forbidden band for both defects shows that these defects mainly consist in p-type orbitals localized on closest neighbors.

This corresponds with the fact that the upper edge of valence band and low part of conduction band GeS mainly consists from p-type states Ge and S.

The authors connect the emission peak at 1,5eV revealed in photoluminescence spectrum of GeS [14]

which corresponds to energy level $\sim 0,25$ eV below the conduction band with deep impurity level. As it is seen our calculations are in satisfactory agreement with experimental data.

Note that in our calculations we don't take under consideration the distortion influence of ideal lattice near local defect. It is obvious that detail quantitative description of experiment data requires the strong consideration of influence connected with distortion of ideal lattice.

CONCLUSION

The calculation of electron spectrum GeS with antistructural defect Ge_S and S_{Ge} self-agreed with Green function method has been carried out. It is found that the one localized level for both defects consisting in p-type orbitals localized on closest neighbours is in the fundamental forbidden band.

The author is thankful to academician F.M. Gashimzade and G.S. Orudjev for useful advises and discussions.

-
- [1]. *O.V. Farberovich, A. Yaresko, K. Kikoin and V. Fleurov.* Phys. Rev. B78, (2008) 085206.
- [2]. *M.C. Esteves, A.B. Rocha, N.V. Vugman, C.E. Bielschowsky,* Chemical Physics Letters, 453 (4), (2008) 188.
- [3]. *S.T. Nakagawa, A. Okamoto, G. Betz,* Nuclear Inst. and Methods in Physics Research, B, 266 (12), (2008) 2711.
- [4]. *W.G. Hu, Z. Wang, B.F. Su, Y.Q. Dai, S.J. Wang, Y.W. Zhao,* Physics Letters A, 332 (3), (2004) 286.
- [5]. *D. Chadi,* Phys. Rev. B, 68 (2003) 19.
- [6]. *M. Lanno, J. Burguen.* Tochechnie defekti v poluprovodnikakh. Teoriya, Mir, M., 1984, 264 s. (in Russian)
- [7]. *P. Kruger and J. Pollmann.* Phys. Rev. B15, (1988) 10578.
- [8]. *J. Bernholc, Nunzio O. Lipari, and S.T. Pantelides.* Phys. Rev. B8, (1980) 3545.
- [9]. *D.J. Chadi.* Phys. Rev. B8, (1977) 3572.
- [10]. *G. Bachelet, D.Hamann and M. Schluter.* Phys. Rev. B8, (1982) 4199.
- [11]. *P. Kemeny, J. Azoulay, M. Cardona et. al.,* Nuovo Cimento, 39B, (1977) 709.
- [12]. *F.M. Gashimzade, D.A. Guseinova, A.M. Aliyev.* FTT, 31, (1989), 21. (in Russian)
- [13]. *F.M. Gashimzade, V.E. Khartsiev.* FTT, 4, (1962) 434. (in Russian)
- [14]. *V.S. Bagaev, L.I. Paduchikh, V.B. Stopachinskiy, R.G. Khakimov, L. Shtourach.* FTT, 21, (1979), 398. (in Russian)

THERMODYNAMIC AND ELECTRONIC PROPERTIES OF HOT ELECTRONS IN A QUANTUM WELL

M.A. MEHRABOVA

*Institute of Radiation Problems, Azerbaijan National Academy of Sciences
AZ-1143, Azerbaijan, Baku, F. Aghayev str., 9*

The thermodynamic and electronic parameters: concentration, chemical potential, heat-capacity and thermal electromotive force (thermal e.m.f.) of hot two-dimensional electron gas in a heterocontact were calculated using a specific distribution function. The obtained expressions describe the dependence of heat-capacity and thermal electromotive force on a film thickness and an electron temperature in a good manner. It was determined that the acquired results calculated for the model under consideration, strongly differed from the results calculated on the base of a Maxwell distribution function.

1. INTRODUCTION

Semiconductor heterostructures have been attracting the attention of the researchers, carrying out studies in the field of Solid-state Physics and Electronics for a long time. An additional degree of freedom connected with the presence of two different semiconductors gives an opportunity to study new physical phenomena and instrumental structures not realized in homogeneous materials.

To obtain and study the properties of hetero-junctions on the base of semiconductors have been of great practical interest for the last years. They are widely applied in microelectronics, drafting integral circuits and optoelectronics for making scintillation detectors. Detectors basing on hetero-junctions have high photosensitivity in a short-wave spectral region at the expense of dissociation and therefore are considered more perspective ones for the operation of detectors in a short-wave spectral region of hetero-junctions.

The study of the properties of hetero-junctions results in both the improvement of the parameters of semiconductor devices of a traditional use and revealing new functional dependences initiating the development of new devices and systems [1]. In our work the thermodynamic and electronic properties of hot electrons were theoretically studied at a lower level of a quantum well formed at the hetero-junction, in the region in the vicinity of and higher than the emission threshold of an optical phonon with the assumption that the electron temperature had been set lower than the threshold. At various values of a quantum well width the dependence of entropy, heat-capacity, thermal e.m.f. on an electron temperature was found. Besides the external electric field an electron-phonon scattering is also taken into account.

2. DISTRIBUTION FUNCTION

Maxwell distribution in the vicinity of the threshold, λ - determines the critical density N_c^+ , higher which the distribution in $E > \hbar\Omega_0$ region differs from the Maxwell one and is defined by the formula

$$\lambda = \pi^{-1/2} \frac{\tau_0}{\tau_{ee}} \left(\frac{k_0 T_e}{\hbar\Omega_0} \right)^{-1/2} = \frac{N}{N_c^+}$$

where τ_0 - emission time of an optical phonon, τ_{ee} - ee-scattering time, specifying the rate of an electron-electron energy exchange.

A layer of a narrow-band-gap semiconductor with d thickness, clamped between two semi-infinite wide-band-gap semiconductors is under consideration. A quantum well appears on a d layer for electrons. It's supposed that the distance between two lowest levels in the well

$$E_1 - E_0 = \frac{3\pi^2 \hbar^2}{2md^2} \gg \hbar\Omega_0, \text{ where } \hbar\Omega_0 - \text{energy of an optical}$$

phonon. When $\kappa_0 T_e \ll \hbar\Omega_0$, all levels besides the lowest one can't be taken into account. The energy spectrum of two-dimensional electron gas (TDEG) is supposed to be a parabolic one:

$$E_k = \frac{\hbar^2 k^2}{2m} + \frac{\hbar^2 \pi^2}{2m d^2} \quad (1)$$

where κ - Boltzmann constant, N - the number of electrons per 1 cm^2 layer, τ_0 - emission time of an optical phonon, τ_{ee} - electron-electron scattering time.

In the work [2] the distribution function of hot electrons was found at a lower level of the quantum well in the region in the vicinity of and higher than the emission threshold of optical phonon under the assumption that the electron temperature had been set lower than the threshold, which had the following view:

$$\begin{aligned} & \sqrt{2\lambda} A; \quad |t| \ll \lambda, \quad t=0 \\ f(E) = & 2\pi^{-1/2} A \lambda t^{-1/2} e^{-t}; \quad t>0, \quad t \gg \lambda \quad (2) \\ & A e^{-t} \text{erf} |t|^{1/2}; \quad t<0, \quad |t| \ll \lambda \end{aligned}$$

$$\text{Here } t = \frac{E_k - \hbar\Omega_0}{k_0 T_e};$$

$$A = \frac{2\pi N \hbar^2}{m k_0 T_e} \exp\left(-\frac{\hbar\Omega_0}{k_0 T_e}\right) \quad (3)$$

3. ENTROPY AND HEAT-CAPACITY OF HOT ELECTRONS IN A QUANTUM WELL

Under this heading we calculated the thermodynamic parameters of hot TDEG in a quantum well. The density of the states corresponding to the spectrum equals to (1):

$$g(E) = \sum_n \delta(E - E_k) = \frac{m}{\pi \hbar^2} \theta(E - E_1),$$

which itself presents a step function. The concentration of conductivity electrons is determined as: $N = \int g(E) f(E) dE$. It can easily be shown that

$$N = \frac{\sqrt{2\lambda mk_0 T_e} \exp(\frac{\mu - \hbar\Omega_0}{k_0 T_e})}{\pi\hbar^2}; \quad t=0$$

$$N = \frac{2mk_0 T_e}{\pi\hbar^2} \lambda \exp(\frac{\mu - \hbar\Omega_0}{k_0 T_e}) (\operatorname{erf} \sqrt{c+1} - \operatorname{erf} \sqrt{c}); \quad t > 0$$

$$N = \frac{\sqrt{2mk_0 T_e}}{\pi\hbar^2} \exp(\frac{\mu - \hbar\Omega_0}{k_0 T_e}) (\operatorname{erf} \sqrt{2(c+1)} - \operatorname{erf} \sqrt{2c}); \quad t < 0$$

$$N_m = \frac{mk_0 T_e}{\pi\hbar^2} (1 - \frac{1}{e}) \exp(\frac{\mu - E_1}{k_0 T_e}) \quad (5)$$

where $c = \frac{E_1 - \hbar\Omega_0}{k_0 T_e}$, μ - chemical potential, (5) corresponds to a Maxwell distribution. According to (4) and (5) expressions the chemical potential is determined:

$$\mu = \hbar\Omega_0 + k_0 T_e \ln \frac{\pi N \hbar^2}{\sqrt{2\lambda mk_0 T_e}} \exp(\frac{\hbar\Omega_0}{k_0 T_e}); \quad t=0$$

$$\mu = \hbar\Omega_0 + k_0 T_e \ln \frac{\pi N \hbar^2}{2mk_0 T_e \lambda} [\operatorname{erf} \sqrt{c+1} - \operatorname{erf} \sqrt{c}]^{-1}; \quad t > 0$$

$$\mu = \hbar\Omega_0 + k_0 T_e \ln \frac{\pi N \hbar^2}{\sqrt{2mk_0 T_e}} [\operatorname{erf} \sqrt{2(c+1)} - \operatorname{erf} \sqrt{2c}]^{-1}; \quad t < 0$$

$$\mu_m = k_0 T_e \ln \frac{\pi N \hbar^2}{mk_0 T_e} (\frac{e}{e-1}) \exp(\frac{E_1}{k_0 T_e}) \quad (7)$$

The main thermodynamic functions were calculated. The entropy calculated on the base of the thermodynamic potential has the following view:

$$S = \sqrt{8\lambda} N k_0 (1 + \frac{\hbar\Omega_0}{k_0 T_e}) \exp(-\frac{\hbar\Omega_0}{k_0 T_e}); \quad t=0$$

$$S = \frac{2\lambda mk_0}{\pi\hbar^2} \exp(\frac{\mu_e - \hbar\Omega_0}{k_0 T_e}) \hbar\Omega_0 [\operatorname{erf} \sqrt{c+1} - \operatorname{erf} \sqrt{c}]; \quad t > 0$$

$$S = \frac{mk_0}{\sqrt{2\pi}\hbar^2} \exp(\frac{\mu_e - \hbar\Omega_0}{k_0 T_e}) \hbar\Omega_0 [\operatorname{erf} \sqrt{2(c+1)} - \operatorname{erf} \sqrt{2c}]; \quad t < 0$$

For heat-capacity the following expression is obtained:

$$C_v = \sqrt{2\lambda} N k_0 [1 + \frac{\hbar\Omega_0}{k_0 T_e} (1 + 4 \frac{E_1}{k_0 T_e})] \exp(-\frac{\hbar\Omega_0}{k_0 T_e}); \quad t=0$$

$$C_v = \frac{2\lambda mk_0}{\pi\hbar^2} \exp(\frac{\mu_e - \hbar\Omega_0}{k_0 T_e}) \hbar\Omega_0 (\frac{1}{2} + \frac{\hbar\Omega_0}{k_0 T_e}) [\operatorname{erf} \sqrt{c+1} - \operatorname{erf} \sqrt{c}]; \quad t > 0$$

$$C_v = \frac{mk_0}{\sqrt{2\pi}\hbar^2} \exp(\frac{\mu_e - \hbar\Omega_0}{k_0 T_e}) \hbar\Omega_0 (\frac{3}{8} + \frac{\hbar\Omega_0}{k_0 T_e}) [\operatorname{erf} \sqrt{2(c+1)} - \operatorname{erf} \sqrt{2c}]; \quad t < 0$$

Basing on the obtained expressions the dependences of heat-capacity on a film thickness and an electron temperature were built. In Fig.1 the heat-capacity curves of TDEG on the threshold of a quantum well on an electron temperature were given. The curve (a)

corresponds to the heat-capacity of TDEG on the threshold, calculated on the base of a distribution function (2), and the straight one (b) to the heat-capacity, calculated on the base of a Maxwell distribution when the

film thickness is $d=100 \text{ \AA}$. As it's shown in the Fig. the difference is essential.

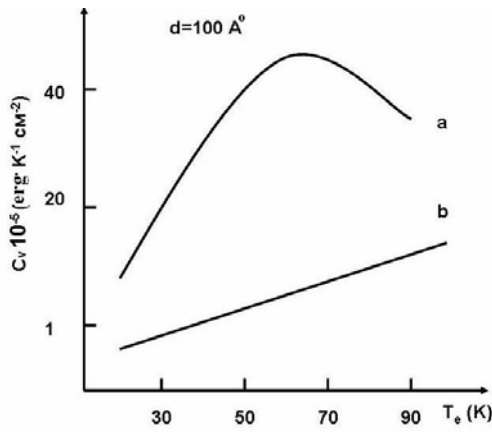


Fig. 1. Dependence of heat-capacity on an electron temperature T_e when the film thickness is $d=100 \text{ \AA}$, a) on the threshold, d) on the base of a Maxwell distribution.

In Fig. 2 the dependences of an electron heat-capacity TDEG on the threshold of a quantum well on the temperatures at different values of film thickness are presented. With decrease in the film thickness the heat-capacity of TDEG at the threshold rises.

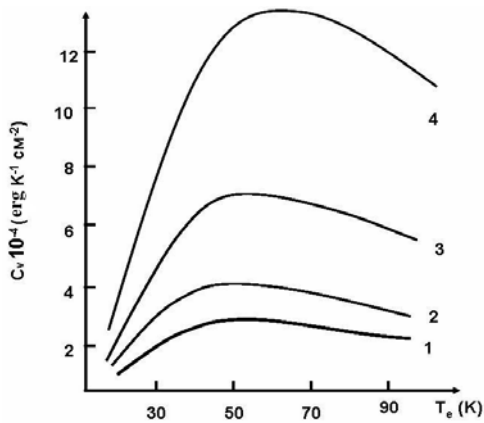


Fig. 2. Dependence of an electron heat-capacity of TDEG on the threshold on the temperature T_e at the film thicknesses: 1. $d=120 \text{ \AA}$, 2. $d=100 \text{ \AA}$, 3. $d=80 \text{ \AA}$, 4. $d=60 \text{ \AA}$,

In Fig. 3a and Fig. 3b the curves of the heat-capacity of TDEG higher than the emission threshold of an optical phonon and at a lower level of a quantum well in dependence with an electron temperature at different values of film thickness were presented which had been built correspondingly on the base of the expression (9). According to the Figures, with decrease in the film thickness, heat-capacity rises.

The results acquired on the base of the distribution functions (2) differ from the results acquired on the base of a Maxwell distribution (3) with T_e temperature (Fig. 4).

During building the curves the values of the parameters of a quantum well in GaAs $N=1.7 \cdot 10^{11} \text{ cm}^{-2}$, $m=0.067 \cdot 10^{-27} \text{ gr}$, $\hbar\Omega_0=10 \text{ meV}$ [3, 4] were used.

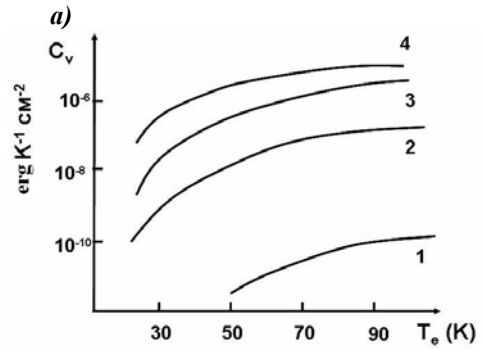
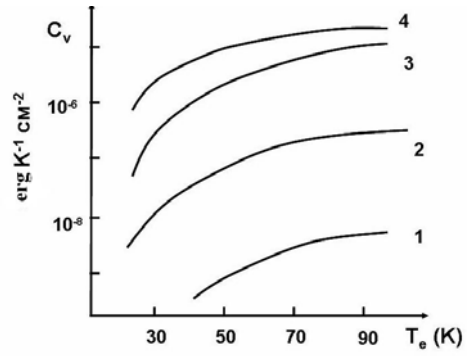


Fig.3. Dependence of an electron heat-capacity of TDEG on the temperature T_e a) higher than the threshold, b) lower than the threshold at the film thicknesses: 1. $d=200 \text{ \AA}$, 2. $d=150 \text{ \AA}$, 3. $d=100 \text{ \AA}$, 4. $d=50 \text{ \AA}$

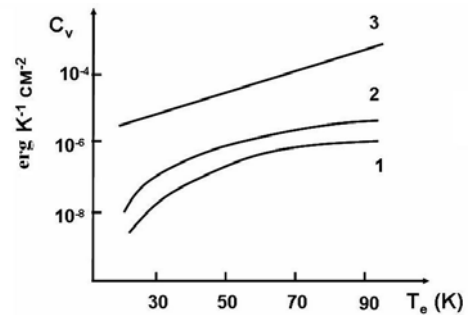


Fig. 4. Dependence of an electron heat-capacity of TDEG on the temperature T_e at the film thicknesses $d=100 \text{ \AA}$ a) higher than the threshold, d) lower than the threshold, b) according to a Maxwell distribution.

4. THERMO-E.M.F. OF HOT ELECTRONS IN A QUANTUM WELL

In the semiconductors, being in high electric fields, the study of thermo-e.m.f. is of interest from the aspect of making detectors with the best parameters with their important advantages: low inertia, generally-recognized universality in the field of measuring several physical magnitudes, the opportunity of a remote control and others [5]. Under the heading we studied the thermo-e.m.f. of hot TDEG.

Let's assume that dimensional-quantum film with a type of carriers (conductivity electrons) is located in the electric field directed to its normals. The temperature gradient is on the plane of the film. In order to calculate

the thermo-e.m.f. [6] we solve the non-collision kinetic equation and obtain the following expression

$$\alpha = -\left(\frac{1}{eT}\right)\langle E - \mu \rangle \quad (7)$$

where the averaging sign has the following meaning

$$\langle E - \mu \rangle = \frac{1}{2N(\pi\hbar)^2} \int f(E)(E - \mu)dP = \frac{m}{\pi N\hbar^2} \int (E - \mu)f(E)dE_{\perp}$$

$$\langle \dots \rangle = \frac{1}{n} \int (\dots)G(E)\left(-\frac{\partial f}{\partial E}\right)dE \quad (8)$$

Then we can write

Taking into consideration the distribution functions (2) and (3) the expression below is obtained:

1. On the threshold and direct vicinity off it $|t| \ll \lambda, t=0$

$$\alpha = -\frac{\sqrt{2\lambda}}{eT_e}(k_0T_e - 2\mu + 2E_1) \quad (9)$$

where μ - chemical potential $\mu = k_0T_e \ln \frac{\pi N\hbar^2 \exp(\frac{\hbar\Omega_0}{k_0T_e})}{2m\lambda k_0T_e (\text{erf}\sqrt{c+1} - \text{erf}\sqrt{c})}$,

$$c = \frac{E_1 - \hbar\Omega_0}{k_0T_e}$$

2. Higher than the threshold $t > 0, t \gg \lambda$

$$\alpha = -4\frac{k_0}{e} \lambda \exp\left(-\frac{\hbar\Omega_0}{k_0T_e}\right) \left[\left(\frac{1}{2} + \frac{\hbar\Omega_0}{k_0T_e} - \frac{\mu}{k_0T_e}\right) (\text{erf}\sqrt{c+1} - \text{erf}\sqrt{c}) + \frac{1}{\pi} (\sqrt{c+1}e^{-(c+1)} - \sqrt{\frac{c}{\pi}}e^{-c}) \right] \quad (10)$$

3. In a quantum well lower than the threshold $t < 0, |t| \ll \lambda$

$$\alpha = -2\frac{k_0}{e} \lambda \exp\left(-\frac{\hbar\Omega_0}{k_0T_e}\right) \left[\frac{1}{\sqrt{2}} \left(\frac{\hbar\Omega_0}{k_0T_e} - \frac{\mu}{k_0T_e} + \frac{3}{8}\right) (\text{erf}\sqrt{2c+1} - \text{erf}\sqrt{2c}) + \left(\frac{E_1}{k_0T_e} - \frac{\mu}{k_0T_e} + 1\right) e^{-c} \text{erf}\sqrt{c} - e^{-(c+1)} \text{erf}\sqrt{c+1} \left(2 + \frac{E_1}{k_0T_e} - \frac{\mu}{k_0T_e}\right) + \frac{e^{-2c}}{2\sqrt{\pi}} \left(\sqrt{c} - \frac{1}{e^2} \sqrt{c+1}\right) \right] \quad (11)$$

4. For a Maxwell distribution:

$$\alpha_m = -2\frac{k_0}{e} \exp\left(-\frac{E_1}{k_0T_e}\right) \left[\left(1 - \frac{1}{e}\right) \left(1 + \frac{E_1}{k_0T_e} - \frac{e}{e-1} \ln \frac{\pi N\hbar^2}{mk_0T_e} \exp\left(\frac{E_1}{k_0T_e}\right) - \frac{1}{e}\right) \right] \quad (12)$$

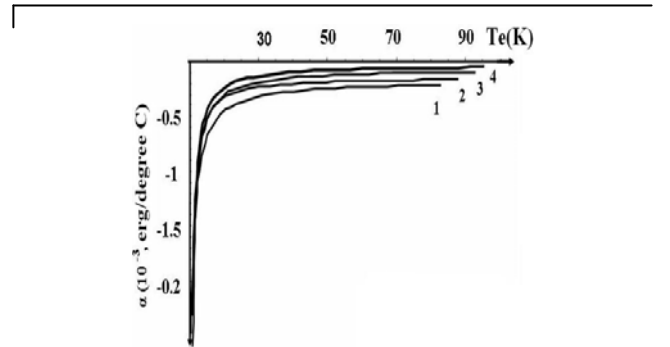
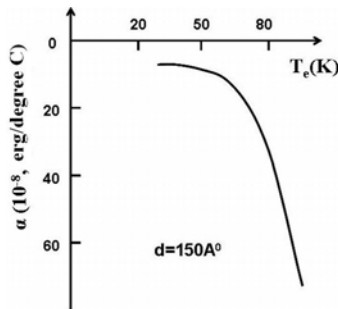


Fig.5. Dependence of thermo-e.m.f. on an electron temperature at the film thickness $d=150 \text{ \AA}$ on the base of a Maxwell distribution.

a)

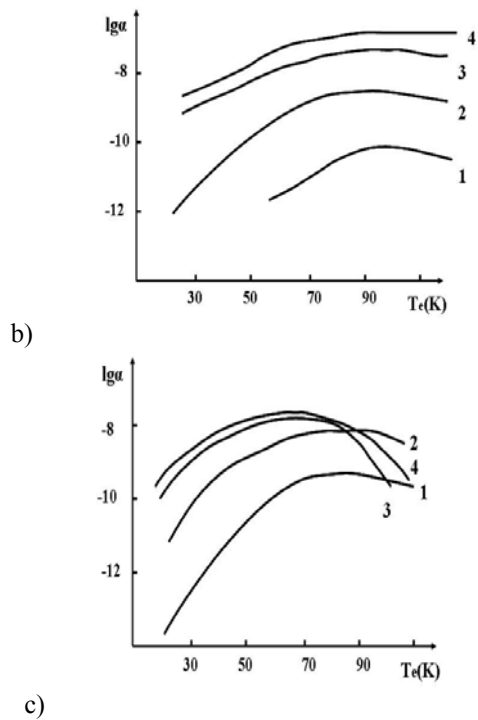


Fig. 6. The dependence of thermo-e.m.f. on an electron temperature at the film thickness: 1) $d=50 \text{ \AA}$, 2) $d=100 \text{ \AA}$, 3) $d=150 \text{ \AA}$, 4) $d=200 \text{ \AA}$ for the case of a quantum well a) on the threshold, b) higher than the threshold, c) lower than the threshold.

In Fig.5 the curves corresponding to a Maxwell distribution were built on the base of the expression (12) [6].

The results obtained on the base of the distribution functions (2) differ from the results acquired basing on a Maxwell distribution. In Fig. 6 the dependence of thermo-e.m.f. on an electron temperature was presented at several values of a film thickness, built according to the expressions (9), (10), (11). It can be concluded from the acquired results that with decrease in the film thickness, thermo-e.m.f. decreases [7].

5. CONCLUSION

In the given work the thermodynamic parameters and thermo-e.m.f. of hot TDEG in a quantum well, formed in a heterojunction depending on a film thickness and an electron temperature were calculated. The results acquired on the base of a distribution function for hot TDEG at a lower level of a quantum well, in the region in the vicinity and higher the emission threshold of an optical phonon with the assumption that an electron temperature has been set lower than the threshold, differ from the results acquired basing on a Maxwell distribution. The difference is essential. It can be concluded from the obtained results that with the decrease in the film thickness, the heat-capacity of electrons rises, and thermo-e.m.f. decreases. These results allow regulate the parameters for an optimal operation mode of devices on the base of heterojunctions.

- [1]. *L. Chenga, K. Ploga*, "Molecular-Beam Epitaxy and Heterostructures", Moscow, «Mir», 1989, p.584.
- [2]. *S.E. Esipov, I.B. Levinson*. JETP, v.90, 1, 1986, p.330-345
- [3]. *M.A. Mehrabova, T.G. Ismayilov*, "Information on SPU Space Researches", 1988, p.215-218
- [4]. *M.A. Mehrabova*, "Information on SPU Space Researches", 1989, p.180-183.
- [5]. *P.I. Baranskiy, V.P. Klochkov, I.V. Potikevich* "Semiconductor Electronics", Kiev, "Naukova Dumka", 1975
- [6]. *B.M. Asgarov*, "Electron Transport Phenomena in Semiconductors", Moscow, "Nauka", 1985, p.348
- [7]. *M.A. Mehrabova*, International Conference on "Perspectives of Peaceful Use of Nuclear Energy", 2009, p.42-45.

ELECTRON DIFFRACTION EXAMINATION OF SHORT – RANGE ATOMIC ORDER IN AgInS₂ AMORPHOUS FILMS

D.I. ISMAILOV, E.E. ALEKPEROVA, N.K. KERIMOVA
Institute of Physics of Azerbaijan National Academy of Sciences
AZ-1143, Baku, Azerbaijan, H. Javid ave., 33

There has been investigated radial distribution of atoms in AgInS₂ compound amorphous films obtained by vacuum deposition. From radial distribution curves interatomic distances are found out and coordination numbers are established.

According to [1] AgInS₂ crystallizes in tetragonal structure with crystal lattice periods: a=0,588; c=1,12 nm SGS I42m.

This paper deals with the short – range order in AgInS₂ amorphous films 25 nm in thickness obtained by vacuum deposition. Amorphous films suitable for electron diffraction examination have been prepared as by individual component sublimation in vacuum as evaporation of AgInS₂(Se)₂ synthesized single crystals. By component sublimation due to high volatility there have been first sublimated S or Se then In and Ag. Weighted samples have been evaporated in vacuum ~ 10⁻³ Pa from tungsten conical spiral on the substrate of KCl fresh spalls at room temperature, deposition rate is 2,5 nm/sec. It should be noted component interaction in the condenser and film homogenization have been occurred at room temperature and need no annealing. Diffraction pattern of AgInS₂ amorphous films is given in Fig.1.

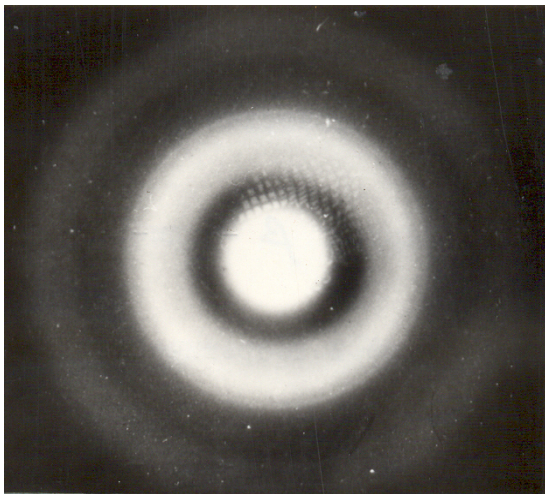


Fig.1 Electron diffraction photograph of AgInS₂ amorphous films

In electron diffraction photographs of AgInS₂ amorphous films there have been well seen 3 diffuse lines which calculation is given in table 1. Amorphous films keep their structure and do not crystallize at room temperature for 5 and more months.

Table 1.

Calculation diffuse lines from electron diffraction pattern of AgInS₂ amorphous films.

Compound	N ₀	Intensity	S=4πsinθ/λ (nm ⁻¹)
AgInS ₂	1	very strong	27,79
	2	average	33,95
	3	very weak	59,61

They can be crystallized at T 393 – 403K. In crystallized films polycrystalline films of AgInS₂(Se)₂ with know tetragonal lattices are taken place. Film crystallization have been carried out under the action of electron beam in the column of EMR electronograph – 102 at maximum cathode filament and accelerated voltage 75 – 100 kw. By electron beam density decrease one can prevent film crystallization. Parameters of short – range order, i.e. coordination number (K4), coordination sphere radii and their width characterizing statistical spreading in particle position can be determined by the curve of atom radial distribution (CARD) obtained from the formula:

$$4 \pi r^2 \rho(r) = 4 \pi r^2 \rho_0 + \frac{2r}{\pi} \int_0^\infty si(s) \sin(sr) ds \quad (1)$$

[2], by Fourier transformation of electron, neutron and X-ray beam coherent scattering intensities.

Here ρ(r) – is a function of atomic distribution, 4πr²ρ(r)dr – is an average number of atoms in spherical layer set by radii r and r+dr; ρ₀ – is an average density of atoms S=4πsinθ/λ, i(S)=[I_H^k(s) – f²(s)]/f²(s); I_H^k(s) – is a normalized intensity of coherent intensity, f(s) – is an atomic factor.

The curve of AgInS₂(Se)₂ amorphous phase scattering has been obtained by two methods: by electric registration on the instrument EMR – 102 at voltage 50 kw using non – elastically scattered electrons and by micro photometry. Providing for the background and normalization of experimental intensity the proposed method [3] has been used. According to intensities obtained by mentioned methods there have been plotted CARD of AgInS₂(Se)₂ amorphous films being in agreement with each other (Fig.2). Upper limit of integration is S_{max}=90 nm⁻¹.

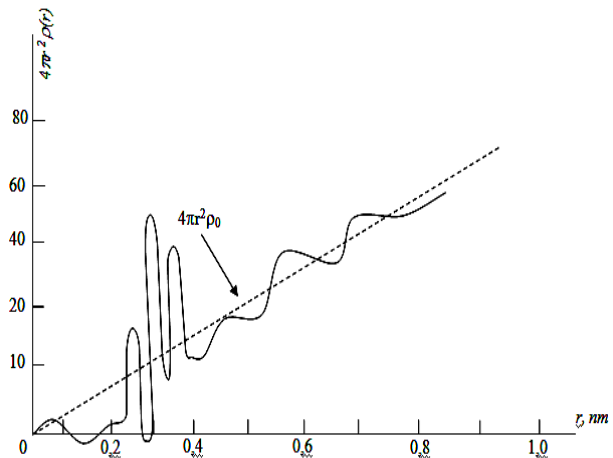


Fig.2 Curve of AgInS₂ amorphous film radial distribution

AgInS₂ CARD is included three maxima, two of them are isolated : radii of the first one (r₁), the second one (r₂) and the third (r₃) are equal to 0,248 nm, 0,296 and 0,336 nm,

respectively. The areas under the appropriate maxima are $\Delta_1=50,3$; $\Delta_2=88,7$; $\Delta_3=72$. Distance of $r_1=0,248$ nm appears to be the distance between the atoms of argentums and sulphur as tetrahedral covalent radii according to [4] are equal to 0,146 and 0,104 nm, respectively. Corresponding coordination number $n_1=3,98 \approx 4$ indicates the tetrahedral environment of Ag and S atoms in AgInS₂ amorphous films. As tetrahedral covalent radii Ag and In are very close and amount to 0,146 nm for Ag and 0,144 nm for In, distance of $r_1=0,248$ nm can be referred to the distance of $r_2=0,296$ nm between atoms of argentums and indium as it is known that in AgInS₂ crystal phase divalent Ag²⁺ is surrounded by eight atoms of In arranged at the distance 0,322 nm [5]. Calculation of

corresponding number of neighbours gives $n_2=5,94 \approx 6$ that is less than corresponding number in crystal lattice.

Proceeding from octahedral radius of In equal to 0,165 nm [4] distance of $r_3=0,336$ nm one can interpret as the distance between atoms In – In if expected that in amorphous structure the equal number of mono – and trivalent atoms of In are included. The number of the same nearest neighbours $n_3=5,98 \approx 6$.

Thus experimentally obtained values of coordination sphere radii and number of nearest neighbors show that AgInS₂ amorphous structure is involved in tetrahedral and octahedral surrounding of atoms. Similar structural motives have been revealed for AgInSe₂ amorphous films. It is established that AgInSe₂ amorphous film matrix is composed of tetrahedral and octahedral structural units.

-
- [1]. *A.V. Novoselova., V.B. Lazareva.* Physical and chemical properties of semiconductive materials. M. Nauka, 1979, p.340.
- [2]. *Ismailov D.I.* Phase formation, structure and kinetics of crystallization in A³- B³- C₂⁶ thin films, epitaxial growth of super structural phases. Phys.-math. science doctor's thesis. Baku. Institute of Physics., Azerbaijan National Academy of Sciences., 2007, 346.
- [3]. *I.D. Nabitovich* Investigation of selenium layer structure. Phys. – math. Sciences doctor's thesis. Lvov., 1970, p. 328.
- [4]. *S.A. Semiletov* Tetrahedral and octahedral covalent radii Crystallography, 1976, 21, 4, p.752-758.
- [5]. Structure reports: In 45 v. N.Y.: Wilay, 1977, p.570.

PHYSICOCHEMICAL AND THERMODYNAMIC PROPERTIES OF THE $\text{GeSe}_2\text{-A}^2\text{B}^6$ ($\text{A}^2 = \text{Hg; Cd; B}^6 = \text{S, Te}$) SYSTEMS

M.M.ASADOV, A.D.MIRZOEV

Institute of Chemical Problems, National Academy of Sciences of Azerbaijan,

H.Javid Pr. 29, AZ 1143 Baku, Azerbaijan

**Tel.: +99412 510 04 13*

E-mail address: mirasadov@gmail.com

The phase diagrams of $\text{GeSe}_2\text{-A}^2\text{B}^6$ ($\text{A}^2 = \text{Hg; Cd; B}^6 = \text{S, Te}$) systems were plotted by the methods of differential thermal and X-ray diffraction analyses, by the measurement of electromotive force (emf), microhardness and density. It is established, that phase equilibria in the pseudo-binary $\text{GeSe}_2\text{-CdTe}$, $\text{GeSe}_2\text{-HgTe}$, $\text{GeSe}_2\text{-HgS}$, $\text{GeSe}_2\text{-CdS}$ systems are characterized by formation of the limited solid solutions on basis of basic components and fourfold intermediate phases such as $\text{A}_2\text{GeSe}_2\text{Te}_2$ and $\text{A}_4\text{GeS}_4\text{Se}_2$: $\text{Cd}_2\text{GeSe}_2\text{Te}_2$ (hexagonal system; $a = 5.69$; $c = 11.32$ Å), $\text{Cd}_4\text{GeS}_4\text{Se}_2$, $\text{Hg}_2\text{GeSe}_2\text{Te}_2$ (tetragonal system; $a = 7.50$; $c = 36.48$ Å), $\text{Hg}_2\text{GeS}_2\text{Se}_2$ (hexagonal system; $a = 7.20$; $c = 36.64$ Å), $\text{Hg}_4\text{GeS}_4\text{Se}_2$ (monoclinic system; $a = 12.38$; $b = 7.14$; $c = 12.40$ Å). New dependences of the important physicochemical properties of solid solutions on basis of the GeSe_2 crosscuts of $\text{GeSe}_2\text{-A}^2\text{B}^6$ ($\text{A}^2 = \text{Hg; Cd; B}^6 = \text{S, Te}$) on composition are obtained. Thermodynamic characteristics of $\text{Cd}_2\text{GeSe}_2\text{Te}_2$ and $\text{Hg}_2\text{GeSe}_2\text{Te}_2$ phases were determined.

Keywords: Chalcogenides; Phase diagram; Crystal structure; E.m.f.; Thermodynamic data

1. INTRODUCTION

Chalcogen compounds with more electropositive chemical elements are semiconductor materials. Among these materials A^2B^6 compounds possess unique physical properties [1–3]. Chalcogenides usually are received by interaction of metal and chalcogen at heating in sealed and evacuated quartz ampoules. Sulfide HgS exists in two modifications α (zinnobar) and β (metazinnobarit). Temperature of transition $\alpha \leftrightarrow \beta$ is 345 °C. Compounds $\beta\text{-HgS}$, HgSe, and HgTe crystallize in a lattice of type blende. HgTe has practically zero forbidden zone. Degree of overlaps of a valent zone and a zone of conductivity for HgTe is 0.001 eV, for HgSe this is 0.07 eV. For $\alpha\text{-HgS}$ width of the forbidden zone is 2.0 eV. HgS is a material for photoresistors, a component of light composition on basis CdS. HgSe is used as a material for photoresistors, gauges of measurement of magnetic fields. Selenides are used as laser materials, as components for luminophores and thermoelectric materials. HgTe is a component of materials for receiver's of infra-red and X-ray radiation. Tellurides are used for photo cells, photosensitive layers of electron beam devices, dosimeters. GeSe_2 also is the semiconductor with width of the forbidden zone equal to 2.49 eV ($\rho = 10^{12} \Omega\text{-cm}$).

Stability of the pseudo-binary $\text{GeSe}_2\text{-CdTe}$, $\text{GeSe}_2\text{-HgTe}$, $\text{GeSe}_2\text{-HgS}$, $\text{GeSe}_2\text{-CdS}$ systems is confirmed by methods of samples' physicochemical analysis and the measurement of electromotive force (e.m.f.) [4,5].

2. EXPERIMENTAL DETAILS

Synthesis of initial binary compounds of the $\text{GeSe}_2\text{-A}^2\text{B}^6$ crosscuts has been carried out by direct fusion of high-purity components taken in stoichiometric ratio, in evacuated up to 10^{-3} MPa quartz ampoules in electric furnace within two days. The heating of ampoules with substances has been gradually carrying out in the furnace up to the fusion temperature of corresponding binary compounds in connection with behavior of exothermic reactions of germanium, cadmium and mercury chalcogenides' formation. At temperatures of chemical reactions' behavior of binary chalcogenides' formation

ampoules were being exposed during 4–6 hours [4]. Then temperature in the furnace has been smoothly increasing up to the fusion temperature of corresponding formed binary compound. During production of the GeSe_2 , CdTe, HgTe and HgS compounds the exposure was made at 740, 1092, 670 and 820 °C correspondingly. The individuality of the obtained GeSe_2 , CdTe, HgTe and HgS chalcogenide compounds has been controlled by methods of the physicochemical analysis by comparison of the obtained for them characteristics to the reference data.

With the purpose of definition of important parameters of intermediate phases and limited solid solutions of the threefold mutual Cd (Hg), Ge || S (Se), Te systems we investigated physicochemical and thermodynamic properties of the pseudo-binary $\text{GeSe}_2\text{-CdTe}$, $\text{GeSe}_2\text{-HgTe}$, $\text{GeSe}_2\text{-HgS}$, $\text{GeSe}_2\text{-CdS}$ systems.

It is known, that using the e.m.f. measurement method [6,7,8] in establishing phase limits binary systems lies in that the potentials of the one-phase alloy electrodes at a fixed temperature, decrease with increasing content of the less noble component in the alloy whereas the potentials of the two-phase alloy electrodes, are constant and independent of composition within a two-phase region. The potentials vary, however, when passing from one-phase region to another. The temperature dependence of the e.m.f. shows a linear character if no phase transition occurs. When within the temperature range applied to the e.m.f. measurements a phase transition occurs in the alloy electrode, the temperature coefficient of the e.m.f. below and above the transition point will take different values.

An e.m.f. method with a liquid electrolyte is used to determine the partial molar thermodynamic properties of Cd in $\text{GeSe}_2\text{-CdTe}$ and Ge in $\text{GeSe}_2\text{-HgTe}$ quaternary solid alloys. The temperature range for the measurement at 298 and 380 K. The cell arrangement is as follows



Under reversible conditions the Gibbs free energy change for the reaction at temperature T is given by

$$\Delta \bar{G}_{Me} = -zFE \quad (1)$$

were $z = 2$, $Me = \text{Cd, Ge}$, F the Faraday constant (96486 C mol^{-1}), E the measured electromotive force of the cell (V).

3. RESULTS AND DISCUSSIONS

The phase diagrams of the pseudo-binary $\text{GeSe}_2\text{-A}^2\text{B}^6$ ($\text{A}^2 = \text{Hg; Cd; B}^6 = \text{S, Te}$) systems were plotted by the methods of differential thermal and X-ray diffraction analyses, by the measurement of electromotive force (e.m.f.), microhardness and density. It was established, that in the $\text{GeSe}_2\text{-CdTe}$ (Fig. 1), $\text{GeSe}_2\text{-HgTe}$ (Fig. 2), $\text{GeSe}_2\text{-HgS}$, $\text{GeSe}_2\text{-CdS}$ systems phase equilibria are characterized by formation of limited solid solutions on basis of GeSe_2 and A^2B^6 components (Table 1) and quaternary intermediate phases such as $\text{A}_2\text{GeSe}_2\text{Te}_2$.

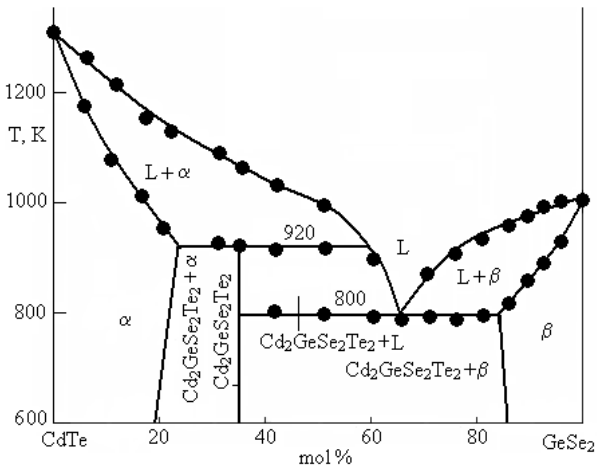


Fig. 1. Phase diagram of the CdTe-GeSe_2 system.

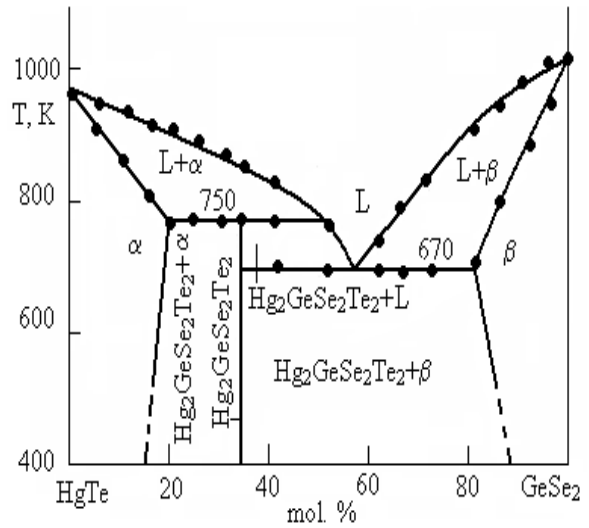


Fig. 2. Phase diagram of the HgTe-GeSe_2 system.

In these systems intermediate phases of $\text{A}_2\text{GeSe}_2\text{Te}_2$ composition are forming at temperatures 477°C ($\text{Hg}_2\text{GeSe}_2\text{Te}_2$; tetragonal system; $a = 7.50$; $c = 36.48 \text{ \AA}$), 647°C ($\text{Cd}_2\text{GeSe}_2\text{Te}_2$; hexagonal system; $a = 5.69$; $c = 11.32 \text{ \AA}$), 707°C ($\text{Hg}_2\text{GeSe}_2\text{S}_2$; hexagonal system; $a = 7.20$; $c = 36.64 \text{ \AA}$) accordingly. In $\text{GeSe}_2\text{-HgS}$ system at 862°C , the $\text{Hg}_4\text{GeSe}_2\text{S}_4$ intermediate phase (monoclinic system; $a = 12.38$; $b = 7.14$; $c = 12.40 \text{ \AA}$) is also forming. All obtained fourfold compounds are to fuse incongruently.

Dependences of solid solutions' properties on a structure have been determined. Samples were annealed at high temperatures (on $5\text{-}10^\circ\text{C}$ lower than eutectic temperature). In the Tables 2-4 concentration dependences of alloys-solid solutions on GeSe_2 basis with a rhombic lattice are resulted.

Areas of solid solutions in the systems such as $\text{GeSe}_2\text{-HgS}$ and $\text{GeSe}_2\text{-HgTe}$

Systems	Solubility, mol %	
	On GeSe_2 basis	On HgS (HgTe) basis
$\text{GeSe}_2\text{-HgS}$	18 mol% HgS (600°C)	5 mol% GeSe_2 (600°C)
$\text{GeSe}_2\text{-HgTe}$	20 mol% HgTe (477°C)	20 mol% GeSe_2 (477°C)
$\text{GeSe}_2\text{-CdTe}$	16 mol% CdTe (647°C)	22 mol% GeSe_2 (647°C)

Table 1

Physicochemical properties of the $(\text{GeSe}_2)_{1-x}\text{-(CdTe)}_x$ solid solutions

Composition, mol% CdTe	Structure parameters of a lattice			Microhardness, MPa	Density, q/sm^3
	$a/\text{\AA}$	$b/\text{\AA}$	$c/\text{\AA}$		
0.0	7.037	11.82	16.82	1400	4.68
2.5	7.040	11.83	16.82	1400	4.69
2.5	7.045	11.84	16.84	1420	4.70
2.5	7.050	11.84	16.84	1440	4.72
2.5	7.054	11.86	16.87	1470	4.72
2.5	7.060	11.86	16.88	1500	4.74
2.5	7.066	11.90	16.90	1510	4.76

Table 2

Table 3

Composition, mol% HgTe	Structure parameters of a lattice			Microhardness, MPa	Density, q/sm ³
	a/Å	b/Å	c/Å		
0.0	7.037	11.82	16.82	1400	4.68
2.0	7.040	11.83	16.82	1400	4.70
3.0	7.038	11.84	16.84	1420	4.70
5.0	7.037	11.81	16.82	1450	4.72
6.0	7.035	11.81	16.80	1460	4.73
7.0	7.032	11.80	16.80	1470	4.75
8.0	7.030	11.80	16.78	1470	4.76
9.0	7.030	11.78	16.75	1480	4.79
10	7.284	11.76	16.72	1480	4.80

Table 4

Composition, mol% HgTe	Structure parameters of a lattice			Microhardness, MPa	Density, q/sm ³
	a/Å	b/Å	c/Å		
0.0	7.037	11.82	16.82	1400	4.68
2.0	7.037	11.82	16.80	1400	4.70
3.0	7.030	11.81	16.78	1420	4.72
5.0	7.024	11.79	16.76	1450	4.83
7.5	7.020	11.77	16.74	1480	4.90
10	7.012	11.74	16.76	1500	5.06

It is established, that formation of solid solutions on A²B⁶ basis in the GeSe₂-A²B⁶ systems is accompanied by an appreciable negative deviation from the Raoult law. For concentration dependences of solid solutions on A²B⁶ basis the following relation don't meet the conditions: $p_{A^2B^6} = x_{A^2B^6} p_{A^2B^6}^*$, where $p_{A^2B^6}^*$ is the steam pressure of pure A²B⁶. For the (GeSe₂)_{1-x}-(A²B⁶)_x solid solutions the appreciable deviation from the Raoult law don't appear.

The thermodynamic analysis of chemical reactions has been carrying out with use of Gibbs-Duhem equation. For conditions of $\sum_i \nu_i d\mu_i = 0$ equilibrium which binds the change of chemical potential of components of system at $T = const, p = const$. For simplicity let's consider a $A \leftrightarrow B$ reaction. Then change of Gibbs function is: $dG = \mu_A d\nu_A + \mu_B d\nu_B$. Let's assume, that the infinitesimal $d\xi$ amount of matter A turns into B ; then $\Delta A = -d\xi$ and $\Delta B = d\xi$. This implies:

$$dG = -\mu_A d\xi + \mu_B d\xi = (\mu_B - \mu_A) d\xi \quad (T = const, p = const). \quad (2)$$

If equation (1) is re-arranged as $(\partial G / \partial \xi)_{p,T} = \mu_B - \mu_A$ it is obvious, that at behavior of $A \leftrightarrow B$ reaction the graph slope of dependence G on ξ will define the $\mu_B - \mu_A$ value. It proceeds on the theory that the chemical reaction flows in direction of G decrease. When $\mu_A > \mu_B$, reaction flows from A to B and on the contrary when $\mu_A < \mu_B$, reaction flows from B to A . At $\mu_A = \mu_B$, the reaction is in equilibrium

position. According to the above for $A \leftrightarrow B$ reaction it is possible to set values of condition's quantities for case when chemical equilibrium is occurring.

The thermodynamic potential of $A \leftrightarrow B$ reaction, according to stability condition in a system equilibrium state, is to be minimal. If take into account, that standard chemical potentials are standard mole Gibbs functions then at $T = const, p = const$ in an equilibrium state the value of ΔG_m^0 is to be minimal. In $\Delta G_m^0 = \Delta H_m^0 - T\Delta S_m^0$ relation values of ΔH_m^0 and ΔS_m^0 poorly depend on temperature. Subject to it for the given values of condition's quantities the probability of behavior of $A \leftrightarrow B$ reaction is estimating.

The following equilibrium conditions are generally fair: a) chemical balance; b) reaction is possible; c) reaction is not possible. In agreement with the theory for these cases

$$\left. \begin{aligned} \Delta G = 0; \Delta H = 0 \\ \Delta G < 0; \Delta H > 0 \\ \Delta G > 0; \Delta H < 0 \end{aligned} \right\} \quad (3)$$

From (3) it follows, that at chemical reactions' calculations calculation of ΔG value is required in every case. It specifies that knowledge of chemical potentials of all reaction participants at given values of condition's quantities is necessary. For calculation of condensed phases it is convenient to use Gibbs – Helmholtz equation subject to phases' heat capacities

$$\Delta G = \Delta H^0 - T\Delta S^0 + \int_{T^0}^T \Delta C_p dT - T \int_{T^0}^T \left(\frac{\Delta C_p}{T} \right) dT \quad (4)$$

The reactions flowing in a reversible galvanic cell concentrating relative to the electrodes have been studied by the method of e.m.f. measurement. The annealed alloys of the $\text{GeSe}_2\text{-CdTe}$, $\text{GeSe}_2\text{-HgTe}$ systems have been used as electrodes. E.m.f. measurements confirm the accuracy of plotted phase diagrams (Fig. 3 and Fig. 4).

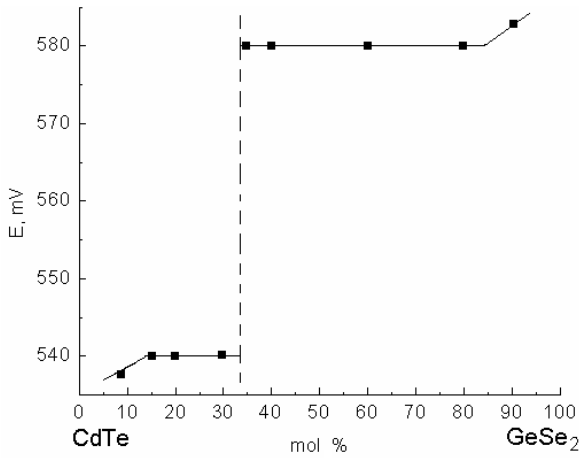


Fig. 3. Dependence of e.m.f. on composition in the CdTe-GeSe_2 system at 298 K.

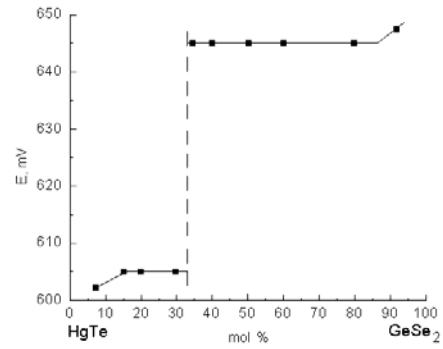


Fig. 4. Dependence of e.m.f. on composition in the HgTe-GeSe_2 system at 298 K.

On the base of plotted phase diagrams and measured partial molar thermodynamic properties of Cd in the system $\text{GeSe}_2\text{-CdTe}$ and Ge in $\text{GeSe}_2\text{-HgTe}$ (Table 5), the integral molar thermodynamic properties of fourfold phases have been calculated (Table 6). At this the standard molar thermodynamic properties of binary compounds GeSe_2 , CdTe , HgTe [2,3] and potential-forming reactions in the pseudo-binary $\text{GeSe}_2\text{-CdTe}$, $\text{GeSe}_2\text{-HgTe}$ cuts mutual Cd (Hg), $\text{Ge} \parallel \text{S}$ (Se), Te systems were also used.

Table 5

The standard partial molar thermodynamic properties of Cd in the system $\text{GeSe}_2\text{-CdTe}$ and Ge in $\text{GeSe}_2\text{-HgTe}$

Phase	$-\Delta_f \bar{G}_{Me}$ kJ mol ⁻¹	$-\Delta_f \bar{H}_{Me}$ kJ mol ⁻¹	$\Delta_f \bar{S}_{Me}$ J mol ⁻¹ K ⁻¹
$\text{Cd}_2\text{GeSe}_2\text{Te}_2$	108.5 ± 11.5	82.8 ± 2.9	86.1 ± 18.9
$\text{Hg}_2\text{GeSe}_2\text{Te}_2$	402.2 ± 46.1	324.3 ± 1.6	261.3 ± 45.8

Table 6

The standard molar thermodynamic functions of quaternary phase in the systems $\text{GeSe}_2\text{-CdTe}$ and $\text{GeSe}_2\text{-HgTe}$

Phase	$-\Delta_f G_{298}^0$ kJ mol ⁻¹ J	$-\Delta_f H_{298}^0$ J mol ⁻¹ K ⁻¹	$\Delta_f S_{298}^0$ J mol ⁻¹ K ⁻¹
$\text{Cd}_2\text{GeSe}_2\text{Te}_2$	298.3 ± 1.9	276.3 ± 13.3	73.8 ± 32.7
$\text{Hg}_2\text{GeSe}_2\text{Te}_2$	605.8 ± 3.9	545.6 ± 21.2	202.0 ± 30.0

4. CONCLUSION

The phase diagrams of the pseudo-binary $\text{GeSe}_2\text{-A}^2\text{B}^6$ ($\text{A}^2 = \text{Hg; Cd; B}^6 = \text{S, Te}$) systems were plotted by the methods of differential thermal and X-ray diffraction analyses, by the measurement of electromotive force (e.m.f.), microhardness and density. New intermediate quaternary $\text{Cd}_2\text{GeSe}_2\text{Te}_2$, $\text{Cd}_4\text{GeS}_4\text{Se}_2$, $\text{Hg}_2\text{GeSe}_2\text{Te}_2$,

$\text{Hg}_2\text{GeS}_2\text{Se}_2$, $\text{Hg}_4\text{GeS}_4\text{Se}_2$ phases and limited solid solutions on the base of binary components GeSe_2 and A^2B^6 have been found. Physicochemical and thermodynamic properties of some compositions of intermediate phases have been studied. The standard mole thermodynamic functions of quaternary $\text{Cd}_2\text{GeSe}_2\text{Te}_2$ and $\text{Hg}_2\text{GeSe}_2\text{Te}_2$ phases were determined.

- [1]. Physics and Chemistry of II-VI Compounds. Edited by M.Aven and J.S.Prenner. GER and Development Center Schenctady, New York, USA. North-Holland Publishing company. Amsterdam. 1967.
- [2]. Physico-Chemical Properties of Semiconductor Matters, Handbook, Composite authors (in Russian), Moscow, Nauka, 1978.
- [3]. O.Kubaschewski, C.B.Alcock, Metallurgical Thermochemistry, Fifth Edition, Pergamon Press, Oxford, New York, Toronto, Sydney, Paris, Frankfurt, 1979.
- [4]. M.M.Asadov, A.C.Mirzoev, O.M.Aliev, Azerb. Chem. J. 2 (2006) 77-81.
- [5]. A.C.Mirzoev, Thesis of Institute of Chemical Problems, NASA (in Azerbaijani), Baku, Azerbaijan, 2008
- [6]. M.M.Asadov, Russ. J. Inorg. Mater. 20 (1984) 38-40.
- [7]. M.M.Asadov, Russ. J. Inorg. Mater. 20 (1984) 1621-1623.
- [8]. Z.Sztuba, K.Wiglusz, I.Mucha, A.Sroka, W.Gawel, CALPHAD 32 (2008) 106-110.

INFLUENCE OF γ - RADIATION ON DIELECTRIC AND ELECTRIC PROPERTIES OF $\text{TlInS}_2 <\text{Cr}>$ CRYSTALS

**R.M. SARDARLI, O.A. SAMEDOV, I.I. ASLANOV, A.P. ABDULLAYEV
N.A. EYYUBOVA, F.T. SALMANOV**

*Institute of Radiation Problems of Azerbaijan NAS
370143, Baku, G.Javid ave., 31a*

The temperature dependences of dielectric constant $\epsilon(T)$, $\sigma(T)$ conduction and $P_s(T)$ polarization in γ -radiated samples of $\text{TlInS}_2 <\text{Cr}>$ crystals have been investigated. The presence of relaxor behavior and hopping has been established. The activation energies, defect concentration, jump lengths, the variation of trap states, localized state densities, spontaneous polarization maxima, Fogel-Fulcher (T_f) and Berns (T_d) temperatures at different radiation doses have been calculated.

Our previous investigation [1-6] show that doping of TlInS_2 crystal by some impurities leads to strong relaxation of dielectric susceptibility in the incommensurate phase region. It is established that the appearance of nanodimensional polar domains leading to the fact that the state of dipole of ferroelectric glass precedes to ordered phase is the reason of relaxation. The doping atoms leading to appearance of relaxor state form the capture levels in the forbidden band of semiconductor ferroelectric TlInS_2 . The charge carriers capturing these levels are space-limited ones and the conduction in this case is carried out by tunneling through potential barriers. This is observed at investigation of charge transfer process in TlInS_2 crystals doped by Cr atoms. The non-activated temperature-dependence hopping [5-6] has been established in these crystals in the region of incommensurate phase.

In the given work the results of complex investigations of influence of γ -radiation on dielectric, polarized and electric properties of compound $\text{TlInS}_2 <\text{Cr}>$ where Cr concentration is 0.1atm%.

The temperature dependences of dielectric constant $\epsilon(T)$ of $\text{TlInS}_2 <\text{Cr}>$ crystal at 200, 400 and 600 milliard doses are presented on fig.1. The investigation is carried out on the frequencies of measuring field 1kHz. The maximum value of dielectric constant at T_{\max} at γ -radiation decreases that shows on tendency to weakening of ferroelectric properties with increase of radiation defect concentration which is general one for all ferroelectrics.

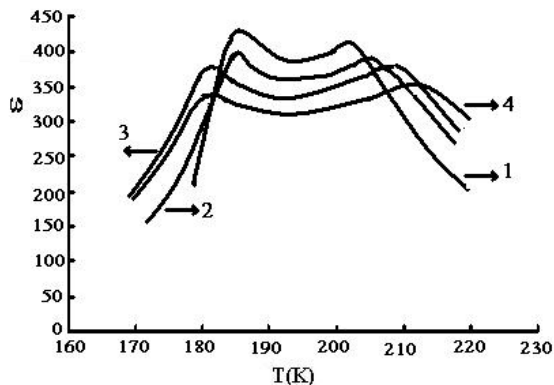


Fig.1. Temperature dependence of dielectric constant $\epsilon(T)$ of $\text{TlInS}_2 <\text{Cr}>$ crystal. The measurements are carried out on frequency 1 kHz (curve 1 is 0, curve 2 is 200, curve 3 is 400, curve 4 is 600 Mrad).

The spontaneous polarization and Curie point are fundamental characteristics of ferroelectrics; these parameters are connected between each other. The changes of dielectric constant at T_{\max} in education process have the complex character, i.e. the shift to the side of ferro-phase (caused by decrease of T_c) at this the definite effect of opposite sign connected with action of internal field. One can suppose that the following formation mechanism of internal field in radiated crystals. Let's think that initial ferroelectric crystal presents the space-homogeneous structure of similar oriented dipoles forming P_s polarization in volume unit.

The micro-heterogeneities, disorder regions not having the properties of initial dipole structure and differing from basic matrix by ϵ , T_c , P_s and σ values appear at radiation (as a result of bond destructions, atom shifting, excitation and carrier transfer in crystal). The last one leads to appearance of space charge (formation of volume charge can cause to carrier drift excited by radiation in conduction band in the field of spontaneous polarization with further capture on boundaries of defect regions) and average macroscopic field directed to the same side as P_s . These are internal fields striving for fixing of polarization.

As we suppose the coincidence of temperature of phase transformation with temperature region of thermal completing of local centers is the condition of relaxor behavior in $\text{TlInS}_2 <\text{Cr}>$ crystal [6]. The relaxor properties can be essentially changed by introduction of even some impurity quantity which influence on charge state of compounds. Moreover the shift of maximum temperature of dielectric constant can be achieved the some degrees.

The fact that in ferroelectrics the dielectric constant is higher than T_m temperature changes not by Curie-Weiss law but by $\epsilon^{-1/2} = A + B(T - T_0)$ one is the one of peculiarities of ferroelectrics with fuzzy phase transformations. The dependences $\epsilon^{-1/2}(T)$ for γ -radiated samples of $\text{TlInS}_2 <\text{Cr}>$ compounds are given on fig.2 (curve 1-2). As it is seen from the figure they cross the temperature axis at Fogel-Fulcher temperature (T_f) from the side of high-temperature phase and at Berns (T_d) temperature from the side of low-temperature one.

As it is known [7-8] the fuzzy character of $\epsilon(T)$ dependence is necessary condition of relaxor state. The fact that $\epsilon^{-1/2}(T)$ dependence changes by linear law is the enough condition. At radiation T_c decreases that shows on tendency to weakening of ferroelectric properties which is general for all with the increase of defect concentration.

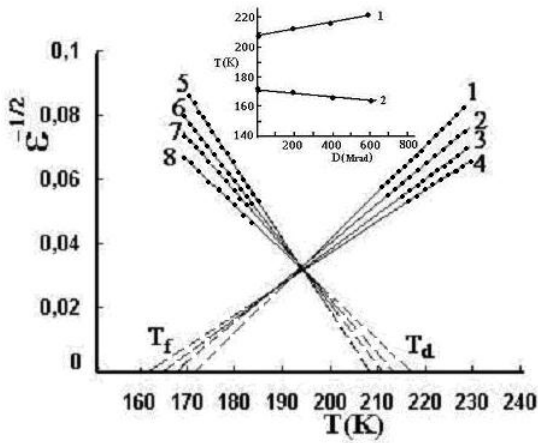


Fig.2. Temperature dependence of dielectric constant $\epsilon^{-1/2}(T)$ of TlInS₂<Cr> crystal. The measurements are carried out on frequency 1 kHz (curve 1,5 is 0, curve 2,6 is 200, curve 3,7 is 400, curve 4,8 is 600 Mrad). The dose dependences of Fogel-Fulchers (T_f) and Burns (T_d) (1 - T_d , 2 - T_f) temperatures are given in insertion.

As it is seen from fig.2 the dependence $\epsilon^{-1/2}(T)$ of initial (non-radiated) crystal cross the temperature axis at $T_f=169K$ (fig.2, curve 1) and at $T_d=207 K$ (fig.2, curve 5). In relaxor ferroelectrics T_f is that temperature at which the freezing of polar dipoles is carried out and crystal transforms from state of ferroelectric glass into order ferroelectric one. This temperature is also characterized by the fact that the temperature completing of trap centers takes place at it and localized charged impurities are neutral ones. The Fogel-Fulcher and Berns temperatures shift to the side of low and high temperatures with increase of radiation dose.

As it is known [1-6] the presence of disorder charge distribution in crystal is the main reason leading to blurring of phase transformation. The increase of blurring at radiation shows on the fact that the dipole charge centers appear at radiation in crystal volume.

On the given investigation stage one can suppose about nature of these dipole centers. These can be radiation defects formed because of electron excitations formed by radiation. Earlier the influence of γ -radiation on dielectric and electric properties of TlInS₂ crystal in the region of transformation incommensurable-commensurable phase [9] had been studied by us and the possibility of obtaining of relaxor state in these compounds had been established. By our opinion the multiple ionization of impurity atom which is chrome is the more obvious mechanism of formation of radiation defects in TlInS₂<Cr> compound. The formed defect increases the energy levels in crystal forbidden band; the thermal completing of these levels takes place at temperature which is lower than one in non-radiated compound, i.e. existence region of ferroelectric glass expands.

On the base of results obtained by us one can say that γ -radiation strongly influences on relaxor state of TlInS₂<Cr> compound and expands the temperature interval of its existence. It is also shown that Fogel-Fulcher T_f temperature shifts to the side of low temperatures and Berns temperature T_d shifts to the side high temperatures (fig.2, insertion).

The defects of ionization type (charged defects) which appear in the result of γ -radiation play the dominating role in these processes. The blurring of phase transformations takes place because of interaction of polar defects with spontaneous polarization of initial crystal [7]. According to [7] the temperature decrease of phase transformation with increase of radiation dose is caused by concentration decrease of ferroelectric active dipoles in crystal.

Thus at γ -radiation characterizing by decrease of ϵ_{max} and essential transformation blurring the defect coagulation, cluster formation which make crystal macroscopically heterogeneous one with different degree of internal voltages in separate micro-volumes play the defining role. This leads to some distribution of crystal local values T_c by volume as a result of which is the transformation blurring.

The dependence of spontaneous polarization P_s on temperature for TlInS₂<Cr> crystals is shown on fig.3. The analysis of results of whole temperature measurement range one can divide on three parts. In temperature region $T > T_d$ the crystal is paraelectric one. At T_d temperature the some polarized clusters with local polarization P_d the value of which increases with temperature decrease. With temperature decrease up to T_m the increase of local polarization P_d takes place (in temperature interval $T_d \div T_m$). At the same time the increase of polarization continues in temperature interval ($T_m \div T_f$). Below T_f the saturation of polar localization value takes place.

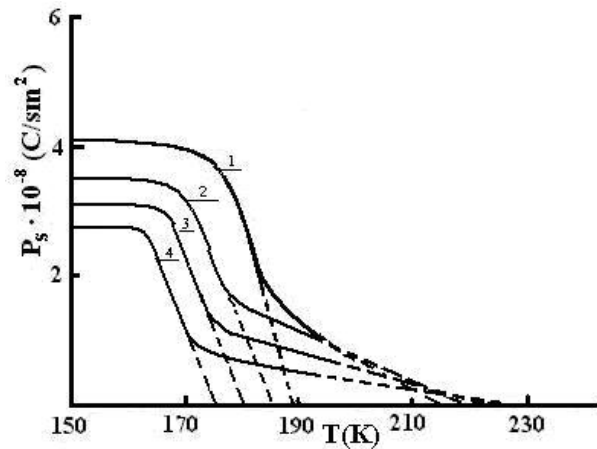


Fig.3. Temperature dependence spontaneous polarization $P_s(T)$ of TlInS₂<Cr> crystal where Cr is 1 atm.%. curve 1 is 0, 2 is 200, 3 is 400, 4 is 600 Mrad

As it is known in TlInS₂ crystal 0,1 atm.% Cr are the random fields connected with disorder in interstices, vacancies of indium and atoms of Cr impurities, i.e. the ferroelectric dipole order in this crystal is destroyed by random fields induced by Cr ion impurities [3,5]. As it is seen from fig. 3 below T_f the saturated loops of dielectric hysteresis are observed and the value of spontaneous polarization is $P_s^{max}=4.2 \cdot 10^{-8}$ KJ/cm². In temperature interval ($T_f - T_d$) the loop of dielectric hysteresis converges up to Berns temperature (T_d). Especially in this temperature interval the ferroelectric glass exists. The dose dependence of P_s value shows that the polarization decrease is connected with defect concentration. The concentration of ferroelectric dipoles is connected with

increase of radiation dose as a result the maximum value of spontaneous polarization decreases.

The investigation of $\text{TlInS}_2\langle\text{Cr}\rangle$ crystal polarization properties shows the existence of three phase regions: paraelectric, ferroelectric nanodomain and ferroelectric macrodomain phases. The temperature interval of existence of ferroelectric nano-domain phase expands (the region of relaxor state) with increase of radiation dose.

As it is known that in ferroelectric semiconductors the electric conduction σ is more sensitive one to radiation than the ferroelectric parameters [9]. As $\text{TlInS}_2\langle\text{Cr}\rangle$ is simultaneously the ferroelectric and semiconductor then the study of electric properties of this crystal presents the big interest.

The existence of radiation defects in $\text{TlInS}_2\langle\text{Cr}\rangle$ leads to high density of states localized near Fermi level. The states localized in forbidden band are responsible for many electron processes taking part in semiconductors.

As it is mentioned above the appearance of relaxor behavior is connected with existing disorder in disposition of $\text{TlInS}_2\langle\text{Cr}\rangle$ crystal atoms. One can observe this on example of all known relaxors and the given fact is only necessary one but not the enough condition. The coincidence of phase transformation temperature with temperature region of heat filling of local centers [10,11] is the additional condition of relaxor behavior. The temperature dependence of electric conduction $\sigma(T)$ of $\text{TlInS}_2\langle\text{Cr}\rangle$ crystal is given on fig.4. This dependence can be divided on three temperature regions characterizing by the different conduction mechanisms. At temperature decrease up to T_f value the dependence $\sigma(T)$ is linear one that is character for bond conduction.

In temperature interval $T_d - T_f$ the dependence $\sigma(T)$ is satisfactory described by Mott law [12] and corresponds to thermoactivated hopping mechanism. By our opinion this evidences about the fact that at $T_d - T_f$ the local centers are thermoactivated yet and charge carriers can't be localized on them. The temperature-independent conduction below T_f observed in $\text{TlInS}_2\langle\text{Cr}\rangle$ is the non-

activated hopping. Especially at low temperatures (below T_f) the charge carriers localize on these centers. The given temperature corresponds to transformation in the state with local spontaneous polarization. That's why one can suppose that local centers in $\text{TlInS}_2\langle\text{Cr}\rangle$ crystal begin to activate at T_f temperature.

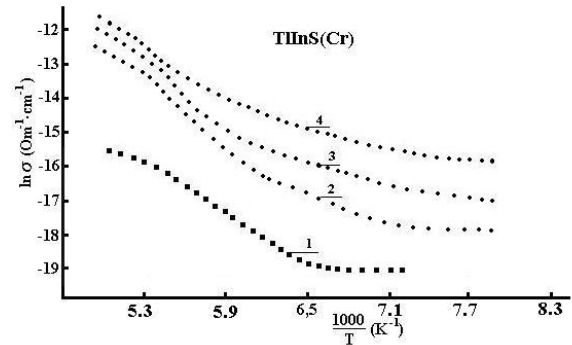


Fig.4. Temperature dependence of electric conduction $\sigma(T)$ in Arrhenius coordinates for $\text{TlInS}_2\langle\text{Cr}\rangle$ crystal where Cr – 0,1 atm.% (curve 1 is 0, 2 is 200, 3 is 400, 4 is 600 Mrad).

Thus the possibility of taking under consideration of charge carrier localization on local centers is shown. The localized charges form the local electric fields and so they stimulate the appearance of induced polarization. The dispersion of dielectric susceptibility is defined by oscillation properties of local states and depends on electron dynamics on capture levels.

In temperature interval $T_d - T_f$ the dependence $\sigma(T)$ is satisfactory described by Mott law [12] and corresponds to hopping mechanism. Especially in this temperature region $\text{TlInS}_2\langle\text{Cr}\rangle$ is in ferro-glass state.

The results obtained at investigation of electric conduction and ferroelectric parameters of $\text{TlInS}_2\langle\text{Cr}\rangle$ crystal are given in table 1.

Table 1

Ferro-electric and electrophysical parameters of γ -radiated $\text{InS}_2\langle\text{Cr}\rangle$ crystals.

Dose (milliard)	E_a (eV)	N_F ($\text{eV}^{-1} \text{cm}^{-3}$)	R (A)	ΔE (eV)	N_t (cm^{-3})	T_d (K)	T_f (K)	$P_s(\text{max})$ (Kl/cm^2)
0	0,26	$4,2 \cdot 10^{17}$	193	0,08	$3,22 \cdot 10^{16}$	207	171	$4,2 \cdot 10^{-8}$
200	0,203	$7,2 \cdot 10^{17}$	168	0,067	$4,79 \cdot 10^{16}$	211	168	$3,5 \cdot 10^{-8}$
400	0,19	$8,6 \cdot 10^{17}$	159	0,062	$5,68 \cdot 10^{16}$	214	165	$3 \cdot 10^{-8}$
600	0,187	$9,8 \cdot 10^{17}$	152	0,065	$7,1 \cdot 10^{16}$	217	162	$2,45 \cdot 10^{-8}$

Thus one can change the dielectric and electric properties of ferroelectrics and obtain the stable the relaxor states by influence of γ -radiation. The complex investigations of $\varepsilon(T)$ and $\sigma(T)$ dependences in γ -radiated $\text{TlInS}_2\langle\text{Cr}\rangle$ crystals allow to us to establish the bond between the behavior dynamics of relaxors in which the relaxor state appears as a result of fixing of heterogeneous polarization in nano-regions in result of charge localization on defects with electric conduction which has the hopping character and is caused by thermoactivated processes of defect level state in radiated crystal $\text{TlInS}_2\langle\text{Cr}\rangle$.

In the dependence on radiation dose the activation energy, concentration of radiated defects, hop length, the spread of trap states and density of localized states strongly changes. In compound $\text{TlInS}_2\langle\text{Cr}\rangle$ under influence of γ -radiation the Fogel-Fulcher temperature T_f shifts to the side of low temperatures and Berns temperature T_d shifts to the side of high temperatures. With increase of radiation dose the widening of temperature interval of relaxor state appearance is observed. γ -radiation strongly influences on polarization of $\text{TlInS}_2\langle\text{Cr}\rangle$ compound. With increase of radiation dose the concentration of ferroactive dipoles decreases, as a

result of maximal values of spontaneous polarization decrease and generated radiation defects increase the concentration of impurity energy levels in forbidden band of TlInS_2 <Cr> crystal. The coincidence of temperatures

of phase transformations in the investigated crystal with temperatures of thermal filling of these levels leads to widening of thermal region of thermoactivated hopping conduction.

-
- [1]. *R.M. Sardarli, O.A. Samedov, A.I. Nadzhafov, I.Sh. Sadikhov.* FTT, 2003, t. 45, v. 6, s. 1085. (in Russian)
- [2]. *R.M. Sardarli, O.A. Samedov, I.Sh. Sadikhov, V.A. Aliyev.* FTT, 2003, t. 45, v. 6, s. 1067. (in Russian).
- [3]. *R.M. Sardarli, O.A. Samedov, I.Sh. Sadikhov.* FTT, 2004, t. 46, v. 10, s. 1852. (in Russian).
- [4]. *R.M. Sardarli, O.A. Samedov, I.Sh. Sadikhov,* neorganicheskiye materialy. 2004, t. 40, № 10, 1163. (in Russian).
- [5]. *A. Sardarli, I.M. Filanovski, R.M. Sardarli, O.A. Samedov, I.Sh. Sadixov, I.I. Aslanov.* // Journal of optoelectronics and advanced materials, 2003, v. 5, No 3, p. 276.
- [6]. *R.M. Sardarly, O.A. Samedov, I.Sh.Sadigov.* // Ferroelectrics, 2004, v. 298, p. 275.
- [7]. *V.V. Курдюков, V.A. ISupov.* Izvestiya AN SSSR, ser.fiz., 1971, t. 35, № 12, s. 2602. (in Russian)
- [8]. *A.A. Markova, N.N. Kraynikh, R.N. Kyut.* FTT, 1991, t. 33, v. 1, s. 35. (in Russian)
- [9]. *R.M. Sardarli, O.A. Samedov, I.Sh. Sadigov, A.I. Najafov, F.T. Salmanov.* FTT, 2005, t.47 v. 9, s.1665. (in Russian)
- [10]. *R.F. Mamina.* FTT, 2001,t. 43, v. 7, s. 1262. (in Russian)
- [11]. *R.F. Mamin, R. Blinc.* FTT, 2003, t. 45, v. 5, s. 896. (in Russian)
- [12]. *N.F. Mott, E.A. Devis.* Elektronniye processi v nekristallicheskih veshshestvakh. Mir. M., 1974 472. (in Russian).

MOLECULAR MECHANISMS OF DIELECTRIC POLARIZATION OF LOW-MOLECULAR AND POLYMER LIQUID CRYSTALS

D. RAGIMOV

*Azerbaijan Medical University,
Baku, Bakikhanov, 23*

On the base of experimental investigation of frequency dependences of the main dielectric constants of some classes of low-molecular and polymer mesomorphic materials with different molecular structure it is established that dipole contribution into parallel component of dielectric constant is caused by molecule rotation round short and long molecular axes. The dipole contribution into perpendicular component of dielectric constant is connected with long molecular axes and also with rotation of long axis of molecule round the direction of the dominant orientation of liquid crystal by cone in the angle limit given by orientation order in the liquid crystal.

According V.N. Tsvetkov theory the dipole dielectric polarization of liquid crystals is caused by reorientation in polar stick-like molecules round the transversal and longitudinal molecular axes and also by molecule rotation by cone surface with θ angle given by the value of order degree $S=1/2 (3\cos^2 \theta - 1)$ of liquid crystal. The energy barriers corresponding to positions of orientation equilibrium of molecules differs by the value for different types of molecule rotation motion as a result of intermolecular interaction supporting the mesomorphic order. The relaxation times corresponding to different orientation transfers can also differ.

The method of experimental investigation of molecular mechanisms of dielectric polarization of liquid crystals is the very effective one for study of dielectric constant dependence and dielectric loss on the electric field frequency. The macroscopic times of dielectric

relaxation τ obtained at from frequency dependences $\epsilon_{||}$ and ϵ_{\perp} can be connected with definite types of molecular rotation.

The role of each molecular mechanisms of dielectric polarization as it is seen from relations essentially depends on the value of dipole moment μ and its direction (angle β) relative the longitudinal axis of molecule. $\mu = \mu \cos \beta$ the contribution of longitudinal component of molecular dipole moment in dielectric polarization of liquid crystal is comfortably studied with use of mesogenes in the molecules of which the dipole moment is directed along the molecule long axis ($\mu_{||} = \mu, \mu_{\perp} = 0$).

The orientation dielectric polarization of liquid crystal in both in direction of dominant orientation of optical axis

$$\chi_{||} = \frac{\epsilon_{||} - 1}{4\pi} = NFh\left(\alpha + \frac{2}{3}\Delta\alpha S\right) + NhF^2 \frac{\mu^2 \cos^2 \beta}{3kT} \cdot (1 + 2S)(1 + \chi_1) + NhF^2 \frac{\mu^2 \sin^2 \beta}{3kT} (1 - S)(1 + \chi_2) \quad (1)$$

And in the direction perpendicular to axis (1.36) is connected only with longitudinal component of dipole moment.

$$\chi_{\perp} = \frac{\epsilon_{\perp} - 1}{4\pi} = NhF\left(\alpha - \frac{1}{3}\Delta\alpha S\right) + NhF^2 \frac{\mu^2 \cos^2 \beta}{3kT} (1 - S) + NhF^2 \frac{\mu^2 \sin^2 \beta}{6kT} (S + 2)(1 + \chi_2) \quad (2)$$

The liquid crystals LC1-LC5 chosen by us as investigation objects have the necessary dipole structure of molecules. The values of molar constants $\epsilon_{||}$, dipole moments μ , anisotropy of molecular polarizability Δb and angles β experimentally defined by us with use of earlier known methods are given in the table 1.

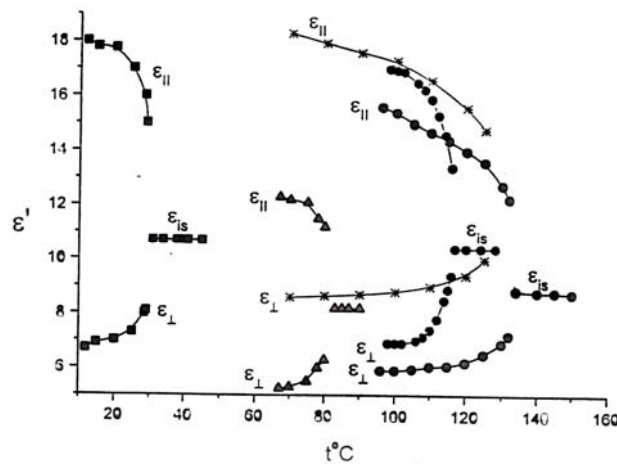


Fig. 1. The dependence of quasistatic dielectric constants $\epsilon_{||}$, ϵ_{\perp} and ϵ_{is} LC1-LC5 from temperature $T^{\circ}C$.

From table it is seen that β angle between dipole moment and longitudinal axis of liquid crystal molecule LC1-LC5 is equal to zero and $\mu_1 = \mu \cos \beta = \mu$.

Table 1

Molecular characteristics and dielectric anisotropy $\Delta \epsilon$ LC1 - LC5 at $T-T_0 = -5$.

1	2	3	4	5	6	7
LC1	$C_6H_{13}-C_6H_4-C_6H_4-CN$ K 12 H 30 И 4-н-hexyl-4-cyanobifenil	4,4	5	130	0	10,5
LC2	$C_7H_{15}-O-C_6H_4N=N-C_6H_4-CN$ K 94 H112 И 4-н-heptyloxi-4-cyanozobenzol	13	5.8	230	0	8.4
LC3	$C_7H_{15}O-C_6H_4N=N-C_6H_4-CN$ OH K 94 H112 И 4-cyano-oxi-4-epitloxianizol	13.6	5.2	310	0	6.3
LC4	$C_5H_{11}O-C_6H_4N=N-C_6H_4-CN$ OH	9	5.3	210	0	6.1
LC5	$C_7H_{15}O-C_6H_4-C_6H_4-CN$ OH K 67 H 81 И 4-н-otylooxi-4'-cyanobifenil	5.1	5.2	160	10	6.0

For LC1 and LC2 in frequency range 1kHz-25 MHz and for LC1 and LC5 in frequency range 1kHz-100 MHz the measurements of main dielectric constants $\epsilon_{||}$, ϵ_{\perp} and ϵ_{u3} in whole temperature interval of anisotropic melt existence and in isotropic phases are carried out.

The dependence of quasistatic values $\epsilon_{||}$, ϵ_{\perp} and ϵ_{u3} on temperature for LC1 and LC5 are given in fig.1. From the fig.1 it is seen that investigated LC have the bigger positive dielectric anisotropy $\Delta \epsilon = \epsilon_{||} - \epsilon_{\perp}$ in the correspondence with dipole structure of molecules and expression (3):

$$\frac{\Delta \epsilon}{4\pi} = NhF(\Delta \alpha - F \frac{\mu^2}{2kT}(1 - \cos^2 \beta))S \quad (3)$$

In frequency range of electric field 1 MHz -100 MHz ϵ' dispersion accompanying by dielectric loss ϵ'' (fig.2) is observed. For analysis of obtained dielectric spectrums the circle diagrams (of dependence ϵ'' on $\epsilon'_{||}$) are used. The diagram construction by experimental values $\epsilon'_{||}$ and $\epsilon''_{||}$ (fig.3) shows that they are semi-circles with the centers on axis of abscissa. Consequently, the observable ϵ dispersion is described by Debye equations.

Meanwhile, from experimental data (fig.2) it is seen that in the investigated frequency range ϵ dispersion leads

to almost total exclusion of orientation dipole part from dielectric polarization ($\epsilon'_{||}$ increases up to square value of index of refraction of extraordinary beam n_e^2). The analogous results are also obtained in [1,2].

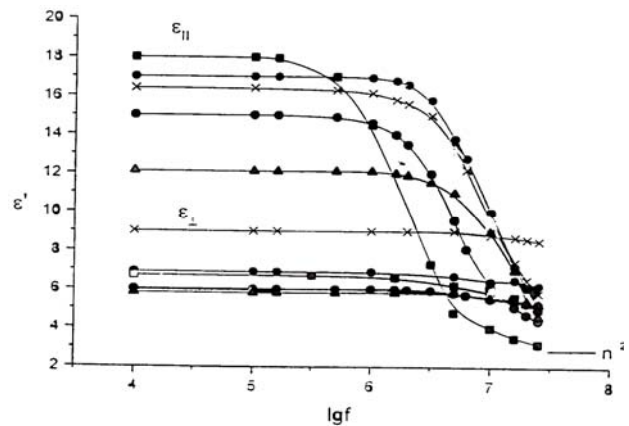


Fig.2. The dependence of dielectric constants ϵ' and ϵ'' on frequency $\lg f$ for LC1-LC5.

The mentioned experimental facts prove that the only one molecular mechanism is responsible for $\epsilon'_{||}$ dispersion of investigated LC. The rotation of molecules round transversal axes is this mechanism in the correspondence with model of LC dielectric polarization taken by us, i.e. the longitudinal dipole component μ_1

makes contribution in dipole polarization in the direction of LC director only because of such type of molecular motion.

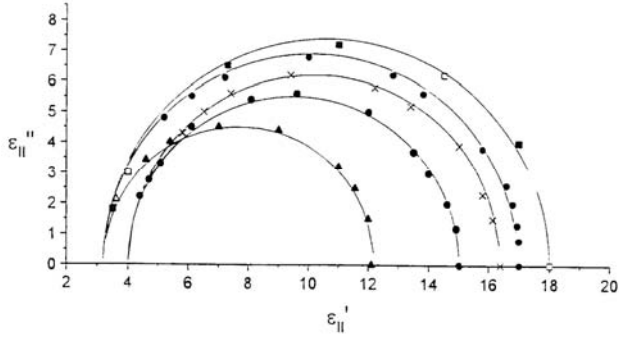


Fig.3. Circle diagrams ϵ^* for LC1-LC5.

The relaxation times of dielectric polarization τ are defined by construction of dependence ϵ'' on $\epsilon' \times 2 \pi f$ (fig.4) or with use of fp frequency corresponding to maximum of dielectric loss $\tau = 1/2 \pi \text{fp}$. The dependences of relaxation times on reversal temperature 1°K for LC1-LC5 are shown on fig.5.

From inclinations of direct lines in the correspondence with expression $\tau = \tau_0 e^{u/kT}$

$$\tau \sim \exp(u/kT) \quad (4)$$

the activation energies U_{II} requiring for molecule reorientation at rotations round transversal axes (table 2) are obtained.

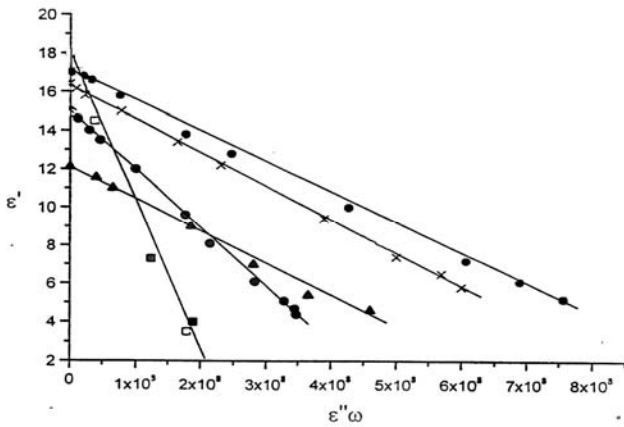


Fig.4. The dependence ϵ'' on $\epsilon' \times 2 \pi f$ for LC1-LC5.

From expression (5) it is seen that longitudinal component of molecular dipole moment $\mu_1 = \mu \cos \beta$ also make the contribution into dipole polarization in direction perpendicular to optical axis LC.

$$\frac{\epsilon_{\perp} - 1}{4\pi} = NhF \left\{ \alpha - \frac{1}{3} \Delta \alpha S + F \frac{\mu^2}{3kT} \left[1 + \frac{1}{2} (1 - 3 \cos^2 \beta) S \right] \right\} \quad (5)$$

In case of LC1-LC5 the other orientation contributions into polarization should absent, i.e. $\mu_2 = 0$.

Table 2

Activation energies U_{II} for LC1-LC5					
Liquid crystal	LC1	LC2	LC3	LC4	LC5
U Kkal/mole	18	15	17	18	20

The experimental study of frequency dependence ϵ_{\perp} given by LC shows that ϵ_{\perp} staying constant (fig.2) essentially exceeds the square of index of refraction by the value for ordinary beam n_0^2 for LC1-LC5 in the investigated frequency range of electric field. This experimentally proves the fact that the longitudinal component of dipole moment μ_1 is responsible not only for mesogene dipole polarization in the direction of its optical axis but in the direction perpendicular of its optical axis.

However, as it was mentioned earlier if ϵ has the strong dispersion in $\sim 5-25\text{MHz}$ region then at the same temperatures and frequencies ϵ_{\perp} value stays constant one.

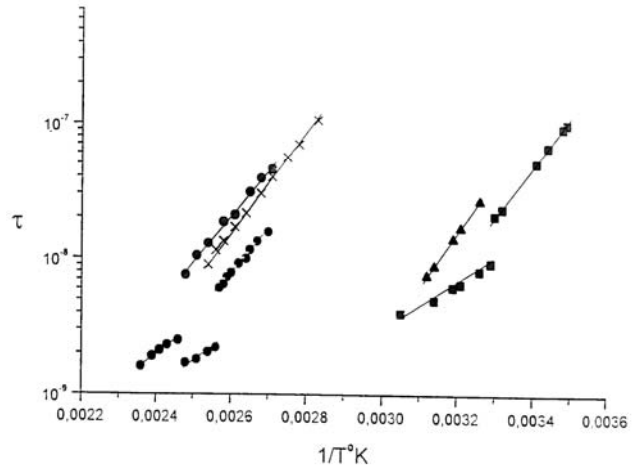


Fig.5. The dependence of relaxation time LC1-LC5 on temperature.

The last one is direct evidence of the fact that different molecular mechanisms connected with longitudinal component of dipole moment μ are responsible for dipole polarization LC1-LC5 in directions parallel and perpendicular to director of homogeneous oriented mesomorphic sample. If the molecule rotation round transversal axis is the mechanism of dipole polarization along director (ϵ_{II}), then dipole polarization (ϵ_{\perp}) is carried out because of molecule rotation in cone limit with θ angle given by value of order degree $S = (3 \cos^2 \theta - 1)/2$. At such molecule reorientation the overcoming of potential barriers supporting the nematic order in the substance is required. By this reason ϵ_{\perp} dispersion connected with contribution exclusion from dipole polarization caused by reorientation of longitudinal

component of dipole moment μ_1 realizes in the region of more high frequencies than dispersion $\varepsilon_{||}$.

The fact that observable dielectric properties of nematic liquid crystals can be explained by the method described above on the sample of LC2 and LC3 quantitatively with use of experimentally obtained values $\varepsilon_{||}$, ε_{\perp} , n_0^2 , n_e^2 , μ , β , b , Δb and expressions for main dielectric constants (1.28) and (1.29). At $\beta=0$ we obtain:

$$\varepsilon_{||0} - n_e^2 = 4\pi N h F^2 \mu^2 (1 + 2S)(1 + \chi_1) / (3kT) \quad (6)$$

$$\varepsilon_{\perp0} - n_0^2 = 4\pi N h F^2 \mu^2 (1 - S) / 3kT \quad (7)$$

The substitution of $\varepsilon_{||0}$, $\varepsilon_{\perp0}$, n_0 , n_e , μ , β values and also h and F found with use of average values $\varepsilon = (\varepsilon_{||0} + 2\varepsilon_{\perp0}) / 3$ in equation systems (6), (7) and solution of system leads to values of S order degree and parameter limitation of molecular rotation x_1 presented at different temperatures in table 2. It is easily to understand that S values found by such way correspond to usual values of order degree of nematics [3-4] and values of parameter x_1 which are negative ones by the sign proposed in theory [5,6] characterize the bifurcation of molecule rotation round short axis in anisotropic melt in the comparison with isotropic-liquid state.

Thus the obtained results shows that the contribution of longitudinal component of molecular dipole moment μ_1 into dielectric polarization of mesomorphic genes in the director direction is carried out because of molecule rotation round transversal axes and in direction perpendicular to director because of reorientation in cone limit with θ angle given by value of S order degree.

The contribution into orientation polarization in the direction of optical axis of liquid crystals ($\varepsilon_{||}$) and in direction perpendicular to it (ε_{\perp}) introduces the dipole moment of molecule. It is obvious that experimental evidence takes place if we will carry out the use of substance in molecules of which the dipole moment is directed under the angle $\beta=90^\circ$ to molecule long axis. Then the longitudinal component of dipole moment μ_1 is equal to zero and consequently, only μ_2 will make the contribution in dipole polarization. However, LC with such dipole structure we can't select his case one should use the mesomorphic genes with possibly bigger β value in order that the contribution into polarization of transversal component of μ_2 dipole would be big one.

That's why LC6 and LC7 are investigation objects (table 4), the molecular dipole moment of which is angle $\beta=60^\circ$ with molecule longitudinal axis.

The dielectric constants and loss of LC6 and LC7 are measured in frequency range of electric field 0,01-30MHz in whole temperature interval of anisotropic melt (nematic interval expands because of overcooling) and in isotropic phase.

The obtained dependences of quasi-static values $\varepsilon_{||}$, ε_{\perp} and ε_{us} of LC6 and LC7 are given on fig. 6. It is seen that for LC6 and LC7 the negative dielectric anisotropy the value and sign of which correspond with expression (8) and with main molecular characteristics: anisotropy of its direction relatively longitudinal axis of molecule ($\beta=63^\circ$) is character one.

$$\frac{\Delta\varepsilon}{4\pi} = N h F (\Delta\alpha - F \frac{\mu^2}{2kT} (1 - \cos^2 \beta)) S \quad (8)$$

Table 3

Degree of orientation order S and x_1 parameter at different temperatures in low-molecular liquid crystals

Liquid crystal	$T^\circ C$	$\varepsilon_{ } - n_e^2$	$\varepsilon_{\perp} - n_0^2$	S	x_1
LC1	109	11,9	5,8	0,4	0,4
	102	13,25	4,65	0,5	-0,4
	94	13,6	4,6	0,6	-0,4
LC2	130	9,35	4,6	0,6	-0,6
	105	11,2	3,75	0,7	-0,6
	95	11,05	3,5	0,7	-0,6

The given molecular parameters and expressions (5) and (6) can be used for establishment of relative role of different molecular mechanisms in equilibrium dielectric polarization of investigated anisotropic liquids. The substitution into (5) and (6) of Δb , μ , β , M , S , h and F values

allows calculating the contributions of each of molecular mechanisms into dielectric polarization LC6 and LC7. The values $\chi_{||}^{\partial e\phi}$, $\chi_{||1}^{op}$, χ_{ii}^{op} , $\chi_{\perp}^{\partial e\phi}$, $\chi_{\perp1}^{op}$ and $\chi_{\perp2}^{op}$ found by such way are presented in table 5.

There the values of limitation parameters of molecular rotation χ_1 , χ_2 calculated with use of quasi-static values $\epsilon_{||}$ and ϵ_{\perp} of expression (5) and (6) are also presented. From table (5) it is seen that regions of frequencies and temperatures where dispersion $\epsilon_{||}$ and

ϵ_{\perp} is absent (fig.7), parameter χ_2 is bigger than zero meanwhile as χ_1 is negative one according to experimental data.

Table 4

Molecular characteristics LC6 and LC7

	Chemical structure and temperatures of phase transformations in Celsius degree	$KM, 10^{-9} \Gamma^{-1} \text{cm}^5 (300B)^{-2}$	μ D	$\Delta b 10^{-25} \text{cm}^3$	β°	$\Delta \epsilon$
LC6	$C_6H_{13}OC_6H_4COOC_6H_4OC_6H_4OC_6H_{13}$ I CN K 85 H 164 И Ди-(4-н-гексилокси)бензоат-2-циано-гидрокиноне	-0,1	4,2	210	58	-0,8
LC7	$C_6H_{13}OC_6H_4COOC_6H_4OC_6H_4OC_6H_{13}$ I NO ₂ K 89 H 163 И Ди-(4-н-гексилокси)бензоат-2-нитро-гидрокиноне	0,1	4,2	210	63	-1,1

This result corresponds to V. N.Tsvetkov theory and experimental data obtained in conditions of equilibrium dielectric anisotropy and equilibrium dielectric polarization. The different signs χ_1 and χ_2 are explained by essential difference of freedom of molecule rotation in anisotropic melt round the presence of potential barriers which are defined by intermolecular interactions supported the further order in liquid crystal. From results presented in table 5 it is followed that transversal μ_2 and longitudinal μ_1 components of molecular dipole moment make contributions close by value into orientation part of dielectric polarization in the direction of optical axis LC6 and LC7, i.e. $\chi_{||}^{op}$ is comparable one with value $\chi_{||1}^{op}$. Vice versa, the orientation part of dielectric polarization in the direction perpendicular to optical axis in LC6 and LC7 firstly is defined by $\chi_{\perp 2}^{op}$ value, i.e. by transversal dipole component μ_2 , i.e. values $\chi_{\perp 1}^{op}$ are essentially less ones than $\chi_{\perp 2}^{op}$ (practically by order and more). The conclusions are indirectly proved by results of experimental investigations of dielectric constant dispersion $\epsilon_{||}$ and ϵ_{\perp} .

The obtained data are presented for LC6 and LC7 on fig.7. The frequency dependences $\epsilon_{||}$ and ϵ_{\perp} are observed and essentially proved about different molecular mechanisms which are responsible for their dispersion. The dependences $\epsilon_{||}$ and ϵ_{\perp} on the frequency at each fixed temperature can be presented by dispersion curve with one relaxation time. Indeed, the solid line ($\epsilon_{||}$) on

fig.7 is theoretic curve obtained with use of Debye equation for dipole relaxation.

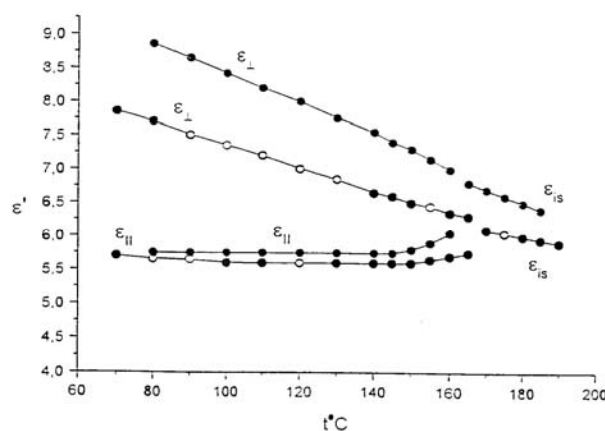


Fig.6. The dependence of main dielectric constants of LC6-LC7 on temperature.

It quantitatively corresponds to experimental results (mentioned by points) at value $\tau = 2.1 \cdot 10^{-7}$ sec. The construction of circle diagram (fig.8) with use of experimental values of real ϵ'_{\perp} and imaginary ϵ''_{\perp} parts of complex dielectric constant of LC6 and LC7 evidences about the same. The given results show on the revealing of one molecular mechanism which is responsible for low-frequency dispersion $\epsilon_{||}$ and one molecular mechanism which is responsible for dispersion ϵ_{\perp} of LC6 and LC7 in investigated temperature-frequency region.

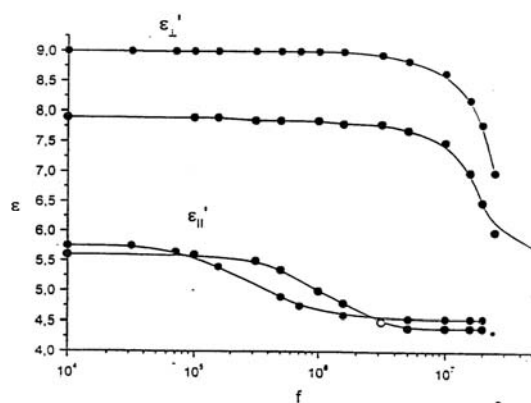


Fig.7. The dependence of dielectric constant ϵ_{\parallel} , ϵ_{\perp} on electric field frequency.

It is obvious that exclusion from dielectric polarization in the direction of optical axis of investigated LC of orientation contribution connected with molecule rotation round short axis $\chi_{\parallel 1}^{op}$ corresponds to low-frequency dispersion ϵ_{\parallel} , i.e. to longitudinal component of dipole moment.

The comparison of theoretic values $\chi_{\parallel 1}^{op}$ calculated with use of experimentally obtained molecular characteristics with $\chi_{\parallel 1}^{op}$ value defined from dielectric increment $(\epsilon_{\parallel 0} - \epsilon_{\parallel 1}) M/4\pi\rho = \chi_{\parallel 1}^{op}$ shows on their coincidence. Then the residual polarization in the direction of optical axis LC6 and LC7 is caused by deformation part of dielectric susceptibility $\chi_{\parallel}^{\partial e\phi}$ and the one connected with molecule rotation round the transversal axes $\chi_{\parallel 2}^{op}$. The essential dispersion $\chi_{\parallel 2}^{op}$ can be expected at the frequencies which are higher ones than used at 30MHz.

The dispersion ϵ_{\perp} becomes to reveal at temperatures below 100°C in frequency region 5-30MHz. The decrease of ϵ_{\perp} at maximum frequency 30MHz is 20-30% from total orientation polarization in the direction perpendicular to optical axis investigated LC. This dispersion is caused by exclusion from dielectric polarization of orientation part, molecule rotation round longitudinal axes and with μ_2 connected with transversal dipole component, as it was above mentioned only this mechanism is responsible for orientation part of ϵ_{\perp} . As the given dispersion mechanism ϵ_{\perp} only begins to develop in the investigated frequency range, then it probably doesn't experimentally reveal in frequency dependence ϵ_{\parallel} .

The discussed relaxation phenomena decrease the contribution into dielectric polarization ϵ_{\parallel} and ϵ_{\perp} of considered types of polar molecule rotation. This decrease can be characterized by change of χ_1 and χ_2 parameters, as they can reflect the decrease of orientation contributions into LC dielectric polarization. χ_1 and

χ_2 values calculated on the use of equations (1) and (2) and experimental data given on fig.7 in region of temperatures and frequencies corresponding to observable dispersion ϵ_{\parallel} and ϵ_{\perp} are presented in table 6. At temperature decrease and frequency increase the both parameters χ_1 and χ_2 become the negative ones by sign and strive for value -1 (theoretic limit) reflecting the total exclusion of corresponding mechanisms from dipole polarization of mesomorphic genes in the correspondence of equations (1) and (2).

Temperature dependence of dielectric relaxation times can be used for finding of activation energies of molecule rotation round transversal U_{\parallel} and longitudinal U_{\perp} axes. The dependences τ_{\parallel} and τ_{\perp} on reversal temperature for LC6 and LC7 are given on fig.9. From inclination of dependence the values $U_{\parallel} = 20$ kkal/mol and $U_{\perp} = 10$ kkal/mol are defined.

It is necessary to note that extreme high-frequency value ϵ_{\perp} defined by circle diagram (fig.8) essentially exceeds the value of square of index of refraction n_0^2 . This means that besides the positions in theory [6-7] and experimentally observed molecular mechanisms of dipole polarization in the direction perpendicular to optical axis LCA there are other dipole mechanisms.

They can be intramolecular rotation of polar groups and conformation reconstructions of molecules. For detail investigation of all polarization dipole mechanisms by LC method of dielectric spectroscopy the use of super-high frequency technique is required. However, there is the possibility of obtaining of information necessary for us only with the help of methods of radio-frequency range. For this reason the mesomorphic genes having the liquid-crystal phase in the region of negative temperatures or having the big viscosity at room temperatures can be used as investigation objects.

At this the relaxation frequencies corresponding to different dispersion regions of dielectric constants of LC shift to the region of low frequencies.

The radio-frequency range is enough for experimental investigation of molecular mechanisms of dielectric polarization connected with longitudinal component of dipole moment (rotation of molecules round transversal axis) by the method of dielectric spectroscopy [83-90].

The quantitative study of total complex of dipole mechanisms which are responsible for dispersion of main values of dielectric constants of individual mesomorphic genes in liquid-crystal and isotropic-liquid states requires the carrying of ϵ_{\parallel} , ϵ_{\perp} and ϵ_{us} measurements in wide frequency range of electric field including the super-high frequencies up to 10^{11} Hz [91-93].

At absence of measuring equipment of super-high-frequency range for investigation of dipole-orientation mechanism one can use the multi-component mixtures of liquid crystals having the anisotropic melt in the region of negative temperatures. At low temperatures the relaxation frequencies from super-high-frequency range shift to the side of radio frequencies as a result of high substance viscosity [8-9].

Table 5

The dielectric susceptibilities χ and limitation parameters of molecules x_1 and x_2 of LC6 and LC7.

	$t^\circ\text{C}$	ϵ_{II}	χ_{II}	$\chi_{II}^{def}, \text{CM}^3$	$\chi_{II1}^{op}, \text{CM}^3$	$\chi_{II2}^{op}, \text{CM}^3$	x_1	x_2
LC6	150	5.6	185	78	$97(1+x_1)$	$37(1+x_2)$	-	
LC7	128	5.4	177	87	$126(1+x_1)$	$33(1+x_2)$	0.40	
							-	
		ϵ_{\perp}	χ_{\perp}	$\chi_{\perp}^{def}, \text{CM}^3$	$\chi_{\perp1}^{op}, \text{CM}^3$	$\chi_{\perp2}^{op}, \text{CM}^3$	x_1	x_2
							0.56	

Table 6

The limitation parameters of molecular rotation molecules x_1 and x_2 in LC6 for different frequencies and temperatures.

$t^\circ\text{C}$	x_1				x_2			
	0,15 MHz	0,5 MHz	1,5 MHz	5-30 MHz	0.15-5 MHz	10 MHz	20 MHz	30 MHz
163	-0.4	-0.4	-0.4	0.7	0.1	0.1	0.1	0.1
110	0.7	0.8	0.85	0.85	0.1	0.1	0.1	0.05
90	-0.9	-0.9	-0.9	-0.9	0.1	0.03	-0.05	-0.1
70					0.15	0	-0.2	0.35

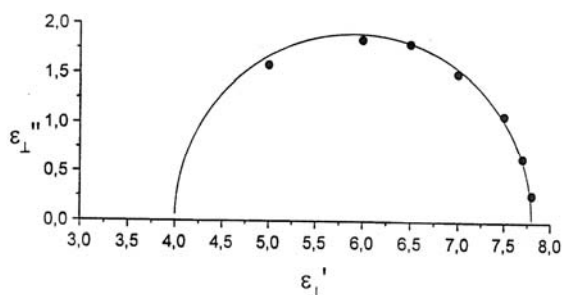


Fig. 8. Circle diagram for ϵ_{\perp}^* LC6.

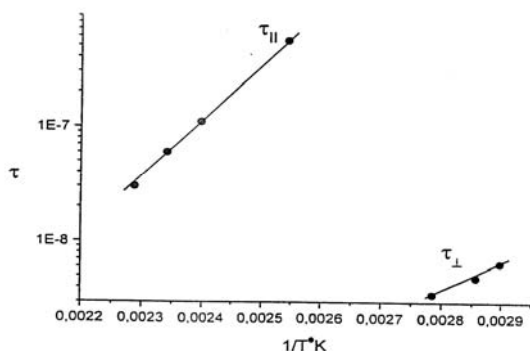


Fig. 9. The dependence of relaxation time τ_{II} and τ_{\perp} on reversal temperature for LC6.

However, in this case the presence of several relaxation times corresponding to different molecules of mesomorphic genes by geometric value and chemical structure consisting in mixture opposites to analysis of experimental results. The another possibility of

quantitative study of all dipole mechanisms can be realized at investigation of individual mesomorphic genes having the low transformation temperature into isotropic phase and also the big geometric sizes of molecules allowing to expect the low values of relaxation frequencies.

In the work for quantitative study of whole complex of dipole mechanisms responsible for dispersion of main values of dielectric constants of individual mesomorphic gene in liquid-crystal and isotropic-liquid states the monotropic 4-cyano-3-chlorfenile ether 4-hexyl-3-chlordefenil-4-carboxylic acid (LC8) is used.

The structural formula, molecular characteristics and temperatures of phase transformations which are presented in table 7.

The investigated sample has the monotropic nematic (N) state in interval $23^\circ - 33^\circ\text{C}$ between crystalline (K) and isotropic (I) phases.

The choice of this substance as investigation object is defined by the fact that firstly it has LC-phase in region of room temperatures, secondly, its molecule consisting three benzene rings, two complex-ether groups and long end alkyl chain has comparably big sizes, thirdly there are some polar groups with different direction of dipole moment in the molecule and consequently, there are transversal and longitudinal components of molecular dipole moments essential by value. The given factors allows us the supposition that all dipole mechanisms connected with molecule rotation round its long and short axes can make the essential contribution into dielectric polarization and reveal at its dispersion in radio-frequency range in both nematic and isotropic phases.

Table 7

Molecular characteristics of LC8

Short name of LC	Chemical structure and phase transformation temperature	$K_M, 10^{-9} \text{ r}^{-1} \text{ cm}^5 \text{ 300B}^{-2}$	$\mu \text{ D}$	$\Delta b \text{ 10}^{-25} \text{ cm}^3$	β°	$\Delta \epsilon$
LC8	$\begin{array}{c} \text{C}_6\text{H}_{13} - \text{C}_6\text{H}_4 - \text{C}_6\text{H}_4 - \text{COO} - \text{C}_6\text{H}_4 - \text{O} - \text{C}_6\text{H}_{13} \\ \quad \\ \text{Cl} \quad \text{Cl} \\ \text{K 85 H 164 И} \\ \text{4-cyano -3- chlorfenile ether 4-hexyl-3-chlobifenil-4-} \\ \text{carboxylic acid} \end{array}$	7,9	6,6	200	25	16

The study of electric double refraction (Kerr effect) and dielectric polarization of dissolved solutions of LC in tetrachlore methane allows the defining of value of molecular dipole moment μ and its direction (angle β) in molecules. The value consideration is equal to 6,6 Debye and 23° (table 7).

The measurements of dielectric constants of LC8 are carried out in frequency range 5Hz-100MHz in isotropic and in liquid-crystal phases. The dependence of imaginary part of dielectric constant ϵ''_{u3} on real one ϵ'_{u3} measured in isotropic state is given on fig.10.

It is easily to see that in frequency region $f=10^2-10^3$ Hz ϵ''_{u3} value treats the strong dispersion in the result of which the dielectric constant value differs from square of index of refraction $n_{u3}^2=2,62$ at the same temperature in frequency region $f=10^2-10^3$ Hz. This means that ϵ''_{u3} dispersion is accompanied by practically total exclusion of dipole mechanisms from dielectric polarization of investigated sample. At the same time the diagram presented on fig.10 obviously shows that for dispersion ϵ''_{u3} are responsible the some molecular mechanisms. That's why for further consideration and analysis of obtained experimental data it is comfortable to use the constructions of ϵ''_{u3} dependences as $\epsilon''_{u3} \cdot 2\pi f$ function. The given construction with use of experimental data (fig.10) is given on fig.10. The presented results indirectly illustrates that dispersion ϵ''_{u3} can be characterized by three dipole mechanisms with essentially differing frequency dispersion regions (practically on order) of dielectric constants (fig.11). The relaxation times τ_{u31} , τ_{u32} and τ_{u33} corresponding to different observed dispersion mechanisms ϵ''_{u3} at several temperatures are given in table 8.

The analogous results are obtained at dispersion experimental investigation of main values of complex dielectric constants $\epsilon''_{u3||}$ и $\epsilon''_{u3\perp}$ measured in directions parallel and perpendicular to optical axes of macroscopically homogeneous oriented sample in nematic phase. Koul-Koul diagram and corresponding construction of dependence $\epsilon''_{u3||}$ on $2\pi f \epsilon''_{||}$ are

presented on fig.12 and 11. The three dispersion regions of main dielectric constant nematic ϵ''_{u3} clear reveal in isotropic phase at each fixed temperature.

According to dispersion $\epsilon''_{u3\perp}$ it is also characterized by several mechanisms of dielectric relaxation that is directly illustrated by experimental data presented on fig.13. However, in last case the construction of dependence ϵ''_{\perp} on $\epsilon''_{\perp} \cdot 2\pi f$ (line 2 on fig.11) leads to smooth curve which doesn't allow emphasizing of different mechanisms responsible for dispersion $\epsilon''_{u3\perp}$ with the use of discussed before method. Probably this is connected with the fact that corresponding mechanisms defining the frequency dependence $\epsilon''_{u3\perp}$ are divided by frequencies essentially less than in dispersions $\epsilon''_{u3||}$.

In the given case for quantitative analysis of relaxation processes one can use the method supposed in ref [7] according to which the dependence construction of generated $d \epsilon''_{\perp} / d(2\pi f \epsilon''_{\perp})$ on $2\pi f \epsilon''_{\perp}$ allows the defining the number of relaxation processes n and their relaxation frequencies f_p . The analysis of curve $\epsilon''_{\perp} = (2\pi f \epsilon''_{\perp})$ with the use f_p and n allows us the emphasizing the contributions made by each relaxation mechanism into dispersion $\epsilon''_{u3\perp}$ and constructing for them the circle diagrams. The circle and Koul-Koul diagrams obtained by such way constructed by experimentally defined ϵ''_{\perp} and ϵ''_{\perp} at 24°C are presented on fig.13. The relaxation times $\tau_{\perp 123} = 1/2\pi f_{p123}$ corresponding to revealed relaxation processes are given in table 8. From the given data it is easily to see that values $\tau_{||2}$ and $\tau_{\perp 2}$ and also $\tau_{||3}$ and $\tau_{\perp 3}$ are practically the same. This can show on the fact that molecular mechanisms responsible for corresponding relaxation processes are similar ones. Probably for understanding and explanation of obtained experimental results it is necessary to consider the analysis of molecule dipole construction of investigated sample.

$\mu=6,6\text{D}$ and $\beta=23^\circ$ values allows the establishing that dielectric properties of LC should be defined by not only one longitudinal component $\mu_{\parallel} = \mu \cos \beta$, but the essential contribution into dipole polarization can be

made by normal component of dipole moment $\mu_2 = \mu \cos\beta$. It is obvious that the more low-frequency mechanism responsible for dispersion of main dielectric constants in isotropic ϵ_{u3}^* and nematic ϵ_{II}^* and ϵ_{u3}^* is caused by mechanism of moment μ_1 . However, if dispersion ϵ_{II}^* and ϵ_{u3}^* is caused by mechanism of molecule rotation round short transversal axis then the other mechanism which is precession motion of molecule longitudinal axis on cone surface the realization of which is possible because of difference of order degree S of liquid crystal from unit [6,3] can be responsible for low-frequency dependence ϵ_{\perp}^* .

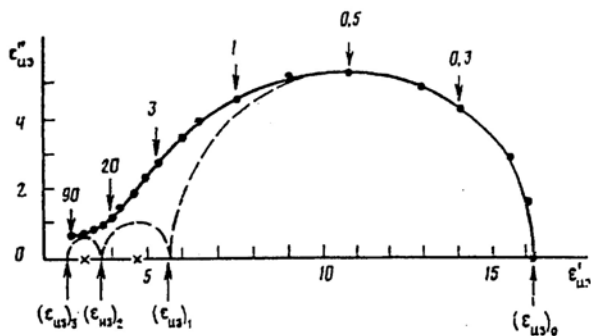


Fig. 10. Koulik diagram for ϵ_{u3} LC8 (67°). The frequencies are shown near hands in MHz.

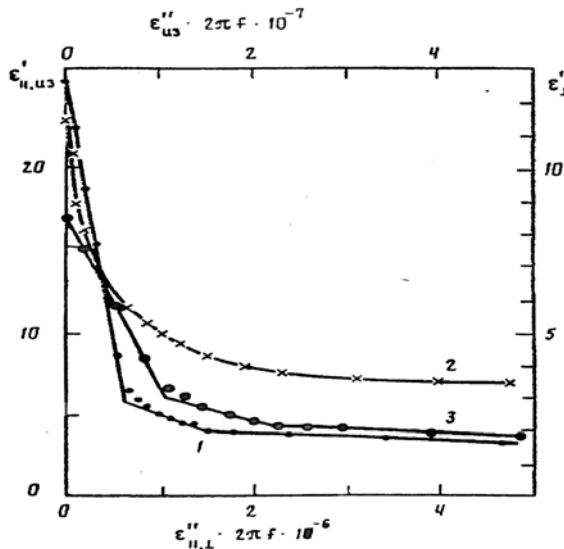


Fig. 11. The dependence ϵ' on $\epsilon''2\pi f$ LC for ϵ_{II} (1), ϵ_{\perp} (2), ϵ_{u3} (3) at temperatures 30°C, 24°C and 50°C correspondingly.

According to above mentioned the difference in time relaxations τ_{II} and τ_{\perp} is possible, i.e. the rotation of molecule longitudinal axis round transversal axis is connected with overcoming of potential barrier responsible for further orientation order in isotropic melt whereas the precession realization doesn't require the overcoming of potential barrier. It is obvious by the same

reason the one and the same mechanism of molecule rotation round short axis in nematic and isotropic states can be characterized by relaxation times τ_{II} and τ_{u3} differing more than one order. Along with mentioned above molecular mechanisms of dielectrically active ones there is the mechanism of molecule rotation round longitudinal axis the exclusion of which from dipole polarization is defined by the presence of dispersion second region ϵ_{II}^* , ϵ_{\perp}^* and ϵ_{u3}^* (fig.10-13).

According to more high-frequency region of dielectric relaxation it is obvious that it can be connected with intramolecular rotations of separate polar groups, for example, chlorcyanofenil fragment round para-aromatic bond of molecule having the conformation of "crankshaft" (8). The contribution of this mechanism into sample dipole polarization reveals in more high-frequency dispersion region ϵ_{II}^* , ϵ_{\perp}^* и ϵ_{u3}^* (fig.10 - 13).

The evidence of mentioned point of view relatively molecular dielectric relaxation in the investigated sample can serve the analysis of dipole construction with the use of obtained dielectric data obtained in present paper. Indeed, the possibility of experimental division of different mechanisms of dipole polarization (fig.10,13) can be used for finding of longitudinal and normal components of molecule dipole moment with the use of limit values of dielectric constants ϵ_{u3} corresponding to different frequency dispersion regions $\epsilon_{u30} = 16$, $\epsilon_{u31} = 5,7$, $\epsilon_{u32} = 3,7$ and $\epsilon_{u3} = n_{u3}^2 = 2,62$ (fig.1) and also formula:

$$\mu_{n+1}^2 = 9kT(\epsilon_n - \epsilon_{n+1})(2\epsilon_n + n_{is}^2 / 4\pi T \epsilon_n (n_{is}^2 + 2))$$

$$n=0,1,2,3...$$

in which $i=0,1,2$ it is easy to obtain the values $\mu_1 = \mu \cos\beta = 5.1D$, $\mu_2 = \mu \sin\beta = 2,4D$ and $\mu = 1,9D^\circ$. The values μ_1 , μ_2 and μ found by given method lead to value $\beta = 29^\circ$ which less differs from one found by independent method in solutions of the same sample. The results obtained in nematic phase can be also used in analysis of molecule dipole construction of investigated liquid crystal.

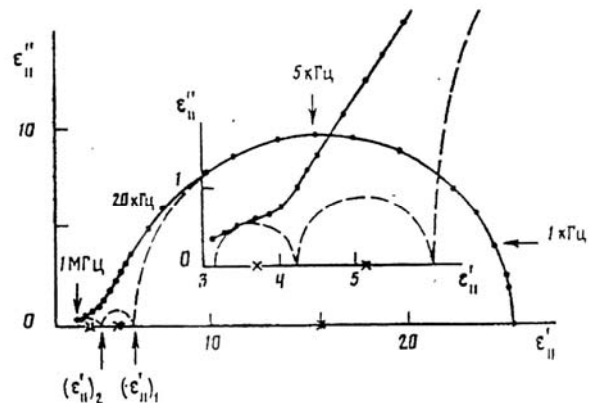


Fig.12. Circle diagrams for ϵ_{II}^* LC8 at temperature 30°C.

With this goal one can use the expressions defining the contributions into dielectric polarization ϵ_{II} и ϵ_{\perp} of dipole mechanisms connected with longitudinal and transversal components of molecular dipole moment:

$$\epsilon_{\parallel 0} - \epsilon_{\parallel 1} = 4\pi N h F^2 \mu_1^2 (1 + 2S) / 3kT \quad (9)$$

$$\epsilon_{\parallel 1} - \epsilon_{\parallel 2} = 4\pi N h F^2 \mu_2^2 (1 - S) / 3kT \quad (10)$$

$$\epsilon_{\perp 0} - \epsilon_{\perp 1} = 4 \pi N h F^2 \mu_1^2 (1 - S) / 3kT \quad (11)$$

$$\epsilon_{\perp 1} - \epsilon_{\perp 2} = 4 \pi N h F^2 \mu_1^2 \left(1 + \frac{S}{2}\right) / 3kT \quad (12)$$

The use of experimental values $\epsilon_{\parallel 0}=28,5$, $\epsilon_{\parallel 1}=6$, $\epsilon_{\parallel 2}=4,2$; $\epsilon_{\perp 0}=12,6$, $\epsilon_{\perp 1}=9,3$, $\epsilon_{\perp 2}=4,3$ of formulas (9)- (10) and $S=0,6$ at 24°C leads to values $\mu_1=\mu\cos\beta=5\text{D}$, $\mu_2=\mu\sin\beta=3,8\text{D}$ (formulas 9 and 10) $\mu_1=\mu\cos\beta=4,5\text{D}$, $\mu_2=\mu\sin\beta=3,8\text{D}$ (formulas 11 and 12). The obtained values some differ from LC found in isotropic phase as a result of approximated value of S orientation order degree value.

The experimental data presented on fig.12 and 13 are obvious illustration of the fact that intramolecular mechanism of polarization makes the contribution not only into dielectric properties in isotropic state but into main values of dielectric constants ϵ_{II}^* , ϵ_{\perp}^* in

anisotropic melt LC8. Thus the investigation of dispersion of main dielectric constants ϵ_{II}^* , ϵ_{\perp}^* and $\epsilon_{\perp 3}^*$ of monotropic LC8 allows the experimentally emphasizing of all dipole-orientation mechanisms of dielectric polarization in both nematic and isotropic phases.

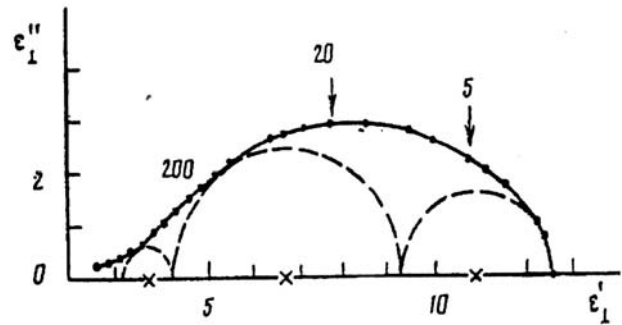


Fig.13. Circle diagrams for ϵ_{\perp}^* LC8 at temperature 24°C .

On the basis of experimental investigation of some classes of liquid-crystal materials with different molecular structure it is established that dipole contribution into parallel component of dielectric constant is caused by molecule rotation round short and long molecular axes. The dipole contribution into perpendicular component of dielectric constant is connected with molecule rotation round long molecular axes and also with rotation of molecule long axis round the direction of dominant orientation of liquid crystal on cone in angle limit given by orientation order in liquid crystal.

- | | |
|---|---|
| <p>[1]. S.V. Lyulin, Yu.Ya. Gotlib. Visokomolekulyarnie soedineniya. 1996. t.38A. № 2. s. 252-257. (in Russian)</p> <p>[2]. V.A. Marinin, L.V. Polyakova, Z.S. Korolkova. Vestnik LGU Seriya fizika i khimiya 1958. t. 3, s C. 73-77. (in Russian)</p> <p>[3]. Ch. Pul, F. Ouens. Nanotekhnologii. M.: Tekhnosfera, 2004. (in Russian)</p> <p>[4]. V.G. Rumyantsev, L.M. Blinov, V.A. Kizel i dr. Kristallografiya, 1973 t.18, №5, s.1101. (in Russian)</p> <p>[5]. Ch. Tauns, A. Shavlov. Radiospektroskopiya. 8</p> | <p>M. 1969.-286s. (in Russian)</p> <p>[6]. R.V. Talroze, G.A. Shandryuk, A.S. Merekalov, A.M. Shatalova, O.A. Otmakhova. Visokomolek. Soed. B. 2009, t. 51. № 3. s. 489. (in Russian)</p> <p>[7]. N. Tolstoy, V. Tsvetkov. DAN. 1941, t. 31. s. 230. (in Russian)</p> <p>[8]. Yu.D. Tretyakov, E.A. Gudilin. Vesti RAN. 2009, t. 79. № 1. s. 3. (in Russian)</p> <p>[9]. D.A. Ragimov. Fizicheskie svoystva i molekulyarnaya struktura makromolekul. Elm, Baku. 2003 -143 s. (in Russian)</p> |
|---|---|

OPTICAL PROPERTIES OF SrTiO₃ FILMS

A.A. AGASIYEV, E.M. MAGERRAMOV, Ch.G. AKHUNDOV,
M.Z. MAMMADOV, S.N. SARMASOV, G.M. MAMMADOV

Baku State University, AZ 1148, Baku, Z.Halilov str., 23

The spectrums of optical absorption of amorphous and single crystalline films SrTiO₃ at temperatures: 105K, 300K, 400K are investigated. The temperature dependences of slope absorption edge, forbidden gap and characteristic constant of Urbah rule are obtained. The forbidden gap of single crystalline film SrTiO₃ $E_g \approx 3.2$ eV and average shift of absorption edge $dE_g/dT = -8 \cdot 10^{-4}$ eV/degree are defined. It is established that edge of optical absorption of SrTiO₃ film is obeyed to Urbah rule and the absorption in the investigated region is caused by the transition of electron interacting with phonon.

1. INTRODUCTION

The semiconductor electronics is the important part of the basis of scientific and technological revolution. The projects of cybernetics and radio engineering, radio-electronic devices and number cruncher appear because of successes of growing technology of semiconductor crystals.

The foundation of semiconductor technology is the science of materials unusually influencing on whole scientific-technical progress. It deals with peculiar "synthetic" substance nature having the super-high frequency and crystalline perfection. The pure level is the sample for other material authority directions. Its conversion in technology of glassy materials allows us to improve the clarity of fibrous light-emitting diodes in milliard times and creating the new perspective type of laser communication: fiber systems. The first periods of industry development of semiconductor electronics were connected with elementary semiconductors: selenium, germanium, silicon.

The silicon is still the "basis" of transistor industry and new microprocessor technology. The more various semiconductor compounds are taken in future period. They are irreplaceable ones in light receivers of different wave band and also in diode radiation sources.

If earlier one can solve the appearing tasks by the way of material selection from known ones, then the problem of "crystal engineering" which is the creation of materials with earlier given properties becomes the more important as far as possible to widen the task circle and increase the requirements to materials. The forbidden gap, the type of band structure, carrier life times, lattice spacing and others are related to given parameters. The oxygen-octahedral compounds ((ABO₃, where A is alkali or alkaline-earth ion and B is ion of transitional element) have the series of interesting properties. They use in information systems and also as catalyzers because of ABO₃ materials have the empty d-states in conduction band [1]. The structure of these compounds consists of BO₆-octahedrons in which the A atoms occupy the empty places. In ABO₃ compound families there are the some basis structures: 1. perovskite structure; 2. trigonal structure; 3. the structure of tetragonal potassium-wolfram bronze.

These materials are already used in devices based on surface-acoustic waves and integral optics and also in holography and cryoelectronics [2-4]. The operation of these devices depends on fundamental properties of materials and external factors. The interest to this

compounds isn't exhausted by applied aspects. The study of BO₆ -octahedron role in ABO₃ materials can explain the many electronic phenomena taking place in these crystals, in particular, the revealing of distortion character of BO₆ octahedron at phase transitions (PhT), the change of interaction between A-O and B-O atoms and their influence on energy spectrum of electrons. Besides that the presence of transitional elements in the form of octahedral complexes in ABO₃ compounds makes these crystals the model ones for study and understanding of catalysis and adsorption processes.

All above mentioned stimulates the investigation of optical properties of thin layers of ABO₃ compounds in wide energy and temperature intervals with the aim of revealing of their electron structure connected with structural changes and character of interband transitions in thin layers of ABO₃ compounds.

In this connection we have carried out the investigation of optical properties of SrTiO₃ films being typical representative of ABO₃ compounds with perovskite structure in the region and on the edge of fundamental absorption.

2. EXPERIMENT TECHNIQUE

For measurement of absorption coefficient we chose the spectrophotometric technique with taking under the consideration of multiple reflections described in refs [5-6]. If the light falls on the sample having the form of plane-parallel plate (by d thickness) and the absorption in it isn't very big one, then one needs to take under consideration the multiple reflections. In the case when the interference isn't observed between transmission coefficient (T), absorption coefficients (α) and surface reflection (r) we obtain the following expression:

$$T = \frac{(1-r)^2 e^{-\alpha d}}{(1-r^2)e^{-2\alpha d}} \quad (1)$$

The measured reflection coefficient of R sample will be:

$$R = \frac{r[1 - e^{-2\alpha d}(2r-1)]}{(1-r^2)e^{-2\alpha d}} \quad (2)$$

Solving (1) and (2) relative to r and taking under consideration that R is always bigger than r we obtain:

$$r = \frac{(T^2 - R^2 + 2R + 1) - \sqrt{(T^2 - R^2 + 2R + 1)^2 - 4R(2 - R)}}{2(2 - R)} \quad (3)$$

Measuring T and R one can calculate r , knowing r by (1) one can find α values.

In the region of strong absorption $T \leq 0.1$, $\alpha d > 1$ and $\exp(-2\alpha d) \ll 1$. If one take under consideration that $r < 1$, then $r^2 \exp(-2\alpha d) \ll 1$.

$$\alpha = \frac{1}{d} \ln \frac{(1-r)^2}{T} \quad (4)$$

Using the expression (4) one can define α only for two samples at d_1 and d_2 thicknesses. If the transparency of both T_1 и $T_2 < 10\%$, then absorption coefficient of samples can be calculated by formula:

$$\alpha = \frac{1}{d_2 - d_1} \ln \frac{T_1}{T_2} = \frac{1}{d_2 - d_1} \ln \frac{E_1}{E_2}, \quad (5)$$

where E_1 and E_2 are intensities of beams passing through samples by d_1 and d_2 thicknesses. In the case $\alpha > 1$ the error at α definition from expression (4) doesn't exceed the maximal experimental one in the definition of reflection and transmission coefficients 2%.

The measurement of transmission T and reflection R coefficients in energy region (1-6eV) carry out on installation, the block scheme of which is shown on fig.1.

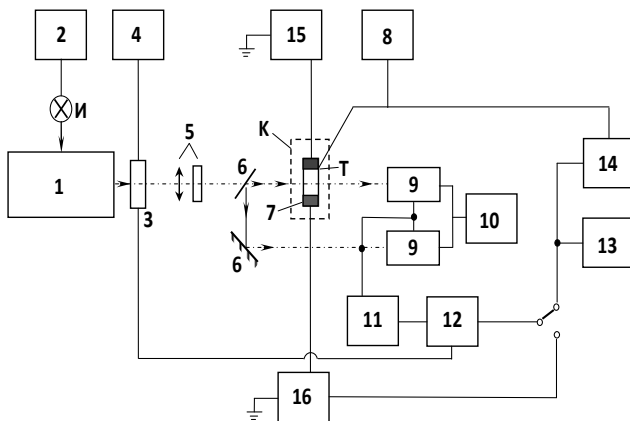


Fig. 1. The block diagram of measuring installation.

И- radiation sourceя (lamps: ДКСШ-150,500; КГМ 24-150);
 1 is monochromator (2-P); 2 is lamp power unit; 3 is mechanical modulator of light intensity; 4 is modulator power unit; 5 are lenses, filters; 6 are mirrors; 7 is sample; 8 is EMF measurer of (BK2-20) thermocouple; 9 are photoelectric multiplier (PhEM-39,51,79,83); 10 is PhEM power unit (Б5-24А); 11 is narrow-band amplifier of alternating current (У2-6); 12 is synchronous detector (К3-2); 13 is electronic numerical voltmeter (B7-21); 14 is two-coordinate potentiometer-self-recorder ЭНДИМ -620-02); 15 is stabilized source of direct current (ТЕС-7,ТЕС-88); 16 is electrometric amplifier of direct current (У5-9); К is cryostat ; Т is thermocouple.

The main parts of installation are:

1. Optical part is monochromators VSU2-P and SPM-2 for spectral region of radiation (1.0±6.0 эВ);

The system of receiving and increasing of the signal is the photoelectric multipliers ФЭУ-39,51,79,83; narrow-band resonance amplifiers У2-6 and Б6-4; synchronous phase-sensitive detector К3-2; modulation systems of light intensity and registration system of the signal which is two-coordinate electronic automatic recorder “ЭНДИМ -620”.

As the edge of optical absorption of the investigated films is in the near ultraviolet spectrum region, then iodide filament lamps with quartz balloon by power 150 watt and xenon lamps ДКСШ-150 the radiation intensity of which are supported as strongly constant one with the help of stabilization of voltage given to the lamp are used as the radiation sources. The change of stabilized supply-line on 10% is voltage ДКСШ-15 10⁻² %. Simultaneously the air lamp cooling is carried out. The prism from dense flint F-1, quartz prism and diffraction lattice on 600 шт/мм² are used for obtaining of monochromatic radiation in the dependence on spectrum region. The resolution of spectral devices along whole given spectrum region are not more than 5·10⁻³ eV.

At measurement of sample transmission the monochromatic radiation with E_0 intensity falling on the sample modulates by specially constructed mechanical interrupter with frequency 78 Hz. The light modulated with the given frequency passing through the sample falls on radiation receiver (ФЭУ-39,51,79,83) with sensitivity spectral region (0.16±0.6 мкм). The signal from ФЭУ arrives on input of selective amplifier У2-6 (Б6-4), increases and is given to input of phase-sensitive detector К3-2. The reference signal of the same frequency by 1,5V value from photodiode embedded in interrupter holder also is given on detector input. The friendly signal is recorded on two-coordinate automatic recorder “ЭНДИМ -620” emphasized on phase-sensitive detector. The record of (E_0) sample radiation is fixed by electronic voltmeters by B7-21 (or BK2-20) type with further record on automatic recorder. The series of neutral filters is used for measurement of light intensity.

All spectrum investigations are carried out in temperature interval (90±400K). The sample temperature is controlled by thermoelectromotive value of calibrated thermocouple cuprum-constantan. The sample heating up to 400K by linear law is provided for. The stabilization of the given temperature at investigation of temperature dependences in stationary mode is carried out with the help of modified block МР-64-02 through which the feed of cryostat heating elements from low-voltage stabilized source Б5-21 is made.

The films SrTiO₃ spread on quartz and glassy substrates are used for measurement of absorption spectrums. The film thickness varies in limits (0.5±3.5mkm). The spectrums of optical absorption of

amorphous and single crystalline films at temperatures: 105K, 300K, 400K.

2. THE RESULTS AND THEIR DISCUSSION

As it is seen from fig.2 and 3 for spectrum of absorption coefficient of single crystalline SrTiO₃ is clearly seen the exponential dependence of absorption coefficient on photon energy. The temperature increase leads to line shift into low-energy region. Moreover, it is also seen the change of absorption edge slope. The character changes are also observed for amorphous films (fig. 2) SrTiO₃. However, the picture isn't enough clearly expressed the dependence that is connected with film amorphism.

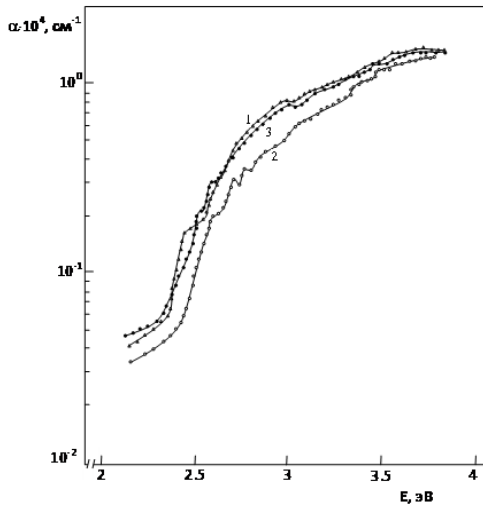


Fig. 2. The spectrums of absorption coefficient of SrTiO₃ amorphous films at different temperatures T: 1-300K, 2-105K, 3-400K.

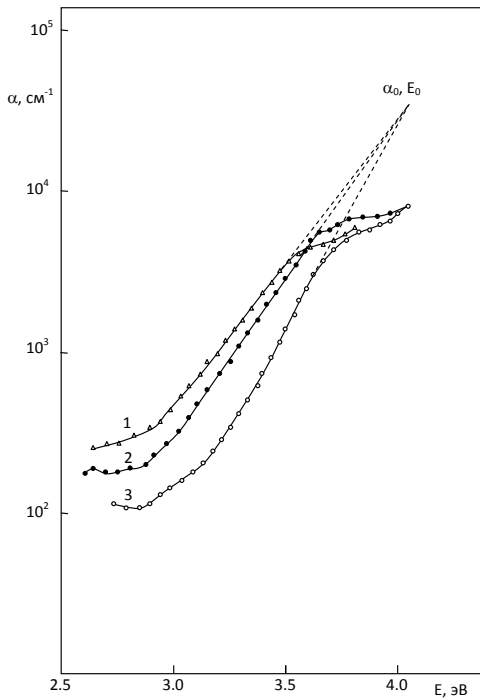


Fig.3. The spectrums of absorption coefficient of SrTiO₃ monocrystalline films at different temperatures T: 1-400K, 2-300K, 3-105K.

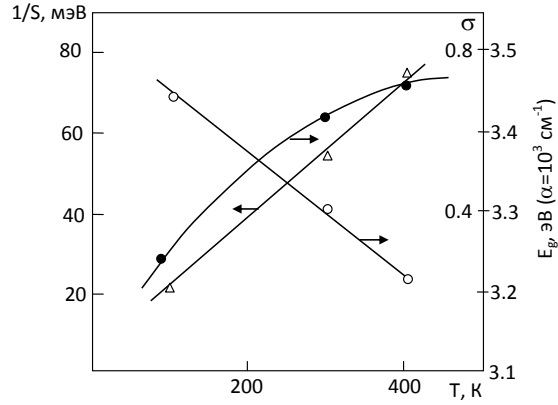


Fig. 4. The temperature dependences of absorption edge slope (1/s), forbidden band width (E_g) and σ (characteristic constant of Urbach rule) for SrTiO₃ monocrystalline film.

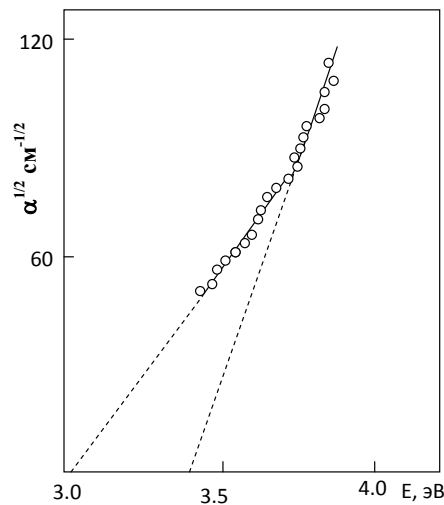


Fig.5. The spectrum $\alpha^{1/2}$ characterizing the presence of indirect transitions in SrTiO₃ monocrystalline films.

As it is seen from the figure the absorption coefficient in the range of values $\alpha=3 \cdot 10^{-3} \text{ cm}^{-1}$ exponentially depends on photon energy by law:

$$\alpha = \alpha_0 \exp \left[\frac{\sigma [T] (\hbar \omega - E_0)}{kT} \right], \quad (6)$$

where $S = \frac{\sigma}{kT}$ — is optical absorption edge slope, E_0 and

α_0 are character constants which are character to the given substance, σ is Urbah character constant. The analysis of spectral dependence α shows that absorption edge slope increases with temperature decrease which is the value by $S^{-1} \approx 53 \text{ meV}^{-1}$ order at room temperature.

The average shift of absorption edge $dE_g/dT = -8 \cdot 10^{-4} \text{ eV/degree}$ has been defined on the basis of carried investigations from temperature dependence of spectral characteristics on the level $\alpha=10^3 \text{ cm}^{-1}$. The temperature dependence of slope edge (S^{-1}), the forbidden gap (E_g) and character constant of Urbah rule [7] (fig.4) have been constructed. The carried investigations show

that absorption edge of SrTiO₃ film is obeyed to Urbah rule and the absorption in the investigated region is caused by electron transfer interacting with phonon. The construction of the dependence $\alpha^{1/2}$ on $h\nu$ reveals the

presence of indirect transition. From obtained data the forbidden gap $E_g \approx 3.2$ eV is defined. These data are well correlated with known single crystals well known from literature [8].

-
- [1]. *J. Pouma, K.G. Meyera.* Tonkiye plyonki, vzaimnaya diffuzii i reakcii, s.575. Moskva «Mir», 1982. (in Russian).
- [2]. *S. Cristoveamu* «Silicon on insulator tecnology and devices: from present to future». Solid Stat electronics, 45, p.1403-1411. 2001.
- [3]. *Yu.Ya. Tomashpolskiy, G.L. Platonov.* «Segnetoelektricheskiye plynki slojnikh okislov metallov», «Metallurgiya», s.200, Moskva. 1978. (in Russian)/
- [4]. *S.Ezhilvalahan, Tseng-Yseng.* «Progress in the development of (Ba, Sr) TiO₃ (BST) thin films fog Gigabit DRAMS», Materials Chemistry and physics. v.65. p. 227-248. 2000.
- [5]. *A.A. Agasiyev, M.M. Panakhov, Ch G. Akhundov, M.Z. Mamedov.* Nano- i mikrosistemnaya tekhnika 2007, № 10, s.17-19. (in Russian).
- [6]. *A.A.Agasiyev, Ch.G.Akhundov, G.M.Eivazova* «Electro conductivity of SrTiO₃ films with integrand barriers», Physic B, North-Holland, p.419, 1990.
- [7]. *Yu.I. Uxanov.* Opticheskiye svoystva poluprovodnikov. M.Nauka, 1997, s..368. (in Russian).
- [8]. *A.A.Agasiyev, Ch.G.Akhundov, M.Z.Mamedov* «Growth regularities and Electroconductivity of SrTiO₃ films obtained by magnetron sputtering» XII Evropean Conference “Investigation of surface”, Sweden, Stockholm. 9-12 September. 1991.

CONTENT

1.	Methods of integration of Yang-Mills self-duality equations M.A. Mukhtarov	3
2.	Investigations on pressure induced phase transition and disorder in ZnAl ₂ Se ₄ S. Meenakshi, V. Vijayakumar, A. Eifler, H. D. Hochheimer	10
3.	CdTe/CdS solar cells prepared by physical vapor deposition and close-spaced sublimation methods N.Fathi, R.Hajimammadov, M.Sadigov, E.Mirzoyev, A. Bayramov, G. Khrypunov, N. Klochko, and T. Li	15
4.	UV-transmission and fluorescence properties of polymer thin foils for use in microlens array fabrication Silvano Donati, Mao-Kuo Wei, Jiun-Haw Lee, Jhih-Hao Cai	20
5.	Growth of multicomponent solid solutions A ³ B ⁵ containing antimony by metal-organic chemical vapor deposition G. S. Gagis, V. I. Vasil'ev, and N.N. Mursakulov	23
6.	Comparison of the valence band structure peculiarities in the Bi _{0.84} -Sb _{0.16} -Sn _{0.1} and pure semiconducting Bi _{1-x} Sb _x alloys Bakir Tairov and Eltaj Yuzbashov	29
7.	Alternative II-IV-V ₂ and Zn-III-IV-As ₃ compounds for photovoltaic applications A. V. Krivosheeva, V. L. Shaposhnikov, V. E. Borisenko, J.-L. Lazzari	33
8.	Effects of pressure and temperature on properties of electronic-ionic conductors (GeS) _{1-x} (CuAsS ₂) _x Nina Melnikova, Ahmedbek Mollaev, Olga Kheifets, Luiza Saypulaeva, Peter Hohlachev, Abdulabek Alibekov, Alexey Filippov, Alexey Babushkin and Kirill Kurochka	37
9.	Electrical properties of multicomponent copper chalcogenides CuSnAsSe ₃ , CuInAsSe ₃ and CuInAsS ₃ Nina Melnikova, Ahmedbek Mollaev, Olga Kheifets, Luiza Saypulaeva, Fazil Gabibov, Abdulabek Alibekov, Alexey Babushkin, Kirill Kurochka	42
10.	Magnetovolume effect and magnetic phase transitions in ferromagnetic semiconductor Cd _{1-x} Mn _x GeAs ₂ under the pressure A.Yu. Mollaev, I.K. Kamilov, R.K. Arslanov, T.R. Arslanov, U.Z Zalibekov, V.M. Novotortsev, S.F. Marenkin	46
11.	The magnetotransport at high pressure in compounds of A ^{II} B ^{IV} C ^V ₂ doped by Mn A. Yu. Mollaev, I. K. Kamilov, R. K. Arslanov, T. R. Arslanov, U. Z Zalibekov, S. F. Marenkin, V.M. Trukhan	49
12.	About application of <i>n</i> -InAs and <i>n</i> -CdAs ₂ samples as reper and calibrator of pressure A.Yu.Mollaev, S.L.Saypulaeva, R.K.Arslanov, A.G.Alibekov, N.S.Abakarova	52
13.	Physical properties of SnS thin films grown by hot wall deposition V.F. Gremenok, S.A. Bashkirov, V.A. Ivanov, D.M. Unuchak, V.V. Lazenka, K. Bente	55
14.	Growth and characterization of GaInAsSb solid solutions with composition near the miscibility gap boundary N.N. Mursakulov, E.V. Kunitsyna, I.A. Andreev, Yu.P. Yakovlev, M. Ahmetoglu (Afrailov), and G. Kaynak	59
15.	Phonon scattering mechanisms in Ga _x In _{1-x} As single crystals M.I.Aliyev, I.X.Mammadov, D.H.Arasly, R.N.Rahimov, A.A.Khalilova	63
16.	Thermodynamical investigation of Yb-S system by EMF method M.A. Makhmudova, A.S. Abbasov, S.Z. Imamaliyeva, M.B. Babanli	67
17.	The longitudinal polarization of <i>B</i> -barion in semi-inclusive reactions S.K. Abdullayev, A.I. Mukhtarov, M.Sh.Gojayev	70
18.	Task solving method of wave diffraction on plane screens with fractional boundary conditions E.I. Veliyev, T.M. Akhmedov	79
19.	Some properties of the central heavy ion collisions Z. Wazir, M. K. Suleymanov, O.B. Abdinov, E. U. Khan, Mahnaz Q. Haseeb, M. Ajaz, K. H. Khan, Sh. Ganbarova	85
20.	Influence of acetic acid on the process of stain porous silicon formation at oxidant insufficiency F.A. Rustamov, N.H. Darvishov, M.Z. Mamedov, E.Y. Bobrova, H.O. Qafarova	89
21.	On interaction of macromolecules with the molecules of solvent in the system polyethyleneglycol – water H.F. Abbasov	92
22.	On the finite-difference analogue of the linear singular oscillator and its <i>su(1,1)</i> dynamical symmetry algebra S.M. Nagiyev, E.I. Jafarov, R.M. Imanov	94
23.	Determination of photo- and electroluminescence spectra of Pb _{1-x} Mn _x Se and Pb _{1-x} Mn _x Te thin films Sh.M.Abbasov, R.M.Mamishova, T.I.Kerimova, G.T.Ismayilova, I.R.Nuriyev, R.A.Ibrahimova	97

24.	Thermodynamic investigation of Yb-S system by EMF method M.A. Makhmudova, A.S. Abbasov, S.Z. Imamaliyeva, M.B. Babanli	99
25.	The temperature, frequency and voltage dependent characteristics of Al-TiW-Pd ₂ Si/n-Si structure using I-V, C-V and G/ω-V measurements I.M. Afandiyeva	102
26.	Deep and shallow acceptor levels in solid solutions Pb _{0,98} Sm _{0,02} S H.A. Hasanov, R.Sh. Rahimov	111
27.	Band structure calculation of GeS compound by LCAO method and deep levels of Ge _S and S _{Ge} antistructural defect investigation Z.A. Djahangirli	113
28.	Thermodynamic and electronic properties of hot electrons in a quantum well M.A. Mehrabova	117
29.	Electron diffraction examination of short – range atomic order in AgInS ₂ amorphous films D.I. Ismailov, E.E. Alekperova, N.K. Kerimova	122
30.	Physicochemical and thermodynamic properties of the GeSe ₂ -A ² B ⁶ (A ² = Hg; Cd; B ⁶ = S, Te) systems M.M.Asadov, A.D.Mirzoev	124
31.	Influence of γ- radiation on dielectric and electric properties of TlInS ₂ <Cr> crystals R.M. Sardarli, O.A. Samedov, I.I. Aslanov, A.P. Abdullayev, N.A. Eyyubova, F.T. Salmanov	128
32.	Molecular mechanisms OFD dielectric polarization of low-molecular and polymer liquid crystals D. Ragimov	132
33.	Optical properties of SrTiO ₃ films A.A. Agasiyev, E.M. Magerramov, Ch.G. Akhundov, M.Z. Mammadov, S.N. Sarmasov, G.M. Mammadov	142



www.physics.gov.az